Habilitation thesis

DIC-Based Measurements of Displacements and Deformations: Lessons Learned

Václav Nežerka

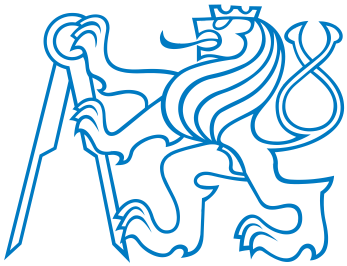

Czech Technical University in Prague
Faculty of Civil Engineering
Department of Physics

Prague, January 2022

Abstract

Digital image correlation (DIC) is a non-contact technique for monitoring of kinetic fields, independent of the material being tested or the length-scale. Mainly for its versatility, it has become indispensable in experimental mechanics for full-field monitoring of displacement and deformation. The use and research into DIC benefited from the rapid evolution of digital cameras and computers in recent years and a plethora of DIC methodologies and software codes, both commercial and independently developed, emerged. Even though these software tools reached their maturity, even the most advanced algorithms cannot compensate for improperly acquired images or poorly designed experiments. The goal of this thesis is to summarize the author's experience, to outline best practices, and to demonstrate the possibilities of DIC for displacement/deformation measurements using affordable equipment. Since experiments are often destructive and cannot be repeated, learning from mistakes and adopting the best practices can save enormous amount of time and resources.

Abstrakt

Korelace digitálního obrazu (DIC) je bezkontaktní metoda pro sledování kinetických polí, nezávisle na testovaném materiálu nebo délkovém měřítku. Především pro svou univerzálnost se stala nepostradatelnou v experimentální mechanice pro sledování polí posunů a deformací. Využití i výzkum DIC v posledních letech těžily z rychlého vývoje digitálních kamer a počítačů a vzniklo množství metodik a DIC programů, a to jak komerčních, tak nabízených jako freeware. Přestože tyto softwarové nástroje dosáhly své vyspělosti, ani nejpokročilejší algoritmy nemohou kompenzovat nesprávně pořízené snímky nebo špatně provedené experimenty. Cílem této práce je shrnout autorovy zkušenosti, nastínit osvědčené postupy a ukázat možnosti DIC pro měření posunů/deformací s využitím cenově dostupného vybavení. Vzhledem k tomu, že experimenty jsou často destruktivní a nelze je opakovat, poučení z chyb a osvojení správných postupů může ušetřit obrovské množství času a prostředků.

Contents

Chapter 1

Introduction

Strain gauges and linear variable differential transformers (LVDTs) used to be the most common instruments for measurements of strains and displacements. The principle of strain gauges, first described by Edward E. Simmons and Arthur C. Ruge in 1938 [1], is based on detecting changes in electric resistance of a fine wire or metalic foil due to its elongation. Strain gauges are usually glued directly to a test specimen surface using adhesives and the specimen deformation is proportional to a change in electrical resistance [2], calculated from recorded voltage. The interface between a strain-gauge carrier and the test specimen is usually the weakest link in the system [3]. For long-term measurements, additional unloaded strain gauge for compensation of temperature-induced changes is required. Moreover, strain-gauges can suffer from fatigue [4] and the measurement accuracy can be compromised due to imperfect attachment [5, 6]. The stiffness contribution to compliant specimens can also negatively influence the measurement [7].

Unlike strain gauges, LVDTs are used for measurements of relative displacements between two discrete points. LVDTs are scalable and their length is limited only by the production technology. In the simplest form, an LVDT consists of a cylindrical array of primary and secondary coils through which a cylindrical core passes as the point to which the LVDT is attached moves. The primary coil is supplied with alternating current, producing an alternating magnetic field in the center of the transducer. This magnetic field induces a signal into secondary coils and its amplitude depends on the position of the movable core. The output signal, after rectification and filtering, is in a form of direct current proportional to the core insertion. The sensor of LVDTs should be shielded to prevent misreadings due to sensitivity to magnetic fields [8].

Despite issues regarding their standardization, non-contact measurement methods have become a well-accepted alternative to strain gauges and LVDTs, or are often used as their complement. Non-contact methods methods allow capturing complex deformations until a total failure of tested specimens or structures [9, 10]. Non-contact methods can be generally categorized on those based on laser technology [11], radars [12], GPS [13], or video/digital image processing [14–18]. The last group, reffered to as optical measurement methods, include holography interferometry [19], speckle interferometry [20], moiré interferometry [21], and most importantly digital image correlation (DIC), being the subject of this thesis. The other optical methods loose their significance due to versatility, capabilities, and costs associated with DIC measurements [22].

DIC is commonly used for evaluation of kinematic fields from a series of pixel-based digital images. The utilization of correlation algorithms for such a purpose was first proposed by Yamaguchi [23] and Peters and Ranson [24]. Since that time, the method has been adopted in a wide range of research and engineering fields, from biomechanics [25, 26] to structural mechanics [27, 28] or dynamics [29]. DIC has no inherent lenght scale and depending on the optical system that is used for image acquisition, it allows to analyze microscopic observations [30, 31] but also large structures such as bridges [32] or dams [33]. The full-field data provided by DIC allow engineers to validate numerical models and easily identify material parameters [34–36], see Appendices A, C, and B. Unlike contact measurement methods, DIC can capture strain localizations, independent of a principal strain direction [22, 37].

As the term *correlation* indicates, the method is based on finding a match between a reference and deformed images. This is usually accomplished separately for small subsets of the images. These subsets have to contain sufficient amount of unique features so that the match can be found with a sufficient certainty. For that purpose, a homogeneous random pattern must be present on the observed surface to provide gray-level variations, either applied or occuring naturally [38]. Sufficient quality of these random patterns is essential for the DIC and the assessment of pattern quality is discussed in detail in Appendix D.

Regarding the correlation and best match seeking procedures, the evaluation of a subset displacements and deformations is accomplished by minimizing a correlation function [39] using a suitable optimization algorithm [40–43]. The optimization procedure becomes more demanding with an increasing size of subsets, however, subsets must be large enough to contain a sufficient number of features to track [44]. The resolution of calculated kinetic fields depends on the image resolution, pattern density, and image sharpness.

Stereo (3D) DIC operates with a series of image couples taken with synchronized cameras. 3D surface geometry is reconstructed from each couple of images based on characteristics of the cameras and their objective lenses and relative positions of the cameras [45]. The correlation and 3D surface reconstruction provide information about the positions of subsets within 3D space and their respective displacement vectors [46, 47]. The computational costs associated with 3D surface reconstruction make stereo DIC much more demanding than 2D DIC, but the same principles for proper design and execution of experiments apply.

1.1 DIC principles

DIC algorithms can be categorized as (i) local (subset-based) [39, 48–51] and (ii) global, assuming continuity of dipslacment field [52–57]. For local DIC, subsets are processed independently, allowing parallelization of the computation. In global DIC, a region of interest is usually discretized into elements connected with nodes. According to Wang and Pan [58], local approach provides higher displacement precision and computational efficiency, while the global DIC can be advantageous for comparisons between numerical models and experimental observations. This thesis focuses only on the local formulation utilized in Ncorr software [59], used in the case studies enclosed to this thesis in Appendices.

The unique correspondence between texture points positioned on a regular grid is sought for each subset of pixels within a deformed image. It is accomplished by finding a maximum of

a correlation matrix calculated for the deformed and reference images. The matching procedure yields a position of the subset within the reference image and an initial displacement having an integer-pixel accuracy. Specific algorithms operating with pixel intensity changes, such as non-linear optimization or curve-fitting [60], are then employed to reach subpixel accuracy. The whole procedure is then repeated for each subset and time-step to obtain a complete dataset. Fitting a plane over a predefined domain using the least squares method is used to calculate strains from displacement fields, in order to tackle the sensitivity of derivatives (strains) to local disturbances in differentiated fields (displacements) [42].

The following paragraphs illustrate the whole matching procedure. Consider a subset transformation (Figure 1.1) and let us introduce local coordinates points (i, j) within the subset, denoted as $1, 2, ..., 7$ as

$$\mathbf{S} = [(-1, 0), (-1, 1), (0, -1), (0, 0), (0, 1), (1, -1), (1, 0)]\,. \tag{1.1}$$

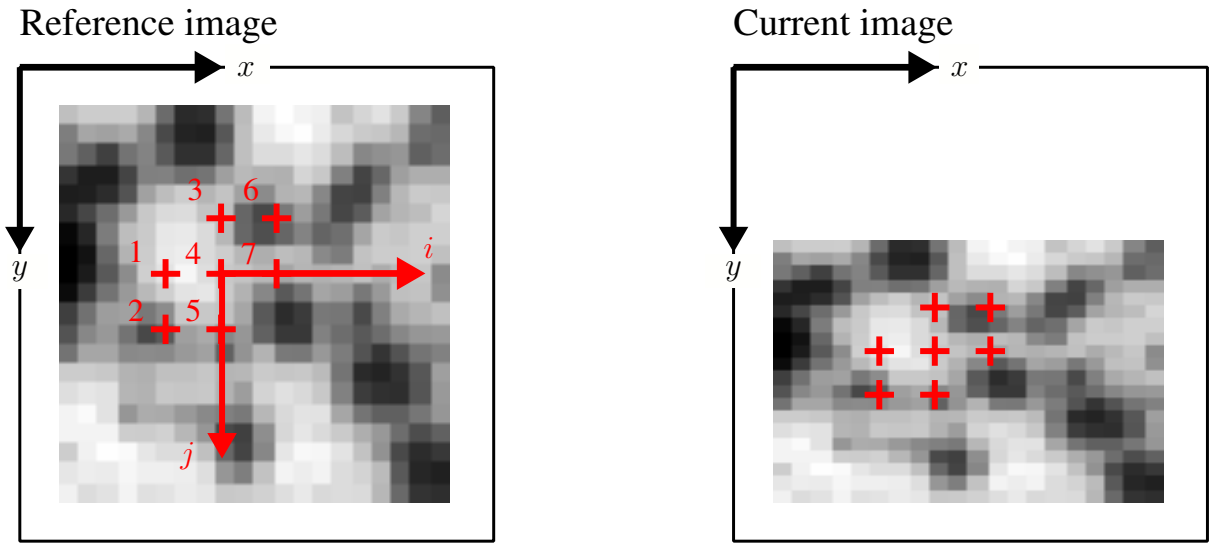

Figure 1.1: Subset local coordinates and matched points located within a reference and a current image, reproduced from [61] (courtesy of Jakub Antoš).

The translation and deformation of the reference subset points is considered to obey linear transformations using a first-order displacement mapping function in the form

$$\begin{aligned} \widetilde{x}_{\mathrm{cur},i} &= x_{\mathrm{ref},i} + u_{\mathrm{rc}} + \frac{\partial u}{\partial x_{\mathrm{rc}}}(x_{\mathrm{ref},i} - x_{\mathrm{ref,c}}) + \frac{\partial \mathrm{u}}{\partial y_{\mathrm{rc}}}(y_{\mathrm{ref},j} - y_{\mathrm{ref,c}}), \\ \widetilde{y}_{\mathrm{cur},j} &= y_{\mathrm{ref},j} + v_{\mathrm{rc}} + \frac{\partial v}{\partial x_{\mathrm{rc}}}(x_{\mathrm{ref},i} - x_{\mathrm{ref,c}}) + \frac{\partial v}{\partial y_{\mathrm{rc}}}(y_{\mathrm{ref},j} - y_{\mathrm{ref,c}}), \end{aligned} \tag{1.2}$$

where $(i, j) \in \mathbf{S}$, $x_{\mathrm{ref},i}$ and $y_{\mathrm{ref},j}$ are the horizontal and vertical coordinates of the initial reference subset point, $x_{\mathrm{ref},c}$ and $y_{\mathrm{ref},c}$ are the coordinates of its the center, $\widetilde{x}_{\mathrm{cur},i}$ and $\widetilde{y}_{\mathrm{cur},j}$ are the coordinates of the final subset point after deformation and $\partial u/\partial x_{\mathrm{rc}}$, $\partial u/\partial y_{\mathrm{rc}}$, $\partial v/\partial x_{\mathrm{rc}}$, $\partial v/\partial y_{\mathrm{rc}}$ are displacement gradient components, and u, v are translations of the subset center in the x and y directions, respectively. The subscript $_{\mathrm{rc}}$ indicates that the coordinate system is transformed from the reference to the deformed (current) one.

A general form of the deformation matrix can be written as

$$\mathbf{p} = \begin{bmatrix} u & v & \frac{\partial u}{\partial x} & \frac{\partial u}{\partial y} & \frac{\partial v}{\partial x} & \frac{\partial v}{\partial y} \end{bmatrix}^{\mathrm{T}} \tag{1.3}$$

with geometrical meaning of individual elements illustrated in Figure 1.2. Any linear combination of the six elements in $\mathbf{p}$ can be described by a warp function w, allowing to rewrite the Equation (1.2) in a matrix form:

$$\xi_{\mathrm{ref,c}} + w(\triangle\xi_{\mathrm{ref}}, \mathbf{p}_{\mathrm{rc}}) = \begin{bmatrix} x_{\mathrm{ref,c}}^{\mathrm{T}} \\ y_{\mathrm{ref,c}}^{\mathrm{T}} \\ 1 \end{bmatrix} + \begin{bmatrix} 1 + \frac{\partial u}{\partial x_{\mathrm{rc}}} & \frac{\partial u}{\partial y_{\mathrm{rc}}} & u_{\mathrm{rc}} \\ \frac{\partial v}{\partial x_{\mathrm{rc}}} & 1 + \frac{\partial v}{\partial y_{\mathrm{rc}}} & v_{\mathrm{rc}} \\ 0 & 0 & 1 \end{bmatrix} \begin{bmatrix} \Delta x_{\mathrm{ref}}^{\mathrm{T}} \\ \Delta y_{\mathrm{ref}}^{\mathrm{T}} \\ 1 \end{bmatrix}, \tag{1.4}$$

where ξ is a vector containing the x and y coordinates of the subset points, Δx and Δy are the distances between the subset points and the center of the subset, and w is the warp function. The deformation of the reference subset to match the current one follows [59]

$$\begin{aligned} \widetilde{x}_{\mathrm{ref},i} &= x_{\mathrm{ref},i} + u_{\mathrm{rr}} + \frac{\partial u}{\partial x_{\mathrm{rr}}}(x_{\mathrm{ref},i} - x_{\mathrm{ref,c}}) + \frac{\partial u}{\partial y_{\mathrm{rr}}}(y_{\mathrm{ref},j} - y_{\mathrm{ref,c}}), \\ \widetilde{y}_{\mathrm{ref},j} &= y_{\mathrm{ref},j} + v_{\mathrm{rr}} + \frac{\partial v}{\partial x_{\mathrm{rr}}}(x_{\mathrm{ref},i} - x_{\mathrm{ref,c}}) + \frac{\partial v}{\partial y_{\mathrm{rr}}}(y_{\mathrm{ref},j} - y_{\mathrm{ref,c}}), \end{aligned} \tag{1.5}$$

where $\widetilde{x}_{\mathrm{ref},i}$ and $\widetilde{y}_{\mathrm{ref},i}$ are the coordinates of the reference subset point position within the current image. The subscript $_{\mathrm{rr}}$ denotes the transformation from the reference coordinate system.

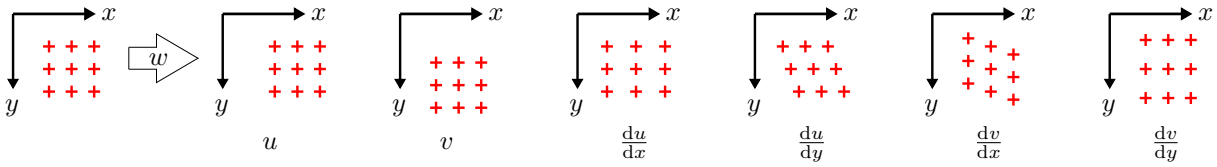

Figure 1.2: Linear transformations for subset coordinates, reproduced from [61] (courtesy of Jakub Antoš).

DIC codes, such as Ncorr, then optimize $\mathbf{p}_{\mathrm{rc}}$ when $\mathbf{p}_{\mathrm{rr}} = 0$ so that the evaluated coordinates $\widetilde{x}_{\mathrm{ref},i}$ and $\widetilde{y}_{\mathrm{ref},j}$ match the coordinates $\widetilde{x}_{\mathrm{cur},i}$ and $\widetilde{y}_{\mathrm{cur},j}$.

There have been numerous similarity criteria developed for comparing gray-scale intensity distributions within subsets, classified according to their definitions: cross-correlation (CC), a sum of absolute differences (SAD), a sum of squared differences (SSD), and parametric sum of squared differences (PSSD) [43, 51, 62–65]. The most commonly used uses normalized cross-correlation (NCC) for the initial guess of the u and v translation as

$$C_{\mathrm{CC}} = \frac{\sum_{(i,j)\in \mathrm{S}} (f(\widetilde{x}_{\mathrm{ref},i}, \widetilde{y}_{\mathrm{ref},j}) - f_{\mathrm{m}})(g(\widetilde{x}_{\mathrm{cur},i}, \widetilde{y}_{\mathrm{cur},j}) - g_{\mathrm{m}})}{\sqrt{\sum_{(i,j)\in \mathrm{S}} \left[f(\widetilde{x}_{\mathrm{ref},i}, \widetilde{y}_{\mathrm{ref},j}) - f_{\mathrm{m}}\right]^2 \sum_{(i,j)\in \mathrm{S}} \left[g(\widetilde{x}_{\mathrm{cur},i}, \widetilde{y}_{\mathrm{cur},j}) - g_{\mathrm{m}}\right]^2}}, \tag{1.6}$$

where f and g represent gray-scale values of the reference and current subsets, respectively, and f_m and g_m are their mean values, defined as

$$\begin{aligned} f_\mathrm{m} &= \frac{\sum_{(i,j)\in \mathrm{S}} f(\widetilde{x}_{\mathrm{ref},i}, \widetilde{y}_{\mathrm{ref},j})}{\mathrm{n}(\mathbf{S})}, \\ g_\mathrm{m} &= \frac{\sum_{(i,j)\in \mathrm{S}} g(\widetilde{x}_{\mathrm{cur},i}, \widetilde{y}_{\mathrm{cur},j})}{\mathrm{n}(\mathbf{S})}, \end{aligned} \tag{1.7}$$

where $\mathrm{n}(\mathbf{S})$ is the number of elements in $\mathbf{S}$. Normalization of the cross-correlation in Equation (1.6) is necessary for practical reasons as light conditions can change during the experiment, shifting the mean gray-scale intensities towards brighter or darker shades.

In the next step, instead of maximizing C_CC defined in Equation (1.6), it is advantageous to optimize the subsets least-squares correlation C_LS to reach a minimum of $C_\mathrm{LS}(\mathbf{p}_\mathrm{rc}) = \mathrm{minimum}$ [66].

$$C_\mathrm{LS} = \sum_{(i,j)\in \mathrm{S}} \left[\frac{f(\widetilde{x}_{\mathrm{ref},i}, \widetilde{y}_{\mathrm{ref},j}) - f_\mathrm{m}}{\sqrt{\sum_{(i,j)\in \mathrm{S}} \left[f(\widetilde{x}_{\mathrm{ref},i}, \widetilde{y}_{\mathrm{ref},j}) - f_\mathrm{m}\right]^2}} - \frac{g(\widetilde{x}_{\mathrm{cur},i}, \widetilde{y}_{\mathrm{cur},j}) - g_\mathrm{m}}{\sqrt{\sum_{(i,j)\in \mathrm{S}} \left[g(\widetilde{x}_{\mathrm{cur},i}, \widetilde{y}_{\mathrm{cur},j}) - g_\mathrm{m}\right]^2}} \right]^2. \tag{1.8}$$

Optimal $\mathbf{p}_\mathrm{rc}$ can be found using different optimization algorithms, e.g., the inverse compositional Gauss-Newton (IC-GN) method [51, 67].

The Green-Lagrangian strains are obtained from the displacement fields as their gradients, following

$$\begin{aligned} \varepsilon_\mathrm{xx} &= \frac{1}{2}\left(2\frac{\partial u}{\partial x} + \left(\frac{\partial u}{\partial x}\right)^2 + \left(\frac{\partial v}{\partial x}\right)^2\right), \\ \varepsilon_\mathrm{xy} &= \frac{1}{2}\left(\frac{\partial u}{\partial y} + \frac{\partial v}{\partial x} + \frac{\partial u}{\partial x}\frac{\partial u}{\partial y} + \frac{\partial v}{\partial x}\frac{\partial v}{\partial y}\right), \\ \varepsilon_\mathrm{yy} &= \frac{1}{2}\left(2\frac{\partial u}{\partial y} + \left(\frac{\partial u}{\partial y}\right)^2 + \left(\frac{\partial v}{\partial y}\right)^2\right). \end{aligned} \tag{1.9}$$

Numerical fitting of a plane within a strain averaging window to find the gradients enables to control the noise in the strain field and the degree of strain smoothing. The equation for fitting linear planes to the displacement fields are defined as

$$u_\mathrm{plane}(x,y) = a_{u,\mathrm{plane}} + \left(\frac{\partial u}{\partial x_\mathrm{plane}}\right)x + \left(\frac{\partial u}{\partial y_\mathrm{plane}}\right)y \tag{1.10}$$

$$v_\mathrm{plane}(x,y) = a_{v,\mathrm{plane}} + \left(\frac{\partial v}{\partial x_\mathrm{plane}}\right)x + \left(\frac{\partial v}{\partial y_\mathrm{plane}}\right)y \tag{1.11}$$

1.2 Camera settings

Sufficient quality of images for DIC analysis is crucial. Camera sensors convert light into electrons and capture the entire image frame at once on a grid, sufficiently large to avoid noise

and small enough to provide high resolutions with sensors that can be fit into a camera [68]. Sensors embedded in mobile phones seem to provide high-quality photos, however, the noise associated with the phones' small sensors (often artificially corrected using an embedded software) and lack of options to avoid automatic focus and stabilization render phone cameras useless for the delicate and sensitive DIC measurements. On the other hand, large DSLR (digital single-lens reflect) or indiustrial cameras equipped with chips having a large physical pixel size offer images with a high dynamic range and little noise provide sufficient resolution and image quality.

Even the most advanced cameras require an experienced operator for their proper setting with respect to the experiment scale and environment. First parameter to adjust after the specimens are set in place and illuminated is aperture, i.e., the lens diaphragm opening. It regulates the amount of light passing onto a sensor when a shutter curtain opens. The parameter does not only regulate the amount of light passing onto the sensor, but also affects the depth of field. Therefore a precise setting is needed to avoid unfocused areas in the region of interest. Another parameter influencing the amount of light passing onto the sensor is shutter speed. Shutter speed must be set high enough, relative to the motion of the observed surface, to avoid its smearing. For quasi-static tests performed under good illumination, 1/10 s is usually optimum but it is not enough for recording abrupt failures after the loss of structural stability. Last parameter that has a crucial impact on the brightness of images is ISO, i.e., a level of sensitivity to light. The ISO parameter should be set as low as possible to avoid excessive noise and grainy images (low signal-to-noise ratio).

1.3 Lenses

Optical lenses play a crucial role in providing high-quality undistorted images. The use of unsuitable or low-quality lenses results in optical aberrations (non-uniform geometric image distortions [69–72]) or additional errors compromising the quality of images [70, 73–75].

Short objective lenses causing fish-eye distortions should be avoided for DIC, despite existence of various camera calibration techniques to compensate these errors [76–79]. Telephoto lenses, having the outermost element of a short focal length and the second set of elements close to a sensor, are the most suitable for DIC measurements since the cone of light entering the camera appears to have come from a lens of a large focal length. This behavior eliminates the effects of perspective vision a gets close to a orthographic view. A perfectly ortographic image can be achieved using telecentric lenses [80]. It is worth mentioning that even in the orthographic view, the unwanted out-of-plane deformations caused by rotations of the observed surface introduce errors in planar projections and should be avoided for 2D DIC [25, 81].

1.4 Image compression and file formats

Common cameras transform exposure of sensor pixels, recorded in an analog form as a voltage level, to a digital signal [82]. The sensors can handle grayscale (monochrome) or red-green-blue (RGB) color channels for each pixel. The intensities for each channel are usually stored

in 8 bits of memory per pixel, yielding $2^8 = 256$ color resolution. Metadata containing information about the light transformation, camera settings, and byte-ordering are usually stored in RAW files along with the matrix representation of the images [83].

The RAW format is in most cases inconvenient to work with and encoding of data bits takes place in a standardized way to enable decoding. There are several established raster image formats (bitmap), such as *bmp*, *jpeg*, *tiff*, and *png*. These formats allow lossy compression based on eliminating redundancies to save memory [84]. Even though the data discarded during the lossy compression are usually nonessential to human perception [87], the loss of detail can be harmful for delicate DIC measurements and high compression rates are not advisible.

Mathematical redundancy elimination, such as replacing repeating patterns using mathematical formulas, is encoded in *tiff* and *png* formats and is lossless [85]. It is most efficient for simple images containing lines and flat colors [86].

1.5 DIC software

Numerous DIC codes have been developed over the last two decades, a period considered a boom period for DIC in experimental mechanics. Two toolkits are used for DIC analyses in this thesis: (i) a widely used open-source software that was complemented with a post-processing tool developed by the author and (ii) software developed by the author and tested under his supervision.

The first software suite (i) is based on Ncorr open-source 2D DIC MATLAB program [59, 88] whose algorithms are introduced in Section 1.1, complemented with the postprocessing tool Ncorr_post[1] (more information in Section 3.1).

The second set of scripts (ii) was developed in Python and is based on a discrete Fourier transform (DFT); the procedures are thoroughly described in Apendices E and F. The DFT-based approach is suitable for fast lightweight calculations as demonstrated in the aforementioned apendices and Appendix G and outlined in Section 3.3.

[1] Available at https://omlab.fsv.cvut.cz/software/

Chapter 2

Lessons learned the hard way

Wrong settings of the subset size, lens distortions, and unwanted camera/sample motion are most frequent causes of improper DIC measurements and the source of inaccuracies [89]. Even if the camera is set properly and secured, the measurement can be completely spoiled by significant changes in the environment (light, temperature, or humidity), equipment failure, or people sabotaging the measurements by standing in the camera view and shielding the region of interest (Figure 2.1). The following examples present the cases when the measurements were compromised due to changes in weather conditions in unexpected ways.

Figure 2.1: Obstructions in a camera view during a long-term experiment: a person (top-left), concrete blocks (top-right), a crane (bottom-left), and laboratory furniture (bottom-right).

2.1 Outdoor measurements and changes in light conditions

During DIC measurements, there are two moments when the experimentalist heart starts pounding: first, when placing the SD card from a camera to a computer and waiting for the images to show up, and second, when studying the image quality and sharpness of the observed patterns or textures. The following example demonstrates how incorrect setting of ISO parameter almost spoiled results of a very expensive test. The experiment took place at the D6 highway before opening a newly built bridge at 40.760 km on September 17, 2020. The loading was prescribed by a structural engineer and accomplished using fully loaded trucks changing their positions to induce critical load combinations.

During laboratory experiments, it is common to set the ISO parameter to a fixed value. Laboratory environment usually offers almost constant illumination and therefore the best practices for laboratory measurements cannot be adopted outdoors, especially if the measurement lasts several hours. Despite clear sky, the sunshine intensity changes rather significantly as demonstrated by this example.

The surface of the monitored concrete bridge had a faint texture, limiting the DIC measurements, and enhancing the texture using color sprays was not possible. Yet, based on previous experience, there was a good chance that even such a poor texture could be sufficient if the parameters affecting the sensitivity to light (the combination of ISO, aperture, and shutter speed) were set correctly. However, not allowing the camera (Canon EOS 70D) to change these parameters dynamically with respect to the light conditions resulted in overexposed images not suitable for DIC (Figure 2.2).

Figure 2.2: Image of the monitored bridge overexposed due to changes in the sunshine intensity over the course of the day.

The loss of detailed texture on the bridge surface rendered the full-field evaluation using the intensity-based correlation impossible. Fortunatelly, the in-house DFT-based correlation scripts allowed to track the motion of the bridge beam's bottom edge and limit the subset displacements

only to vertical movements. The scatter of the recorded data indicated the absolute accuracy of the measurement about 0.25 mm. Camera movements due to wind gusts were eliminited by calculations of relative displacements with a reference subset of assumed zero movement above the right bridge support (Figure 2.3). The measured deflection curve was in agreement with LVDTs and predictions of numerical models.

Figure 2.3: Bridge deflection measured from deck edge translation tracking using DFT-based correlation algorithms.

2.2 Effect of camera temperature during long-term measurements

Long-term measurement of minute translations (< 10% of a pixel size) using DIC algorithms is somewhat of a nightmare for every experimentalist. All measurements are to some extent affected with the environment and even vibrations caused by the camera shutter introduce a noise that is hard to eliminate. The most typical sources if inaccuracies, such as camera vibrations, the effect of lens distortions, camera movement due to its improper attachment, or out-of-plane motions of the observed surface, can be quite easily identified and some of these even corrected. All these effects were taken into a considereation during the long-term shrinkage measurents (axial deformation) of sealed concrete beams (Figure 2.4) that exhibited completely different behavior than predicted using numerical models.

First, the effect of bending was eleminated, but the axial deformation was still very different from the predicted values and oscilated with a somewhat regular period that changed over the course of year. The images were thoroughly studied for sunlight occurances and temperature was measured on the surface of specimens to evaluate the effect of temperature changes. It was found that sunlight did not reach the studied beams, but the fluctuation in temperature hinted its effect, yet, the contraction/expasion of the observed beams was still larger by a significant

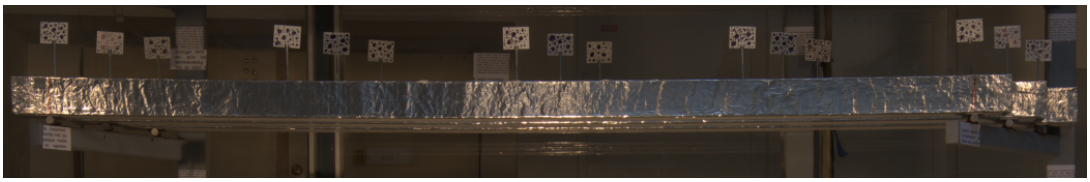

Figure 2.4: Simply supported 2.5 m long concrete beam analysed to study axial strains.

factor. Eventually, after a thorough analysis, it was found that not heating and cooling of the beams, but the camera temperature changes due to sun radiation comming from skylight was the source of inaccuracies. Since the camera temperature was not measured during the experiment, the axial deformation data had to be discarded.

Despite the robust body of common DSLR and advanced materials used for their production, temperature changes can spoil the DIC measurements where the highest quality of images is pursued [90, 91]. This issue was placed under scrutiny and tested. In this straightforward test, a completely sealed DSLR camera was heated for 10 minutes (too short for beam to deform due to temperature changes or shrinkage) using resistance wires, the camera temperature at its objective lens surface was recorded, and the images were taken to evaluate apparent axial deformations. From this test, clear correlation between these two parameters was revealed (Figure 2.5). Note that the results of this simple test should be used only to confirm the hypothesis, but more precise and well-designed measurements should be carried out to seek correction coefficients.

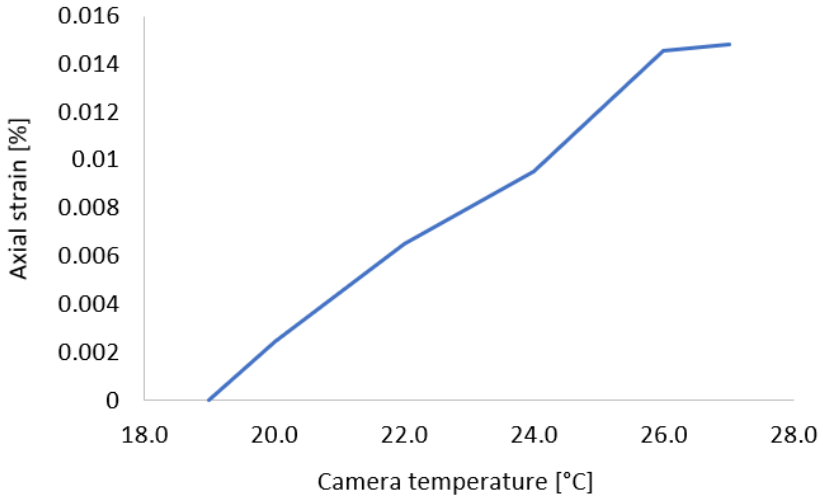

Figure 2.5: Relationship between the DSLR camera temperature and apparent axial strain of the monitored beam.

Chapter 3

Ongoing research

Beside the research activities reported in publications enclosed in Appendix A through G, the author engages in other activities related to non-contact measurements of displacements and deformations. These activities are briefly presented in the following sections.

3.1 Continuous development of Ncorr_post software

Ncorr_post has been developed in Matlab [92] for postprocessing and visualization of DIC data provided by Ncorr software [88]. The first version was released in 2014 and since then, more than 600 downloads worldwide have been reported in the website analytics, more than 50 queries related to the software functionalities have been answered, and the software was mentioned in more than 30 papers according to Google Scholar. Interestingly, manuals created by software users on how to use the software were posted on YouTube without author's involvement.

The program is controlled using a graphical user interface (Figure 3.1) and offers funcionalities that make the data processing convenient for common engineering applications, including:

- Scaling of displacements to the physical units of length,
- Placement of an arbitrary number of virtual extensometers and their management to extract information about displacements at discrete locations,
- Export options for images, videos, or text files,
- Extraction of DIC data along arbitrary lines, including the option of averaging band (Figure 3.2),
- Setting the transparency of color ovelays representing displacement and deformation fields,
- Calculation of principal strains and their directions (Figure 3.3),
- Calculaiton of strain norms, including volumetric and the Von Mises strain,

- Averaging displacement/deformation fields over an arbitrary region.

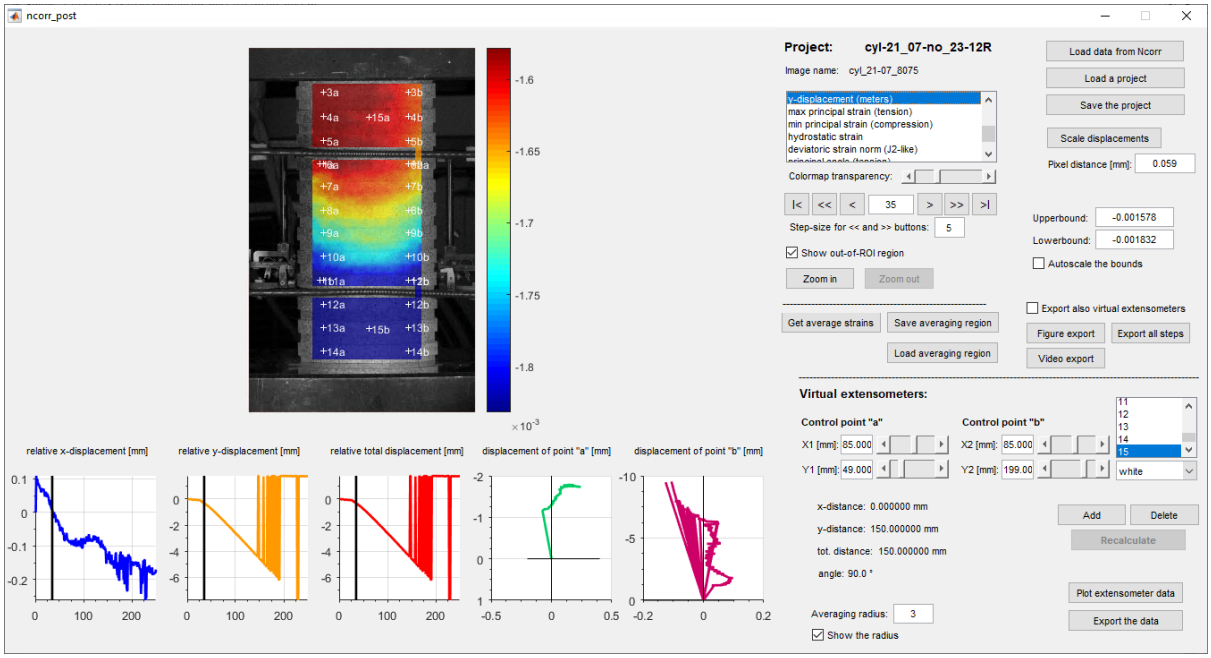

Figure 3.1: Graphical user interface of Ncorr_post v2.1.

3.2 Real-time remote measurements using IoT devices

Development of the internet-of-things (IoT) technologies opened the way for remote measurement of displacements and deformations for an instantaneous structural health assessment. Such an assesment can be based both on detecting changes in structural stiffness, manifested through excessive displacements under (semi)static loading, changes in vibration frequencies due to dynamic excitation, or both.

The ongoing research is focused on the development of a portable autonomous devices for remote monitoring of in-plane displacements and deformations on-site (Figure 3.4). Implementation of the light-weight DFT algorithms enables the use of small processing units (Raspberry Pi 4) and instant data preview. To reach that goal, the research agenda includes the development of data transfer strategies, saving the data to a database, and live preview in a user-friendly web application.

3.3 Particle image velocimetry

Particle image velocity (PIV) [93–96] has been widely used in experimental fluid mechanics for tracking velocities of tracer particles seeded in fluids, but can be also used for tracking movements of soils [97]. The method borrows heavily from DIC in principles and algorithms, and the main difference between these two methods is mainly in the apparatus used for the

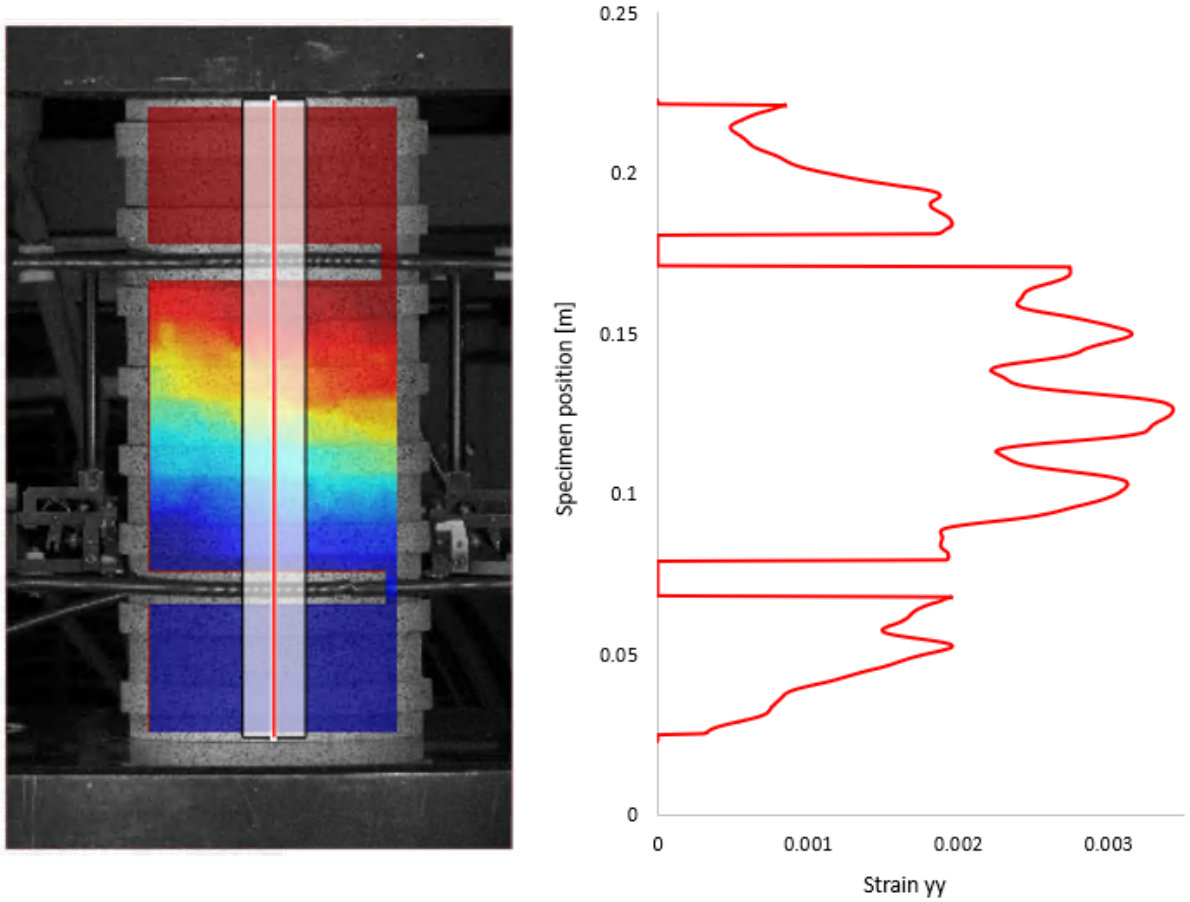

Figure 3.2: Distribution of vertical strains along a line parallel to the axis of a cylindrical concrete specimen confined with aluminum rings.

measurement. Unlike for DIC measurements, postprocessing of PIV data is focused on flow visualization, however the calculation of velocity fields allows to use slightly modified DFT-based procedures as outlined in Appendix F: (i) split images into pixel subsets (interrogation areas) and (ii) calculate displacement vectors for each subset using DFT. These subsets have to be updated for each couple of images because of changing pattern (orientation and swarming of particles) and geometry of the region of interest. Additionally, velocity is calculated using the time between image shots and the physical size of each pixel.

This procedure was implemented into an in-house software written in Python (PyPIV) and validated using sample experiments carried out at the Charles University (Prague), Institute of Geology and Paleontology (Figure 3.5). This tool differs from commonly available software tools for its ability to calculate velocity fields for dynamically growing/shrinking regions of interest (Figure 3.6).

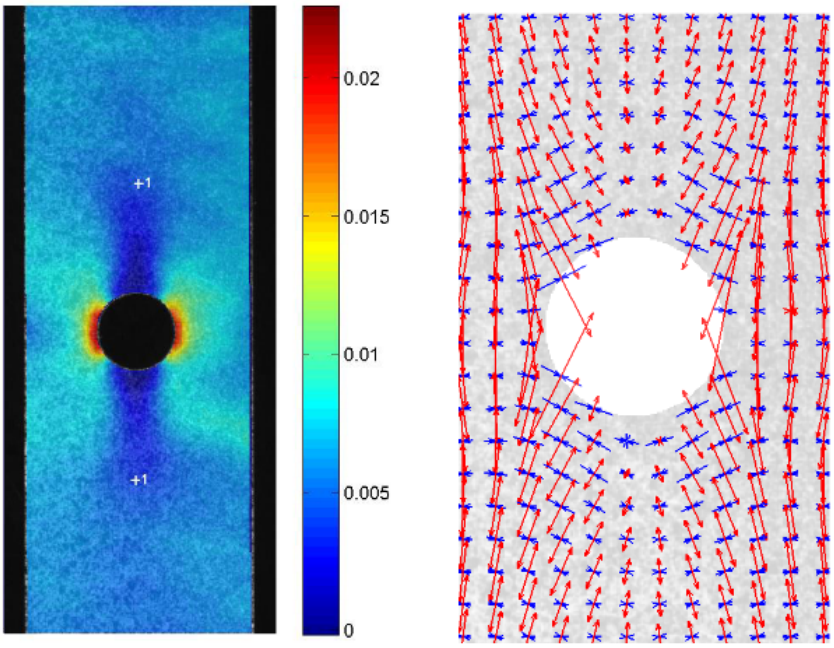

Figure 3.3: Colormap (left, limited to the map of maximum principal strains) and arrow (right) representation of principal strains on an axially loaded steel plate with a circular hole.

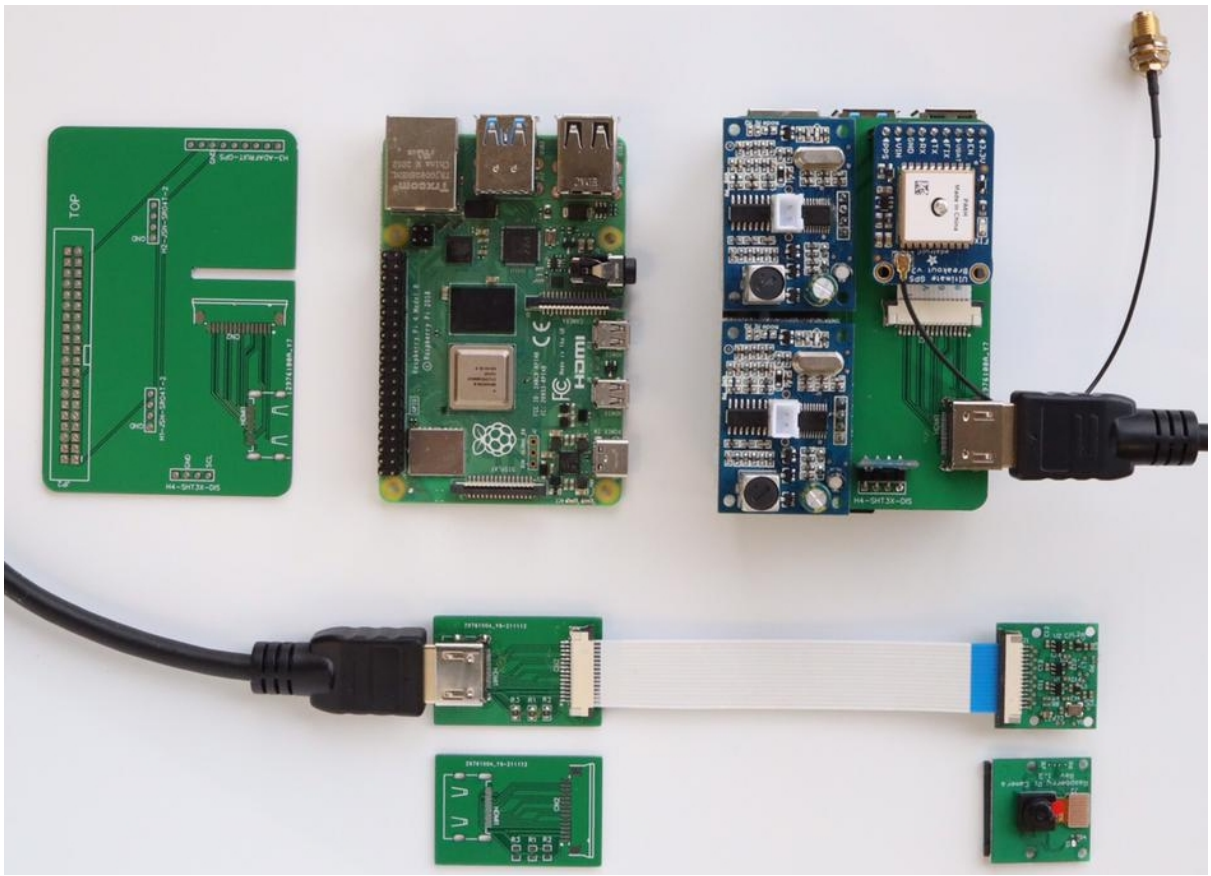

Figure 3.4: Development prototype of printed circuit boards (PCB) designed for connection of Raspberry Pi microcomputer, GPS modules, ultrasound distance sensors, and a camera.

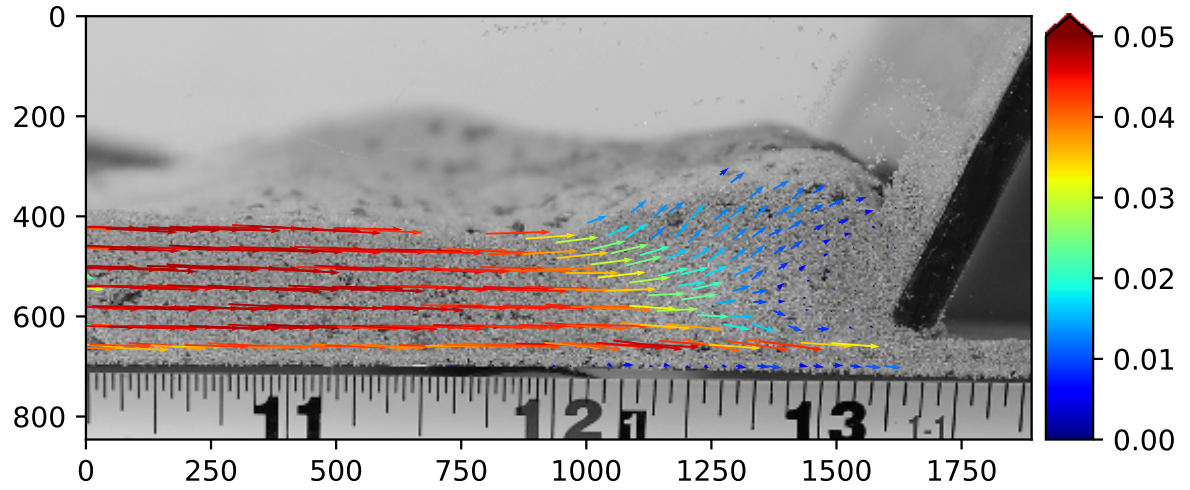

Figure 3.5: Quiver plot representing velocity field [mm/s] for sand grains subjected to a simulated subduction experiment.

3.4 Shrapnel velocity measurement

PIV principles were also adopted for analysis of shrapnel movement after a bomb explosion. However, the density of particles here is very low and the projected trajectory between individual frames very high due to the high velocity of the flying fragments and limited sampling rate of high-speed cameras operating outdoor without additional illumination. For this reason, the DFT-based algorithms have to be enhanced to seek the particles of interest and locate them in the following frame. Semi-automatic measurements, where the particles were identified manually and sought automatically, have been already carried out (Figure 3.7), but further improvements are needed.

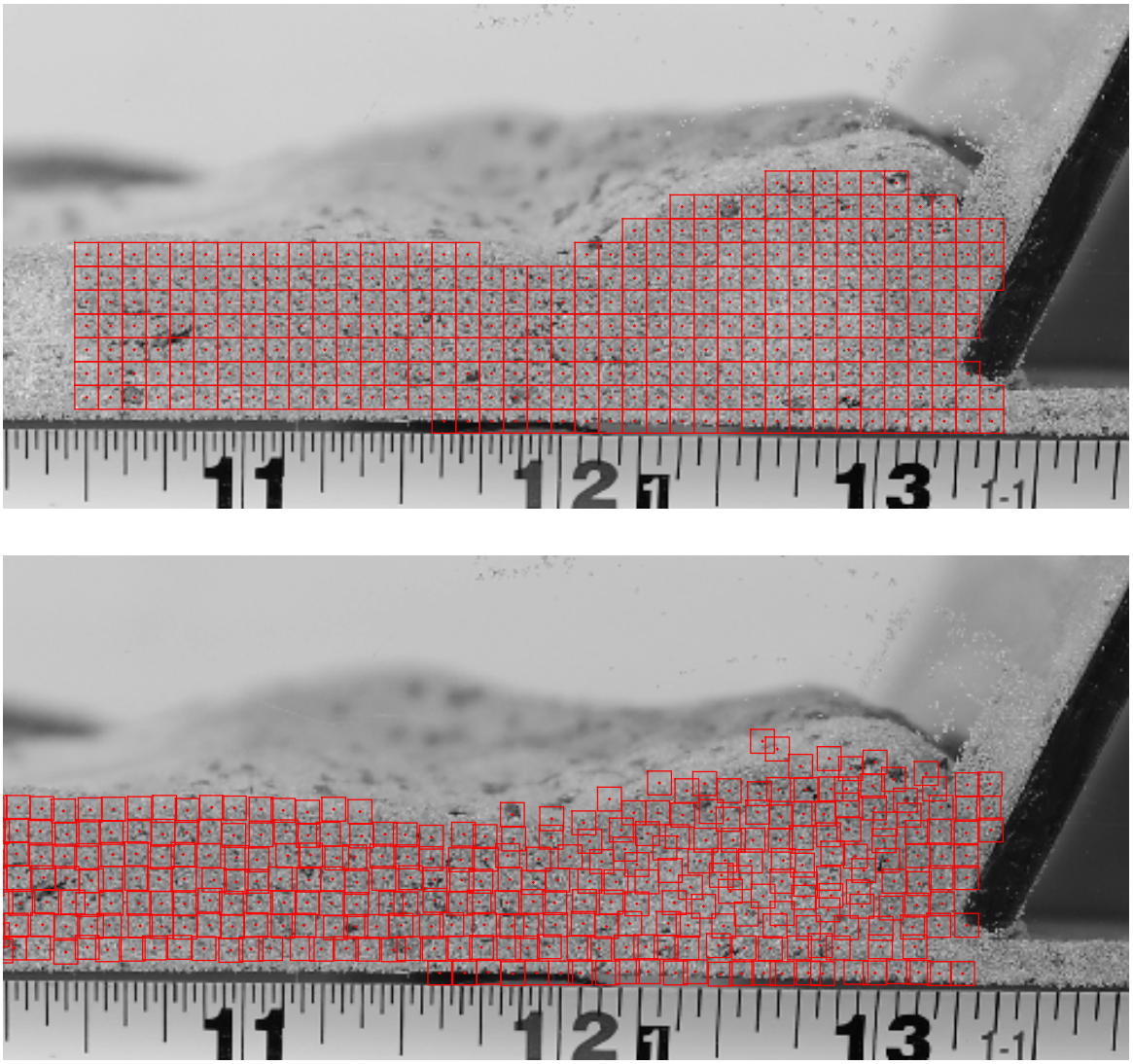

Figure 3.6: Change of the region of interest and deformation of the soil body over the course of the experiment (sequence of 100 images); increase of the soil body volume required reverse motion analysis and update of subset positions for each step (image).

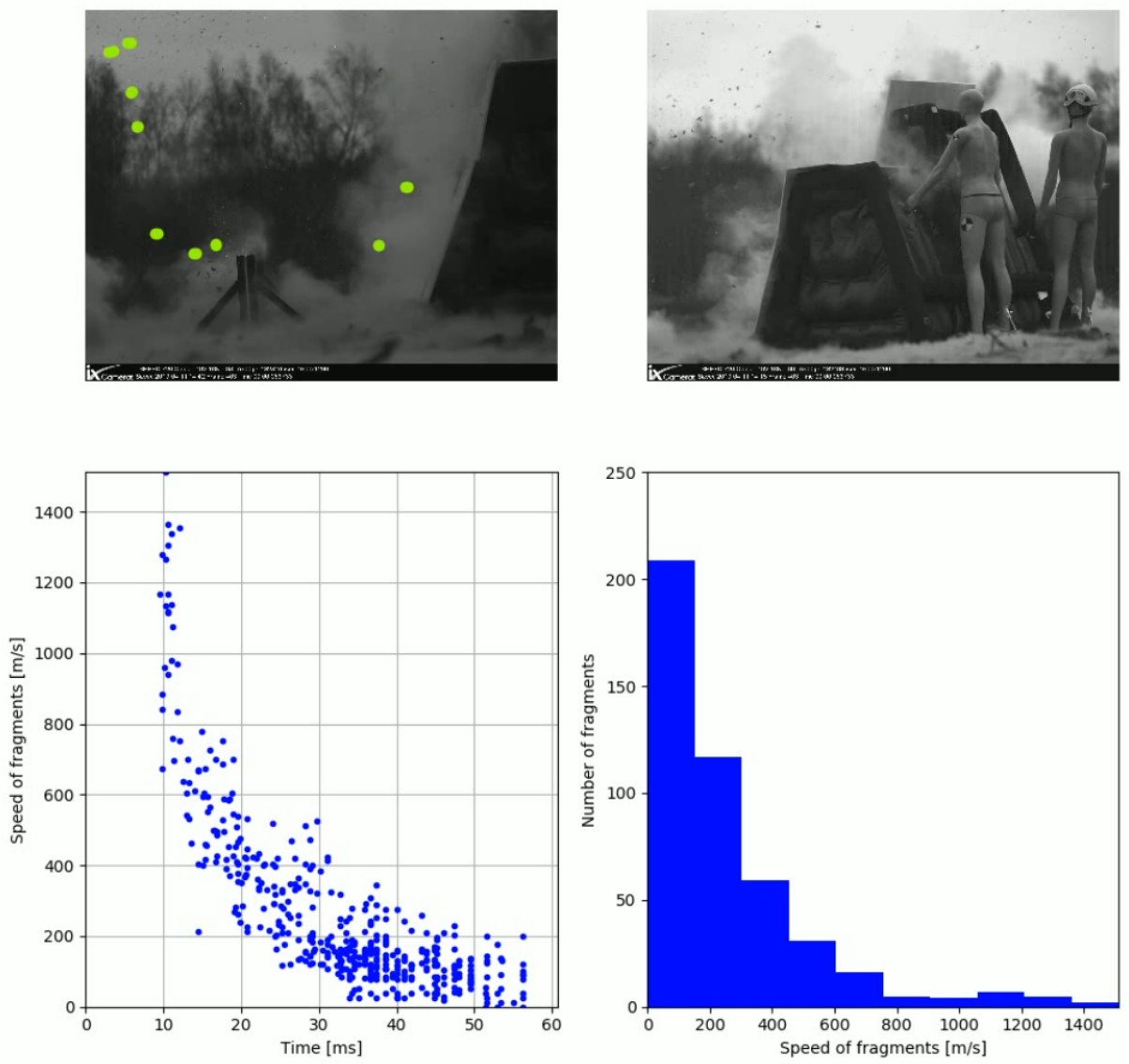

Figure 3.7: Detection of shrapnels and distribution of their velocities projected to a camera plane from a sequence of images recorded using high-speed cameras during explosion tests in a military zone Boletice.

References

[1] V. V. Shabarov. Wide-range strain-gauge device for static strain measurement. *Measurement Techniques*, 14:1851–1853, 1971. DOI: 10.1007/bf00994948.

[2] Stefan Keil. *Technology and Practical Use of Strain Gages With Particular Consideration of Stress Analysis Using Strain Gages*. Wilhelm Ernst & Sohn, 2017. DOI: 10.1002/9783433606667.

[3] J. A. Coutts and A. J. Coombs. A method of installing a strain gauge. *Strain*, 5:101–104, 1969. DOI: 10.1111/j.1475-1305.1969.tb01588.x.

[4] Yu. I. Koval and V. I. Boiko. Reliability of foil strain gauges in multiple cyclic deformations. *Strength of Materials*, 12:1047–1050, 1980. DOI: 10.1007/bf00770540.

[5] Sam-Deok Cho, Kwang-Wu Lee, Zhuang Li, and Uk-Gie Kim. Evaluation of reliability of strain gauge measurements for geosynthetics. *Journal of the Korean Geosynthetic Society*, 14:87–96, 2015. DOI: 10.12814/jkgss.2015.14.4.087.

[6] Majid Talebi, Christopher L. Meehan, and Tyler M. Poggiogalle. Strain in a GRS bridge abutment: Strain gauge attachment techniques, performance and survivability during construction and operation. In *IFCEE 2018*. American Society of Civil Engineers, 2018. DOI: 10.1061/9780784481608.025.

[7] S. Zike and L P Mikkelsen. Correction of gauge factor for strain gauges used in polymer composite testing. *Experimental Mechanics*, 54:393–403, 2013. DOI: 10.1007/s11340-013-9813-7.

[8] David S. Nyce. The LVDT. In *Linear Position Sensors*, pages 94–108. John Wiley & Sons, Inc., 2003. DOI: 10.1002/0471474282.ch6.

[9] J.N. Périé, S. Calloch, C. Cluzel, and F. Hild. Analysis of a multiaxial test on a c/c composite by using digital image correlation and a damage model. *Experimental Mechanics*, 42(3):318–328, sep 2002. DOI: 10.1007/bf02410989.

[10] K. H Laermann, editor. *Optical Methods in Experimental Solid Mechanics*. Springer Nature, 2000. DOI: 10.1007/978-3-7091-2586-1.

[11] Hani H. Nassif, Mayrai Gindy, and Joe Davis. Comparison of laser doppler vibrometer with contact sensors for monitoring bridge deflection and vibration. *NDT & E International*, 38:213–218, 2005. DOI: 10.1016/j.ndteint.2004.06.012.

[12] Carmelo Gentile and Giulia Bernardini. An interferometric radar for non-contact measurement of deflections on civil engineering structures: laboratory and full-scale tests. *Structure and Infrastructure Engineering*, 6:521–534, 2009. DOI: 10.1080/15732470903068557.

[13] G.A. Stephen, J.M.W. Brownjohn, and C.A. Taylor. Measurements of static and dynamic displacement from visual monitoring of the humber bridge. *Engineering Structures*, 15: 197–208, 1993. DOI: 10.1016/0141-0296(93)90054-8.

[14] J. J. Lee and M. Shinozuka. Real-time displacement measurement of a flexible bridge using digital image processing techniques. *Experimental Mechanics*, 46:105–114, 2006. DOI: 10.1007/s11340-006-6124-2.

[15] Jong Jae Lee and Masanobu Shinozuka. A vision-based system for remote sensing of bridge displacement. *NDT & E International*, 39:425–431, 2006. DOI: 10.1016/j.ndteint.2005.12.003.

[16] M. Malesa, D. Szczepanek, M. Kujawińska, A. Świercz, and P. Kołakowski. Monitoring of civil engineering structures using digital image correlation technique. *EPJ Web of Conferences*, 6:31014, 2010. DOI: 10.1051/epjconf/20100631014.

[17] E Bell, J Peddle, and A Goudreau. Bridge condition assessment using digital image correlation and structural modeling. In *Bridge Maintenance, Safety, Management, Resilience and Sustainability*, pages 330–337. CRC Press, 2012. DOI: 10.1201/b12352-41.

[18] David V. Jáuregui, Kenneth R. White, Clinton B. Woodward, and Kenneth R. Leitch. Noncontact photogrammetric measurement of vertical bridge deflection. *Journal of Bridge Engineering*, 8:212–222, 2003. DOI: 10.1061/(asce)1084-0702(2003)8:4(212).

[19] Vlatko Brčić. Basic concepts in holography and hologram interferometry. In *Application of Holography and Hologram Interferometry to Photoelasticity*, pages 12–18. Springer Vienna, 1974. DOI: 10.1007/978-3-7091-2646-2_2.

[20] Pascal Picart. Evaluation of phase shifting speckle interferometry accuracy. In *Interferometry in Speckle Light*, pages 431–438. Springer Berlin Heidelberg, 2000. DOI: 10.1007/978-3-642-57323-1_53.

[21] Daniel Post, Bongtae Han, and Peter G. Ifju. Moiré methods for engineering and science — moiré interferometry and shadow moiré. In *Topics in Applied Physics*, pages 151–196. Springer Berlin Heidelberg, 2000. DOI: 10.1007/3-540-48800-6_5.

[22] H. Schreier, J. Orteu, and M. Sutton. *Image Correlation for Shape, Motion and Deformation Measurements*. Springer Nature, 2009. DOI: 10.1007/978-0-387-78747-3.

[23] I. Yamaguchi. A laser speckle strain gauge. *Journal of Physics E: Scientific Instruments*, 14:1270, 1981. DOI: 10.1088/0022-3735/14/11/012.

[24] W. H. Peters and W. F. Ranson. Digital imaging techniques in experimental stress analysis. *Optical Engineering*, 21:427–431, 1982. DOI: 10.1117/12.7972925.

[25] M.A. Sutton, J.H. Yan, V. Tiwari, H.W. Schreier, and J.J. Orteu. The effect of out-of-plane motion on 2D and 3D digital image correlation measurements. *Optics and Lasers in Engineering*, 46:746–757, 2008. DOI: 10.1016/j.optlaseng.2008.05.005.

[26] Marco Palanca, Gianluca Tozzi, and Luca Cristofolini. The use of digital image correlation in the biomechanical area: a review. *International Biomechanics*, 3:1–21, 2015. DOI: 10.1080/23335432.2015.1117395.

[27] A. H. Salmanpour and N. Mojsilović. Application of Digital Image Correlation for strain measurements of large masonry walls. *APCOM & ISCM*, 2013.

[28] S. H. Tung, M. H. Shih, and W. P. Sung. Development of digital image correlation method to analyse crack variations of masonry walls. *Sadhana*, 33:767–779, 2008.

[29] Christopher Niezrecki, Peter Avitabile, Christopher Warren, Pawan Pingle, Mark Helfrick, and E. P. Tomasini. A review of digital image correlation applied to structura dynamics. AIP, 2010. DOI: 10.1063/1.3455461.

[30] S. Russev, G. Tsutsumanova, S. Angelov, and K. Bachev. An electron beam lithography and digital image acquisition system for scanning electron microscopes. *Journal of Microscopy*, 226(1):64–70, 2007. DOI: 10.1111/j.1365-2818.2007.01753.x.

[31] C.E. Slone and M.J. Mills. Analysis of strain localization at high angle grain boundaries during creep of a polycrystalline superalloy using SEM-based digital image correlation. *Microscopy and Microanalysis*, 22:2018–2019, 2016. DOI: 10.1017/s143192761601093x.

[32] A. Hoag, N. Hoult, A. Take, and H. Le. Monitoring of rail bridge displacements using digital image correlation. In *Structural Health Monitoring 2015*. Destech Publications, 2015. DOI: 10.12783/shm2015/52.

[33] C. Popescu, G. Sas, and B. Arntsen. Structural health monitoring of a buttress dam using digital image correlation. In *Sustainable and Safe Dams Around the World*, pages 1671–1680. CRC Press, 2019. DOI: 10.1201/9780429319778-151.

[34] P. Wang, F. Pierron, and O. T. Thomsen. Identification of material parameters of PVC foams using digital image correlation and the virtual fields method. *Experimental Mechanics*, 53:1001–1015, 2012. DOI: 10.1007/s11340-012-9703-4.

[35] Roberto Fedele and Roberta Santoro. Extended identification of mechanical parameters and boundary conditions by digital image correlation. *Procedia IUTAM*, 4:40–47, 2012. DOI: 10.1016/j.piutam.2012.05.005.

[36] B. Thimm, J. Steden, M. Reuber, and H.-J. Christ. Using digital image correlation measurements for the inverse identification of constitutive material parameters applied in metal cutting simulations. *Procedia CIRP*, 82:95–100, 2019. DOI: 10.1016/j.procir.2019.04.156.

[37] V. Nežerka, J. Antoš, T. Sajdlová, and P. Tesárek. Use of open source DIC tools for analysis of multiple cracking in fiber-reinforced concrete. *Applied Mechanics and Materials*, 827:336–339, 2016. DOI: 10.4028/www.scientific.net/amm.827.336.

[38] Jakub Antoš, Václav Nežerka, and Michael Somr. Assessment of 2D-DIC stochastic patterns. *Acta Polytechnica CTU Proceedings*, 13:1–10, 2017. DOI: 10.14311/app.2017.13.0001.

[39] B. Pan, H. Xie, and Z. Wang. Equivalence of digital image correlation criteria for pattern matching. *Applied Optics*, 49:5501–5509, 2010.

[40] A. W. Gruen. Adaptive least squares correlation: a powerful image matching technique. *South African Journal of Photography, Remote Sensing and Cartography*, 14:175–187, 1985.

[41] Y. Altunbasak, R. M. Mersereau, and A. J. Patti. A fast parametric motion estimation algorithm with illumination and lens distortion correction. *IEEE Transactions on Image Processing*, 12:395–408, 2003. DOI: 10.1109/tip.2003.809012.

[42] B. Pan, A. Asundi, H. Xie, and J. Gao. Digital image correlation using iterative least squares and pointwise least squares for displacement field and strain field measurements. *Optics and Lasers in Engineering*, 47:865–874, 2009. DOI: 10.1016/j.optlaseng.2008.10.014.

[43] B. Pan, Z. Wang, and H. Xie. Generalized spatial-gradient-based digital image correlation for displacement and shape measurement with subpixel accuracy. *The Journal of Strain Analysis for Engineering Design*, 44:659–669, 2009. DOI: 10.1243/03093247jsa546.

[44] K. Triconnet, K. Derrien, F. Hild, and D. Baptiste. Parameter choice for optimized digital image correlation. *Optics and Lasers in Engineering*, 47:728–737, 2009. DOI: 10.1016/j.optlaseng.2008.10.015.

[45] Zhenxing Hu, Huimin Xie, Jian Lu, Tao Hua, and Jianguo Zhu. Study of the performance of different subpixel image correlation methods in 3d digital image correlation. *Applied Optics*, 49:4044–4052, 2010. DOI: 10.1364/ao.49.004044.

[46] Zhenxing Hu, Huimin Xie, Jian Lu, Huaixi Wang, and Jianguo Zhu. Error evaluation technique for three-dimensional digital image correlation. *Applied Optics*, 50: 6239–6248, 2011. DOI: 10.1364/ao.50.006239.

[47] Thorsten Siebert, Thomas Becker, Karsten Spiltthof, Isabell Neumann, and Rene Krupka. Error estimations in digital image correlation technique. *Applied Mechanics and Materials*, 7–8:265–270, 2007. DOI: 10.4028/www.scientific.net/amm.7-8.265.

[48] H. A. Bruck, S. R. McNeill, M. A. Sutton, and W. H. Peters. Digital image correlation using newton-raphson method of partial differential correction. *Experimental Mechanics*, 29:261–267, 1989. DOI: 10.1007/bf02321405.

[49] Jun Zhang, Guanchang Jin, Shaopeng Ma, and Libo Meng. Application of an improved subpixel registration algorithm on digital speckle correlation measurement. *Optics & Laser Technology*, 35:533–542, 2003. DOI: 10.1016/s0030-3992(03)00069-0.

[50] B. Pan, K. Qian, H. Xie, and A. Asundi. Two-dimensional digital image correlation for in-plane displacement and strain measurement: a review. *Measurement Science and Technology*, 20:062001, 2009. DOI: 10.1088/0957-0233/20/6/062001.

[51] B. Pan, K. Li, and W. Tong. Fast, robust and accurate Digital Image Correlation calculation without redundant computations. *Experimental Mechanics*, 53:1277–1289, 2013.

[52] Yaofeng Sun, John H. L. Pang, Chee Khuen Wong, and Fei Su. Finite element formulation for a digital image correlation method. *Applied Optics*, 44:7357–7369, 2005. DOI: 10.1364/ao.44.007357.

[53] G. Besnard, F. Hild, and S. Roux. "finite-element" displacement fields analysis from digital images: Application to portevin–le châtelier bands. *Experimental Mechanics*, 46: 789–803, 2006. DOI: 10.1007/s11340-006-9824-8.

[54] Shaopeng Ma, Zilong Zhao, and Xian Wang. Mesh-based digital image correlation method using higher order isoparametric elements. *The Journal of Strain Analysis for Engineering Design*, 47:163–175, 2012. DOI: 10.1177/0309324712437488.

[55] J. Réthoré, T. Elguedj, P. Simon, and M. Coret. On the use of NURBS functions for displacement derivatives measurement by digital image correlation. *Experimental Mechanics*, 50:1099–1116, 2009. DOI: 10.1007/s11340-009-9304-z.

[56] Gilles Besnard, Hugo Leclerc, François Hild, Stéphane Roux, and Nicolas Swiergiel. Analysis of image series through global digital image correlation. *The Journal of Strain Analysis for Engineering Design*, 47:214–228, 2012. DOI: 10.1177/0309324712441435.

[57] L. Wittevrongel, P. Lava, S. V. Lomov, and D. Debruyne. A self adaptive global digital image correlation algorithm. *Experimental Mechanics*, 55:361–378, 2014. DOI: 10.1007/s11340-014-9946-3.

[58] Bo Wang and Bing Pan. Subset-based local vs. finite element-based global digital image correlation: A comparison study. *Theoretical and Applied Mechanics Letters*, 6: 200–208, 2016. DOI: 10.1016/j.taml.2016.08.003.

[59] J. Blaber, B. Adair, and A. Antouniou. Ncorr: Open-source 2d digital image correlation matlab software. *Experimental Mechanics*, 55:1105–1122, 2015. DOI: 10.1007/s11340-015-0009-1.

[60] P. Bing, X. Hui-min, X. Bo-qin, and D. Fu-long. Performance of sub-pixel registration algorithms in digital image correlation. *Measurement Science and Technology*, 17: 1615–1621, 2006. DOI: 10.1088/0957-0233/17/6/045.

[61] J. Blaber. Ncorr digital image correlation software algorithms, http://www.ncorr.com/index.php/dic-algorithms. *Georgia Institute of Technology*, 2014.

[62] Bing Pan, Huimin Xie, Jianxin Gao, and Anand Asundi. Improved speckle projection profilometry for out-of-plane shape measurement. *Applied Optics*, 47:5527..5542, 2008. DOI: 10.1364/ao.47.005527.

[63] D. Lecompte, A. Smits, Bossuyt S., H. Sol, J. Vantomme, D. Van Hemelrijck, and A.M. Habraken. Quality assessment of speckle patterns for digital image correlation. *Optics and Lasers in Engineering*, 44:1132–1145, 2006.

[64] B. Pan, H. Xie, Z. Wang, K. Qian, and Z. Wang. Study on subset size selection in digital image correlation for speckle patterns. *Optics Express*, 16:7037, 2008. DOI: 10.1364/oe.16.007037.

[65] B. Pan, Z. Lu, and H. Xie. Mean intensity gradient: An Effective global parameter for quality assessment of the speckle patterns used in digital image correlation. *Optics and Lasers in Engineering*, 48:469–477, 2010.

[66] Markus J. Hochrainer. A cost effective DIC system for measuring structural vibrations. In *Rotating Machinery, Hybrid Test Methods, Vibro-Acoustics & Laser Vibrometry, Volume 8*, pages 139–146. Springer International Publishing, 2016. DOI: 10.1007/978-3-319-30084-9_12.

[67] Simon Baker and Iain Matthews. Lucas-Kanade 20 Years On: A Unifying Framework. *International Journal of Computer Vision*, 56:221–255, 2004. DOI: 10.1023/b:visi.0000011205.11775.fd.

[68] R. E. Jacobson, S. F. Ray, G. G. Attridge, and N. R. Axford. *The Manual of Photography*. Reed Educational and Professional Publishing Ltd, 2000. ISBN 0-240-51574-9.

[69] H. W. Schreier, D. Garcia, and M. A. Sutton. Advances in light microscope stereo vision. *Experimental Mechanics*, 44:278–288, 2004. DOI: 10.1007/bf02427894.

[70] Saturu Yoneyama. Lens distortion correction for digital image correlation by measuring rigid body displacement. *Optical Engineering*, 45:023602, 2006. DOI: 10.1117/1.2168411.

[71] V. Tiwari, M. A. Sutton, and S. R. McNeill. Assessment of high speed imaging systems for 2d and 3d deformation measurements: Methodology development and validation. *Experimental Mechanics*, 47:561–579, 2007. DOI: 10.1007/s11340-006-9011-y.

[72] H. Haddadi and S. Belhabib. Use of rigid-body motion for the investigation and estimation of the measurement errors related to digital image correlation technique. *Optics and Lasers in Engineering*, 46:185–196, 2008. DOI: 10.1016/j.optlaseng.2007.05.008.

[73] S. N. Bezdidko. Orthogonal aberrations: theory, methods, and practical applications in computational optics. *Journal of Optical Technology*, 83:351, 2016. DOI: 10.1364/jot.83.000351.

[74] Jie Jiang. Distortion correction for a wide-angle lens based on real-time digital image processing. *Optical Engineering*, 42:2029, 2003. DOI: 10.1117/1.1580155.

[75] Qiucheng Sun, Yueqian Hou, and Jian Chen. Lens distortion correction for improving measurement accuracy of digital image correlation. *Optik*, 126:3153–3157, 2015. DOI: 10.1016/j.ijleo.2015.07.068.

[76] R. Tsai. A versatile camera calibration technique for high-accuracy 3d machine vision metrology using off-the-shelf TV cameras and lenses. *IEEE Journal on Robotics and Automation*, 3:323–344, 1987. DOI: 10.1109/jra.1987.1087109.

[77] J. Weng, P. Cohen, and M. Herniou. Camera calibration with distortion models and accuracy evaluation. *IEEE Transactions on Pattern Analysis and Machine Intelligence*, 14:965–980, 1992. DOI: 10.1109/34.159901.

[78] Z. Zhang. A flexible new technique for camera calibration. *IEEE Transactions on Pattern Analysis and Machine Intelligence*, 22:1330–1334, 2000. DOI: 10.1109/34.888718.

[79] B. Pan, L. Yu, D. Wu, and L. Tang. Systematic errors in two-dimensional digital image correlation due to lens distortion. *Optics and Lasers in Engineering*, 51:140–147, 2013. DOI: 10.1016/j.optlaseng.2012.08.012.

[80] Rory Bigger, Benoît Blaysat, Christofer Boo, Manuel Grewer, Jun Hu, Amanda Jones, Markus Klein, Kavesary Raghavan, Phillip Reu, Timothy Schmidt, Thorsten Siebert, Micah Simenson, Daniel Turner, Alessandro Vieira, and Thorsten Weikert. A good practices guide for digital image correlation. Technical report, 2018.

[81] L. Wittevrongel, M. Badaloni, R. Balcaen, P. Lava, and D. Debruyne. Evaluation of methodologies for compensation of out of plane motions in a 2D digital image correlation setup. *Strain*, 51:357–369, 2015. DOI: 10.1111/str.12146.

[82] Robert Whitrow. Image file formats. In *OpenGL Graphics Through Applications*, pages 39–59. Springer London. DOI: 10.1007/978-1-84800-023-0-2.

[83] Nanette Salvaggio. *Basic Photographic Materials and Processes*. Routledge, 2013. DOI: 10.4324/9780080927664.

[84] Weidong Kou. Principles of digital image compression. In *Digital Image Compression*, pages 1–8. Springer US, 1995. DOI: 10.1007/978-1-4757-2361-8_1.

[85] Rohit M. Thanki and Ashish Kothari. *Hybrid and Advanced Compression Techniques for Medical Images*. Springer International Publishing, 2019. DOI: 10.1007/978-3-030-12575-2.

[86] L.K. Tan. Image file formats. *Biomedical Imaging and Intervention Journal*, 2:1–7, 2006. DOI: 10.2349/biij.2.1.e6.

[87] Xiangui Kang, Xianyu Xu, Anjie Peng, and Wenjun Zeng. Scalable lossy compression for pixel-value encrypted images. In *2012 Data Compression Conference*. IEEE, 2012. DOI: 10.1109/dcc.2012.55.

[88] J. Blaber. Ncorr digital image correlation software, http://www.ncorr.com/. *Georgia Institute of Technology*, 2014.

[89] Phillip L. Reu. A realistic error budget for two dimension digital image correlation. In *Advancement of Optical Methods in Experimental Mechanics, Volume 3*, pages 189–193. 2016. DOI: 10.1007/978-3-319-22446-6_24.

[90] P. Podbreznik and B. Potočnik. Influence of temperature variations on calibrated cameras. *International Journal of Computer and Information Engineering*, 2:546–551, 2008.

[91] M. Smith and E. Cope. The effects of temperature variation on single-lens-reflex digital camera calibration parameters. *International Archives of Photogrammetry, Remote Sensing and Spatial Information Sciences*, page 5, 2012.

[92] Inc. The MathWorks. Matlab release 2011a, http://www.mathworks.com/products/matlab/. *Natick, Massachusetts, U.S.*, 2011.

[93] C. E. Willert and M. Gharib. Digital particle image velocimetry. *Experiments in Fluids*, 10:181–193, 1991. DOI: 10.1007/bf00190388.

[94] F Scarano. Iterative image deformation methods in PIV. *Measurement Science and Technology*, 13:R1–R19, 2001. DOI: 10.1088/0957-0233/13/1/201.

[95] Dana Dabiri. Digital particle image thermometry/velocimetry: a review. *Experiments in Fluids*, 46:191–241, 2008. DOI: 10.1007/s00348-008-0590-5.

[96] Andrea Sciacchitano, Bernhard Wieneke, and Fulvio Scarano. PIV uncertainty quantification by image matching. *Measurement Science and Technology*, 24(4):045302, 2013. DOI: 10.1088/0957-0233/24/4/045302.

[97] D. J. White, W. A. Take, and M. D. Bolton. Soil deformation measurement using particle image velocimetry (PIV) and photogrammetry. *Géotechnique*, 53:619–631, 2003. DOI: 10.1680/geot.2003.53.7.619.

Appendix A

V. Nežerka et al., An integrated experimental-numerical study of the performance of lime-based mortars in masonry piers under eccentric loading, *Construction and Building Materials* 114 (2016) 913–924, doi: 10.1016/j.conbuildmat.2016.04.013

Author's contribution: main idea, design of experiments, preparation of specimens, DIC, numerical modeling.

Construction and Building Materials 114 (2016) 913–924

Contents lists available at ScienceDirect

Construction and Building Materials

journal homepage: www.elsevier.com/locate/conbuildmat

An integrated experimental-numerical study of the performance of lime-based mortars in masonry piers under eccentric loading

V. Nežerka *, J. Antoš, J. Litoš, P. Tesárek, J. Zeman

Faculty of Civil Engineering, Czech Technical University in Prague, Thákurova 7, 166 29 Praha 6, Czech Republic

HIGHLIGHTS

- Mortars containing metakaolin are stronger than pure-lime or lime-cement ones.
- Mortar strength can be increased by the addition of crushed bricks.
- Hydraulic reactions are promoted by water retained within brick fragments.
- Mortars with metakaolin and crushed bricks produce strong masonry.
- Mortar compressive strength is key parameter influencing the masonry strength.

ARTICLE INFO

Article history:
Received 9 December 2015
Received in revised form 30 March 2016
Accepted 4 April 2016

Keywords:
Masonry
Mortar
Mechanical properties
Load-bearing capacity
Finite element method
Digital image correlation

ABSTRACT

The paper focuses on the performance of various lime-based materials, alternative to Portland cement mortars, intended for application in repairing historic structures when subjected to mechanical loading. Results of basic material tests indicate that the use of metakaolin as a pozzolanic additive produces mortars with superior strength and sufficiently low shrinkage. Moreover, mortar strength can be further enhanced by the addition of crushed brick fragments, which explains the longevity of Roman concretes rich in pozzolans and aggregates from crushed clay products such as tiles, pottery, or bricks. An integrated experimental-numerical approach was used to identify key mortar parameters influencing the load-bearing capacity of masonry piers subjected to a combination of compression and bending. The simulations indicate increased load-bearing capacities for masonry piers containing metakaolin-rich mortars with crushed brick fragments, as a result of their superior compressive strength.

1. Introduction

Ancient structures embody the culture and stories of people, who built, used and lived in them. This charm attracts tourists to the sites with well-preserved cultural heritage, which in turn has an enormous positive impact on the economy of the region. From this reason, the conservation and restoration of architectural heritage is encouraged in the majority of countries. However, an inappropriate intervention can cause a huge harm, and therefore the authorities established numerous requirements on the procedures and materials used for the conservation and repairs.

A vast number of ancient structures are made of masonry, being a traditional construction material that exhibits an extraordinary durability if an adequate maintenance is provided. Masonry bed joints are usually the weakest link and the deterioration and damage concentrates there. It has been established that the mortars used for repairs should be compatible with the original materials; serious damage to a number of historic masonry structures has been caused by an extensive use of Portland cement mortar over the past decades. The intention for its use was to avoid the inconveniences connected with the originally used lime-based mortars, such as slow setting, high shrinkage and low strength [1]. However, the use of the Portland cement mortars has been reconsidered for their low plasticity, excessive brittleness and early stiffness gain [2–5]. Moreover, the relatively high content of soluble salts that leach over time [4,5,3] can severely damage the original masonry units because of large crystallization pressures [6,7] and produce anaesthetic layers on their surface.

The strict regulations with respect to the Portland cement use led to the exploitation of traditional additives to lime-based mortars, such as volcanic ash, burnt clay shale [8] or increasingly popular metakaolin [5]. These additives, known as *pozzolans*, have been

* Corresponding author.
E-mail addresses: vaclav.nezerka@fsv.cvut.cz (V. Nežerka), jakub.antos@fsv.cvut.cz (J. Antoš), litos@fsv.cvut.cz (J. Litoš), tesarek@fsv.cvut.cz (P. Tesárek), zemanj@cml.fsv.cvut.cz (J. Zeman).

http://dx.doi.org/10.1016/j.conbuildmat.2016.04.013
0950-0618/

used since the ancient times in combination with lime to improve a moisture and free-thaw resistance of mortars [9], to increase their durability [1,5] and also their mechanical strength [10,11]. The use of pozzolans is essential not only for bed joint mortar but also for rendering ones, because pure-lime mortars suffer from enormous shrinkage cracking that has a negative aesthetic impact and can even cause spalling of the facade surface layers [12].

If there was no natural source of pozzolans available in the region, ancestors tried to find alternatives. Phoenicians were probably the first ones to add crushed clay products, such as burnt bricks, tiles or pieces of pottery, to the mortars in order to increase their durability and strength. Crushed bricks were often added to mortars used in load-bearing walls during the Roman Empire [13] and Romans called the material *cocciopesto* [14]. Cocciopesto mortars were then extensively used from the early Hellenistic up to the Ottoman period in water-retaining structures to protect the walls from moisture, typically in baths, canals and aqueducts [15,16]. The brick dust was mainly used for rendering, while large pebbles up to 25 mm in diameter appeared mainly in masonry walls, arches and foundations [17]. However, our previous studies [18–20] revealed that the positive impact of ceramic fragments should not be attributed to the formation of hydration products due to limited reactivity, but rather to their compliance which limits shrinkage-induced cracking among aggregates and ensures a perfect bond with the surrounding matrix.

The presented study was focused on the investigation of various mortars commonly used for repairs of cultural heritage and their structural performance through comprehensive experimental and numerical analyses. In particular, lime-based mortars with various additives and aggregates, introduced in Section 2, were used in bed joints of masonry piers subjected to a combination of quasi-static compression and bending. The purpose of the experimental analysis, described in Section 3, was to study the failure modes and crack patterns using Digital Image Correlation (DIC), assess the structural performance of individual mortars, and verify the proposed material model used for the Finite Element (FE) predictions, presented in Section 4. The FE analysis was consequently utilized in Section 4.4 to assess the key material parameters influencing the load-bearing capacity, and to study the failure modes of the masonry piers containing mortars with variable properties, subjected to a combination of compression and bending.

2. Materials

Compared to historic limes, today's commercial ones are very pure, despite the very benevolent regulating standard EN 459-1 [21] requiring the mass of CaO and MgO in the commonly used CL-90 lime hydrate higher than 90%. However, the presence of impurities in historic limes mortars was not always harmful [22], since the content of silica (SiO_2) and alumina (Al_2O_3) was responsible for their hydraulic character [23].

The inconveniences connected to the use of modern lime, such as limited binder strength, slow hardening, enormous shrinkage, and consequent cracking and poor cohesion between the mortar and surrounding masonry blocks [12] can be overcome by the use of reactive additives rich in aluminosilicates, such as metakaolin or Portland cement. While metakaolin has been generally accepted by the restoration community [5,22], the use of Portland cement is on decline and the authorities for cultural heritage in many countries prohibit its additions to repair mortars [2,3,7]. According to a few studies, calcium-silicate-hydrates (CSH) and calcium-aluminum-silicate-hydrates (CASH) are the main hydrated phases formed at the room temperature after the pozzolanic reaction of metakaolin and $Ca(OH)_2$ [24–26]. The metakaolin presence in lime-based mortars results in an enhanced strength and durability [18], while the vapor transport properties are superior to the mortars containing Portland cement [7].

Beside the addition of pozzolans, shrinkage can be efficiently reduced by increasing the content of inert aggregates, since the stiff inclusions restrain the volume changes of the surrounding matrix [12,27], which is more pronounced in the case of bigger inclusions [28]. However, large stiff pebbles are responsible for a formation of microcracks [20]. that have a negative impact on the mortar integrity and reduce the mortar strength and stiffness [1,23,29]. Moreover, the shrinkage-induced cracking of mortars poor in pozzolans, or containing unsuitable aggregates, limits their use as renderings because of their poor aesthetic performance [30].

Even though it is generally accepted that the presence of sand aggregates increases the resistance of mortars against mechanical loading, there is a threshold beyond which any addition of aggregates makes the mortar weaker due to excessive microcracking and loss of cohesion between the grains and the surrounding matrix [1]. By experience, the 1:3 binder to aggregate volume ratio has been established as the most suitable for repair mortars, providing a reasonable strength, shrinkage and porosity. Based on the study by Stefanidou and Papayianni [28] it seems most favorable to use the sand of grain-size ranging between 0 and 4 mm, resulting in mortars of the highest strength.

Vitrivius, Roman author, architect and engineer, who lived in the first century BC, recommended in his *Ten Books on Architecture* to add some portion of crushed bricks into mortars in order to increase their durability and strength. According to Silva et al. [31], the amorphous components of brick fragments, mainly represented by aluminosilicates, are able to react with lime and make the interfacial surface alkaline. The reaction products are supposed to give mortars a hydraulic character, and fill the voids and discontinuities in the thickness of about 20 μm from the interface between the crushed brick fragments and the surrounding matrix [32,33]. However, such processes can take place only if the ceramic clay is fired at appropriate temperatures between 600 and 900 °C [34], and the mortar is hardening in a sufficiently wet environment [35] for a considerable amount of time [32]. Even if the reaction takes place, the reaction-rim thickness is very limited and does not have any significant impact on the mortar properties, as proven by the results of nanoindentation of ancient mortar samples in our previous work [19]. More importantly, the relatively compliant crushed brick fragments relieve the shrinkage-induced stresses and reduce the number of microcracks within the mortar matrix [36,20].

Beside the positive impact of crushed brick fragments on the mechanical properties and durability of the cocciopesto mortars, the use of crushed bricks brings another benefit—the use of waste by-products from ceramic plants leads to a cost reduction and production of a more sustainable material.

2.1. Prepared and tested mortars

For our study, we used a commonly available white air-slaked lime (CL90) of a great purity (98.98% of CaO + MgO). The most frequent particle diameter found in the lime hydrate was equal to 15 μm and its specific surface area, determined by the gas adsorption, was equal to 16.5 m^2/g. The finely ground burnt claystone metakaolin, rich in SiO_2 (52.1%) and Al_2O_3 (43.4%), was chosen as the pozzolanic material. Both constituents, lime and metakaolin were produced in the Czech Republic and the detailed chemical composition is listed in [18]. Portland cement CEM I 42.5 R produced in Radotín, the Czech Republic, was used as an alternative to metakaolin. The selected Portland cement was rich in CaO (66%), SiO_2 (20%), Al_2O_3 (4%), Fe_2O_3 (3%), SO_3 (3%) and MgO (2%), as provided by XRF analysis [18].

Beside the investigation of metakaolin and Portland cement additions on the mechanical properties of lime-based mortars, the study was also focused on the influence of aggregate composition. River sand of grain size ranging between 0 and 4 mm from Zálezlice was selected based on experience as the most suitable for the application as the bed joint mortar. The industrially produced crushed brick fragments of the grain-size 2–5 mm, from a brick plant Bratronice, the Czech Republic, were chosen based on results of previous studies [37] and experience of authors acquired by analyses of ancient mortar samples [17,38,32]. The grain size distribution of the sand and crushed bricks aggregates, obtained by a sieve analysis, is presented in Fig. 1.

The mass ratio of lime and metakaolin/Portland cement was equal to 7:3 in all mortars. The amount of water was adjusted so that the fresh mortars fulfilled the workability slump test in accordance with ČSN EN 1015-3 [39] and the mortar cone expansion reached 13.5 ± 0.3 cm. Such consistency ensured a sufficient workability while keeping the water to binder ratio (w/b) as low as possible to avoid shrinkage cracking. The amount of aggregates was designed based on our experience, previous studies [1,23,28] and results of micromechanical modeling [20] towards high strength and acceptable shrinkage. The composition of the tested mortars is summarized in Table 1.

The crushed bricks aggregate retains more water than sand (see the water/ dry mass ratio records in Table 1). Based on such finding, we conjecture that the presence of water-retaining crushed bricks can promote the hydraulic reactions within the binder, and increase mortar strength and stiffness.

3. Experimental testing

The experimental testing consisted of two stages—first the individual components, i.e. the mortars and masonry units, were subjected to series of three-point bending and compression tests in order to acquire the data necessary for the calibration of the FE model. The second stage involved a full-scale compression test of masonry piers.

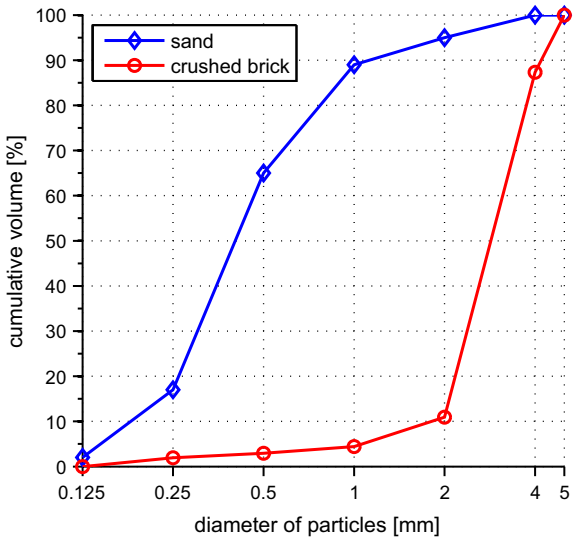

Fig. 1. Grading curves of sand and crushed brick aggregates.

3.1. Acquisition of basic material parameters

The basic material parameters, describing the mechanical behavior of mortars and bricks, were obtained from results of three-point bending and uniaxial compression tests, carried out according to EN 1015-11 [40]. To that purpose six control specimens were cast into $160 \times 40 \times 40$ mm prismatic molds, compacted using shaking table to get rid of excessive air bubbles, and removed after 48 h. Curing was executed at the temperature of 20 ± 1 °C and relative humidity ranging between 60 and 80%.

Common fired clay bricks with dimensions $290 \times 140 \times 65$ mm, produced in the brick plant Štěrboholy, the Czech Republic, were used as the masonry units for the construction of the tested masonry piers. In order to obtain the basic mechanical parameters, six $140 \times 40 \times 40$ mm prisms were cut off the bricks and subjected to the three-point bending and compression tests. The same procedure was adopted for the mortar specimens.

Beside the bending and uniaxial compression tests, the dynamic Young's modulus was assessed by the resonance method on 90-day old samples, and the tensile strength of the interface between mortars and bricks was evaluated based on series of pull-out tests carried out in accordance with EN 1015-21 [41]. The tests revealed that the interface was not the weakest link in the case of all tested mortars, since the failure plane was not located at the brick boundary, Fig. 2. The satisfactory interface strength is attributed to the relatively big roughness of the bricks and suitable workability of the fresh mortars.

3.1.1. Resonance method

The non-destructive resonance method was utilized to assess the dynamic Young's modulus, E_{dyn}, of both, mortars and brick. Such approach was chosen to overcome the inconvenience connected to the measurement of the static Young's modulus arising from the load-dependent compliance of the loading frame or improper attachment of strain-gauges. According to Malaikah et al. [42] the ratio between static and dynamic moduli measured on the same material should be within the range between 0.9 and 1.1.

The dynamic Young's modulus measurement is based on the equation for a longitudinal vibration of the beam with a continuously distributed mass and free-free boundary condition, following

$$E_{dyn} = \frac{4Lmf_l^2}{bt}, \tag{1}$$

where L is the length of the specimen [m], m is the mass of the specimen [kg], f_l is the fundamental longitudinal resonant frequency of the specimen [Hz], b is the width [m] and t is the thickness of the specimen [m]. For detailed information on the procedure of the dynamic Young's modulus assessment the reader is referred e.g. to [43].

The obtained values of the dynamic Young's modulus were used for re-scaling the displacements provided by the gauge attached to the loading frame, when evaluating the load-displacement diagrams provided by the three-point bending and uniaxial compression tests.

3.1.2. Three-point bending

The displacement-controlled three-point bending tests were performed on unnotched $160 \times 40 \times 40$ mm simply supported beams with distance between supports equal to 100 mm in order to obtain the tensile failure-related material parameters. The loading was introduced in the midspan at the rate of 0.025 mm/min in order to capture the descending part of the load-displacement diagram and monitored using MTS Alliance RT 30 kN load cell.

3.1.3. Uniaxial compression

The uniaxial compression test was carried out on cubic $40 \times 40 \times 40$ mm specimens, cut off the halves of the cracked beams from the three-point bending test, using the same device as for the three-point bending. A uniform contact and force distribution was accomplished by loading the flat lateral sides, being in contact with mold during preparation of the specimens. The loading was displacement-controlled at the rate of 0.3 mm/min.

3.2. Testing of masonry piers

The geometry of the tested masonry piers of a square cross-section is described in the scheme provided in Fig. 3. The piers were subjected to a displacement controlled quasi-static compression with an eccentricity to introduce a combination of bending and compression. The geometry, loading, boundary conditions, and material of the masonry blocks (clay bricks) were the same for all tested piers, because the study was focused on the influence of the bed joint mortar. The bed joint thickness was equal to 15 mm, while the vertical joints were 10 mm thick, and the bricks were arranged in five layers to make a proper bond.

Table 1
Mass ratios of constituents in the tested mortars and their shrinkage after 90 days of hardening; PC and CB abbreviations stand for Portland cement and crushed bricks, respectively.

Mix	Binder			Aggregate		Water/dry mass	90-Days
	Lime	PC	Metakaolin	Sand	CB	(water/ binder)	shrinkage (%)
LC-S	0.7	0.3	–	3	–	0.175 (0.704)	0.71
LMK-S	0.7	–	0.3	3	–	0.180 (0.714)	0.83
LMK-SCB	0.7	–	0.3	1	1.5	0.250 (0.875)	0.64
L-SCB	1.0	–	0.3	1	1.5	0.320 (0.940)	1.10

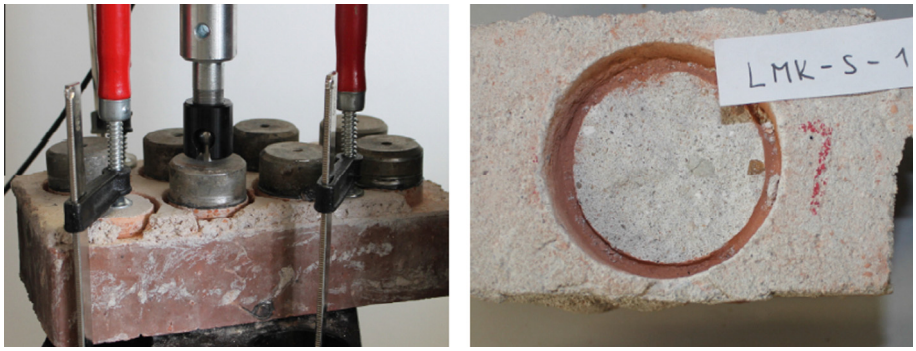

Fig. 2. Interface strength pull-out testing: experiment set-up (left) and the failure plane located within the mortar layer (right).

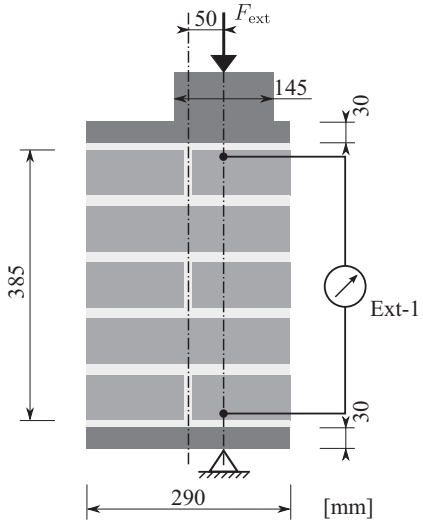

Fig. 3. Loading of the tested piers and placement of virtual extensometers.

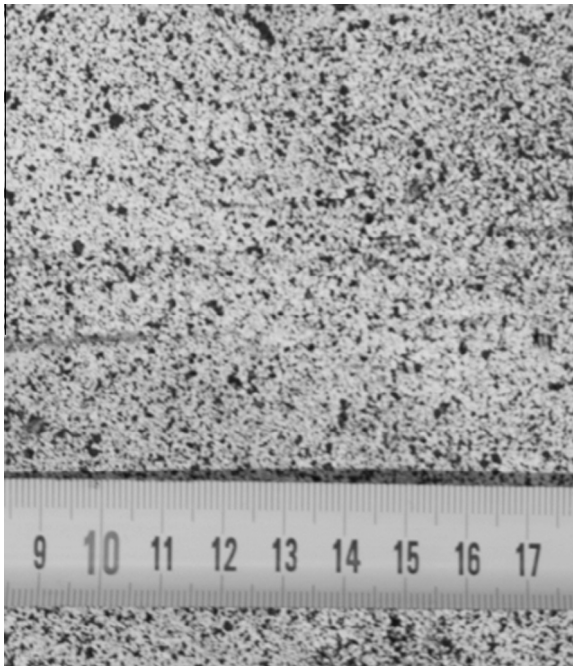

Fig. 4. Black and white stochastic pattern applied onto the pier surface for the purposes of DIC; the main scale units represent centimeters.

The loading of the piers was accomplished using a steel loading frame with a hydraulic actuator of 1 MN loading capacity. The steel slabs ensured a uniform distribution of stresses from the loading and a joint assembly allowed a rotation of the pier ends in all directions. The test was displacement-controlled with a loading rate of 1 mm/min in order to capture the descending part of the force-displacement diagram after the loss of pier integrity.

3.3. DIC

Extensometers and strain-gauges, conventionally used to measure displacements and deformation at pre-determined locations, cannot provide information about strain localization phenomena, such as cracking. The full-field DIC measurement allows to track the strain-field over the region of interest and capture the damage initiation and its progression until the complete loss of structural integrity. This non-contact method was first mentioned in papers by Yamaguchi [44], followed by Peters and Ranson [45], and their pioneering work established the basic principles.

DIC is based on tracking the in-plane deformation and displacement of a surface texture or a stochastic pattern applied artificially on a sample, Fig. 4). A subset of gray-scale pixels in the reference image (representing an initial state) is matched to a subset with the best correlation within the deformed surface and its displacement and deformation are consequently evaluated. Using DIC, the deformation is not averaged over the strain-gauge length, because the averaging of strains depends purely on the camera resolution. Moreover, the technique is not limited to the measurement of small strains and the surface can be relatively rough as in the case of masonry, where strain gauges usually fail. The studies focused on the evaluation of errors in the field of displacements and deformations obtained by DIC, e.g. [46,47], demonstrate a relatively good accuracy of the method compared to conventional measurement techniques. A portion of the data can be lost if a spalling of the surface layer occurs, which easily happens in the case of quasi-brittle materials subjected to extreme loading, limiting the analysis of the post-peak behavior.

The optical monitoring of masonry piers was accomplished using high-definition Canon 70D camera taking pictures at 5-s time intervals, set equally for all tested piers, to yield on average 210 images documenting the deformation of a single pier until its complete failure. The light sensitivity ISO parameter was manually set to 100, since a powerful artificial lighting was available, Fig. 5. The perfect illumination allowed the short exposure time (1/125 s) and the low aperture number set to $f/8$, which was kept constant for all images in the series. In order to minimize the effect of lens distortion [48], the distance between the camera and the observed surface was approximately 1 m, and the focal length (zoom) was set to 55 mm. The resulting DIC real scale resolution equal to

Fig. 5. Tested masonry pier subjected to the combination of compression and bending, introduced via eccentric loading and supporting.

0.202 mm/pixel was computationally feasible while preserving the required precision.

The displacement and strain fields were evaluated using an open source DIC software Ncorr [49], and post-processing of the results was accomplished using Ncorr_post tool [50,51], both operating in MATLAB environment. The DIC results were used for the validation of the numerical model introduced next in Section 4 and for capturing the strain localization. Fig. 6 clearly demonstrates the difference between strain localization in bed joints in the case of a compliant (L-SCB) and a stiff mortar (LMK-SCB).

4. Numerical simulations

The traditional design of masonry structures, based on rules-of-thumb, has been replaced by the numerical approach to address their complex failure mechanisms [52]. Our FE simulations were employed to find the optimum properties of the bed-joint mortars to be used in masonry piers subjected to a combination of compression and bending, which represents a typical loading of masonry walls, columns, and vaults. Mortar shrinkage was neglected in the numerical simulations. The verification process was accomplished by comparing the numerical predictions with the experimentally obtained data; DIC allowed to compare the predicted and observed failure modes, and easily construct the force-displacement diagrams.

In order to provide reliable predictions, the FE model must be supplied with a proper constitutive model. Based on experimental observations of masonry failure modes, damage-plastic models seem to provide the best description of both components, bricks and mortar. In the studies by Wawrzynek and Cincio [53] and Zhou et al. [54] the isotropic damage-plastic models were able to accurately describe the response of masonry to mechanical loading even in non-linear domain after plasticity and cracking took place.

In our simulations we used 15 k (uniaxial compression test specimen), 30 k (three-point bending test specimen), and 80 k (masonry pier) linear tetrahedral elements and employed a phenomenological damage-plastic constitutive model proposed by Jirásek and Grassl [55], implemented in the open-source FE package OOFEM [56]. The model was developed for the predictions of concrete failure subjected to general triaxial stress, and verified through a comprehensive experimental analysis.

The mesh generation was accomplished using Salome open-source generic platform and the post-processing of results and plotting the force-displacement diagrams was done using MATLAB scripts, while the graphical output was prepared in Paraview software.

4.1. Material model

The material model [55] chosen to represent all components of the investigated masonry piers, i.e. studied mortars and bricks, considers the stress-strain law in the form of

$$\boldsymbol{\sigma} = (1-\omega)\mathbf{D}_e : (\boldsymbol{\varepsilon} - \boldsymbol{\varepsilon}_p), \tag{2}$$

where $\boldsymbol{\sigma}$ is the stress tensor, ω is a scalar damage parameter (damage is assumed to be isotropic) and $\mathbf{D}_e$ is the elastic stiffness tensor. In contrast to pure damage models the damage evolution is not driven by the total strain, $\boldsymbol{\varepsilon}$, but it is linked to the evolution of elastic strain, $\boldsymbol{\varepsilon} - \boldsymbol{\varepsilon}_p$. The plastic part of the model formulation consists of a three-invariant yield condition, non-associated flow rule and a pressure-dependent hardening law. The mesh-independent response in the post-peak regime was achieved by the crack band approach [57,58].

4.2. Identification of material model parameters

The independent material model parameters to represent individual mortars and clay bricks were adjusted through an inverse analysis by reproducing the experimentally obtained data. First, the Young's modulus, E, and parameters to influence the flexural strength (tensile strength, f_t, and fracture energy, G_f) were adjusted to reproduce the results of the three-point bending tests, Fig. 7.

The material model parameters to characterize the response to compression (compressive strength, f_c, softening and hardening parameters, A_{soft} and A_{hard}—see [55] for details) were calibrated by fitting the results from uniaxial compression tests. The Poisson's ratio was selected based on a literature study [59–61] as 0.2 to represent both, mortars and bricks. The influence of Poisson's ratio, ν, representing individual components was also analyzed to confirm its negligible impact on results when considered within reasonable bounds between 0.1 and 0.3, as reported in literature, e.g. [62,63].

Even though the nature of the chosen material model did not allow to accurately reproduce the entire experimentally obtained load-displacement path, the results are, with respect to the large scatter of the experimental data (indicated by the shaded area in Figs. 8–10), considered satisfactory. The summary of the material model input parameters to represent individual mortars and bricks are summarized in Table 2.

4.3. Numerical simulations of masonry pier failure

The geometry of the 3D FE model was following the geometry of the experimentally tested masonry piers, as described in Fig. 3; the FE mesh is presented in Fig. 11. The interface between bricks and surrounding mortar was not explicitly defined and modeled using interface elements, because the interface was not the weakest link in tension, recall Section 3.1.

In order to define the loading of the piers and boundary conditions in a realistic way, the model also consisted, beside the auxiliary steel slabs, of the cylindrical load cell, both modeled as

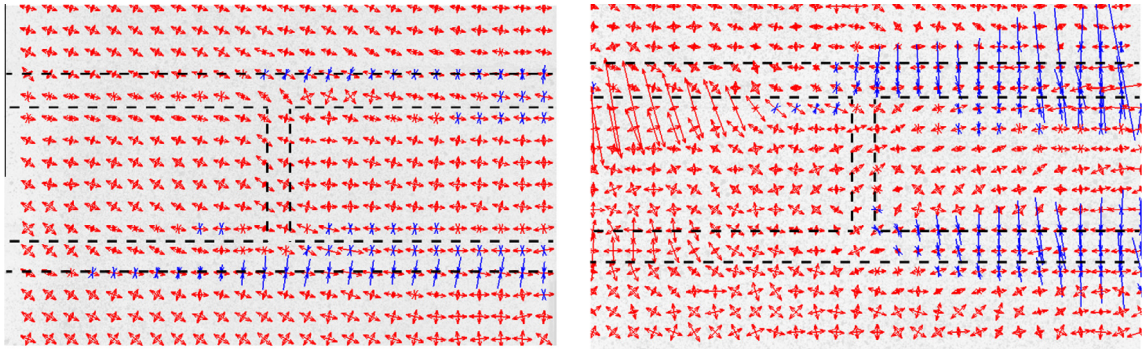

Fig. 6. Direction and relative magnitude of principal strains on the surface of masonry piers: stiff LMK-SCB mortar joints (left) and compliant L-SCB joints (right); red and blue arrows indicate principal tension and compression, respectively, and the dashed line represents the outlines of bricks and mortar. (For interpretation of the references to colour in this figure legend, the reader is referred to the web version of this article.)

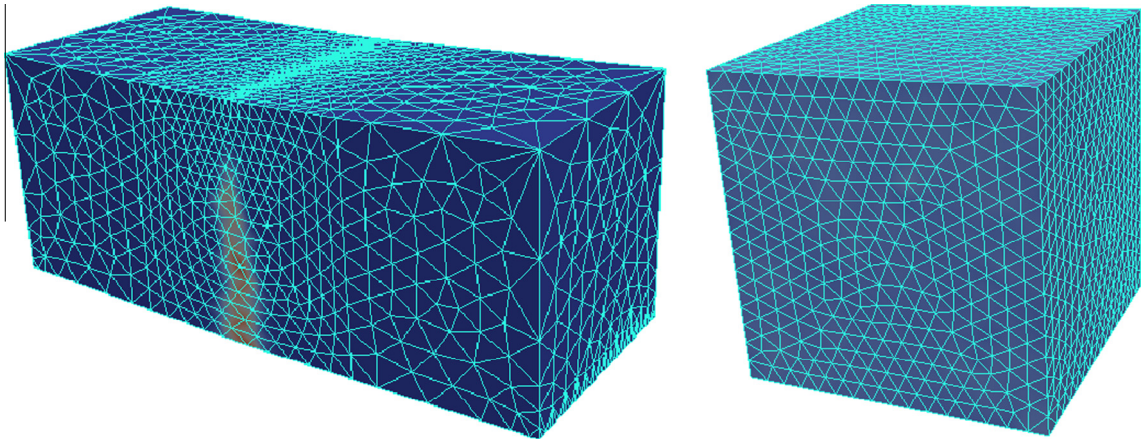

Fig. 7. FE model of specimens for three-point bending (left) and uniaxial compression (right) tests.

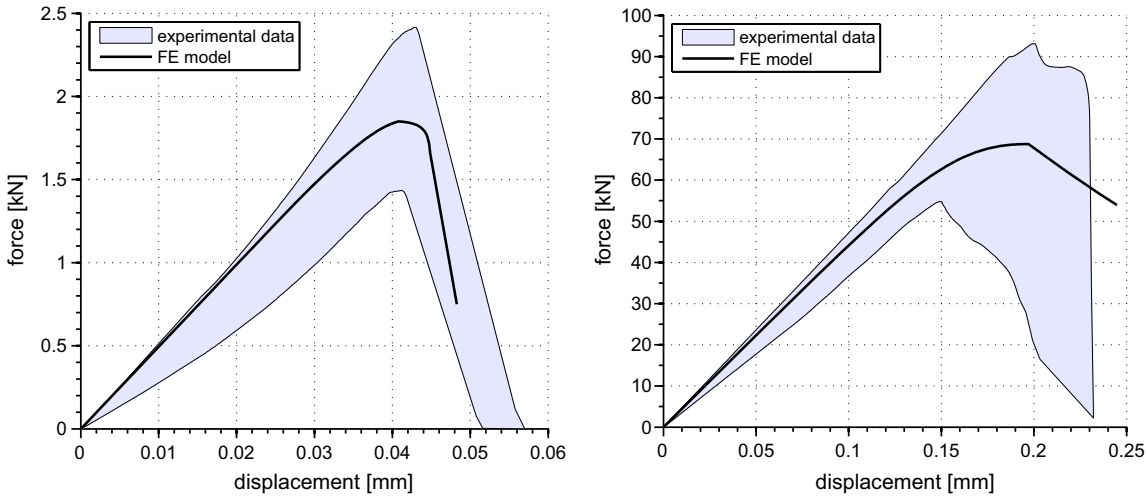

Fig. 8. Fit of the material model input parameters representing bricks to reproduce the results of three-point bending (left) and uniaxial compression (right) tests.

an isotropic elastic continuum. The loading was accomplished by an incremental displacement imposed to a single node at the crest of the steel cylinder in order to allow rotations around all axes. The load-step increments were adjusted for each loading stage individually in order to reach convergence for a minimum computational cost.

The FE model was at first validated by comparing the predicted and measured load-displacement diagrams, as presented in Fig. 12. Both, the reactions in a load cell and the displacements obtained from DIC by placing virtual extensometers at the top and bottom of the tested piers, were in a good agreement with the numerically obtained predictions, Fig. 3. The agreement between the predicted cracking patterns (reflected in the field of damage distribution) and the observed development of cracks (visualized as a map of maximum principal strains obtained from DIC) is not perfect for all tested piers. However, considering the non-homogeneous

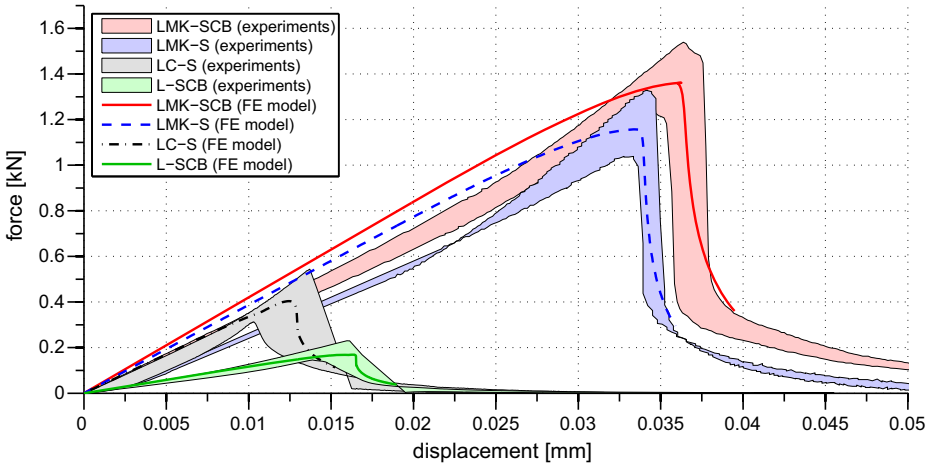

Fig. 9. Fit of the material model input parameters representing the individual tested mortars to reproduce the results of three-point bending tests.

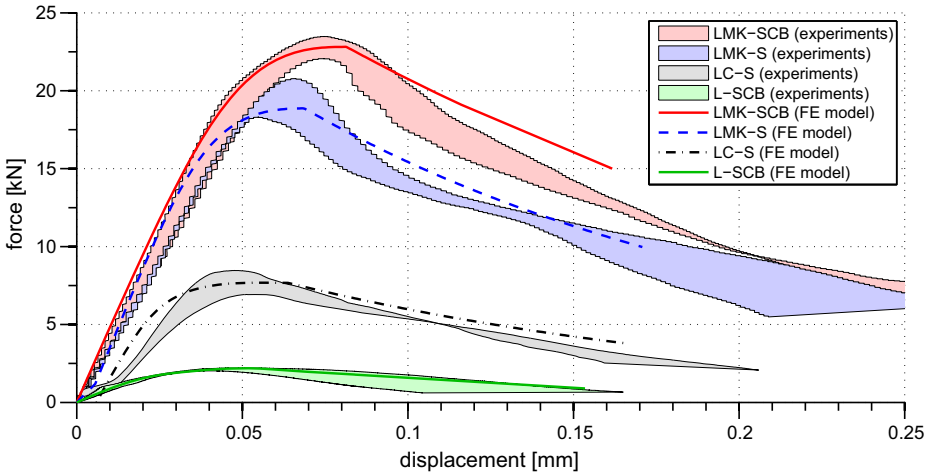

Fig. 10. Fit of the material model input parameters representing the individual tested mortars to reproduce the results of uniaxial compression tests.

Table 2
Key material input properties of bricks and the tested mortars; E, ν, f_c, f_t and G_f denote the Young's modulus, Poisson's ratio, compressive strength, tensile strength and fracture energy, respectively.

Material	E [GPa]	ν [−]	f_c [MPa]	f_t [MPa]	G_f [J/m^2]
bricks	14.0	0.20	30.0	2.70	30.0
LC-S	7.10	0.20	4.80	0.55	3.20
LMK-S	7.40	0.20	11.3	1.53	13.5
LMK-SCB	10.0	0.20	14.7	1.92	26.0
L-SCB	2.45	0.20	1.30	0.26	1.55

microstructure of the tested materials, the FE analysis results cab be considered satisfactory.

In the case of piers with lime-cement mortar LC-S (Fig. 13a), the model correctly predicted the formation of multiple cracks at the compressed side of the tested piers and the formation of two major cracks at the opposite side due to tensile stresses from the pier bending. The DIC results in the case of lime-metakaolin mortar LMK-S (Fig. 13b) were influenced by a spalling of pier surface at the bottom, but the major crack formation in the middle of the tested pier can be identified in both, model predictions and DIC results. On the other hand, the formation of the major splitting crack in the case of mortar LMK-SCB (Fig. 13c), containing metakaolin and crushed bricks, was perfectly predicted by the FE simulation, as well as the distributed cracking at the compressed pier edge in the case of the weak mortar L-SCB (Fig. 13d).

In conclusion, the strategy to model the masonry units and mortar separately allowed us to capture the failure mode quite realistically (see Fig. 13)[1], enabling to study the relationship between the mechanical resistance of the masonry piers and bed-joint mortar properties.

4.4. Influence of mortar properties on mechanical resistance of masonry piers

The aim of the presented study was to show the relationship between the individual mortar material parameters and the load-bearing capacity of masonry piers having the same configuration of geometry and loading conditions as described in Sections 3 and 4.3. The lime-metakaolin mortar without crushed bricks (LMK-S) was chosen as the reference material, for which a single material parameter was changed at a time to assess its impact on the load-bearing capacity of the masonry pier.

[1] Scales cannot be included since the DIC outputs are provided in the form of maximum principal strain which is dependent in the case of localized cracks on the choice of subset radius, spacing and strain averaging radius, set during the DIC analysis.

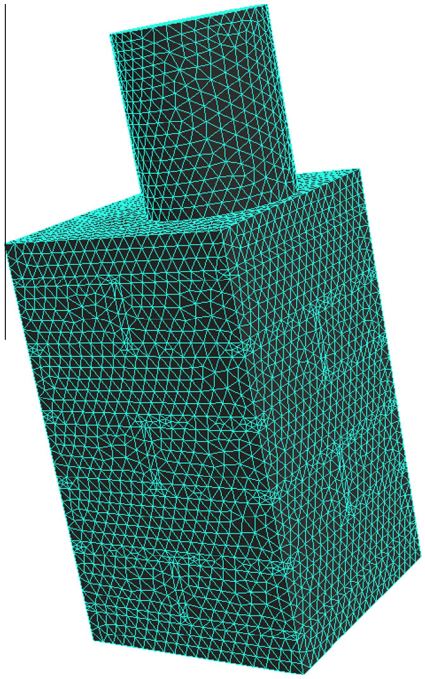

Fig. 11. FE mesh of the investigated masonry piers.

Such analysis clearly indicated what the key material parameters were, and how to optimize the mortar composition towards a higher mechanical resistance of masonry structures. Similar approach was adopted e.g. by Sandoval and Roca [63], who studied the influence of geometry and material properties of individual constituents on the buckling behavior of masonry walls.

4.4.1. Influence of mortar stiffness

The plot in Fig. 14 clearly demonstrates that the value of the mortar Young's modulus has just a minor impact on the load-bearing capacity of the studied masonry pier, and that there is no abrupt change when the mortar stiffness becomes superior to the stiffness of masonry units. However, the failure mode changes quite significantly. The use of a compliant mortar results in a multiple cracking of bricks at the more loaded side due to poor supporting, while a major crack passing through the entire column in the middle forms if the bed joints are stiff, see Fig. 15.

It could seem advantageous to use mortars lacking pozzolanic additives because of their lower stiffness, in order to produce masonry of a higher deformation capacity within the elastic range. Such masonry would in theory better resist seismic loading or imposed displacements, e.g. due to differential subsoil settlement. However, the compliant pure-lime mortars without additives promoting the hydraulic reactions are weak and suffer from an increased shrinkage cracking [18].

4.4.2. Influence of mortar tensile strength

The tensile strength and fracture energy had to be modified carefully at the same time in order to avoid snap-back in the stress-strain diagram, and to preserve the same post-peak ductility for all investigated mortars. In particular, these were 1.19, 5.95, 11.90, 23.80, 29.75 and 32.13 J/m^2 for the investigated tensile strengths 0.1, 0.5, 1.0, 2.0, 2.5 and 2.7 MPa, respectively.

Given the studied masonry pier and the boundary conditions, the tensile strength appears to have just a minor effect if it is lower than the strength of masonry units (bricks), see Fig. 16. The reduction of the masonry pier load-bearing capacity is very small and it can be attributed to early-stage cracking of mortar and favorable redistribution of stresses, since the cracked mortar becomes more compliant. On the other hand, the mortars of higher strength in tension act as a confinement of the units and the masonry reinforcement. Since common lime- or cement-based mortars hardly attain the tensile strength superior to the strength of masonry units, the bed joint strengthening is accomplished e.g. by means of embedded steel rods [64].

According to our numerical simulations, the confinement imposed by the strong mortars resulted in the cracking of the bricks and eventually the formation of the wedge-like failure as opposed to the vertical splitting of the pier containing a very weak mortar as indicated in Fig. 17.

4.4.3. Influence of mortar compressive strength

The bed-joint mortar compressive strength appears to be the crucial parameter with respect to the load-bearing capacity of masonry subjected to a combination of compression and bending. Mortars of a low compressive strength suffer an irreversible deformation at relatively low levels of external load, and masonry units are consequently subjected to uneven distribution of stresses due to imperfect supporting and excessive deformation of the bed joints.

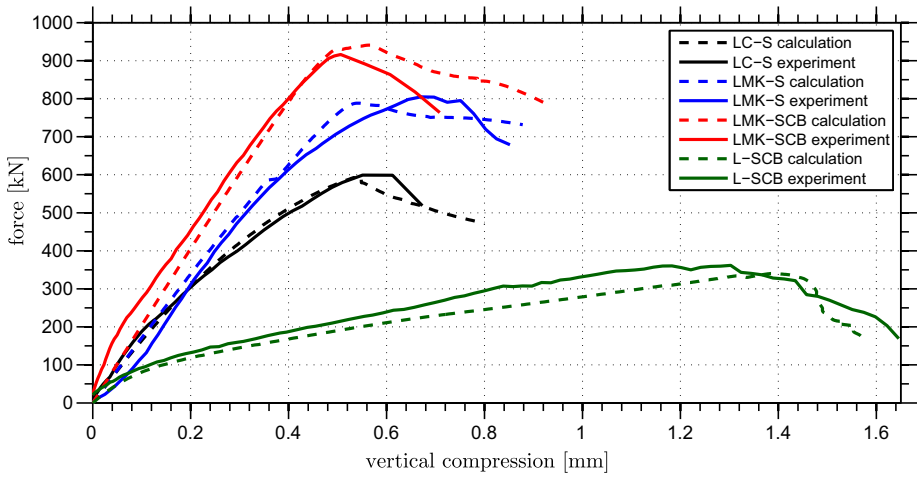

Fig. 12. Comparison between the numerically and experimentally obtained load-displacement diagrams, describing the response of the tested masonry piers to the imposed vertical displacement at the crest of the loading cell.

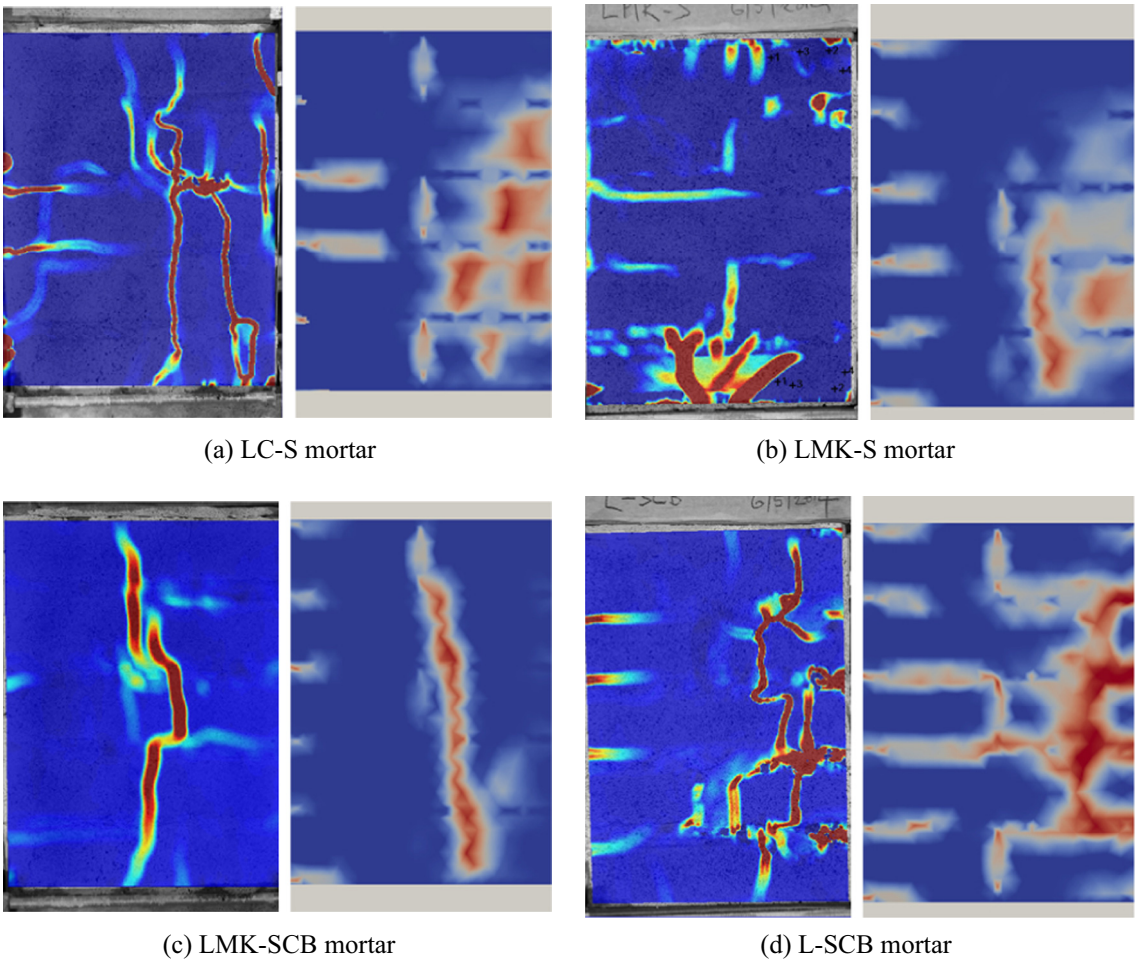

Fig. 13. Field of maximum principal strain obtained by DIC (left within the couples) and FE model damage predictions (right) on the face of the tested piers after reaching the peak load. The images provide a qualitative comparison between the predicted cracking patterns and experimental observations using DIC; the red areas represent the localized cracks.

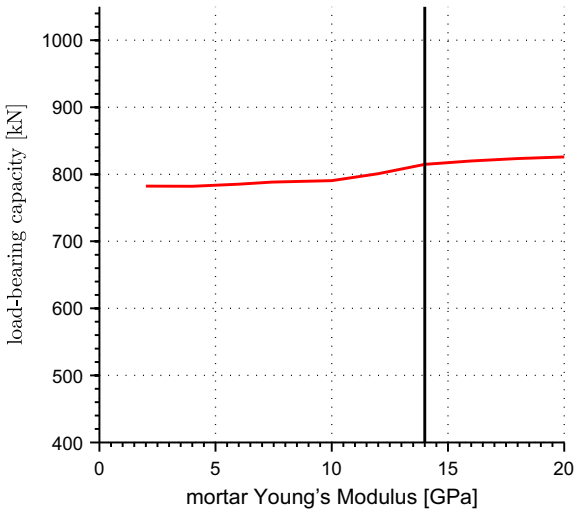

Fig. 14. Dependence of the masonry pier maximum load-bearing capacity on mortar stiffness; black line represents the brick Young's modulus $E^{(b)}$ = 14 GPa.

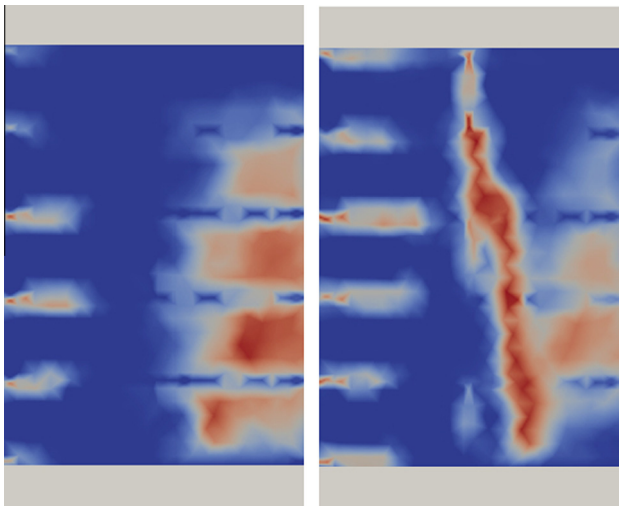

Fig. 15. Crack patterns on masonry piers containing compliant ($E^{(m)}$ = 2 GPa, left) and stiff ($E^{(m)}$ = 20 GPa, right) mortar.

In the case of the modeled masonry piers, the early crushing of the weak bed-joint mortar resulted in cracking of bricks at the more loaded pier periphery, Fig. 19. This phenomenon limited the load-bearing capacity of the tested pier rather significantly, especially in the case of very poor mortars ($f_c^{(m)} < 10$ MPa), see Fig. 18. The bed joints containing mortars of a high compressive strength did not suffer the inelastic deformation before the major splitting vertical crack appeared due to transversal expansion, resulting in a high load-bearing capacity. Therefore, the mortars

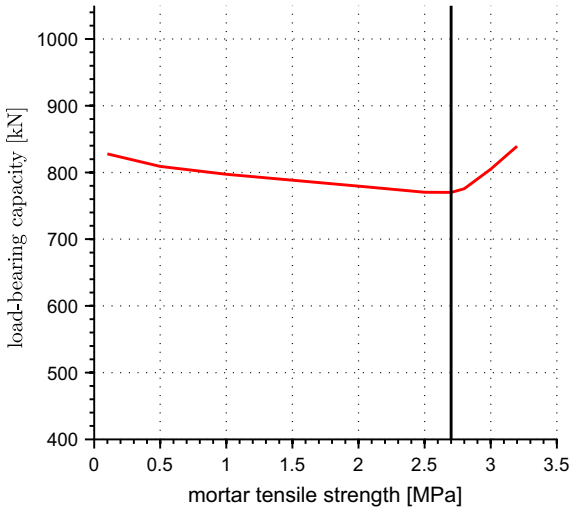

Fig. 16. Dependence of the masonry pier maximum load-bearing capacity on mortar tensile strength; black line represents the brick tensile strength $f_t^{(b)}$ = 2.7 MPa.

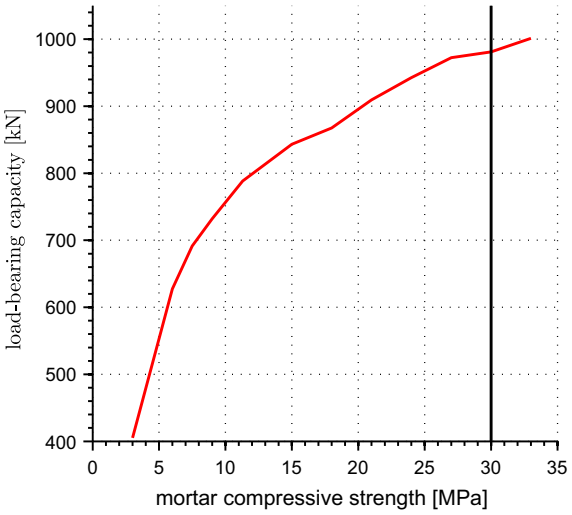

Fig. 18. Dependence of the masonry pier maximum load-bearing capacity on mortar compressive strength; black line represents the brick compressive strength $f_c^{(b)}$ = 30 MPa.

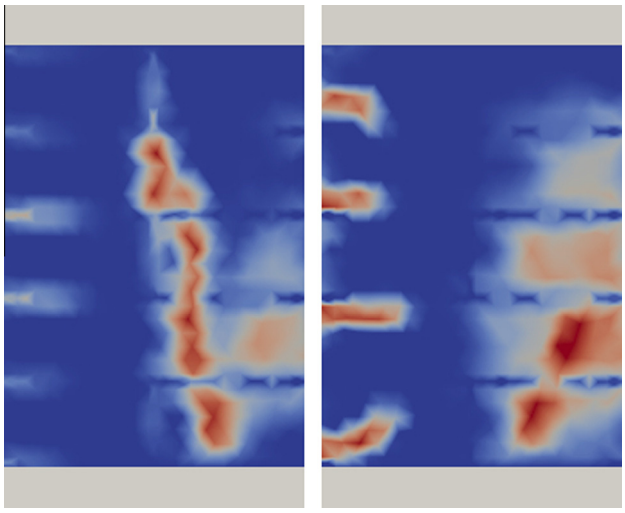

Fig. 17. Crack patterns on masonry piers containing weak (f_t = 0.1 MPa, left) and strong (f_t = 3.2 MPa, right) mortar in tension.

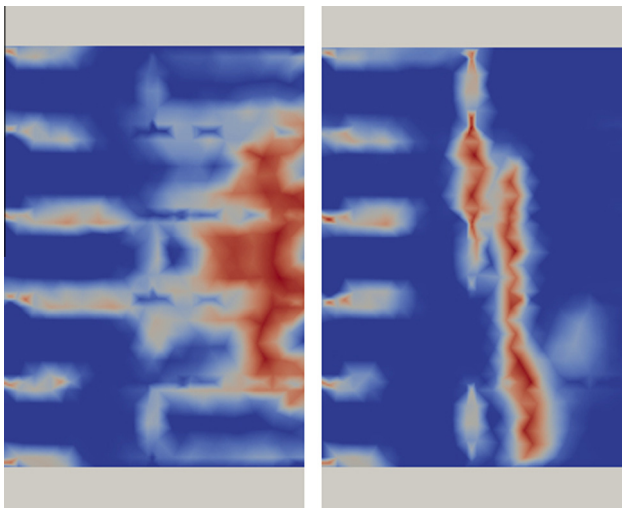

Fig. 19. Crack patterns on masonry piers containing weak (f_c = 3 MPa, left) and strong (f_c = 33 MPa, right) mortar in compression.

with superior compressive strength should be used especially if a bed joint reinforcement is introduced so that the high strength can be efficiently exploited.

5. Discussion of results

The eccentrically compressed masonry pier was selected as a model example to address both, behavior in compression, being the most frequent loading of masonry elements, and tension, which is considered critical for masonry. The performance of the conventionally used lime-cement mortar was compared with mortars containing the pozzolanic alternative—metakaolin. To reach even better performance, crushed brick fragments were also used to replace a portion of stiff river sand. Such approach was adopted based on findings from the previous studies, e.g. [18,36,37], claiming that mortars containing active pozzolans and relatively compliant crushed brick fragments exhibit a superior strength.

Series of compression and three-point bending tests were carried out primarily in order to obtain the input parameters characterizing individual materials in the FE model. The results of the basic material tests conclusively indicate that the addition of metakaolin provides the lime-based mortars with significantly higher strength than the addition of Portland cement. On the other hand, the pure-lime mortars lacking any additives appeared to be very poor. These findings are in agreement with several studies; e.g. by Vejmelková et al. [22] claiming that by replacing 20% of lime with metakaolin the mortar compressive strength can increase up to five times and the flexural strength up to three times, which is in agreement with the study by Velosa et al. [5].

The partial replacement of sand grains by crushed brick fragments further improved the mechanical performance of the mortars, justifying their extensive use in ancient times [13,16,17]. The higher strength is attributed to a reduction of shrinkage-induced cracking due to presence of the compliant brick fragments. This in turn leads to a better mortar integrity as suggested by Nežerka et al. [19,18], and lower stress concentrations in the vicinity of aggregates, as studied in detail in [20].

The superior strength of the metakaolin-enriched mortars was also reflected by the increased load-bearing capacity of the tested piers, in particular from 360 kN and 600 kN, reached in the case of

pure-lime (L-SCB) and lime-cement mortar (LC-S), respectively, up to 800 kN when 30% of the binder was replaced by metakaolin (LMK-S). Moreover, the load-bearing capacity was further increased with the use of mortar containing crushed bricks (LMK-SCB), reaching up to 915 kN. This strength enhancement can explain the resistance and longevity of numerous ancient masonry structures containing cocciopesto [32,65]. The extraordinary strength of the LMK-SCB mortar together with the good adhesion between the mortar and bricks should also result in an increased seismic resistance, as suggested by Costa et al. [66].

Knowing the basic material parameters, the damage-plastic material model used for the 3D FE simulations allowed to reproduce the experimental results with a relatively high accuracy, despite the complex composite action taking place in masonry. Even the simplest case of uniaxial compression leads to a triaxial compression in mortar, while introducing a uniaxial compression and biaxial tension in usually stiffer masonry units. Such scenario usually leads to the formation of vertical splitting cracks leading to a complete failure [67].

The chosen strategy to model the bricks and mortars as two distinct materials allowed to investigate the relationship between the individual material parameters and structural behavior of the masonry pier. Our findings that the mortar compressive strength has the biggest impact on the load-bearing capacity is in contradiction with the conclusions of Gumaste et al. [68] and Pavía and Hanley [69]. They claim that mortar compressive strength has just a minor impact on the behavior of masonry subjected to uniaxial compression. This discrepancy can be probably attributed to a different experimental set-up, in particular to the eccentricity of loading introduced in our study. The eccentric loading was responsible for a significant deformation of the bed joints, leading to a non-linear response at relatively early loading-stage.

The assumption that the difference between the Young's modulus of bricks and mortar is the precursor of the compression failure [70] was not confirmed, and the load-bearing capacity of the masonry piers was almost independent of mortar stiffness.

6. Conclusions

The chosen strategy to combine the comprehensive experimental analysis together with the numerical modeling revealed new findings to be considered during the design of bed joint mortars. Even though the study was focused purely on the lime-based mortars, because these are accepted by the authorities for cultural heritage, our findings can also help with the design of mortars and masonry based on modern materials.

The results of the basic material tests demonstrate the superior strength of mortars containing metakaolin, when compared to a pure-lime or lime-cement ones. The mortar strength was further increased by the addition of crushed bricks, which is attributed to the reduction of microcracking due to shrinkage around the relatively compliant ceramic fragments. It can be also conjectured that the hydraulic reaction in mortars containing metakaolin was promoted by the presence of water retained within the crushed brick fragments.

The enhanced strength of the metakaolin-rich mortars, and especially those containing crushed bricks, was reflected in the significantly increased load-bearing capacity of masonry piers loaded by the combination of compression and bending. This can explain the extraordinary resistance and durability of ancient masonry structures with cocciopesto mortars. Moreover, the utilization of the waste by-products from ceramic plants makes the material sustainable for a relatively low cost, since the fragments partially replace binder, being the most expensive mortar component.

Based on experimental observations the damage-plastic material model seemed to be the most appropriate to describe the constitutive behavior of mortars and bricks in the FE model. The chosen strategy to model the mortars and bricks as distinct materials allowed the relatively accurate reproduction of the experimentally obtained data in terms of the predicted crack patterns and load-displacement diagrams. Results of the numerical simulations and DIC analysis clearly demonstrate that the mortar properties have an enormous impact on the load-bearing capacity of masonry, strain localization, and the formation of cracks.

The numerical analysis, based on the FE model verified through the comprehensive experimental analysis, revealed that mortar compressive strength is the key material parameter with respect to the load-bearing capacity of the piers subjected to the combination of bending and compression. Considering the studied geometry and boundary conditions, tensile strength and mortar Young's modulus influence the pier behavior and modes of failure, however, do not have any significant impact on the load-bearing capacity.

Acknowledgments

The authors acknowledge financial support provided the Czech Science Foundation, Project No. GA13-15175S, and by the Ministry of Culture of the Czech Republic, Project No. DF11P01OVV008.

References

[1] A. Arizzi, G. Cultrone, Aerial lime-based mortars blended with a pozzolanic additive and different admixtures: a mineralogical, textural and physical-mechanical study, Constr. Build. Mater. 31 (2012) 135–143, http://dx.doi.org/10.1016/j.cemconres.2012.03.008.
[2] F. Veniale, M. Setti, C. Rodriguez-Navarro, S. Lodola, W. Palestra, A. Busetto, Thamasite as decay product of cement mortar in brick masonry of a church near Venice, Cem. Concr. Compos. 25 (2003) 1123–1129, http://dx.doi.org/10.1016/s0958-9465(03)00159-8.
[3] K. Callebaut, J. Elsen, K. Van Balen, W. Viaene, Nineteenth century hydraulic restauration mortars in the Saint Michael's Church (Leuven, Belgium). Natural hydraulic lime or cement?, Cem Concr. Res. 31 (2001) 397–403, http://dx.doi.org/10.1016/s0008-8846(00)00499-3.
[4] A. Moropoulou, A. Bakolas, S. Anagnostopoulou, Composite materials in composite structures, Cem. Concr. Compos. 27 (2005) 295–300, http://dx.doi.org/10.1016/j.cemconcomp.2004.02.018.
[5] A. Velosa, F. Rocha, R. Veiga, Influence of chemical and mineralogical composition of metakaolin on mortar characteristics, Acta Geodyn. Geomater. 153 (2009) 121–126.
[6] M. Seabra, J. Labrincha, V. Ferreira, Rheological behaviour of hydraulic lime-based mortars, J. Eur. Ceram. Soc. 27 (2007) 1735–1741, http://dx.doi.org/10.1016/j.jeurceramsoc.2006.04.155.
[7] A. Sepulcre-Aguilar, F. Hernández-Olivares, Assessment of phase formation in lime-based mortars with added metakaolin, Portland cement and sepiolite, for grouting of historic masonry, Cem. Concr. Res. 40 (2010) 66–76, http://dx.doi.org/10.1016/j.cemconres.2009.08.028.
[8] A. Moropoulou, A. Bakolas, E. Aggelakopoulou, Evaluation of pozzolanic activity of natural and artificial pozzolans by thermal analysis, Thermochim. Acta 420 (2004) 135–140, http://dx.doi.org/10.1016/j.tca.2003.11.059.
[9] Z. Slížková, Characteristics of metakaoline modified mortars applied on historic objects, Metakaolin, Brno (2009) 146–155.
[10] I. Papayianni, The longevity of old mortars, Appl. Phys. A 83 (2006) 685–688, http://dx.doi.org/10.1007/s00339-006-3523-2.
[11] I. Papayianni, M. Stefanidou, Durability aspects of ancient mortars of the archeological site of Olynthos, J. Cult. Heritage 8 (2007) 193–196, http://dx.doi.org/10.1016/j.culher.2007.03.001.
[12] D. Wilk, L. Bratasz, R. Kozlowski, Shrinkage cracking in Roman cement pastes and mortars, Cem. Concr. Res. 53 (2013) 168–175, http://dx.doi.org/10.1016/j.cemconres.2013.03.012.
[13] L. Mallinson, I. Davies, A historical examination of concrete, in: Office for Official Publications of the European Communities, Luxembourg, Final Report CD-NA-10937-EN-C.
[14] A. Farci, D. Floris, P. Meloni, Water permeability vs. porosity in samples of Roman mortars, J. Cult. Heritage 6 (2005) 55–59, http://dx.doi.org/10.1016/j.culher.2004.08.002.
[15] L. Sbordoni-Mora, Les matériaux des enduits traditionnels, in: Proceedings of the ICCROM Symposium on Mortars, Cements and Grouts used in the Conservation of Historic Buildings, Rome, 1981, pp. 375–383.
[16] P. Degryse, J. Elsen, M. Waelkens, Study of ancient mortars from Sagalassos (Turkey) in view of their conservation, Cem. Concr. Res. 21 (2002) 1457–1463, http://dx.doi.org/10.1016/s0008-8846(02)00807-4.
[17] G. Baronio, L. Binda, N. Lombardini, The role of brick pebbles and dust in conglomerates based on hydrated lime and crushed bricks, Constr. Build. Mater. 11 (1997) 33–40, http://dx.doi.org/10.1016/s0950-0618(96)00031-1.

[18] V. Nežerka, Z. Slížková, P. Tesárek, T. Plachý, D. Frankeová, V. Petráňová, Comprehensive study on microstructure and mechanical properties of lime-pozzolan pastes, Cem. Concr. Res. 64 (2014) 17–29, http://dx.doi.org/10.1016/j.cemconres.2014.06.006.
[19] V. Nežerka, J. Němeček, Z. Slížková, P. Tesárek, Investigation of crushed brick-matrix interface in lime-based ancient mortar by microscopy and nanoindentation, Cem. Concr. Compos. 55 (2015) 122–128, http://dx.doi.org/10.1016/j.cemconcomp.2014.07.023.
[20] V. Nežerka, J. Němeček, J. Zeman, Micromechanics-based simulations of compressive and tensile testing on lime-based mortars, Submitted to Mechanics of Materials.
[21] CEN, Building Lime – Part 1: Definitions, Specifications and Conformity Criteria, CEN, Brussels (Belgium), 2010.
[22] E. Vejmelková, M. Keppert, Z. Keršner, P. Rovnaníková, R. Černý, Mechanical, fracture-mechanical, hydric, thermal, and durability properties of lime-metakaolin plasters for renovation of historical buildings, Constr. Build. Mater. 31 (2012) 22–28, http://dx.doi.org/10.1016/j.conbuildmat.2011.12.084.
[23] J. Lanas, J. Pérez Bernal, M. Bello, J. Alvarez Galindo, Mechanical properties of natural hydraulic lime-based mortars, Cem. Concr. Res. 34 (2004) 2191–2201, http://dx.doi.org/10.1016/j.cemconres.2004.02.005.
[24] O. Cizer, Competition between carbonation and hydration on the hardening of calcium hydroxide and calcium silicate binders (Ph.D. thesis), Katholieke Universiteit Leuven, 2009.
[25] P. De Silva, F. Glasser, Phase relations in the system $CaO - Al_2O_3 - SiO_2 - H_2O$ relevant to metakaolin-calcium hydroxide hydration, Cem. Concr. Res. 23 (1993) 627–639, http://dx.doi.org/10.1016/0008-8846(93)90014-z.
[26] M. Rojas, J. Cabrera, The effect of temperature on the hydration rate and stability of the hydration phases of metakaolin-lime-water systems, Cem. Concr. Res. 32 (2002) 133–138, http://dx.doi.org/10.1016/s0008-8846(01)00642-1.
[27] T. Rougelot, F. Skoczylas, N. Burlion, Water desorption and shrinkage in mortars and cement pastes: experimental study and poromechanical model, Cem. Concr. Res. 39 (2009) 36–44, http://dx.doi.org/10.1016/j.cemconres.2008.10.005.
[28] M. Stefanidou, I. Papayianni, The role of aggregates on the structure and properties of lime mortars, Cem. Concr. Compos. 27 (2005) 914–919, http://dx.doi.org/10.1016/j.cemconcomp.2005.05.001.
[29] J. Lanas, J. Alvarez, Masonry repair lime-based mortars: factors affecting the mechanical behaviour, Cem. Concr. Res. 33 (2003) 1867–1876, http://dx.doi.org/10.1016/s0008-8846(03)00210-2.
[30] M. Mosquera, B. Silva, B. Prieto, E. Ruiz-Herrera, Addition of cement to lime-based mortars: effect on pore structure and vapor transport, Cem. Concr. Res. 36 (2006) 1635–1642, http://dx.doi.org/10.1016/j.cemconres.2004.10.041.
[31] J. Silva, J. Brito de, R. Veiga, Incorporation of fine ceramics in mortars, Constr. Build. Mater. 23 (2009) 556–564, http://dx.doi.org/10.1016/j.conbuildmat.2007.10.014.
[32] A. Moropoulou, A. Cakmak, G. Biscontin, A. Bakolas, E. Zendri, Advanced Byzantine cement based composites resisting earthquake stresses: the crushed brick/lime mortars of Justinian's Hagia Sophia, Constr. Build. Mater. 16 (2002) 543–552, http://dx.doi.org/10.1016/s0950-0618(02)00005-3.
[33] H. Böke, S. Akkurt, B. İpekoglu, E. Ugurlu, Characteristics of brick used as aggregate in historic brick-lime mortars and plasters, Cem. Concr. Res. 36 (2006) 1115–1122, http://dx.doi.org/10.1016/j.cemconres.2006.03.011.
[34] J. Elsen, Microscopy of historic mortars: a review, Cem. Concr. Res. 36 (2006) 1416–1424, http://dx.doi.org/10.1016/j.cemconres.2005.12.006.
[35] G. Baronio, L. Binda, Study of the pozzolanicity of some bricks and clays, Constr. Build. Mater. 11 (1997) 41–46, http://dx.doi.org/10.1016/s0950-0618(96)00032-3.
[36] V. Nežerka, P. Tesárek, J. Zeman, Fracture-micromechanics based model of mortars susceptible to shrinkage, Key Eng. Mater. 592–593 (2014) 189–192, http://dx.doi.org/10.4028/www.scientific.net/kem.592-593.189.
[37] P. Tesárek, V. Nežerka, P. Padevět, J. Antoš, T. Plachý, Influence of aggregate stiffness on fracture-mechanical properties of lime-based mortars, Appl. Mech. Mater. 486 (2014) 289–294, http://dx.doi.org/10.4028/www.scientific.net/amm.486.289.
[38] A. Moropoulou, A. Bakolas, K. Bisbikou, Characterization of ancient, Byzantine and later historic mortars by thermal and X-ray diffraction techniques, Thermochem. Acta 269 (270) (1995) 779–995, http://dx.doi.org/10.1016/0040-6031(95)02571-5.
[39] CEN, Methods of Test for Mortar for Masonry – Part 3: Determination of Consistence of Fresh Mortar (by Flow Table), ČSN, 2000. EN 1015-3.
[40] CEN, Methods of Test for Mortar for Masonry: Determination of Flexural and Compressive Strength of Hardened Mortar, CEN, Brussels (Belgium), 1999.
[41] CEN, Methods of test for mortar for masonry: Determination of the compatibility of one-coat rendering mortars with substrates, CEN, Brussels (Belgium), 2002.
[42] A. Malaikah, K. Al-Saif, R. Al-Zaid, Prediction of the dynamic modulus of elasticity of concrete under different loading conditions, in: International Conference on Concrete Engineering and Technology, Universiti Malaya, 2004, pp. 32–39.
[43] M. Radovic, E. Curzio-Lara, L. Riester, Comparison of different techniques for determination of elastic properties of solids, Mater. Sci. Eng. A368 (2004) 56–70, http://dx.doi.org/10.1016/j.msea.2003.09.080.
[44] I. Yamaguchi, A laser speckle strain gauge, J. Phys. E 14 (1981) 1270, http://dx.doi.org/10.1088/0022-3735/14/11/012.
[45] W. Peters, W. Ranson, Digital imaging techniques in experimental stress analysis, Opt. Eng. 21 (1982) 427–431, http://dx.doi.org/10.1117/12.7972925.
[46] P. Lava, S. Cooreman, S. Coppieters, M. De Strycker, D. Debruyne, Assessment of measuring errors in DIC using deformation fields generated by plastic FEA, Opt. Lasers Eng. 47 (2009) 747–753, http://dx.doi.org/10.1016/j.optlaseng.2009.03.007.
[47] M. Bornert, F. Brémand, P. Doumalin, J. Dupré, M. Fazinni, M. Grédiac, F. Hild, S. Mistou, J. Molimard, J. Orteu, L. Robert, Y. Surrel, P. Vacher, B. Wattrisse, Assessment of digital image correlation errors: methodology and results, Exp. Mech. 49 (2009) 353–370, http://dx.doi.org/10.1007/s11340-012-9704-3.
[48] B. Pan, L. Yu, D. Wu, L. Tang, Systematic errors in two-dimensional digital image correlation due to lens distortion, Opt. Lasers Eng. 51 (2013) 140–147, http://dx.doi.org/10.1016/j.optlaseng.2012.08.012.
[49] J. Blaber, B. Adair, A. Antouniou, Ncorr: open-source 2D digital image correlation Matlab software, Exp. Mech. 55 (2015) 1105–1122, http://dx.doi.org/10.1007/s11340-015-0009-1.
[50] V. Nežerka, Ncorr_post: DIC Post-Processing Tool, <http://mech.fsv.cvut.cz/nezerka/dic/index.htm>, CTU in Prague.
[51] V. Nežerka, J. Antoš, T. Sajdlová, P. Tesárek, Open source DIC tools for analysis of multiple cracking in fiber-reinforced concrete, Appl. Mech. Mater. 827 (2016) 336–339, http://dx.doi.org/10.4028/www.scientific.net/AMM.827.336.
[52] P. Lourenço, Computations on historic masonry structures, Prog. Struct. Mater. Eng. 4 (2002) 301–319, http://dx.doi.org/10.1002/pse.120.
[53] A. Wawrzynek, A. Cincio, Plastic-damage macro-model for non-linear masonry structures subjected to cyclic or dynamic loads, In: Proc. Conf. Analytical Models and New Concepts in Concrete and Masonry Structures, AMCM, Gliwice, Poland.
[54] W.F. Zhang, H. Wang, Elasticity damage and plastic analyses of masonry, Appl. Mech. Mater. 166–169 (2012) 1454–1458, http://dx.doi.org/10.4028/www.scientific.net/amm.166-169.1454.
[55] M. Jirásek, P. Grassl, Damage-plastic model for concrete failure, Int. J. Solids Struct. 43 (2006) 7166–7196, http://dx.doi.org/10.1016/j.ijsolstr.2010.12.005.
[56] B. Patzák, Z. Bittnar, Design of object oriented finite element code, Adv. Eng. Software 32 (2001) 759–767, http://dx.doi.org/10.1016/s0965-9978(01)00027-8. <www.oofem.org>.
[57] Z. Bažant, B. Oh, Crack band theory for fracture of concrete, Mater. Struct. 16 (1983) 155–177, http://dx.doi.org/10.1007/bf02486267.
[58] M. Jirásek, M. Bauer, Numerical aspects of the crack band approach, Comput. Struct. 110–111 (2012) 60–78, http://dx.doi.org/10.1016/j.compstruc.2012.06.006.
[59] M. Drdácký, D. Michoinová, Lime mortars with natural fibres, Britle matrix composites, in: Proceedings of the 7th Int. Symposium, 2003, pp. 523–532.
[60] J. Vorel, V. Šmilauer, Z. Bittnar, Multiscale simulations of concrete mechanical tests, J. Comput. Appl. Math. 236 (2012) 4882–4892, http://dx.doi.org/10.1016/j.cam.2012.01.009.
[61] V. Nežerka, J. Zeman, A micromechanics-based model for stiffness and strength estimation of cocciopesto mortars, Acta Polytech. 52 (2012) 29–37.
[62] V. Corinaldesi, Mechanical behavior of masonry assemblages manufactured with recycled-aggregate mortars, Cem. Concr. Compos. 31 (2009) 505–510, http://dx.doi.org/10.1016/j.cemconcomp.2009.05.003.
[63] C. Sandoval, P. Roca, Study of the influence of different parameters on the buckling behaviour of masonry walls, Constr. Build. Mater. 35 (2012) 888–899, http://dx.doi.org/10.1016/j.conbuildmat.2012.04.053.
[64] M. Valluzzi, L. Binda, C. Modena, Mechanical behaviour of historic masonry structures strengthened by bed joints structural repointing, Constr. Build. Mater. 19 (2005) 63–73, http://dx.doi.org/10.1016/j.conbuildmat.2004.04.036.
[65] A. Moropoulou, A. Bakolas, K. Bisbikou, Investigation of the technology of historic mortars, J. Cult. Heritage 1 (2000) 45–58, http://dx.doi.org/10.1016/s1296-2074(99)00118-1.
[66] A. Costa, A. Arêde, A. Costa, J. Guedes, B. Silva, Experimental testing, numerical modelling and seismic strengthening of traditional stone masonry: comprehensive study of a real Azorian pier, Bull. Earthquake Eng. 10 (2012) 135–159, http://dx.doi.org/10.1007/s10518-010-9209-3.
[67] H. Kaushik, D. Rai, S. Jain, Stress-strain characteristics of clay brick masonry under uniaxial compression, J. Mater. Civ. Eng. 19 (2007) 728–739, http://dx.doi.org/10.1061/(asce)0899-1561(2007) 19:9(728).
[68] K. Gumaste, K. Nanjunda Rao, B. Venkatarama Reddy, K. Jagadish, Strength and elasticity of brick masonry prisms and wallettes under compression, Mater. Struct. 40 (2007) 241–253, http://dx.doi.org/10.1617/s11527-006-9141-9.
[69] S. Pavía, R. Hanley, Flexural bond strength of natural hydraulic lime mortar and clay brick, Mater. Struct. 43 (2010) 913–922, http://dx.doi.org/10.1617/s11527-009-9555-2.
[70] A. Zucchini, P. Lourenço, Mechanics of masonry in compression: results from a homogenisation approach, Comput. Struct. 85 (2007) 193–204, http://dx.doi.org/10.1016/j.compstruc.2006.08.054.

Appendix B

V. Nežerka, P. Havlásek, and J. Trejbal, Mitigating inclusion-induced shrinkage cracking in cementitious composites by incorporating recycled concrete fines, *Construction and Building Materials* 248 (2020) 118673, doi: 10.1016/j.conbuildmat.2020.118673

Author's contribution: design and preparation of experiments, DIC.

Construction and Building Materials 248 (2020) 118673

Contents lists available at ScienceDirect

Construction and Building Materials

journal homepage: www.elsevier.com/locate/conbuildmat

Mitigating inclusion-induced shrinkage cracking in cementitious composites by incorporating recycled concrete fines

V. Nežerka *, P. Havlásek, J. Trejbal

Faculty of Civil Engineering, Czech Technical University in Prague, Thákurova 7, 166 29 Praha 6, Czech Republic

HIGHLIGHTS

- Recycled concrete fines (RCF) can mitigate shrinkage cracking between aggregates.
- High amounts of RCF (40
- Addition of fly ash to pastes containing RCF increased resistance to microcracking.
- High cracking resistance of pastes with RCF is attributed to enhanced fracture energy.

ARTICLE INFO

Article history:
Received 22 November 2019
Received in revised form 21 February 2020
Accepted 3 March 2020

Keywords:
Shrinkage
Cracking
Recycling
Concrete
Modeling

ABSTRACT

Recent studies on utilization of recycled concrete have demonstrated that usually discarded finest fractions can be incorporated into cementitious composites without scarifying their structural performance. It has been shown that these fines can increase the resistance of a cementitious matrix to tensile stresses and reduce shrinkage, and that these effects can be boosted by addition of mineral admixtures. Such findings led us to a consideration that incorporating recycled concrete fines into a concrete mix could possibly mitigate aggregate-induced shrinkage cracking. Here, this hypothesis was put under scrutiny in a comprehensive experimental-numerical study, confirming that blending Portland cement with recycled concrete fines can mitigate inclusion-induced shrinkage cracking, especially when combined with fly ash. The results of coupled hygro-mechanical modeling indicate that incorporating recycled concrete fines leads not only to a decrease of shrinkage but also increases fracture energy and thus has a major impact on the reduction of micro-cracks between inclusions.

1. Introduction

The worldwide effort to reduce waste production has led to the development of building materials derived from construction and demolition (C&D) waste. Given the large amount of C&D waste produced annually, its recycling has an enormous environmental impact. This fact has led to legislation changes, e.g., a directive adopted by the European Parliament [1,2] targeting reuse and recycling of significant portions of C&D waste.

The recycling of old concrete involves uncomplicated and well-established techniques such as crushing, grinding, and sieving. Due to a relatively cheap extraction of aggregate from crushed concrete and the high costs of landfilling, reprocessing sites can produce commercially competitive materials. Even though the use of recycled aggregate from old concrete has become common practice [3–7], high amounts of fine fractions (a residual material of a fraction 0/16 mm after separating rebars and large aggregates) that constitute about 15–50% of crushed concrete weight [8,9] pose a burden on the environment. Not only that the use of recycled concrete fines (RCF) rich in stripped mortar has not been established in the construction industry, it is even forbidden in some cases [10,11]. The generally accepted misconceptions about RCF have been corrected in recent years by findings indicating that incorporation of RCF into concrete can have beneficial effects [12–17].

In our previous studies of RCF and their performance in cementitious pastes, we reached the following conclusions: (i) residual anhydrous clinker is present in RCF and can be recovered by grinding [18], (ii) replacing Portland cement (PC) with RCF in pastes leads to enhanced resistance to tensile stresses [19], (iii) performance of pastes blended with RCF can be improved with an addition of mineral admixtures such as fly ash (FA) or blast furnace slag (BFS) [19]. Based on these findings, we conjectured that suitable amounts of RCF and mineral admixtures in a cementitous matrix

* Corresponding author.
E-mail address: vaclav.nezerka@fsv.cvut.cz (V. Nežerka).

https://doi.org/10.1016/j.conbuildmat.2020.118673
0950-0618/

could mitigate shrinkage cracking around stiff aggregate inclusions. These inclusions restrain contractive volumetric changes of the matrix, i.e. shrinkage, [20–23] and reduce it by up to an order of magnitude [24–26], but in turn also produce tensile stresses in the matrix [27,21].

The presence of shrinkage cracks in cementitious composites at the micro-level affects their strength and stiffness [28–31,27]. Moreover, the network of cracks allows access to harmful substances that can reduce concrete durability [32–34]. In this experimental–numerical study, we investigate the possibility of mitigating inclusion-induced shrinkage cracking in cementitious pastes by incorporating RCF blended with fly ash or blast furnace slag. Digital image correlation (DIC) was employed to assess the development of cracking within planar samples having a deterministic geometry, while a 2D coupled hygro-mechanical finite element (FE) model allowed us to identify and evaluate crucial parameters with respect to shrinkage cracking at early stages of hydration.

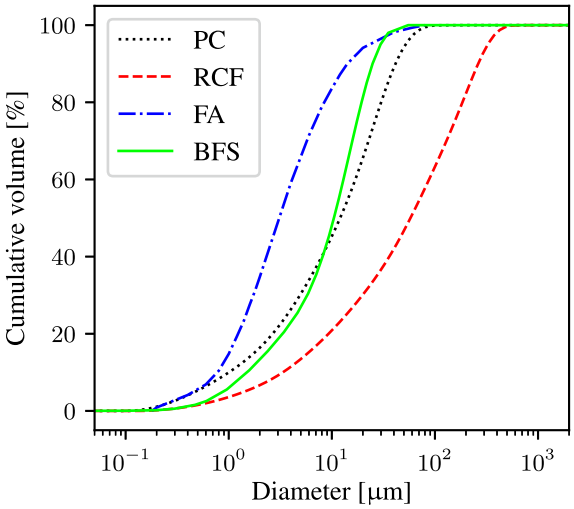

Fig. 1. Particle size distribution curves for all input materials used in this study.

2. Materials and samples

2.1. Input materials

The studied materials were selected based on the outcomes of our previous studies [19,18]. RCF powder was blended with ordinary PC CEM I/42.5R (EN 197-1:2001 [35]) in 20 and 40% wt. concentrations. The RCF material was prepared from a recycled railway sleeper using hydraulic crushers, followed by separators for extraction of aggregate particles over 16 mm in diameter, and a high-speed Lavaris SKD 600 electric mill (2×30 kW) for grinding the stripped mortar and small aggregates to a 0–1 mm fraction. The sleeper had originally been manufactured from high-quality concrete of class C 45/55-XF1 [36] and subjected to weathering in a railway track for 45 years. To support cement hydration, FA and BFS were added to mixtures containing 40% wt. RCF. FA was originally produced by a Mělník coal-fired power plant and fine fractions of BFS were selected from depots in a heap near the former Poldi Kladno ironworks, Czech Republic.

Chemical composition of all materials was determined by X-ray fluorescence spectroscopy (XRF) using a SPECTRO XEPOS spectrometer equipped with a 50 W/60 kV X-ray tube. The XRF results are summarized in Table 1. The contents of CaO and SiO_2 indicate that PC was rich in C_3S and contained a lower amount of C_2S. The RCF sample was rich in SiO_2 and Al_2O_3, indicating the presence of sand and aggregate residues, while Fe_2O_3 was introduced during grinding due to wear of blades in the mill. The high content of amorphous SiO_2 in FA was provided by glassy components that can be chemically activated in an alkaline environment [37], as well as Al_2O_3 contained in BFS.

Particle size distribution curves were determined using a Fritsch Analyssete 22 Micro Tec Plus laser diffraction particle size analyzer. The curves provided in Fig. 1 show that the distributions of PC and BFS were similar, while the distribution of FA particles was shifted towards smaller diameters and the RCF particles were larger. Specific surfaces of input materials, equal to 380, 265, 242, and 452 m^2/kg for PC, RCF, FA, and BFS, respectively, were determined by employing the Blaine method (using a Matest E009 device). The same device was used for measuring bulk densities, equal to 3105, 2575, 2852, and 2989 kg/m^3 for these materials in the same order.

2.2. Mixtures and specimens

PC was blended with RCF and FA or BFS to produce pastes specified in Table 2. Mixing was accomplished using an electric blender for 5 min at 100 rotations per minute, and 5 min at the same speed after adding water. Water-to-binder weight ratio (w/b) was kept constant for all pastes, w/b = 0.32. Results of a flow test, defined in EN 12350–2 [38], indicate improvement of workability with the addition of RCF and FA or BFS. Such an improvement can be attributed to a higher packing density of relatively large RCF (when compared to smaller PC grains) and a low absorption [39] of this nearly inert material (4.96±0.73% when measured on fragments before grinding), but also to the shape of particles [18] and their chemical composition [40–42].

The pastes were cast into custom-made 66×100×10 mm molds shown in Fig. 2. Five stiff aluminum cylindrical inclusions having 12 mm in diameter were deterministically distributed along the

Table 1
Most important oxides identified in PC, RCF, FA, and BFS, and loss on ignition (LOI) provided by XRF.

Component	PC	RCF	FA	BFS
	wt% (±0.5%)			
CaO	65.5	21.1	1.71	38.0
SiO_2	20.1	40.5	55.7	24.1
Al_2O_3	4.40	11.8	30.0	11.3
Fe_2O_3	2.50	4.10	1.12	4.33
SO_3	3.00	1.22	1.10	4.46
MgO	1.51	2.30	0.81	5.09
Na_2O	0.12	1.51	0.00	2.01
K_2O	0.75	1.83	0.00	0.95
other	0.21	0.83	1.09	2.52
LOI	1.91	14.8	8.53	7.33

Table 2
Compositions of the prepared mixes (amount of individual components expressed in wt.%).

Mixture	PC	RCF	FA	BFS	w/b	Flow test [mm]
C	100%	0%	0%	0%	0.32	184
CR_{20}	80%	20%	0%	0%	0.32	199
CR_{40}	60%	40%	0%	0%	0.32	243
$CR_{40}A_{10}$	50%	40%	10%	0%	0.32	239
$CR_{40}S_{10}$	50%	40%	0%	10%	0.32	241

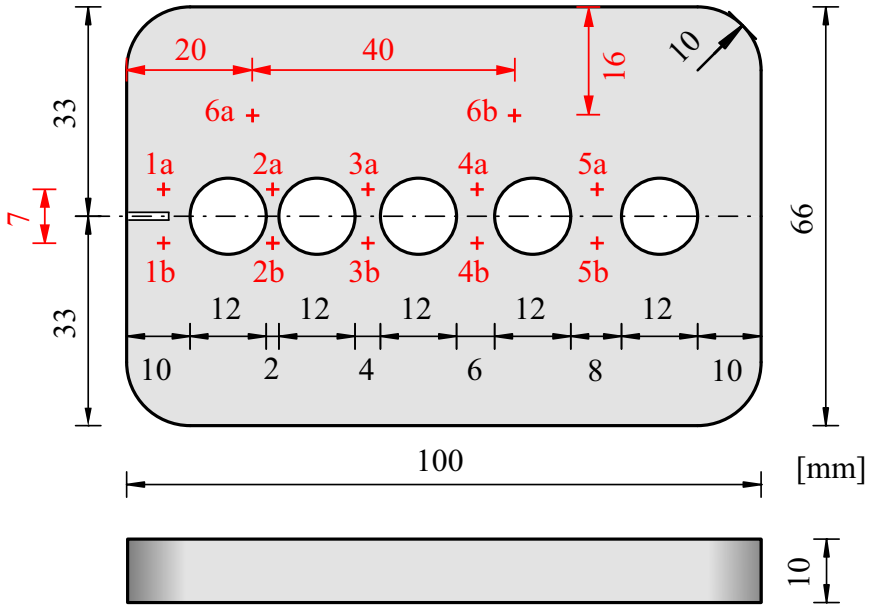

Fig. 2. Geometry of molds containing hollow metalic cylindrical inclusions (wall thickness 0.8 mm); couples of points #a–#b that formed virtual extensometers used in DIC analysis and their positions marked in red.

mold axis. An 8 mm notch was formed using two polyethylene terephthalate (PET) plates before the first inclusion to preordain a course of cracks that were supposed to form sequentially between the inclusions. The gaps between inclusions increased from 2 to 8 mm—the smaller the gaps the larger the tensile stresses due to shrinkage constrained by inclusions [21,31,27]. The inclusions were much stiffer than pastes and also inert, because of their polypropylene (PP) covers.

A second set of specimens having the same dimensions was prepared for the measurement of weight loss. Prismatic 40×40×160 mm specimens were cast for assessment of Young's moduli and demoled after 24 h. All the specimens were stored in a laboratory at 21±0.5°C and relative humidity 31±1%. This environment was chosen to provide a suitable difference in the chemical potential of kneading water and the vapor in the air [43]. Displacement and deformation fields were continuously monitored at the surface of specimens containing inclusions using a DSLR camera. During the first 5 h after casting, the pastes were sealed to avoid premature drying. Such curing minimized formation of cracks due to non-uniform drying at initial setting [44,45].

After 3 months of hardening, the pastes were investigated by microscopy and subjected to an assessment of porosity (Table 3), carried out according to EN 480–11 [46] using a RapidAir 457 system. The increase in porosity with the addition of RCF, FA, and BFS can be attributed to their higher w/c ratios [47–49].

Table 3
Porosity of studied pastes; mean values and standard deviations of six measurements.

C	CR_{20}	CR_{40}	$CR_{40}A_{10}$	$CR_{40}S_{10}$
20.35 ± 0.32	21.30 ± 0.14	22.11 ± 0.31	26.21 ± 0.40	27.38 ± 0.37

3. Experimental methods

The experimental agenda was aimed at the assessment of stiffness development of the studied pastes, to record weight loss during their hardening and to monitor cracking between inclusions. The weight of specimens was measured using Adventurer Pro AV4101CDM laboratory scales Ohaus Corporation, USA. Digital image correlation (DIC) [50,51] was employed to calculate displacement fields at the surface of monitored specimens. These data were used for calibration of the material model in FE analysis. Because the selected material model has not been developed for predicting the behavior at an initial setting (the first 5 h), and the data would be biased by evaporation of bleed water from the surface of specimens after removal of the sealing foil (following 12 h), experimental measurements from the first 17 h period were disregarded in the modeling.

3.1. Stiffness assessment

The Young's modulus was determined non-destructively using a resonance method according to the ASTMD3497 standard [52]. The method is based on measuring longitudinal vibration of prismatic specimens and proved to be suitable for monitoring of stiffness development even at early stages of hardening [53].

3.2. DIC

The analyzed images were taken in 30-min intervals by a Canon EOS 70D camera in uncompressed format (.raw), yielding a resolution of 9 px/mm. The effect of lens distortion was minimized by

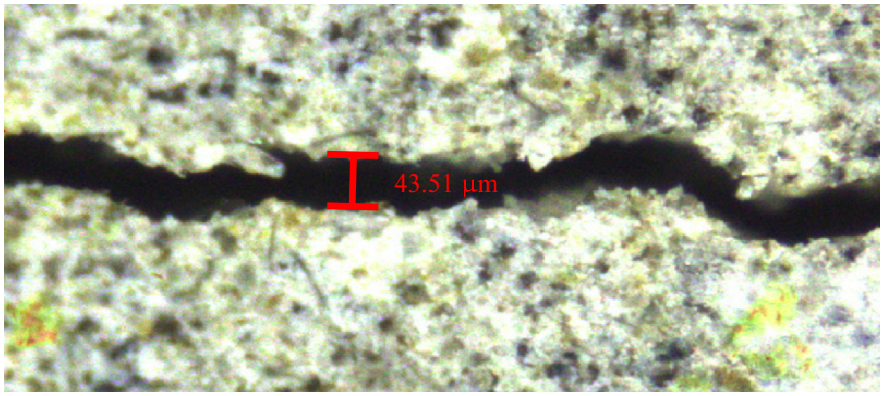

Fig. 3. Microscopy images showing width of an epoxy-filled shrinkage crack between inclusions.

setting the focal length to 55 mm and placement of the camera 2.5 m from the specimens. The displacement and deformation fields were evaluated using a non-commercial open-source software, Ncorr [54], and postprocessing of the calculated data was accomplished using an in–house software, Ncorr_post [55]. The latter tool allowed for visualization of principal strain concentrations that indicated crack formations and placement of virtual extensometers marked in Fig. 2. The results were validated using RTCorr software utilizing different algorithms based on sub-pixel image registration [56,57].

3.2.1. Microscopy

Microscopy observations were accomplished using a Zeiss Axio Zoom.V16 microscope with focus on crack widths between inclusions at the bottom of observed specimens. The specimens were embedded in epoxy resin and sequentially polished in an alcohol-based solution using a Struers Tegramin grinding plate with 1200 grain/cm^2 grit under 5 N compression. The measurement of crack widths (Fig. 3) was conducted using Zeiss AxioVision software on all specimens except $CR_{40}S_{10}$, which did not withstand stresses during polishing and lost its integrity.

4. FE modeling

All numerical simulations were carried out using the OOFEM open-source FE package [58,59]. The analyses were run in a one-way coupled staggered scheme with the moisture transport problem followed by humidity-dependent structural analysis.

The objective of modeling was to identify optimum values of material parameters for the hardened cementitious pastes (HCPs) subjected to drying. This was accomplished via inverse analysis requiring repeated simulations with different combinations of material parameters for every type of mixture. To reduce the computational cost associated with this approach, the problem had to be simplified and analyzed under an assumption of plane stress conditions, despite the three-dimensional nature of the problem.

The modeling of restrained shrinkage-induced has been approached using a similar strategy in a recent study by the author [60], but the specimens modeled there were only 2 mm thick and dried symmetrically [22]. In this study, the specimens were 10 mm thick and drying was limited to one side only. Therefore, the computational model in the structural analysis corresponded to the mean behavior averaged over the entire thickness of the specimen and the identified material parameters represent mean behavior of the matrix. Despite such simplifications, we believe that this approach was suitable for quantitative comparison among different compositions of HCPs. Yet, 3D analysis allowing for moisture gradients across the specimen thickness would most likely yield a slightly different set of parameters.

The modeling strategy was straightforward, as follows. First, humidity evolution—being the only driving force in the model responsible for shrinkage—was calibrated inversely from a measured free shrinkage evolution to obtain a good fit of the corresponding shrinkage strain on the top surface of specimens exposed to drying. Consequently, the model was calibrated to match development of crack widths in the structural analysis.

4.1. FE mesh

A 2D FE mesh for the structural problem was created using the T3D mesh generator [61,62] (Fig. 4). The mesh consisted of 6517 nodes and 7584 elements and was composed of regions with structured mesh (quadrilateral 4-node linear plane stress elements) and an irregular mesh (triangular 3-node plane stress elements) that covered regions where no cracking was anticipated. The structured mesh that surrounded inclusions was aligned with the direction of principal stresses to minimize locking problems after the onset of cracking. The mesh-independent response was ensured by using the crack-band approach [63].

The nodes on matrix-inclusion interfaces were doubled and a master-slave condition allowing for a tangential slip but preventing opening or overlap was prescribed. Even though this simplification can be viewed as less accurate than incorporation of interface elements, it prevented an introduction of additional material parameters and enabled more straightforward identification, this being the aim of this study.

4.2. Material models

The transport problem in a staggered scheme prescribes an evolution of relative humidity which subsequently enters the structural problem. Therefore, the constitutive model for moisture transport and its material parameters are not presented here.

The material model for an HCP uses a serially coupled viscoelastic model described by the reformulated and modified microprestress-solidification (MPS) theory [64,65] and a very simple model with a fixed orientation of orthogonal cracks that form if tensile strength is exceeded. Under sealed conditions (constant temperature and prevented drying), the MPS theory reduces to a more simple B3 model for concrete creep [66] and its basic creep compliance function is entirely described by four material parameters only, q_1 through q_4. These parameters for modeling of structural concrete can be roughly estimated from the 28-day compressive strength and a composition of the concrete mixture; for HCP, q_1 through q_4 had to be calibrated by matching a

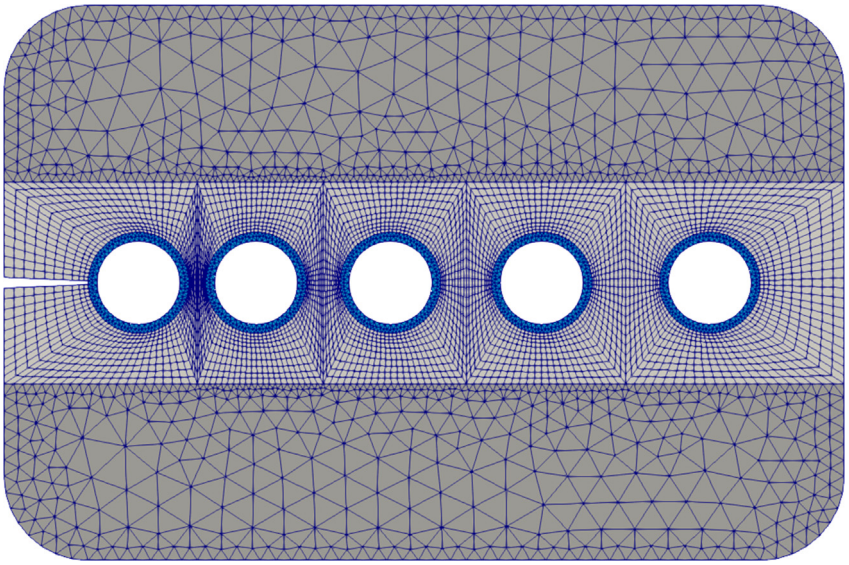

Fig. 4. FE mesh for the computational model, generated using the T3D mesh generator.

development of Young's modulus to the inverse of a compliance function evaluated for the duration of loading $t - t\prime = 0.01$ day, see Fig. 7. In the B3 model, aging is incorporated through $t\prime$, the age at loading, and parameters q_1 through q_4 are time-independent constants.

In FE models, the decrease in relative humidity is followed by an additional increase in compliance, referred to as drying creep, that is controlled by a dimensionless parameter k_3. Humidity changes then give rise to shrinkage strain ε_{sh}, linked to a relative humidity h via a linear relationship

$$\dot{\varepsilon}_{sh} = k_{sh}\,\dot{h}, \tag{1}$$

where k_{sh} is one of the identified material parameters.

Variable relative humidity of pores within the material impacts the rate of transformed times in the model. One of these times affects maturity, which stops evolving very rapidly once the relative humidity drops below 90%. Here, in order to match the initial shrinkage evolution soon after the onset of drying, the relative humidity had to be dropped below this threshold value. As a consequence, such an approach would have caused premature

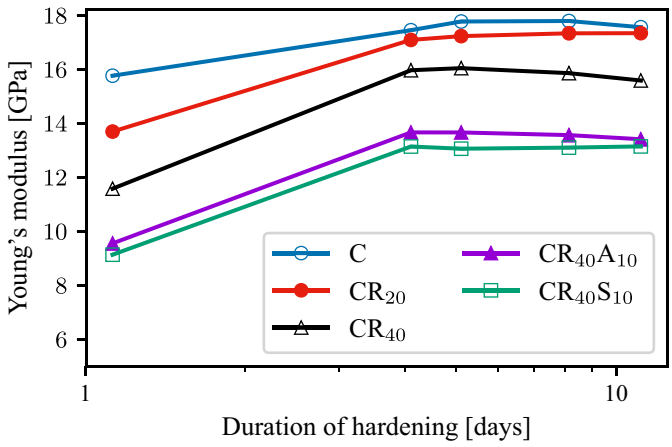

Fig. 6. Development of the dynamic Young's modulus.

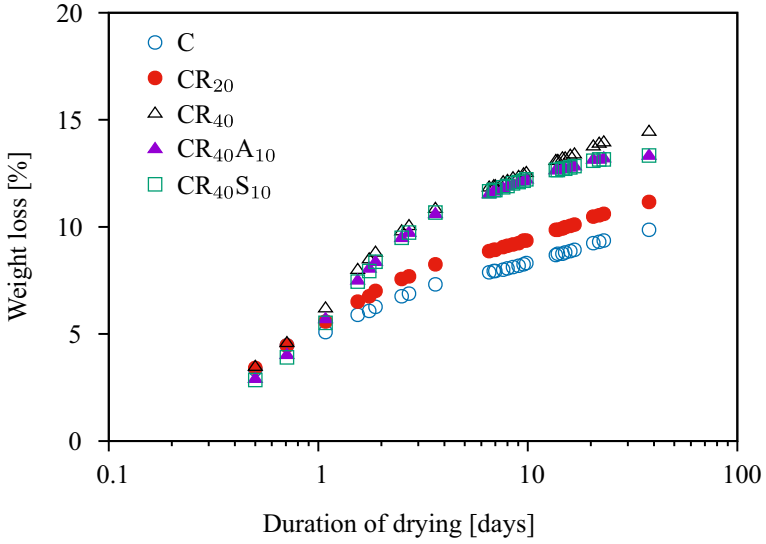

Fig. 5. Weight loss of pastes during the first 28 days of hardening, recorded beginning 5 h after preparation of the mixtures (corresponding to the removal of plastic foil that prevented their drying).

Table 4
Parameters of the B3 model for basic creep calibrated to match the development of stiffness of HCPs.

Mixture	q_1 [10^{-6} MPa^{-1}]	q_2 [10^{-6} MPa^{-1}]	q_3 [10^{-6} MPa^{-1}]	q_4 [10^{-6} MPa^{-1}]
C	35	40	35	20
CR_{20}	30	90	30	20
CR_{40}	30	125	30	20
$CR_{40}S_{10}$	40	145	30	20
$CR_{40}A_{10}$	40	145	30	20

termination of aging in the model, tackled by setting an auxiliary parameter controlling the rate of transformed time α_E to 0.

The traction-separation law with exponential softening was used to capture tensile cracking once the tensile strength was exceeded. Because of the adopted simplifications and the focus on comparison of performance between different mixtures, the material properties—tensile strength f_t and mode I fracture energy G_f—were treated as time-independent constants. Since cracks developed in almost pure opening mode, the constitutive law for crack shearing does not need to be described here. The behavior of metal inclusions was described by a linear isotropic material with material properties specific for aluminum: Young's modulus $E = 69.5$ GPa and Poisson's ratio $\nu = 0.33$.

5. Results and discussion

5.1. Water retention

Water evaporation is undesirable in cementitious materials because an adequate amount of water is vital for clinker hydration.

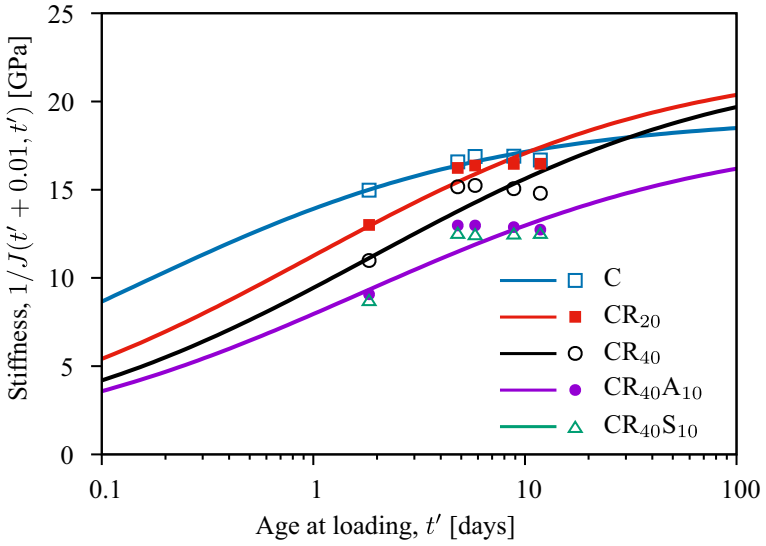

Fig. 7. Aging of the experimentally measured static modulus of an HCP (marked points) and the stiffness computed from the calibrated compliance function; the function for $CR_{40}S_{10}$ is equivalent to that for $CR_{40}A_{10}$.

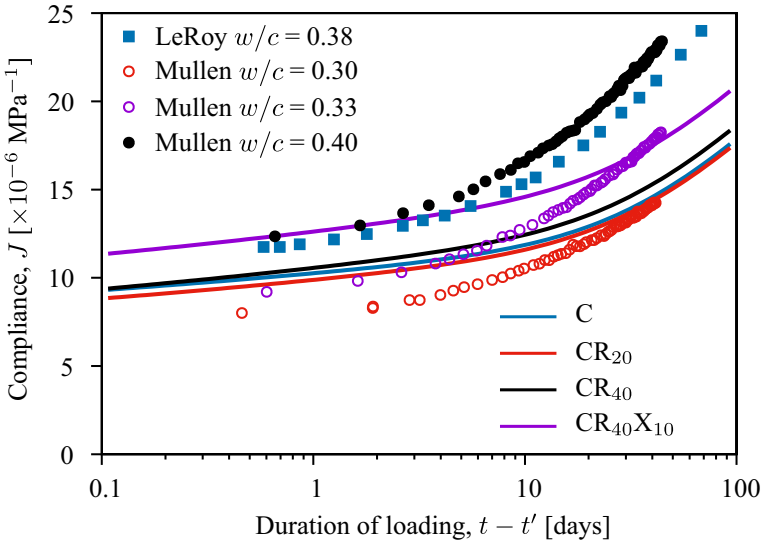

Fig. 8. Comparison of the compliance functions calibrated to match the development of the elastic modulus in Fig. 7 with the experimental data on HCPs having a similar w/c and loaded at 28 days.

Pastes containing RCF released more water than a pure cement paste, which was confirmed by the measurement of weight loss presented in Fig. 5. A portion of this excessive water absorbed by RCF can promote hydration of clinker within PC via internal curing [67]. Hydration of minerals contained in FA and BFS [68] manifested through a drop of weight loss rate in $CR_{40}A_{10}$ and $CR_{40}S_{10}$, compared with CR_{40}, most significantly after 10 days of hardening.

5.2. Stiffness development

The additional porosity and impurities introduced with RCF resulted in a deterioration of stiffness in the samples. This reduction of the dynamic Young's modulus at the early stage of hardening is obvious from Fig. 6 and correlates with the porosity of pastes (Table 3).

5.3. Compliance and creep fitting

Experimental data on early-age creep of HCPs with a high content of admixtures are not available in the literature. For this reason, parameters of basic creep compliance functions required by the B3 model were calibrated to match the static Young's modulus evolution. We assume that capturing of aging has superior importance to calibrating the compliance function at a single age at loading because, in the present case, loading is not constant but applied gradually as the pastes shrink.

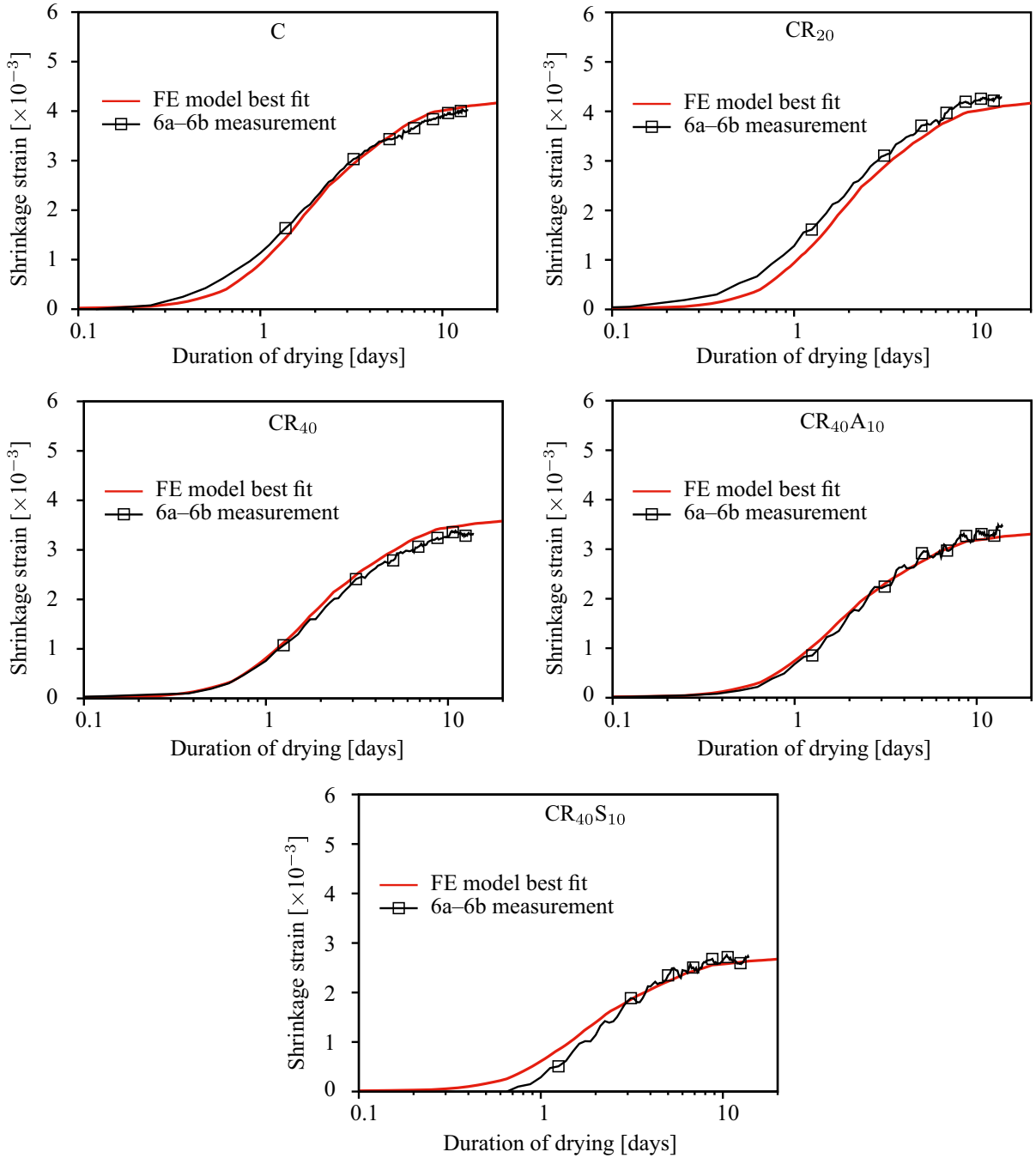

Fig. 9. Shrinkage of pastes measured by the virtual extensometer 6a–6b (see Fig. 2) beginning 17 h after preparation of the mixtures and best fit of the FE model.

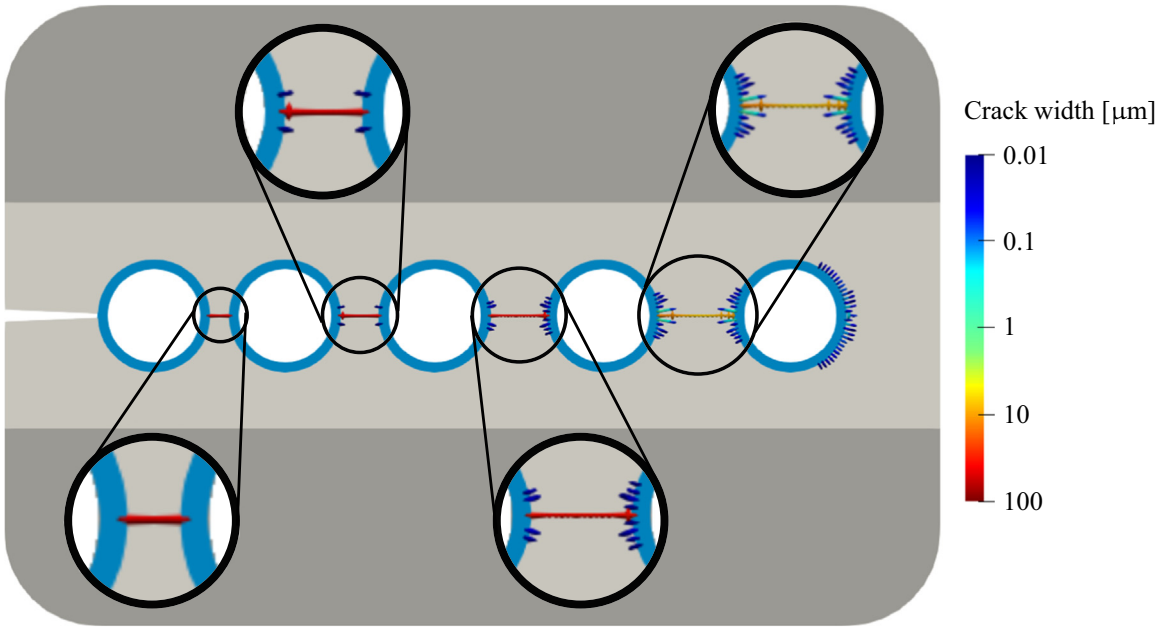

Fig. 10. Distribution and width of cracks predicted by the FE analysis for $CR_{40}A_{10}$ paste after 18.3 days of drying (corresponding to the time since casting, 19 days).

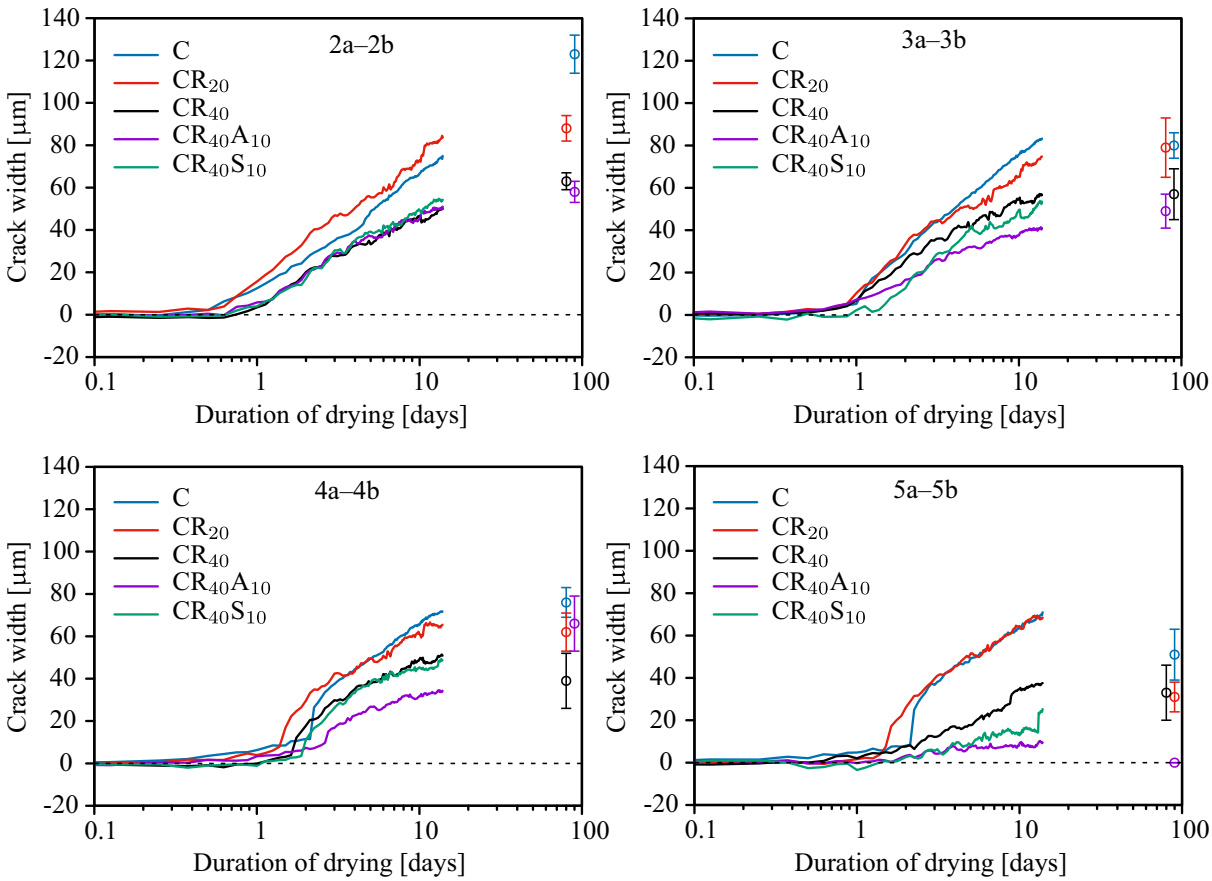

Fig. 11. Crack width development measured by distinct extensometers 2a–2b through 5a–5b by utilizing DIC data and results of measurement using microscopy images after 3 months of hardening; microscopy investigation could not be carried out on $CR_{40}S_{10}$ because the specimen disintegrated during grinding and polishing.

According to Bažant and Baweja [66], the Young's modulus can be considered approximately equal to a reciprocal value of the compliance function of the B3 model if the duration of loading, $t - t\prime$, is set to 15 min ≈ 0.01 day. Based on our own measurements of cementitious pastes and studies of other authors [69,70], the static Young's modulus can be considered approximately 95% of the dynamic modulus, monitored in this study. A hand-optimized set of creep parameters is listed in Table 4 and the comparison of

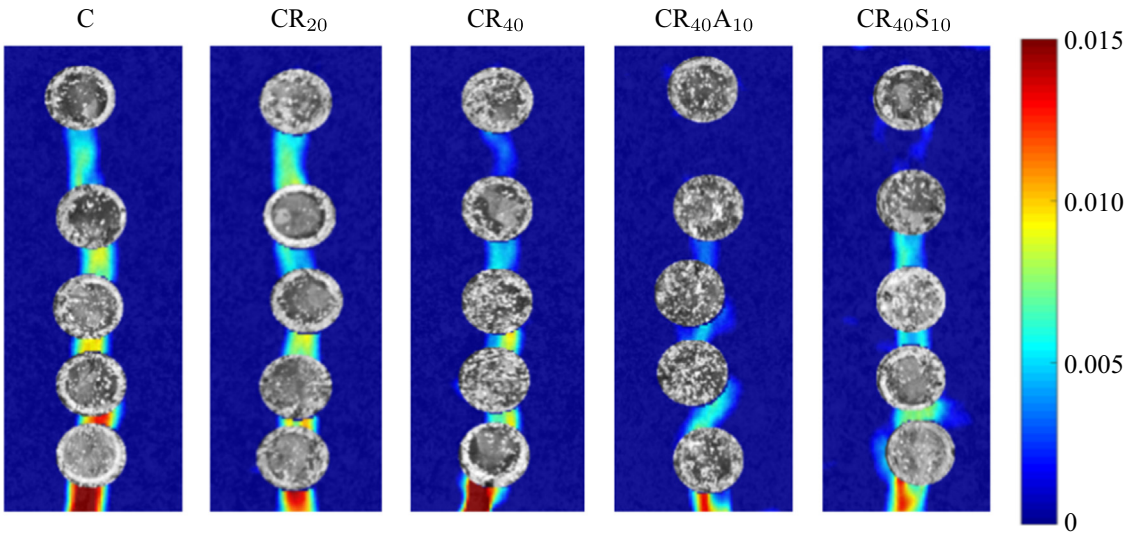

Fig. 12. Maps of principal strain indicating positions and a width of cracks between inclusions after 7 days of drying.

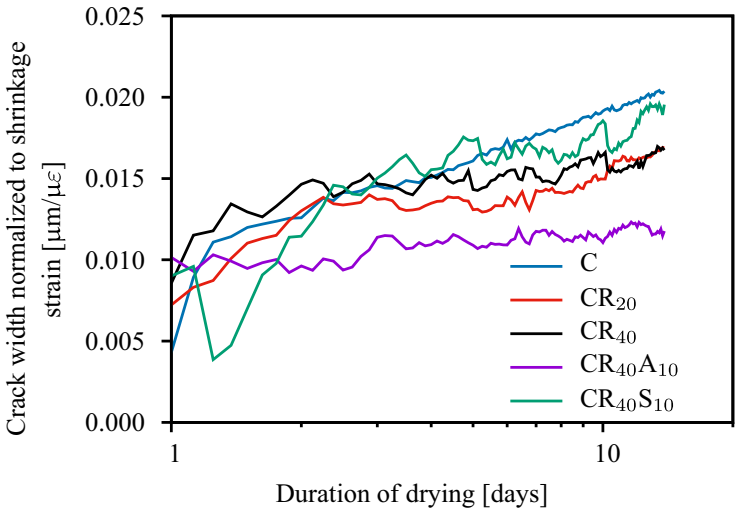

Fig. 13. Development of crack width measured by the extensometer 3a-3b (see Fig. 2) normalized to shrinkage strain.

stiffness development for individual pastes is provided in Fig. 7. The value of the q_4 coefficient, which defines the long-term creep rate and has only a negligible impact on the modulus, was set to a constant value. The emphasis was on reproducing experimental data during the first 1–3 days of drying as shrinkage cracking developed in this period. Fig. 8 demonstrates that the long-term creep rate and the initial stiffness agree with the experimental data measured on mature cement pastes with a similar water-to-cement ratio [71,72]. However, the calibrated compliance functions consistently exhibit a rather delayed transition to the long-term logarithmic creep.

5.4. Shrinkage cracking

Numerical simulations revealed that the mechanical response of pastes was very sensitive to relative humidity within pores. Shrinkage measurement data (Fig. 9) indicate that the tested pastes varied mainly in the ultimate value of drying shrinkage, while shrinkage evolution was almost identical despite different water loss development (Fig. 5). Therefore, it can be assumed that capillary pressures due to changes in relative humidity were the main driving force behind shrinkage evolution and the role of free water was not significant.

Given the linear relationship between drying shrinkage and changes in relative humidity (Eq. (1)), an identical function describing relative humidity $h(t)$ was adopted for all mixtures to match the onset and course of shrinkage strain evolution measured on CR_{40} and $CR_{40}A_{10}$. Despite small oscillations in measured shrinkage strains, the function $h(t)$ was monotonous and smooth (Fig. 9) because even minor fluctuations in relative humidity would have caused a spurious increase in compliance of the MPS model [73]. The initial value of relative humidity was set to 98% (generally accepted for non-cured specimens without self-desiccation), gradually decreasing to 35% (ambient air humidity).

After identification of basic creep parameters, remaining material constants left for identification were the shrinkage parameter k_{sh}, the drying creep parameter k_3, tensile strength f_t, and fracture energy G_f. These parameters could not be considered mutually independent, and their optima were sought using the implicit enumeration method [74] to reproduce development of cracks between inclusions.

By assuming that shrinkage ε_{sh} and cracking ε_{cr} represented dominant strains detected by DIC, crack width w_{cr} could be calculated from the total strain ε_{tot} measured across cracks as

$$w_{cr} = \varepsilon_{cr} L = (\varepsilon_{tot} - \varepsilon_{sh}) L \tag{2}$$

in which $L = 7$ mm is the distance between endpoints of the virtual extensometers and ε_{sh} is the strain measured by the extensometer 6a–6b with a length of 40 mm (Fig. 2). The validity of this hypothesis is proven by very consistent results in Fig. 11, showing almost zero crack widths until the age of approximately 1 day, followed by their rapid development and widening. The magnitude of crack widths also nicely matched microscopic observations.

The spacing of inclusions within the planar specimens was designed carefully based on findings of other authors [75,76,34,77] and the results of our previous studies [31,27]. This geometry enabled an analysis of the impact of RCF, FA, and BFS on the development of shrinkage cracking as well as quantitative comparison between experiments and FE simulations. The distance between inclusions influenced the criterion for crack development as well as the crack width; severe cracking was detected in smaller gaps and crack widths decreased with an increasing distance between inclusions (Fig. 10). Large shrinkage and high stiffness in a pure cement paste (C) led to developing wider cracks compared to pastes rich in RCF. These conclusions can be reached based on both, DIC measurements of crack opening using extensometers

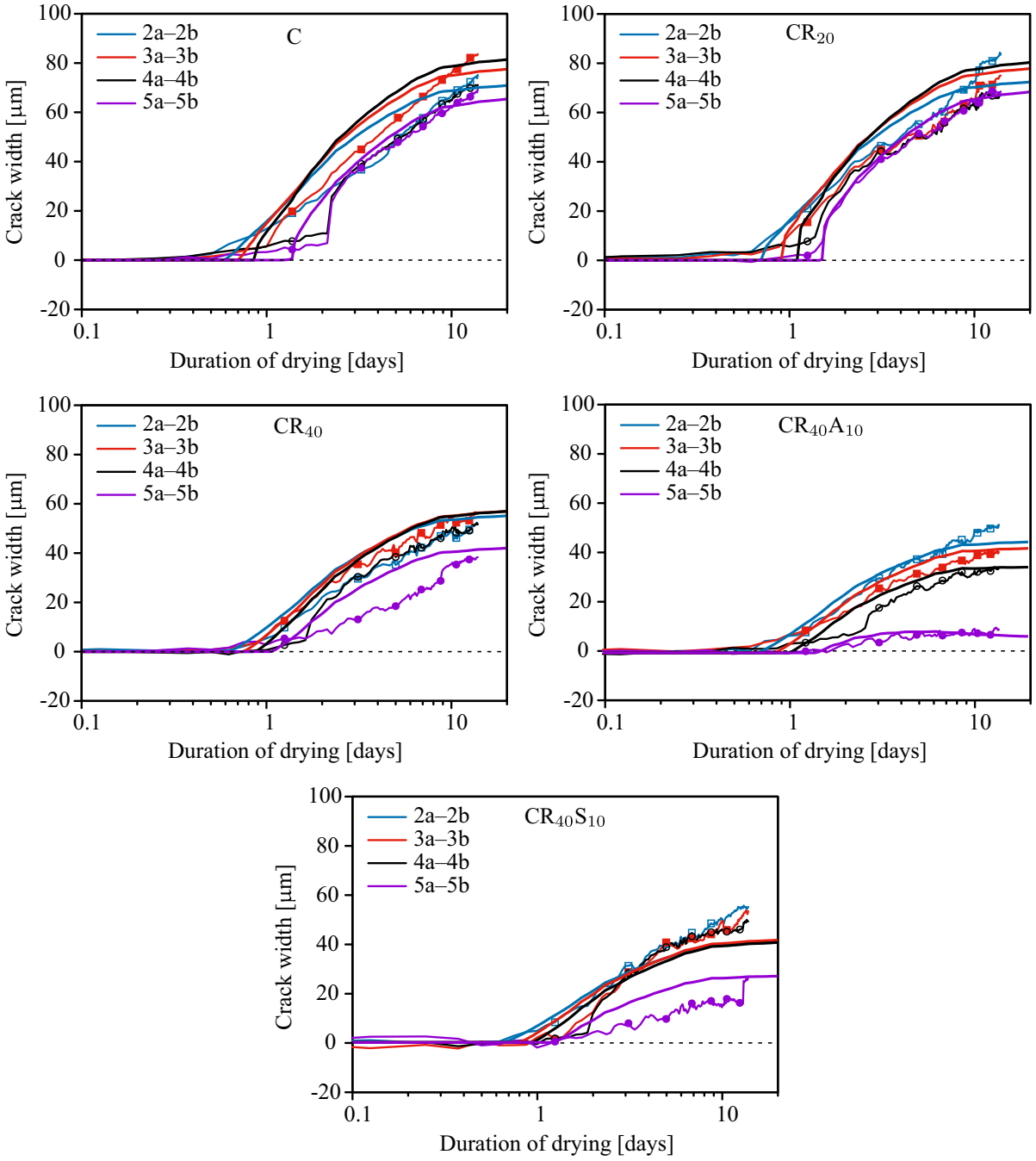

Fig. 14. Results of f_t, G_f, and k_3 optimization for studied pastes by matching experimentally obtained developments of crack width between individual inclusions; noisy line with markers represents DIC measurements, while smooth lines represent the best fit according to the FE model.

Table 5
Parameters identified by fitting the FE model to the measurements of crack width and shrinkage development at the surface of specimens by DIC.

Mixture	f_t [MPa]	G_f [J/m^2]	k_3 [–]	k_{sh} [$\times 10^{-3}$]
C	6	40	40	7
CR_{20}	8	40	30	7
CR_{40}	5	100	30	6
$CR_{40}A_{10}$	4	140	30	5.5
$CR_{40}S_{10}$	3	60	30	4.5

2a–2b through 5a–5b and on microscopy observations, see Fig. 11. It is worth mentioning that despite measuring the crack widths from microscopy images on the opposite side of specimens, DIC results converge to crack widths observed by microscopy. This fact justifies the use of a simplified 2D FE model.

Maps of principal strain calculated using DIC (Fig. 12) indicate that the addition of RCF can result not only the reduction of crack widths but even mitigate cracking completely if the distance between inclusions is large enough, see Fig. 12. The rather negligible crack widths measured by 5a–5b on $CR_{40}A_{10}$ correspond to a sum of creep deformation and untraceable micro-cracking. The maps of principal strain show that $CR_{40}A_{10}$ was least prone to cracking, which is in agreement with the findings of Humad et al. [78] who reported that FA significantly limited the micro-cracking of a binder matrix in concrete.

The capability of pastes to diminish opening of cracks that have already developed can be deduced from the plot in Fig. 13, in which crack widths were normalized to shrinkage strain. It shows that cracks open most easily in paste C, followed by $CR_{40}S_{10}$. While the inability to suppress crack opening in paste C results from its high stiffness (Fig. 6), the inability of $CR_{40}S_{10}$ to deform without developing wide cracks was rather surprising. This result indicates that the addition of BFS contributed to a reduction of creep, which is in agreement with findings of other studies [79,80]. On the other hand, $CR_{40}A_{10}$ outperformed all pastes, indicating that small additions of FA are suitable for producing composites capable of accommodating moderate deformations at the micro-level.

The complexity of processes leading to the development of cracks between inclusions led to multi-parameter optimization. Even though the best fits of the model outcomes to the experimental measurements of crack opening are not perfect (Fig. 14), the results indicate the impact of RCF, FA, and BFS on properties of cementitious pastes (Table 5). Even though tensile strength can be enhanced by moderate additions of RCF, here 20% wt., it turned out to have a negligible impact on cracking between inclusions. On the other hand, higher amounts of RCF and FA/BFS contributed to tensile strength deterioration, but lower shrinkage rates of RCF-rich pastes combined with their increased fracture energy render a paste more resistant to cracking between inclusions.

In our previous studies [19,18] we found that additions of RCF and FA/BFS resulted in a significant increase in bending strength. This enhanced resistance to tensile stresses should not be attributed to an increase in tensile strength as often incorrectly interpreted, but rather to a higher fracture energy and size of the fracture process zone [63,81], rendering the pastes less sensitive to the presence of defects.

6. Conclusion

This study suggests that addition of finest fractions of recycled concrete can be utilized in concrete production and mitigate shrinkage cracking between aggregates, rendering concrete stronger and more durable, but also eco-friendly. Such a positive impact was hinted at by previous studies indicating increased resistance of cementitious pastes to tensile stresses and reduced shrinkage when containing recycled concrete fines.

By employing a coupled hygro-mechanical finite element model calibrated using experimental data, we found that lower sensitivity of drying shrinkage to changes in relative humidity, lower stiffness gains during hardening, and enhanced fracture energy had major impacts on the development of micro-cracks between stiff inclusions.

The introduction of a sufficient amount of recycled concrete fines (40% wt. in this study) contributed to reduction of drying shrinkage. This reduction was more significant with the presence of mineral admixtures—fly ash and blast furnace slag. The pastes rich in recycled concrete fines and mineral admixtures also exhibited lower stiffness gains, resulting in lower shrinkage-induced stresses. Modeling of inclusion-induced shrinkage cracking revealed that even though the tensile strength of cementitious pastes decreased with the addition of admixtures, fracture energy responsible for restricting the crack development increased by up to 250% in case of recycled concrete and fly ash additions. On the other hand, the presence of blast furnace slag diminished the positive impact of recycled concrete fines on the reduction of shrinkage cracking, favoring the use of fly ash. Even though the results clearly reveal trends related to the addition of admixtures, one has to keep in mind all the simplifications in the modeling and the rather small sensitivity to input parameters.

The study indicates that incorporating recycled concrete fines can reduce the environmental burden associated with the disposal of finest fractions produced in concrete recycling and can concurrently increase the integrity and strength of new cement-based products containing these fines.

Funding

This work was supported by the Czech Science Foundation [grants GA ČR 17-06771S (V. Nežerka, J. Trejbal) and GA ČR 19-20666S (P. Havlásek)].

Declaration of Competing Interest

The authors declare that they have no known competing financial interests or personal relationships that could have appeared to influence the work reported in this paper.

Acknowledgments

The authors wish to thank Zdeněk Prošek and Jakub Antoš at the Czech Technical University in Prague for assistance with the preparation of specimens, microscopy investigation and help with processing DIC data. The help of Dr. Stephanie Krueger, who provided editorial assistance, is also gratefully acknowledged.

References

[1] The European, Parliament and of the council on waste, directive regarding demolition waste, Official J. Eur. Union (2008).
[2] L. Oksri-Nelfia, P.-Y. Mahieux, O. Amiri, P. Turcry, J. Lux, Reuse of recycled crushed concrete fines as mineral addition in cementitious materials, Mater. Struct. 49 (2015) 3239–3251, https://doi.org/10.1617/s11527-015-0716-1.
[3] S.W. Tabsh, A.S. Abdelfatah, Influence of recycled concrete aggregates on strength properties of concrete, Constr. Build. Mater. 23 (2009) 1163–1167, https://doi.org/10.1016/j.conbuildmat.2008.06.007.
[4] R. Silva, J. de Brito, R. Dhir, Properties and composition of recycled aggregates from construction and demolition waste suitable for concrete production, Constr. Build. Mater. 65 (2014) 201–217, https://doi.org/10.1016/j.conbuildmat.2014.04.117.
[5] K. Kapoor, S. Singh, B. Singh, Durability of self-compacting concrete made with recycled concrete aggregates and mineral admixtures, Constr. Build. Mater. 128 (2016) 67–76, https://doi.org/10.1016/j.conbuildmat.2016.10.026.

[6] F. Colangelo, A. Forcina, I. Farina, A. Petrillo, Life cycle assessment (LCA) of different kinds of concrete containing waste for sustainable construction, Buildings 8 (2018) 70, https://doi.org/10.3390/buildings8050070.

[7] E. Khoury, W. Ambrós, B. Cazacliu, C.H. Sampaio, S. Remond, Heterogeneity of recycled concrete aggregates, an intrinsic variability, Constr. Build. Mater. 175 (2018) 705–713, https://doi.org/10.1016/j.conbuildmat.2018.04.163.

[8] Z. Shui, D. Xuan, H. Wan, B. Cao, Rehydration reactivity of recycled mortar from concrete waste experienced to thermal treatment, Constr. Build. Mater. 22 (2008) 1723–1729, https://doi.org/10.1016/j.conbuildmat.2007.05.012.

[9] X. Ma, Z. Wang, Effect of ground waste concrete powder on cement properties, Adv. Mater. Sci. Eng. 2013 (2013) 1–5, https://doi.org/10.1155/2013/918294.

[10] L. Evangelista, J. de Brito, Concrete with fine recycled aggregates: a review, Eur. J. Environ. Civil Eng. 18 (2013) 129–172, https://doi.org/10.1080/19648189.2013.851038.

[11] L. Evangelista, J. de Brito, Durability of crushed fine recycled aggregate concrete assessed by permeability-related properties, Mag. Concr. Res. (2018) 1–9, https://doi.org/10.1680/jmacr.18.00093.

[12] J. Khatib, Properties of concrete incorporating fine recycled aggregate, Cem. Concr. Res. 35 (2005) 763–769, https://doi.org/10.1016/j.cemconres.2004.06.017.

[13] S. Levy, P. Helène, Durability of concrete mixed with fine recycled aggregates, Exacta 5.https://doi.org/10.5585/exacta.v5i1.1027..

[14] L. Evangelista, J. de Brito, Durability performance of concrete made with fine recycled concrete aggregates, Cem. Concr. Compos. 32 (2010) 9–14, https://doi.org/10.1016/j.cemconcomp.2009.09.005.

[15] P. Pereira, L. Evangelista, J. de Brito, The effect of superplasticizers on the mechanical performance of concrete made with fine recycled concrete aggregates, Cem. Concr. Compos. 34 (2012) 1044–1052, https://doi.org/10.1016/j.cemconcomp.2012.06.009.

[16] E. Anastasiou, K.G. Filikas, M. Stefanidou, Utilization of fine recycled aggregates in concrete with fly ash and steel slag, Constr. Build. Mater. 50 (2014) 154–161, https://doi.org/10.1016/j.conbuildmat.2013.09.037.

[17] F. Cartuxo, J. de Brito, L. Evangelista, J. Jiménez, E. Ledesma, Rheological behaviour of concrete made with fine recycled concrete aggregates – influence of the superplasticizer, Constr. Build. Mater. 89 (2015) 36–47, https://doi.org/10.1016/j.conbuildmat.2015.03.119.

[18] Z. Prošek, J. Trejbal, V. Nežerka, V. Goliáš, M. Faltus, P. Tesárek, Recovery of residual anhydrous clinker in finely ground recycled concrete, Resour. Conserv. Recycl. 155 (2020), https://doi.org/10.1016/j.resconrec.2019.104640 104640.

[19] Z. Prošek, V. Nežerka, R. Hlužek, J. Trejbal, P. Tesárek, G. Karra'a, Role of lime, fly ash, and slag in cement pastes containing recycled concrete fines, Constr. Build. Mater. 201 (2019) 702–714, https://doi.org/10.1016/j.conbuildmat.2018.12.227.

[20] P. Goltermann, Mechanical predictions of concrete deterioration — part 2: classification of crack patterns, ACI Mater. J. 92 (1995) 58–63.

[21] B.F. Dela, H. Stang, Two-dimensional analysis of crack formation around aggregates in high-shrinkage cement paste, Eng. Fract. Mech. 65 (2000) 149–164, https://doi.org/10.1016/s0013-7944(99)00113-7.

[22] J. Bisschop, J.G.M. van Mier, Effect of aggregates on drying shrinkage microcracking in cement-based composites, Mater. Struct. 35 (2002) 453–461, https://doi.org/10.1007/bf02483132.

[23] A. Idiart, J. Bisschop, A. Caballero, P. Lura, A numerical and experimental study of aggregate-induced shrinkage cracking in cementitious composites, Cem. Concr. Res. 42 (2012) 272–281, https://doi.org/10.1016/j.cemconres.2011.09.013.

[24] D. Hobbs, Influence of aggregate restraint on the shrinkage of concrete, ACI J. Proc. 71 (1974) 445–450, https://doi.org/10.14359/7089.

[25] A.M. Neville, Properties of Concrete, fourth ed., Longman, 1996.

[26] T. Fujiwara, Effect of aggregate on drying shrinkage of concrete, J. Adv. Concr. Technol. 6 (2008) 31–44, https://doi.org/10.3151/jact.6.31.

[27] V. Nežerka, J. Zeman, J. Němeček, Micromechanics-based simulations of compressive and tensile testing on lime-based mortars, Mech. Mater. 105 (2017) 49–60, https://doi.org/10.1016/j.mechmat.2016.11.011.

[28] V. Kanna, R. Olson, H. Jennings, Effect of shrinkage and moisture content on the physical characteristics of blended cement mortars, Cem. Concr. Res. 28 (1998) 1467–1477, https://doi.org/10.1016/s0008-8846(98)00120-3.

[29] I. Yurtdas, N. Burlion, F. Skoczylas, Triaxial mechanical behaviour of mortar: Effects of drying, Cem. Concr. Res. 34 (2004) 1131–1143, https://doi.org/10.1016/j.cemconres.2003.12.004.

[30] N. Burlion, F. Bourgeois, J.-F. Shao, Effects of desiccation on mechanical behaviour of concrete, Cem. Concr. Compos. 27 (2005) 367–379, https://doi.org/10.1016/j.cemconcomp.2004.05.004.

[31] V. Nežerka, P. Tesárek, J. Zeman, Fracture-micromechanics based model of mortars susceptible to shrinkage, Key Eng. Mater. 592–593 (2014) 189–192, https://doi.org/10.4028/www.scientific.net/kem.592-593.189.

[32] C.-M. Aldea, S.P. Shah, A. Karr, Effect of cracking on water and chloride permeability of concrete, J. Mater. Civ. Eng. 11 (1999) 181–187, https://doi.org/10.1061/(asce)0899-1561(1999)11:3(181).

[33] H. Wong, M. Zobel, N. Buenfeld, R. Zimmerman, Influence of the interfacial transition zone and microcracking on the diffusivity, permeability and sorptivity of cement-based materials after drying, Mag. Concr. Res. 61 (2009) 571–589, https://doi.org/10.1680/macr.2008.61.8.571.

[34] A.E. Idiart, C.M. López, I. Carol, Chemo-mechanical analysis of concrete cracking and degradation due to external sulfate attack: a meso-scale model, Cem. Concr. Compos. 33 (2011) 411–423, https://doi.org/10.1016/j.cemconcomp.2010.12.001.

[35] EN 197-1:2011: Cement. Composition, specifications and conformity criteria for very low heat special cements, BSI British Standards, 2011.https://doi.org/10.3403/03054726..

[36] EN 1992-1-1:2004: Design of concrete structures, Part 1-1: General rules and rules for buildings, BSI British Standards, 2004.https://doi.org/10.12691/ajcea-4-1-6..

[37] B.K. Marsh, R.L. Day, Pozzolanic and cementitious reactions of fly ash in blended cement pastes, Cem. Concr. Res. 18 (1988) 301–310, https://doi.org/10.1016/0008-8846(88)90014-2.

[38] BS EN 12350-5:2009: Testing fresh concrete. Flow table test, BSI British Standards, 2009.https://doi.org/10.3403/30164891..

[39] A.M. Alhozaimy, Effect of absorption of limestone aggregates on strength and slump loss of concrete, Cem. Concr. Compos. 31 (2009) 470–473, https://doi.org/10.1016/j.cemconcomp.2009.04.010.

[40] H. He, L. Courard, E. Pirard, F. Michel, Shape analysis of fine aggregates used for concrete, Image Anal. Stereol. 35 (2016) 159, https://doi.org/10.5566/ias.1400.

[41] F. Collins, J. Sanjayan, Workability and mechanical properties of alkali activated slag concrete, Cem. Concr. Res. 29 (1999) 455–458, https://doi.org/10.1016/s0008-8846(98)00236-1.

[42] K.-H. Yang, J.-K. Song, K.-I. Song, Assessment of CO2 reduction of alkali-activated concrete, J. Clean. Prod. 39 (2013) 265–272, https://doi.org/10.1016/j.jclepro.2012.08.001.

[43] R. Mills, Mass transfer of water vapour through concrete, Cem. Concr. Res. 15 (1985) 74–82, https://doi.org/10.1016/0008-8846(85)90010-9.

[44] Z.P. Bažant, W.J. Raftshol, Effect of cracking in drying and shrinkage specimens, Cem. Concr. Res. 12 (1982) 209–226, https://doi.org/10.1016/0008-8846(82)90008-4.

[45] J. Bisschop, F.K. Wittel, Contraction gradient induced microcracking in hardened cement paste, Cem. Concr. Compos. 33 (2011) 466–473, https://doi.org/10.1016/j.cemconcomp.2011.02.004.

[46] BS EN 480-11:2005: Admixtures for concrete, mortar and grout—Test methods—Part 11: Determination of air void characteristics in hardened concrete, BSI British Standards, 2013.https://doi.org/10.3403/30129094..

[47] L. Bágel, Strength and pore structure of ternary blended cement mortars containing blast furnace slag and silica fume, Cem. Concr. Res. 28 (1998) 1011–1022, https://doi.org/10.1016/s0008-8846(98)00078-7.

[48] C.-S. Poon, L. Lam, S. Kou, Y.-L. Wong, R. Wong, Rate of pozzolanic reaction of metakaolin in high-performance cement pastes, Cem. Concr. Res. 31 (2001) 1301–1306, https://doi.org/10.1016/s0008-8846(01)00581-6.

[49] P. Chindaprasirt, C. Jaturapitakkul, T. Sinsiri, Effect of fly ash fineness on compressive strength and pore size of blended cement paste, Cem. Concr. Compos. 27 (2005) 425–428, https://doi.org/10.1016/j.cemconcomp.2004.07.003.

[50] H. Lu, P.D. Cary, Deformation measurements by digital image correlation: Implementation of a second-order displacement gradient, Exp. Mech. 40 (2000) 393–400.

[51] B. Pan, H. Xie, Z. Wang, Equivalence of digital image correlation criteria for pattern matching, Appl. Opt. 49 (2010) 5501–5509, https://doi.org/10.1364/ao.49.005501.

[52] ASTM International, Test Method for Dynamic Youngs Modulus, Shear Modulus, and Poissons Ratio by Impulse Excitation of Vibration, 2006. https://doi.org/10.1520/e1876-01r06..

[53] V. Nežerka, Z. Slížková, P. Tesárek, T. Plachý, D. Frankeová, V. Petráňová, Comprehensive study on microstructure and mechanical properties of lime-pozzolan pastes, Cem. Concr. Res. 64 (2014) 17–29, https://doi.org/10.1016/j.cemconres.2014.06.006.

[54] J. Blaber, B. Adair, A. Antouniou, Ncorr: open-source 2d digital image correlation matlab software, Exp. Mech. 55 (2015) 1105–1122, https://doi.org/10.1007/s11340-015-0009-1.

[55] V. Nežerka, J. Antoš, J. Litoš, P. Tesárek, J. Zeman, An integrated experimental-numerical study of the performance of lime-based mortars in masonry piers under eccentric loading, Constr. Build. Mater. 114 (2016) 913–926, https://doi.org/10.1016/j.conbuildmat.2016.04.013.

[56] M. Guizar-Sicairos, S.T. Thurman, J.R. Fienup, Efficient subpixel image registration algorithms, Opt. Lett. 33 (2008) 156–158, https://doi.org/10.1364/ol.33.000156.

[57] J. Antoš, V. Nežerka, M. Somr, Real-time optical measurement of displacements using subpixel image registration, Exp. Tech. 43 (2019) 315–323, https://doi.org/10.1007/s40799-019-00315-1.

[58] B. Patzák, OOFEM home page, 2000.http://www.oofem.org..

[59] B. Patzák, OOFEM – an object-oriented simulation tool for advanced modeling of materials and structures, Acta Polytechnica 52 (6) (2012) 59–66.

[60] P. Havlásek, M. Jirásek, Multiscale modeling of drying shrinkage and creep of concrete, Cem. Concr. Res. 85 (2016) 55–74, https://doi.org/10.1016/j.cemconres.2016.04.001.

[61] D. Rypl, T3D Mesh Generator, 2019.http://mech.fsv.cvut.cz/dr/t3d.html..

[62] D. Rypl, Z. Bittnar, Generation of quad-dominant meshes using a triangular mesh generator, in: cturep: Contributions to Mechanics and Structures, vol. 4, CTU Publishing House, Prague, Czech Republic, 2000, pp. 23–38, iSBN 80-01-02320-6..

[63] Z.P. Bažant, B.H. Oh, Crack band theory for fracture of concrete, Mater. Struct. 16 (1983) 155–177, https://doi.org/10.1007/bf02486267.

[64] M. Jirásek, P. Havlásek, Microprestress-solidification theory of concrete creep: Reformulation and improvement, Cem. Concr. Res. 60 (2014) 51–62, https://doi.org/10.1016/j.cemconres.2014.03.008.

[65] Z. Bažant, P. Havlásek, M. Jirásek, Microprestress-solidification theory: modeling of size effect on drying creep, in: N. Bicanic, H. Mang, G. Meschke, R. de Borst (Eds.), Computational Modelling of Concrete Structures, CRC Press/Balkema, EH Leiden, The Netherlands, 2014, pp. 749–758.
[66] Creep and shrinkage prediction model for analysis and design of concrete structures—model b3, Materials and Structures 28 (1995) 357–365.https://doi.org/10.1007/bf02473152..
[67] M. Limbachiya, M.S. Meddah, Y. Ouchagour, Use of recycled concrete aggregate in fly-ash concrete, Constr. Build. Mater. 27 (2012) 439–449, https://doi.org/10.1016/j.conbuildmat.2011.07.023.
[68] D. Foti, M. Lerna, M. Sabbà, V. Vacca, Mechanical characteristics and water absorption properties of blast-furnace slag concretes with fly ashes or microsilica additions, Appl. Sci. 9 (2019) 1279, https://doi.org/10.3390/app9071279.
[69] N. Swamy, G. Rigby, Dynamic properties of hardened paste, mortar and concrete, Matériaux et Constructions 4 (1971) 13–40, https://doi.org/10.1007/bf02473927.
[70] K. Jurowski, S. Grzeszczyk, Influence of selected factors on the relationship between the dynamic elastic modulus and compressive strength of concrete, Materials 11 (2018) 477, https://doi.org/10.3390/ma11040477.
[71] Q. Zhang, R. Le Roy, M. Vandamme, B. Zuber, Long-term creep properties of cementitious materials: comparing microindentation testing with macroscopic uniaxial compressive testing, Cem. Concr. Res. 58 (2014) 89–98, https://doi.org/10.1016/j.cemconres.2014.01.004.
[72] W. Mullen, Creep of Portland Cement Paste, Purdue University, 1963.
[73] R. Sovják, P. Havlásek, J. Vítek, Long-term behavior of concrete slabs prestressed with CFRP rebars subjected to four-point bending, Constr. Build. Mater. 188 (2018) 781–792, https://doi.org/10.1016/j.conbuildmat.2018.08.084.
[74] M.D. Ašić, V.V. Kovačević-Vujčić, An implicit enumeration method for global optimization problems, Comput. Math. Appl. 21 (1991) 191–201, https://doi.org/10.1016/0898-1221(91)90173-2.
[75] P. Grassl, H.S. Wong, N.R. Buenfeld, Influence of aggregate size and volume fraction on shrinkage induced micro-cracking of concrete and mortar, Cem. Concr. Res. 40 (2010) 85–93, https://doi.org/10.1016/j.cemconres.2009.09.012.
[76] J. Bisschop, Effect of aggregates on drying shrinkage microcracking in cement-based composites, Mater. Struct. 35 (2005) 453–461, https://doi.org/10.1617/12627.
[77] F. Lagier, X. Jourdain, C.D. Sa, F. Benboudjema, J. Colliat, Numerical strategies for prediction of drying cracks in heterogeneous materials: comparison upon experimental results, Eng. Struct. 33 (2011) 920–931, https://doi.org/10.1016/j.engstruct.2010.12.013.
[78] A.M. Humad, A. Kothari, J.L. Provis, A. Cwirzen, The effect of blast furnace slag/fly ash ratio on setting, strength, and shrinkage of alkali-activated pastes and concretes, Front. Mater. 6 (2019).
[79] A. Castel, S.J. Foster, T. Ng, J.G. Sanjayan, R.I. Gilbert, Creep and drying shrinkage of a blended slag and low calcium fly ash geopolymer concrete, Mater. Struct. 49 (2015) 1619–1628, https://doi.org/10.1617/s11527-015-0599-1.
[80] E.E. Ambrose, J.P. Forth, Influence of relative humidity on tensile and compressive creep of concrete amended with ground granulated blast-furnace slag, Nigerian J. Technol. 37 (2018) 19, https://doi.org/10.4314/njt.v37i1.3.
[81] N. Dutler, M. Nejati, B. Valley, F. Amann, G. Molinari, On the link between fracture toughness, tensile strength, and fracture process zone in anisotropic rocks, Eng. Fract. Mech. 201 (2018) 56–79, https://doi.org/10.1016/j.engfracmech.2018.08.017.

Appendix C

V. Nežerka et al., A jigsaw puzzle metamaterial concept, *Composite Structure* 202 (2018) 1275–1279, doi: 10.1016/j.compstruct.2018.06.015

Author's contribution: DIC, numerical modeling.

Composite Structures 202 (2018) 1275–1279

Contents lists available at ScienceDirect

Composite Structures

journal homepage: www.elsevier.com/locate/compstruct

A jigsaw puzzle metamaterial concept

V. Nežerka, M. Somr, T. Janda, J. Vorel, M. Doškář, J. Antoš, J. Zeman, J. Novák*

Faculty of Civil Engineering, Czech Technical University in Prague, Thákurova 7, 166 29 Praha 6, Czech Republic

ARTICLE INFO

Keywords:
Modular metamaterial
Auxetic behavior
Additive manufacturing
Customized assembly
Digital image correlation

ABSTRACT

A concept of a planar modular mechanical metamaterial inspired by the principle of local adaptivity is proposed. The metamaterial consists of identical pieces similar to jigsaw puzzle tiles. Their rotation within assembly provides a substantial flexibility in terms of structural behavior, whereas mechanical interlocks enable re-assembly. The tile design with a diagonal elliptical opening allows us to vary elastic properties from stiff to compliant, with positive, zero, or negative Poisson's ratio. The outcomes of experimental testing on additively manufactured specimens confirm that the assembly properties can be accurately designed using optimization approaches with finite element analysis at heart.

1. Introduction

Nature efficiently distributes material and designs optimal structure across scales with respect to anticipated loading. Bone tissue is a perfect example of such a multiscale hierarchical structure in which the organization of mineral nanoparticles and collagen microfibrils governs the bone's elastic properties [1]. Here we propose to mimic such local adaptivity by material design similarly to a way children assemble images decomposed into jigsaw puzzle pieces. We create a planar block of mechanical metamaterial [2] with required overall elastic stiffness emanating from the geometry and composition of mesostructural units, similar to the concepts proposed in, e.g., [3–6]. In particular, the assemblies are composed of mutually rotated identical tiles with elliptic openings, Fig. 1, as proposed by Taylor et al. [7]. In addition, the subscale, tile-level, geometry design also allows us to tune Poisson's ratio [8,9] and thus fabricate materials exhibiting conventional or auxetic [10,11] behavior. The tiles in assemblies can be connected through jigsaw puzzle interlocks [12], or the modularity concept can serve for optimization and design purposes and the conglomerates can be printed out as monolithic pieces [4]. In this work, the interlocks are not glued together, they utilize only frictional forces to meet the requirement on reasonably stiff contact and non-destructive reassembly. In order to obtain comprehensive full-field information on strain and displacement fields, a digital image correlation (DIC) [14,15] analysis is employed throughout the study.

2. Modular concept

The main ingredient of the proposed concept are square tiles of a jigsaw puzzle-like shape, as shown in Fig. 2(a). Besides the obvious assembly into periodic arrangements, Fig. 2(b), the rotational symmetry of the interlocks allows us to perturb the regular arrangement leading to locally adjusted elastic behavior [13].

3. Metamaterial assembly

To illustrate the adaptivity through local tile rotations, assemblies consisting of 5×5 tiles were arranged to exhibit auxetic, non-auxetic, and mixed behavior and subjected to a displacement-controlled compression applied at the top edge/facet of the specimen. First, we explored two regular cases: (i) an auxetic arrangement and (ii) a non-auxetic arrangement, see Figs. 2(b) and 3(a and b). In addition to the two configurations illustrated also in Fig. 4(a and b), a mixed arrangement (iii) supposed to combine the behavior of previous assemblies was also experimentally tested, Figs. 3(c) and 4(c).

The regular zigzag arrangement of ellipses (i) yielded the smallest value for both elastic constants, Young's modulus and Poisson's ratio. As expected, the specimen contracted in horizontal direction when compressed vertically, Fig. 5(b), demonstrating the desired auxetic response. On the other hand, the configuration (ii) with star-like openings exhibited twice as stiff response, see Fig. 5(a), and Poisson's ratio exceeding the one of the virgin polylactic acid (PLA) filament. The deformation of the mixed arrangement (iii) clearly proves that Poisson's ratio can be tuned locally, the bottom layer expands horizontally, while the upper part exhibits the auxetic behavior, Fig. 5(b). This is also evident from the binary patterns in Fig. 4(c).

* Corresponding author.
E-mail address: novakja@fsv.cvut.cz (J. Novák).

https://doi.org/10.1016/j.compstruct.2018.06.015
Received 14 February 2018; Received in revised form 10 May 2018; Accepted 4 June 2018
Available online 05 June 2018

Fig. 1. Additively manufactured jigsaw puzzle tiles and partly disassembled auxetic aggregate with effective Poisson's ratio equal to −0.55.

4. Customized assemblies

The merit of the proposed material system goes beyond many periodic metamaterial designs [16–18] because of its modularity [3,5,19] and inherent aperiodicity [13]. Rotation of a few tiles by 90° within an assembly significantly changes the response to loading. The assembly plan can be adjusted with respect to anticipated loading and specific requirements on both local and global behavior [20,21]. To demonstrate this feature, two modular assemblies (fabricated without interfaces and with imperfect mechanical interlocks) of 4×4 tiles were optimized employing a finite element analysis to eliminate tilt angle ϕ due to eccentric loading, as indicated in Fig. 6(a).

Two variants of the customized assemblies were considered. First, interfaces between individual tiles were considered perfectly rigid as these are way easier to handle within the numerical framework. Tested assemblies were then manufactured as monoliths, but with the modular design strategy with compatible meshes without contacts in mind. Second, imperfect contacts within aggregates with mechanical interlocks were introduced into the finite element model by means of contact elements and the entire procedure from design to fabrication sustained fully modular.

The tilt angle ϕ of the upper edge across all admissible assembly combinations ranged from −0.100° to 1.912° for solid assemblies and from −0.108° to 2.249° for those with imperfect contacts. The optimal assemblies that were supposed to yield zero tilt angle, both solid and with mechanical interlocks, were additively manufactured and tested to validate the numerical model. As expected, the optimum assembly plan with mechanical interlocks was completely different from the one with fixed contacts, as shown in Fig. 6(b and c), demonstrating the key role of connections. The experimental tilt angle was measured from the displacement distribution maps using virtual extensometers within the DIC framework. The optimum solid and mechanically connected assemblies yielded $\phi = -0.00022°$ and $\phi = 0.01°$, respectively.

5. Materials and methods

5.1. Optimization of customized assemblies

In the spirit of the explicit complete enumeration method, the computation of all $2^{16} = 65,403$ combinations of 4×4 assemblies with the selection of the best solution was done using in–house scripts developed in MATLAB[1] software linked to ANSYS[2]. These were discretized by 6,184 linear triangular (assemblies without interfaces, see Fig. 6) and 13,322 isoparametric four-node quadrilateral (assemblies with imperfect interlocks) finite elements PLANE182 under plane strain assumptions. Properties of the contact elements, used for simulations of imperfect interfaces between tiles, were calibrated based on experimental measurements and inverse calculations on pairs of interlocked tiles. In particular, the augmented Lagrangian contact algorithm was employed with the automatic update, using the default values for interfacial contact stiffness parameters provided by the ANSYS program.

5.2. Fabrication and materials

The $2 \times 2 \times 1$ cm tiles for experimental verification were additively manufactured from PLA filament with Young's modulus of about 1,800 MPa and Poisson's ratio equal to 0.3 [22], using Prusa i3 3D printer.

5.3. Mechanical testing and data acquisition

The aim of the experimental analysis was to measure macroscopic response of the tested assemblies to displacement-controlled compression. The experiments were carried out using LabTest 4.100SP1 testing machine. The 5×5 assemblies were loaded at rate 1.2–2.0 mm/min until the displacement reached 1.6 mm, while the optimized 4×4 assemblies were loaded at the same rate until the eccentrically applied force (see Fig. 6) reached 200 N. In both cases, a steel plate of 1 cm in thickness was used to distribute the loading over the upper edge of the assemblies.

The analyzed images were taken in 2-second intervals by a high-definition camera Canon EOS 70D in uncompressed format (.raw), yielding a resolution of 12 px/mm. The effect of lens distortion was minimized by setting the focal length to 55 mm. A non-commercial open-source software Ncorr [15] was used to evaluate the fields, and a postprocessing of the DIC data was accomplished using an in–house software Ncorr_post[3]. Virtual extensometers were placed at distinct locations, as depicted in Fig. 3, in order to quantify the relative vertical and horizontal displacements of the entire assemblies.

6. Conclusions

Presented results demonstrate that even such an elementary modular system based on a single unit provides a substantial flexibility in controlling overall mechanical properties by local rotations of mesostructural units by 90°. The outcomes of experimental tests performed on the additively manufactured specimens confirm that the assembly properties can be accurately designed using a numerical analysis and optimization.

On the other hand, avoiding numerical analyzes in the design process is difficult, given the emergence of highly-localized instability-like behavior when snapping from one configuration to another (pronounced namely for aggregates with imperfect contacts). Because of this phenomenon, we were unable to devise any simple heuristic, analytical, or semi-analytical tool for predicting the overall assembly response *a priori*. To further highlight this difficulty, Fig. 7 shows the intricate, often counter-intuitive dependence of the tilt angle on the tile configurations, whereas Fig. 8 depicts two distinct assemblies delivering nearly the same structural response.

Nonetheless, to the merit of the proposed modular concept, it is scalable up to the limits of the manufacturing hardware and extensible to three dimensions. New possibilities in terms of the design flexibility are foreseen by incorporating the concept of Wang tiles [23–26]. As

[1] The MathWorks, Inc., Matlab release 2015a, http://www.mathworks.com/products/matlab/, Natick, Massachusetts, U.S.

[2] ANSYS Mechanical, Academic research, release 16.2,http://www.ansys.com/, Pennsylvania, U.S.

[3] V. Nežerka, Ncorr_post v2.0: DIC Post-Processing Tool,http://mech.fsv.cvut.cz/nezerka/DIC/index.htm, Czech Technical University in Prague.

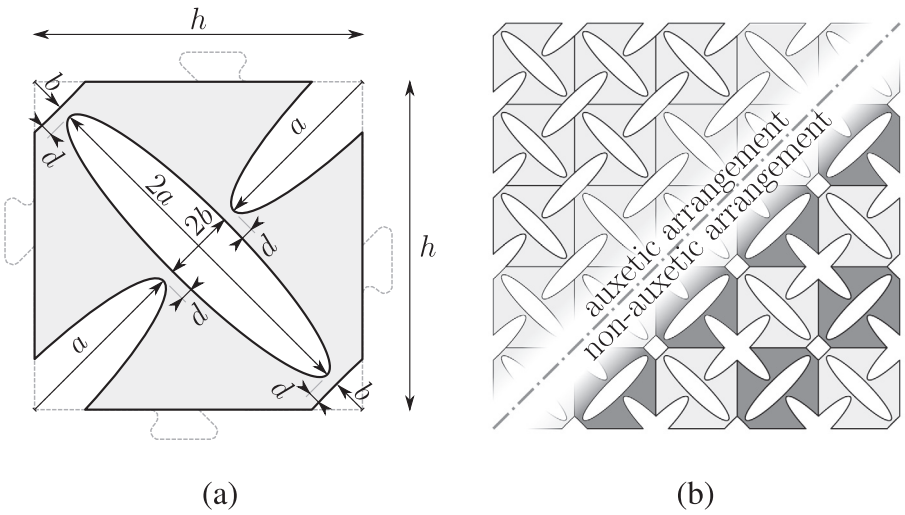

Fig. 2. (a) geometry of single jigsaw puzzle tile with interlocks outlined by dotted contours. (b) regular assemblies into either auxetic or non-auxetic arrangements. Highlighted tiles in the latter arrangement are rotated by 90°. Particular dimensions of individual parameters of single tile are derived from the tile edge length h, here set to 20 mm, as follows: major semiaxis $a = h/2$, minor semiaxis $b = h/10$, yielding ligament thickness $d \approx h/12$.

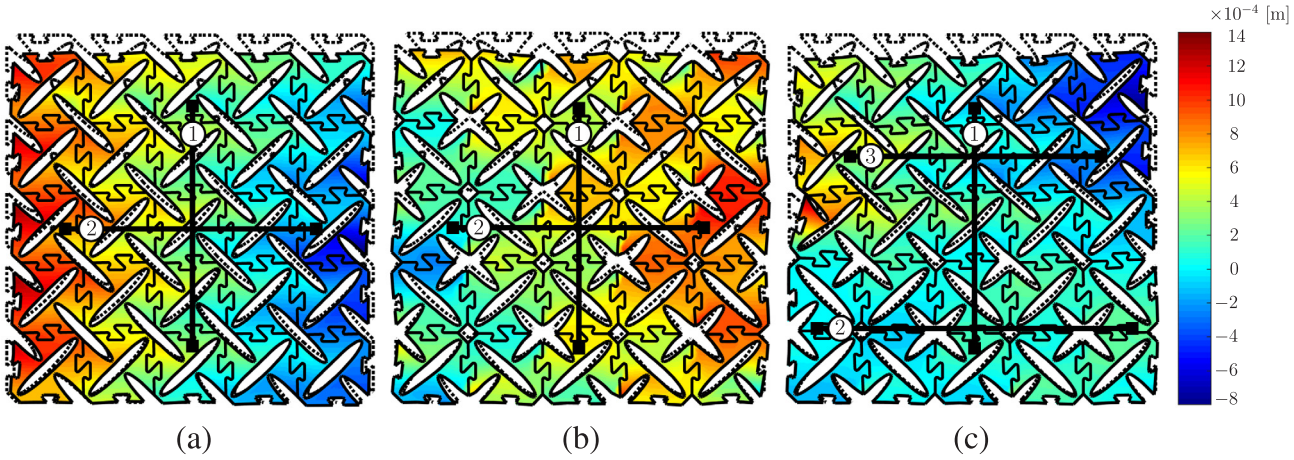

Fig. 3. Specimen deformation (original shape indicated by dotted contours) and horizontal displacement distribution maps, obtained by DIC, under uniaxial compression applied to (a) auxetic, (b) non-auxetic, and (c) mixed assemblies. Virtual extensometers are indicated with boldface lines. Positive displacements are measured according to x and y axes pointing right- and up-wards from the specimen center.

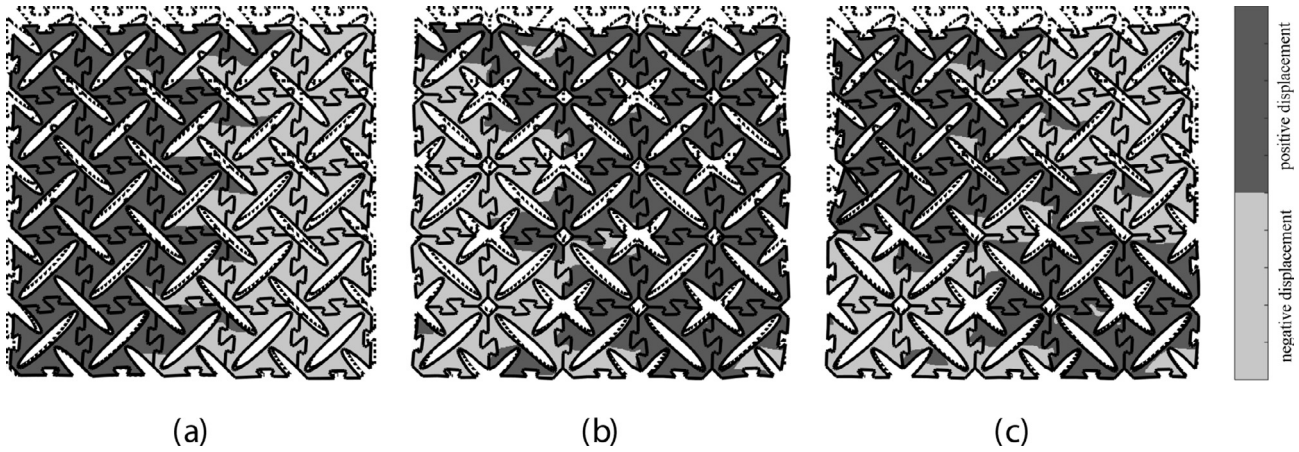

Fig. 4. Specimen deformations with binary representation of horizontal displacements, obtained by DIC, under uniaxial compression applied to (a) auxetic, (b) non-auxetic, and (c) mixed assemblies. Positive displacements are measured according to x and y axes pointing right- and up-wards from the specimen center.

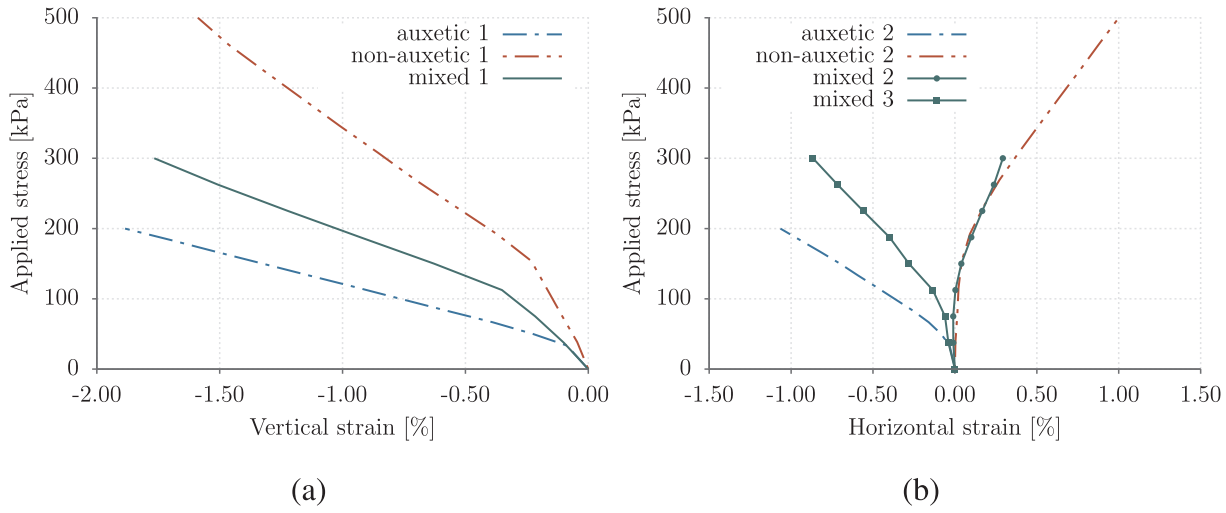

Fig. 5. Effective stress-strain curves for (a) vertical and (b) horizontal extensometers placed in auxetic, non-auxetic, and mixed assemblies according to Fig. 3.

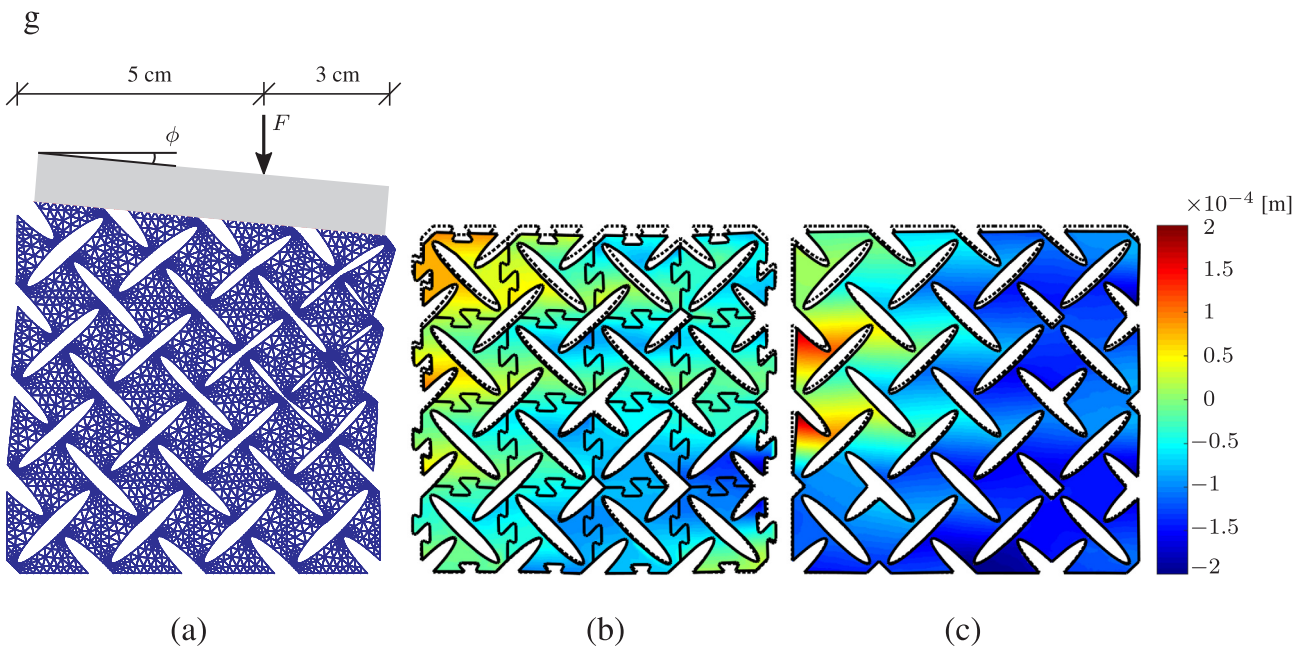

Fig. 6. (a) Eccentric loading scheme and the measured tilt angle ϕ. Experimentally obtained horizontal displacements (original shape indicated by dotted contours) obtained by DIC measurements on specimens designed to compensate eccentric loading: (b) assembly with imperfect mechanical interlocks and (c) without interfaces.

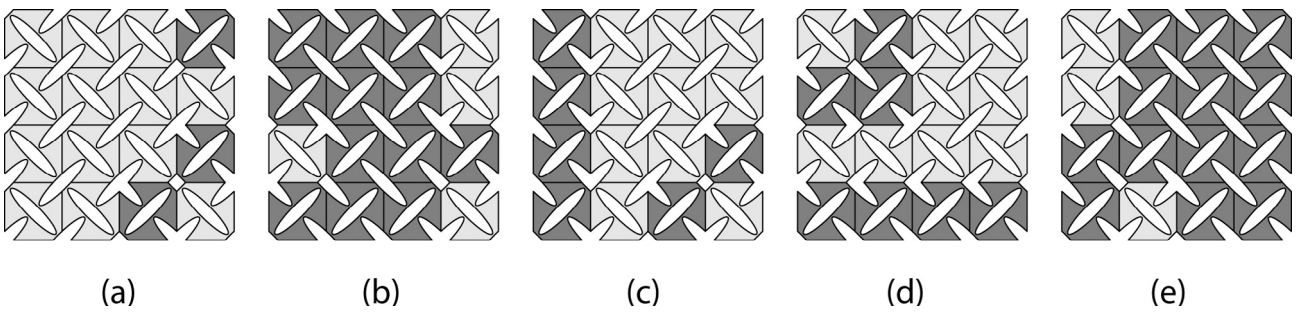

Fig. 7. Solid assemblies for tilt angles (a) $\phi = -0.100°$, (b) $\phi = 0.273°$, (c) $\phi = 0.575°$, (d) $\phi = 0.912°$, (e) $\phi = 1.912°$. Highlighted tiles are rotated by 90° with respect to the setting adopted in Fig. 2(a).

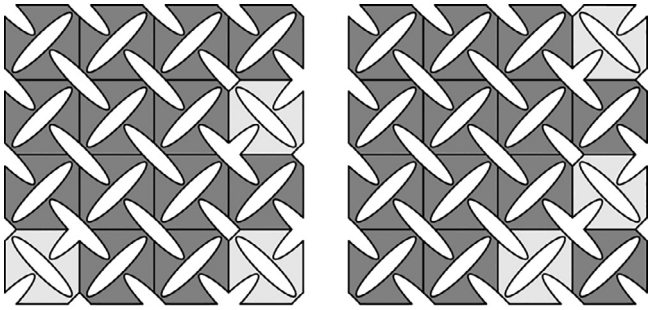

Fig. 8. Solid assemblies for tilt angles, (a) $\phi = 0.00022°$, (b) $\phi = 0.00029°$. Highlighted tiles are rotated by 90° with respect to the setting adopted in Fig. 2(a).

opposed to commonly produced disordered structures, e.g., metal foams, the behavior of the jigsaw puzzle system augmented with Wang tiling would be fully predictable and customizable with respect to specific needs. After translating the concept to practical applications, automated assembly of tiles/modules based on optimized plans is envisaged.

Acknowledgment

The support by the Technology Agency of the Czech Republic and Ministry of Industry and Trade of the Czech Republic under research projects Nos. TACR TH02020420 and MPO FV10202, respectively, is gratefully acknowledged. In addition, this work was partly sponsored by CTU grant No. SGS18/037/OHK1/1T/11

Appendix A. Supplementary data

Supplementary data associated with this article can be found, in the online version, athttp://dx.doi.org/10.1016/j.compstruct.2018.06.015.

References

[1] Granke M, Gourrier A, Rupin F, Raum K, Peyrin F, Burghammer M, Saded A, Laugier P. Microfibril orientation dominates the microelastic properties of human bone tissue at the lamellar length scale. PLoS ONE 2013;8:e58043. http://dx.doi.org/10.1371/journal.pone.0058043.
[2] Wegener M. Metamaterials beyond optics. Science 2013;342:939–40. http://dx.doi.org/10.1126/science.1246545.
[3] Wu Z, Harne R, Wang K. Exploring a modular adaptive metastructure concept inspired by muscle's cross-bridge. J. Intell. Mater. Syst. Struct. 2015;27:1189–202. http://dx.doi.org/10.1177/1045389x15586451.
[4] Schumacher C, Bickel B, Rys J, Marschner S, Daraio C, Gross M. Microstructures to control elasticity in 3d printing. ACM Trans. Graphics 2015;34:136:1–136:13. http://dx.doi.org/10.1145/2766926.
[5] Mousanezhad D, Kamrava S, Vaziri A. Origami-based building blocks for modular construction of foldable structures. Sci. Rep. 2017;7:14792. http://dx.doi.org/10.1038/s41598-017-13654-z.
[6] Cheung KC, Gershenfeld N. Reversibly assembled cellular composite materials. Science 2013;341:1219–21. http://dx.doi.org/10.1126/science.1240889.
[7] Taylor M, Francescony L, Gerendás M, Shanian A, Carson C, Bertoldi K. Low porosity metallic periodic structures with negative Poisson's ratio. Materials 2014;26:2365–70. http://dx.doi.org/10.1002/adma.201304464.
[8] Overvelde JTB, Shan S, Bertoldi K. Compaction through buckling in 2D periodic, soft and porous structures: effect of pore shape. Adv. Mater. 2012;24:2337–42. http://dx.doi.org/10.1002/adma.201104395.
[9] Overvelde JTB, Bertoldi K. Relating pore shape to the non-linear response of periodic elastomeric structures. J. Mech. Phys. Solids 2014;64:351–66. http://dx.doi.org/10.1016/j.jmps.2013.11.014.
[10] Lakes R. Foam structures with a negative Poisson's ratio. Science 1987;235:1038–40. http://dx.doi.org/10.1126/science.235.4792.1038.
[11] Ai L, Gao X-L. Three-dimensional metamaterials with a negative poisson's ratio and a non-positive coefficient of thermal expansion. Int. J. Mech. Sci. 2018;135:101–13. http://dx.doi.org/10.1016/j.ijmecsci.2017.10.042.
[12] Malik IA, Mirkhalaf M, Barthelat F. Bio-inspired jigsaw-like interlocking sutures: modeling, optimization, 3D printing and testing. J. Mech. Phys. Solids 2017;102:224–38. http://dx.doi.org/10.1016/j.jmps.2017.03.003.
[13] Coulais C, Teomy E, de Reus K, Shokef Y, van Hecke M. Combinatorial design of textured mechanical metamaterials. Nature 2016;535:529–32. http://dx.doi.org/10.1038/nature18960.
[14] Peters WH, Ranson WF. Digital imaging techniques in experimental stress analysis. Opt. Eng. 1982;21:427–31. http://dx.doi.org/10.1117/12.7972925.
[15] Blaber J, Adair B, Antouniou A. Ncorr: Open-source 2d digital image correlation matlab software. Exp. Mech. 2015;55:1105–22. http://dx.doi.org/10.1007/s11340-015-0009-1.
[16] Florijn B, Coulais C, van Hecke M. Programmable mechanical metamaterials. Phys. Rev. Lett. 2014;113:175503. http://dx.doi.org/10.1103/physrevlett.113.175503.
[17] Coulais C, Sounas D, Alù A. Static non-reciprocity in mechanical metamaterials. Nature 2017;542:461–4. http://dx.doi.org/10.1038/nature21044.
[18] Zheng X, Lee H, Weisgraber TH, Shusteff M, DeOtte J, Duoss EB, Kuntz JD, Biener MM, Ge Q, Jackson JA, Kucheyev SO, Fang NX, Spadaccini CM. Ultralight, ultrastiff mechanical metamaterials. Science 2014;344:1373–7. http://dx.doi.org/10.1126/science.1252291.
[19] Yang N, Silverberg JL. Decoupling local mechanics from large-scale structure in modular metamaterials. Proc. Nat. Acad. Sci. 2017;114:3590–5. http://dx.doi.org/10.1073/pnas.1620714114.
[20] Tammas-Williams S, Todd I. Design for additive manufacturing with site-specific properties in metals and alloys. Scr. Mater. 2017;135:105–10. http://dx.doi.org/10.1016/j.scriptamat.2016.10.030.
[21] Ma J, Song J, Chen Y. An origami-inspired structure with graded stiffness. Int. J. Mech. Sci. 2018;136:134–42. http://dx.doi.org/10.1016/j.ijmecsci.2017.12.026.
[22] Tymrak BM, Kreiger M, Pearce JM. Mechanical properties of components fabricated with open-source 3-D printers under realistic environmental conditions. Mater. Des. 2014;58:242–6. http://dx.doi.org/10.1016/j.matdes.2014.02.038.
[23] Wang H. Proving theorems by pattern recognition – II. Bell Syst. Tech. J. 1961;40:1–41. http://dx.doi.org/10.1002/j.1538-7305.1961.tb03975.x.
[24] Novák J, Kučerová A, Zeman J. Microstructural enrichment functions based on stochastic Wang tilings. Modell. Simul. Mater. Sci. Eng. 2013;21:025014. http://dx.doi.org/10.1088/0965-0393/21/2/025014.
[25] Doškář M, Novák J. A jigsaw puzzle framework for homogenization of high porosity foams. Comput. Struct. 2016;166:33–41. http://dx.doi.org/10.1016/j.compstruc.2016.01.003.
[26] Doškář M, Zeman J, Jarušková D, Novák J. Wang tiling aided statistical determination of the Representative Volume Element size of random heterogeneous materials. Eur. J. Mech. A. Solids 2018;70:280–95. http://dx.doi.org/10.1016/j.euromechsol.2017.12.002.

Appendix D

J. Antoš, **V. Nežerka**, and M. Somr, Assessment of 2D-DIC stochastic patterns, *Acta Polytechnica CTU Proceedings* 13 (2017) 1–10, doi: 10.14311/APP.2017.13.0001

Author's contribution: main idea, supervision, programming.

Acta Polytechnica CTU Proceedings **13**:1–10, 2017
doi:10.14311/APP.2017.13.0001

available online at http://ojs.cvut.cz/ojs/index.php/app

ASSESSMENT OF 2D-DIC STOCHASTIC PATTERNS

Jakub Antoš*, Václav Nežerka, Michael Somr

Czech Technical University in Prague, Faculty of Civil Engineering, Thákurova 7, 166 29 Prague 6, Czech Republic

* corresponding author: jakub.antos@fsv.cvut.cz

Abstract. Cost of experimental testing of materials and structures subjected to mechanical loading often constitutes a significant portion of a project budget. Therefore a collection of data in a maximum possible amount is desirable. Extensometers and strain-gauges attached to the specimen surface often fail and cannot provide full-field information about the development of displacements and strains. Digital Image Correlation (DIC) is capable of providing such information. Unsuitable texture or artificially applied pattern, essential for DIC analysis, can spoil the DIC outcomes completely. An additional investment into preparation of new experimental testing can be avoided with the use of tools employing algorithms for stochastic pattern assessment. The development of such algorithms and their implementation into an open-source DIC software is the goal of the presented research.

Keywords: digital image correlation, stochastic pattern, full-field displacement.

1. Introduction

The measurement of strains and displacements is utilized when investigating behavior of materials or specimens in laboratories, but also for assessment of existing structures. Traditionally, contact measurement techniques have been used, but these introduce challenges in terms of accuracy, require sufficiently flat surface, and their attachment requires a lot of effort. The group of contact methods includes strain gauges, extensometers, or linear variable differential transformers (LVDTs) [1].

Contact methods techniques have a few drawbacks compared to optical full field monitoring: the strain must be within a certain range and is averaged over the strain-gauge length, the measurement is accomplished at discrete locations, and the investigated surface must be smooth enough to attach the gauge.

Quite recently alternatives to non-contact measurement have been developed. These include e.g., laser vibrometry, laser range finders, optical correlation methods, interferometry, moiré, or photo/videogrammetry [2, 3]. Optical measurements, such as Digital Image Correlation (DIC), are capable of capturing even the most complex deformation until the ultimate material failure [3, 4]. Because of that reason, optical methods became accepted in the field of experimental solid mechanics. The availability of compact and sensitive light sources, detectors, optical components, and powerful computers have been promoting the use of DIC in both commercial and academic research. The full-field data can be easily processed and provides data valuable for engineers who are used to employing finite element programs in their calculations.

2. Digital Image Correlation

DIC became indispensable to monitoring and analyzing a development of displacement or strain fields over time by matching stochastic pattern of deformed images with respect to a reference one [5]. The method is capable of capturing strain localization on a surface of a loaded structure (such as plasticity or cracking) in any direction. As DIC tools for 3D analysis emerge [6], the method is becoming more versatile and widely used in the industry and research.

DIC is not only limited to the relative measurement of discrete points as conventional contact methods and is frequently more accurate than monitoring by means of extensometers or strain-gauges that often suffer from imperfect attachment to the measured surface. Moreover, the use of DIC can significantly reduce the cost of the experiment. DIC reached its maturity during last decade owing it to the fast and successful development and elaboration of computers, digital cameras and specialized software for image processing. DIC has even been characterized as "a major development in the art of experimental mechanics" [7]. The boom of DIC has been reflected in the emergence of new commercial and open source software to perform DIC with differently optimized correlation functions and calculation methods, most recently summarized by Pan et al. [8].

2.1. DIC Algorithms

DIC utilizes a correlation algorithm to obtain displacements and subset deformations by identifying areas of matching grey-scale values between the speckle pattern in each subset of deformed and underformed (reference) images (Figure 1). To facilitate the correlation, a stochastic speckle pattern must be applied (if not present naturally) to a specimen surface in order to provide a random grey-level variations at

the sufficient quality of which is fundamental to the precision of the measured displacement data. It is well established that the trade-off between the data resolution and precision is affected by the quality of a pattern.

To perform DIC, each image must be divided into a grid of interrogation cells, or subsets, containing a finite number of pixels. Resolution of the data is maximized by reducing the size of the subsets, but as the interrogation cell size decreases, the uncertainty in the strain measurement increases due to a reduction in the number of features to track within the subset [9]. Therefore, the resolution and accuracy of the displacement and deformation fields are limited by the total number of pixels within the images. The center position of each target subset is obtained through searching the peak position of the correlation coefficient field and its deformation is calculated using an iterative approach [10, 11].

DIC has traditionally utilized subset-based local approach [5] that has been very well developed and widely used in commercial or academic DIC packages. However, there are certain drawbacks that make the method useless for some applications, such as experiments producing high strain gradients [12]. The reason is non-continuity of the displacement field, as the displacements of the subsets are sought separately. Therefore smoothing of the noisy displacement field is required [8, 9, 11]. A local polynomial smoothing over a rectangular area (strain window) is usually employed [8]. The amount of smoothing is controlled by the subset size, step size, and strain window size. The results are then highly dependent on setting these parameters by a user [13].

An alternative global approach has been developed quite recently based on the procedures used in the Finite Element Method (FEM) [14, 15]. Using the global DIC approach, a complete element mesh is tracked on images, ensuring C^0-continuity[1], resulting in elimination of noise in strain fields. This method was initially proposed by Cheng et al. [16] and later Besnard et al. developed the Q4-DIC [17] with implementation of a bilinear (Q4) or quadratic (Q8) mesh. The global algorithms may be refined using user experience, or using adaptive mesh refinement [18].

2.2. DIC accuracy

The accuracy of DIC is an issue frequently discussed by both, theoreticians and experimentalists [19, 20]. Although originally restricted to the size of one-pixel, various sub-pixel techniques have been proposed and used to improve the method accuracy. The most popular techniques include curve-fitting, gradient-based and Newton-Raphson algorithms. The last two cases are based on the identification of the parameters that define the mapping of a subset of pixels in order to maximize the image correlation. The results show that the Newton-Raphson approach is considered as the most accurate and stable. Other interesting approaches such as genetic algorithms, finite element interpolations and B-splines are reported in [8] but they generally appear to have a lower performance. Bing et al. [21] compared performance of three most used sub-pixel techniques by simulating image distortions, demonstrating the suitability of Newton-Rapson approach.

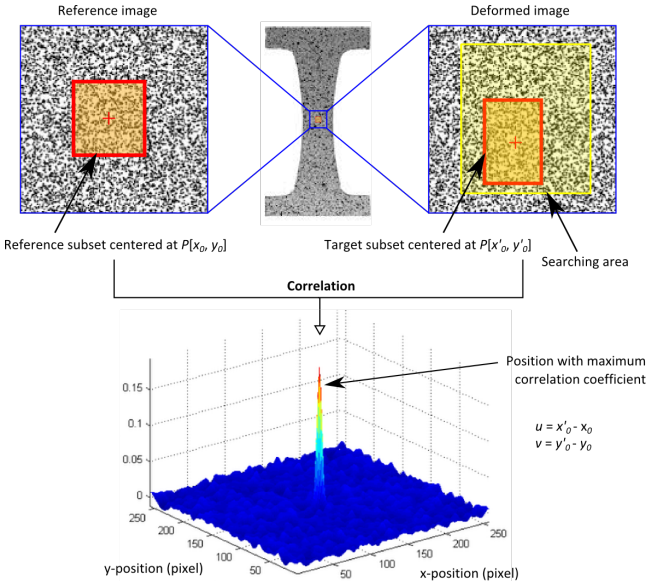

Figure 1. Example of the subset tracking procedure using DIC.

Besides the choice of the most suitable DIC algorithm, other factors substantially influence the DIC accuracy. The measurement errors may be classified into two categories: (i) systematic experimental errors such as bad calibration and setting of image acquisition system and (ii) errors produced by correlation algorithm.

The experimental errors are related to variations in illumination and the quality of the acquisition system, i.e., the noise during the acquisition and digitalization, image distortion, or position of the camera with respect to the monitored surface. The errors related to the correlation algorithms arise from inappropriate selection of correlation methods or input parameters, such as subset size, correlation function, sub-pixel algorithm, shape function, or interpolation scheme.

3. Stochastic Pattern Assessment

A majority of research into the accuracy of DIC is focused on correlation algorithms and processing parameters (recall Section 2.2), such as subset size [22], shape function selection [23], or methods of obtaining sub-pixel accuracy [24]. Less attention has been paid to the effect of the quality of the speckle pattern. It is important for the artificial pattern or natural texture to be adjusted in accordance with the expected displacement field in order to maximize measurement

[1] C^i differentiability class corresponds to the existence of i derivatives of a function. The class C^0 consists of all continuous functions.

accuracy, as speckles can be both too large and too small for the particular measurement [25]. Quantitative error analysis [26–29] shows that the measurement error depends crucially on the presence of large intensity gradients within the pattern. Therefore, the technique in most cases requires a specimen preparation procedure to enhance the surface texture, since the natural one does not provide a required quality in terms of intensity gradients and speckle-size distribution.

Pattern assessment has been discussed by a few authors [5, 30, 31], offering a number of methods to evaluate the quality of applied patterns. Pan et al. [32] presented a number of assessment criteria based upon the local subset intensity gradients [20] and the global mean intensity gradient (MIG) throughout the image. The latter criteria showed a good agreement to results obtained numerically. The benefit of applying the global criteria is that these are astraightforward. High MIG values typically result in smaller bias and less dispersion in DIC measurements. On the other hand, Crammonde et al. [33] objected that global parameters, such as MIG, are not sufficient to evaluate strain accuracy. Based on their findings, simple means of a randomness assessment is to employ the outcomes of the Shannon entropy theory [34].

Cintrón et al. [35] demonstrated that the speckle size should range from 2×4 px for a high accuracy in the strain measurement. The speckle size should have a lower limit according to the study by Sutton et al. [5] of 3×3 px.

In the presented study, various patterns produced by the spraying white / black dots on a contrast background were investigated. In addition, natural textures of various materials were studied as well, to demonstrate their performance. The knowledge of a texture suitability is essential when monitoring existing structures where application of artificial patterns is not possible. To eliminate the impact caused by image acquisition system (such as the distortion of the camera lens, lighting variation, etc.) during the experiment, numerical approach was utilized to investigate the relationship between Shannon entropy, mean intensity gradient, values of correlation coefficient, and error in DIC measurements. The explanation of the mentioned parameters is provided next.

3.1. Normalized Cross-Correlation

Correlation between two signals (also reffered to as cross-correlation) is a standard approach to feature detection and image registration [36–38]). The normalized form of correlation takes into account intensities relative to the highest one, thus eliminating the sensitivity to changes in illumination intensity. However, it does not have a correspondingly simple and efficient frequency domain expression. For this reason, normalized cross-correlation must be computed in a spatial domain and fast spatial domain matching methods had to be developed. Detailed description of cross-correlation equation is beyond the scope of this article. Reader can find it in Barnea et al. [39].

3.2. Mean Intensity Gradient (MIG)

MIG was proposed by Pan et al. [32] as a global parameter for evaluating the quality of a speckle pattern over the entire domain. Both, a mean bias error and standard deviation of measured displacements are influenced by the MIG of the speckle pattern. The speckle pattern with a large MIG is supposed to produce small displacement measurement errors. MIG is defined as

$$\delta_f = \sum_{i=1}^{W}\sum_{j=1}^{H} \left|\nabla \mathrm{f}\left(x_{ij}\right)\right| \frac{1}{W \times H}, \tag{1}$$

where W and H are the image width and height in pixels, $\left|\nabla \mathrm{f}\left(x_{ij}\right)\right| = \sqrt{f_i\left(x_{ij}\right)^2 + f_j\left(x_{ij}\right)^2}$ is the modulus of the local intensity gradient. $f_i\left(x_{ij}\right)$ and $f_j\left(x_{ij}\right)$ are the i- and j-directional intensity derivatives at pixel (x_{ij}) respectively, which can be computed using a central difference algorithm.

3.3. Shannon Entropy

A high Shannon entropy value indicates a high level of texturing, or broadness in the greyscale distribution of the image, beneficial for maximizing the correlation function peak when a correct match has been found. The Shannon entropy parameter is defined as [40]

$$\Psi = \sum_{i=1}^{W}\sum_{i=j}^{H} f(x_{ij}) \log\left(f(x_{ij})\right). \tag{2}$$

4. Assessment of Patterns and Textures

Randomly distributed speckles must not exhibit any preferential directions. High contrasts are required to provide sharp peaks in the correlation function. To test this requirement, initial synthetic tests on samples of 400×400 px were performed on six model patterns (Figure 2). The patterns / textures were tested with respect to four quality indicators: value of cross-correlation coefficient for two different subset sizes (10×10 px and 30×30 px), Shannon entropy, and MIG. The summary of the investigated patterns and textures is provided in Table 1.

Based on the values of normalized cross-correlation functions presented in the form of surface plots in Figures 3 and 4, it can be concluded that the correlation function peaks can be highlighted by setting bigger subset size since these contain more distinct features. Especially in the case of small subset size, 10×10 px, the correlation peaks on coarse textures could not be clearly identified. This could lead to huge errors of DIC measurements in the case of significantly distorted images. However, the findings cannot be generalized, since in some patterns the cross-correlation correlation function does not exhibit any distinct peak

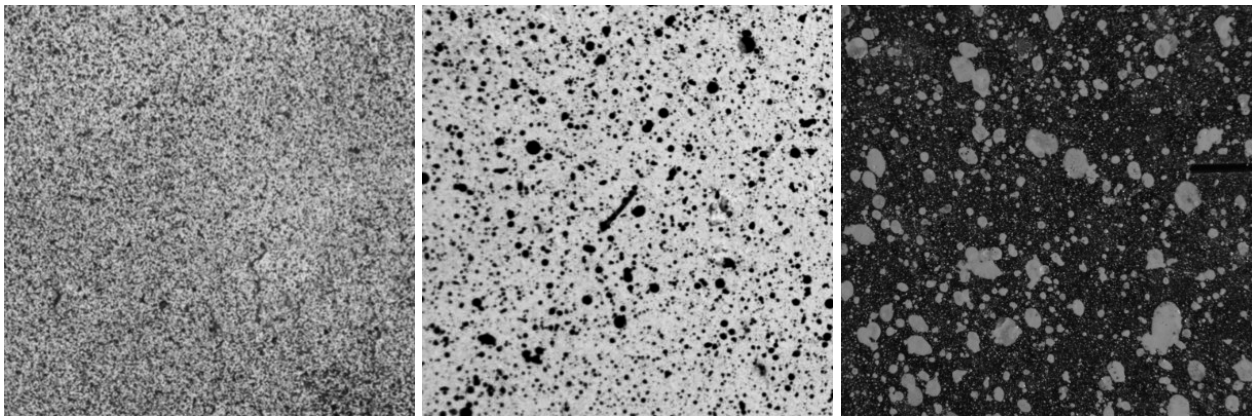

(A) . fine spray pattern (B) . coarse air-brush pattern (C) . white sprayed dots

(D) . natural texture of concrete (E) . masonry wall (F) . texture of wood

Figure 2. Investigated artificial patterns (top) and natural textures (bottom).

in for small subsets, while correlation of the larger one results in unique match and low value of mean correlation coefficient (cf. Figures 3(b,f), 4(b,f), and Table 1). Therefore, the pattern assessment based on the the mean value of the cross-correlation function must be carried out for any subset size independently. Moreover, a statistical information about number of peaks in the form of a decay in the power law distribution would provide more accurate description.

Based on observation of distribution of correlation coefficient a power law distribution can be assumed (Figure 5, 6). The power law function is defined by equation $y_p = x_p^{-\alpha}$, where α is the decay parameter which provides information about the distribution of correlation coefficient over the investigated domain. Larger α indicates smaller amount of unwanted correlation peaks which is desirable.

It is also clear that neither Shannon entropy nor MIG are capable of providing clear indication of the pattern quality since these two are not in agreement — once the pattern is, relative to other ones, regarded as superior to others based on Shannon entropy, MIG provides completely different results, see Table 1. Therefore, new more universal criteria taking into account size, contrast, and size-distribution of speckles should be proposed.

5. Virtual Stretching of Patterns and Textures

The artificial patterns and natural textures were tested in the proof-of-concept experiments carried out virtually on a computer by prescribing a constant deformation. Special attention was paid to the ability of the pattern to provide high-accuracy measurements at deformations reaching 5%, at which poor patterns fail [41].

The evaluation and testing of patterns was performed using own MATLAB scripts by placing virtual extensometers at the edges of the tested samples. In this initial study the images containing 8-bit speckle patterns were virtually stretched up to 5% in 10 steps. Image sequences were then evaluated in open-source 2D-DIC software package Ncorr [10] with the same setting of parameters. Subset sizes of 10 px and 30 px were chosen to demonstrate the correlation between the mean correlation coefficient mentioned in the Section 4 and measurement errors.

As the number of speckles within the patterns increased, the measurement errors decreased. Moreover, larger sized speckles provided lower error than patterns with smaller speckles. Global pattern quality parameters were discussed and Shannon entropy was used as an example to demonstrate that the global measures are not sufficient to assess the quality and

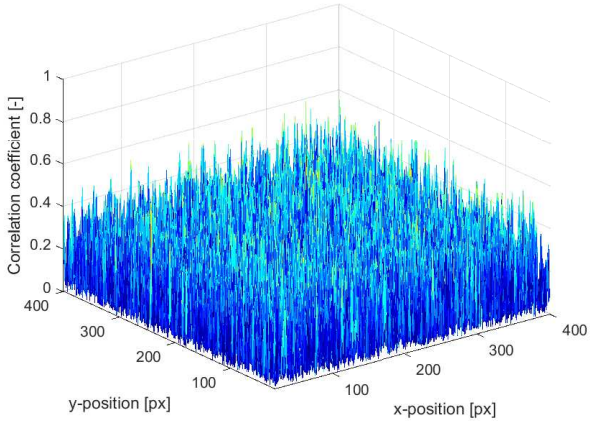

(A) . fine spray pattern

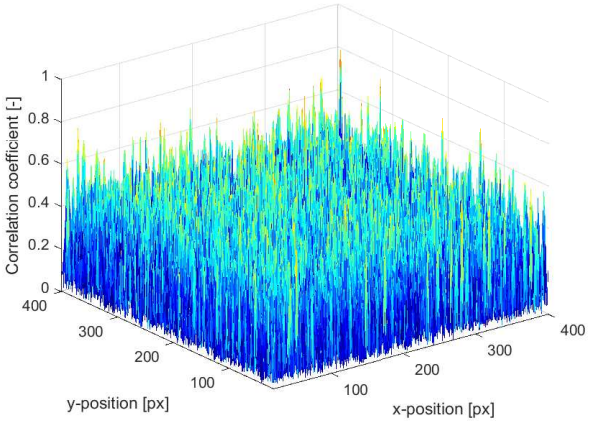

(B) . coarse air-brush pattern

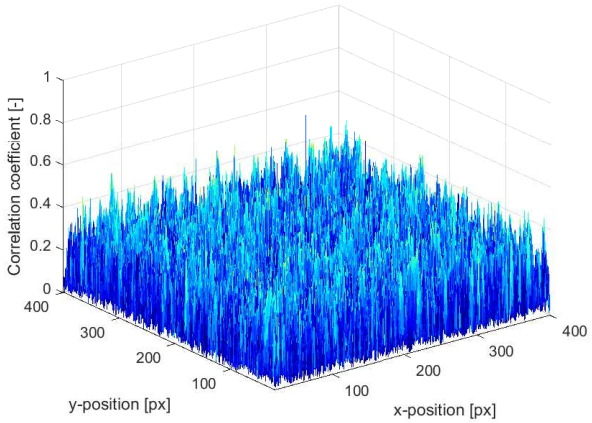

(C) . white sprayed dots

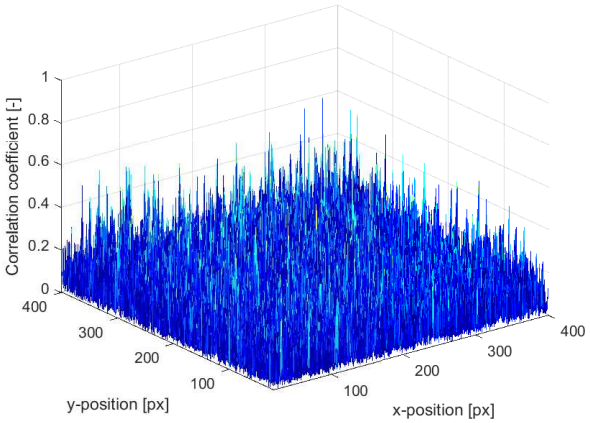

(D) . natural texture of concrete

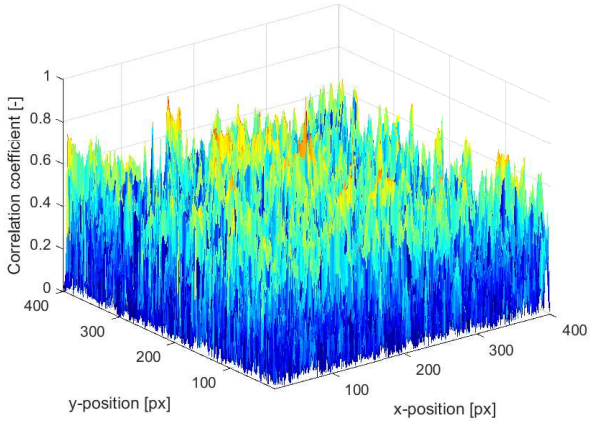

(E) . masonry wall

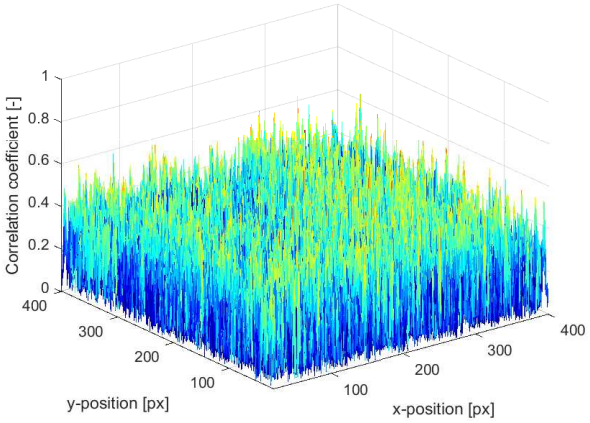

(F) . texture of wood

FIGURE 3. Correlation function values for 10×10 px subset size.

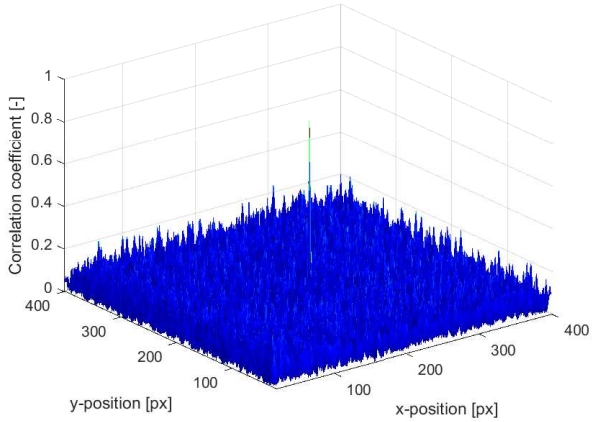

(a) . fine spray pattern

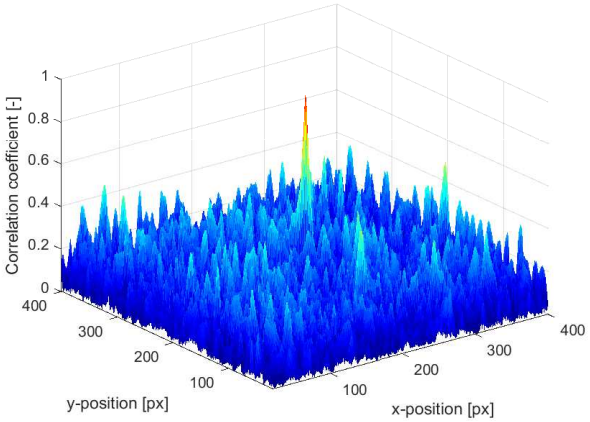

(b) . coarse air-brush pattern

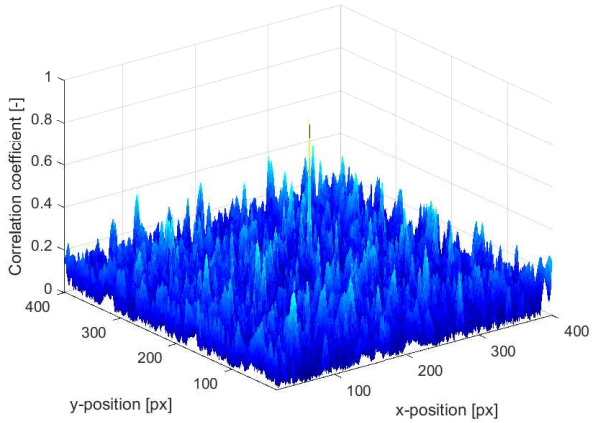

(c) . white sprayed dots

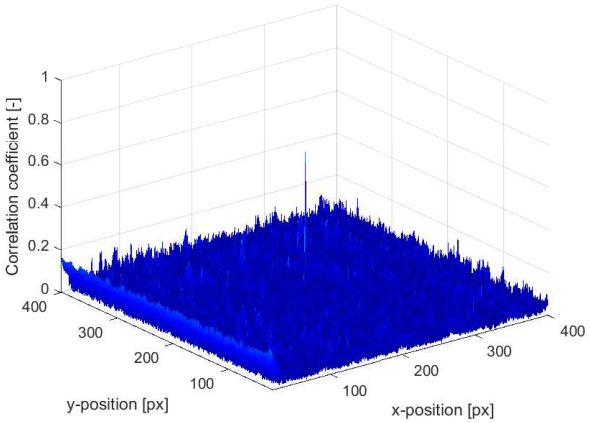

(d) . natural texture of concrete

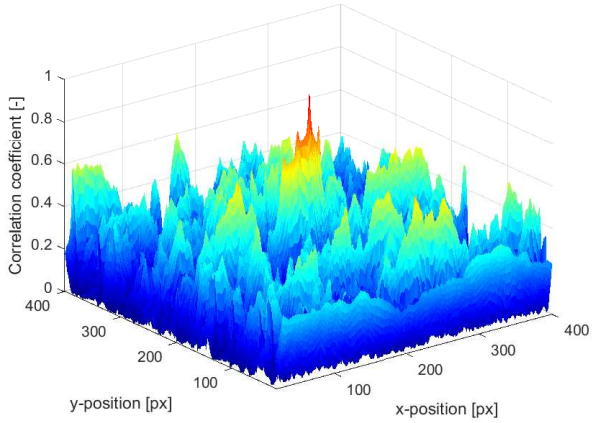

(e) . masonry wall

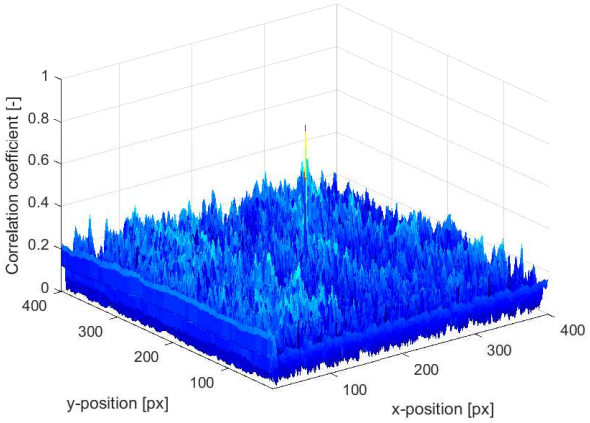

(f) . texture of wood

Figure 4. Correlation function values for 30×30 px subset size.

Sample	$\overline{\gamma(x_{ij})}$		α		Ψ	δ_f
	10×10	30×30	10×10	30×30		
Fine spray pattern (a)	0.152	0.054	0.847	0.959	5.524	121.182
Coarse air-brush pattern (b)	0.190	0.107	1.009	1.046	5.413	127.614
White spray dots (c)	0.089	0.138	1.148	0.997	4.972	82.198
Natural texture of concrete (d)	0.090	0.039	1.027	0.975	6.292	75.849
Masonry wall (e)	0.200	0.187	0.879	0.939	4.250	50.914
Texture of wood (f)	0.208	0.097	0.878	0.981	5.012	29.027

TABLE 1. Mean correlation coefficient, $\overline{\gamma(x_{ij})}$, power law distribution decay parameter α, Ψ, and δ_f for tested patterns / textures and different size of subsets.

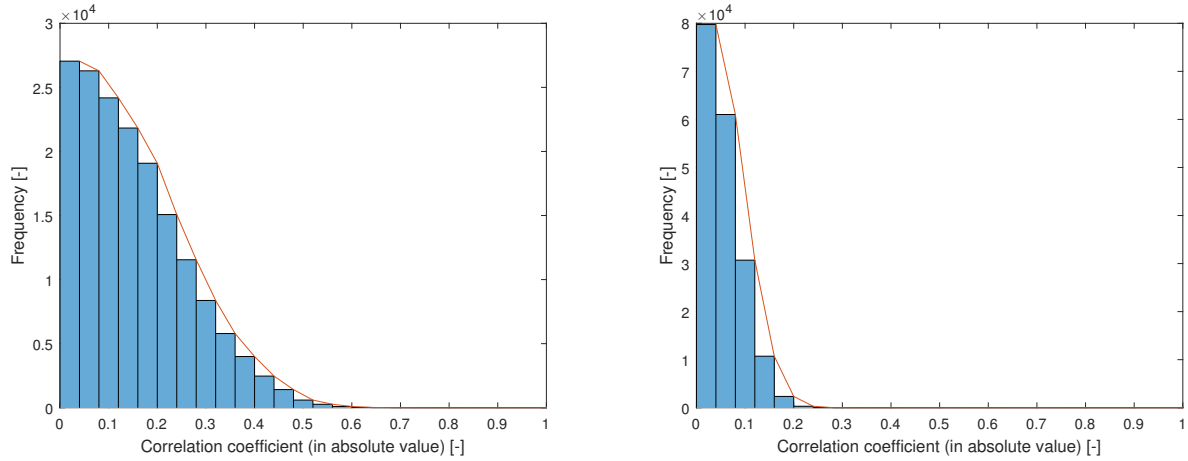

(A) . subset 10×10 px ($\alpha = 0.847$) (B) . subset 30×30 px ($\alpha = 0.959$)

FIGURE 5. Distribution of correlation coefficient, fine spray pattern.

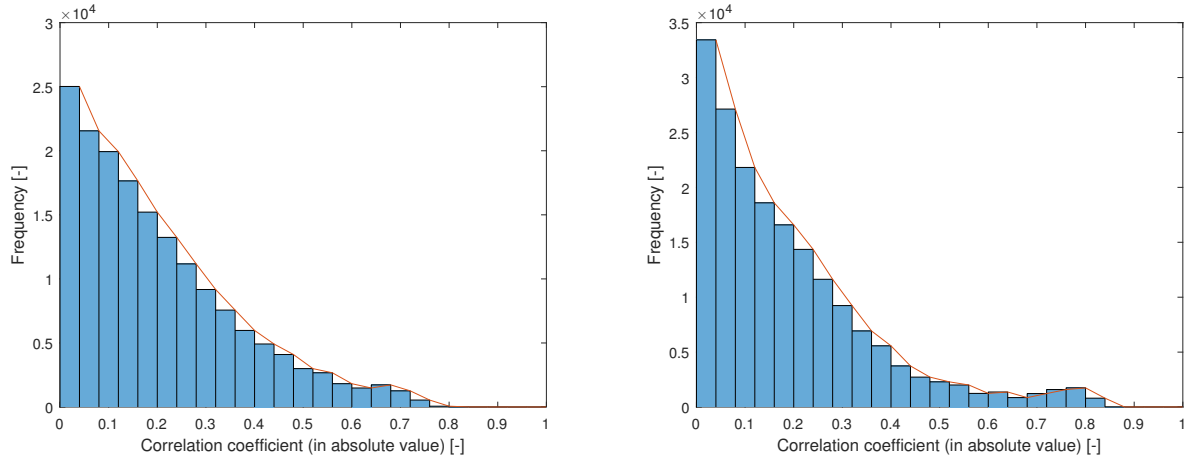

(A) . subset 10×10 px ($\alpha = 0.879$) (B) . subset 30×30 px ($\alpha = 0.939$)

FIGURE 6. Distribution of correlation coefficient, masonry wall.

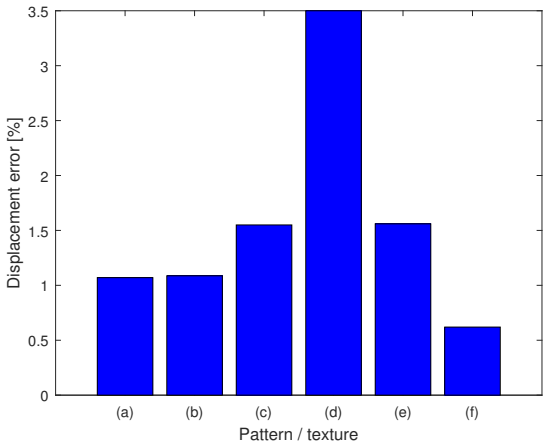

(A) . 1% deformation

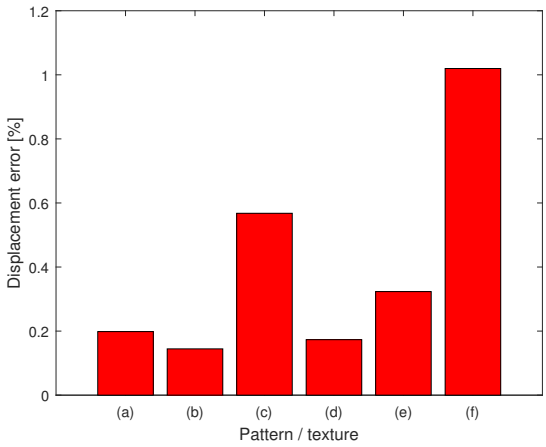

(B) . 5% deformation

Figure 7. Displacement error for 10×10 px subset size.

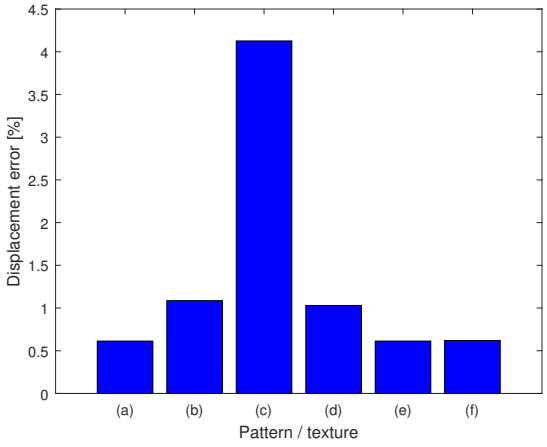

(A) . 1% deformation

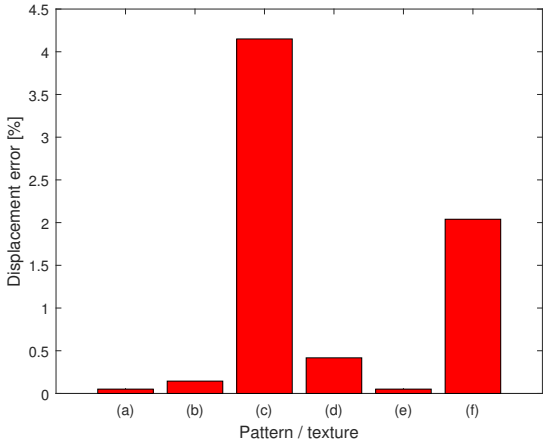

(B) . 5% deformation

Figure 8. Displacement error for 30×30 px subset size.

properties of the patterns. This is illustrated by comparing errors at different stretching magnitude for different speckle sizes (Figure 7 and 8).

6. Conclusions

Based on the research of Crammond et al. [33] and outcomes of the presented study it can be concluded that multi-criteria approach has to be addressed. So far it appears that a combination of Shannon entropy and evaluation of decay in power law distribution of correlation coefficient values provide the most accurate estimate of a pattern performance. Moreover, the speckle-size histogram analysis will be carried out in future to provide new, hopefully more reliable, assessment criteria.

Acknowledgements

This work was financially supported by Czech Technical University in Prague – SGS project SGS17/043/OHK1/1T/11.

References

[1] C. A. Sciammarella, F. M. Sciammarella. *Experimental Mechanics of Solids*. Wiley-Blackwell, 2012. doi:10.1002/9781119994091.

[2] T. Yoshizawa (ed.). *Handbook of Optical Metrology*. Informa UK Limited, 2015. doi:10.1201/b18328.

[3] K. H. Laermann (ed.). *Optical Methods in Experimental Solid Mechanics*. Springer Nature, 2000. doi:10.1007/978-3-7091-2586-1.

[4] J. Périé, S. Calloch, C. Cluzel, F. Hild. Analysis of a multiaxial test on a c/c composite by using digital image correlation and a damage model. *Experimental Mechanics* **42**(3):318–328, 2002. doi:10.1007/bf02410989.

[5] H. Schreier, J. Orteu, M. Sutton. *Image Correlation for Shape, Motion and Deformation Measurements*. Springer Nature, 2009. doi:10.1007/978-0-387-78747-3.

[6] V. Nežerka, J. Antoš, T. Sajdlová, P. Tesárek. Use of open source DIC tools for analysis of multiple cracking in fiber-reinforced concrete. *Applied Mechanics and Materials* **827**:336–339, 2016. doi:10.4028/www.scientific.net/amm.827.336.

[7] F. Chiang. Super-resolution digital speckle photography for micro/nano measurements. *Optics and Lasers in Engineering* **47**:274–279, 2009.

[8] B. Pan, K. Qian, H. Xie, A. Asundi. Two-dimensional digital image correlation for in-plane displacement and strain measurement: a review. *Measurement Science and Technology* **20**(6):062001, 2009. DOI:10.1088/0957-0233/20/6/062001.

[9] K. Triconnet, K. Derrien, F. Hild, D. Baptiste. Parameter choice for optimized digital image correlation. *Optics and Lasers in Engineering* **47**(6):728–737, 2009. DOI:10.1016/j.optlaseng.2008.10.015.

[10] J. Blaber, B. Adair, A. Antouniou. Ncorr: Open-source 2d digital image correlation matlab software. *Experimental Mechanics* **55**:1105–1122, 2015. DOI:10.1007/s11340-015-0009-1.

[11] B. Pan, A. Asundi, H. Xie, J. Gao. Digital image correlation using iterative least squares and pointwise least squares for displacement field and strain field measurements. *Optics and Lasers in Engineering* **47**(7-8):865–874, 2009. DOI:10.1016/j.optlaseng.2008.10.014.

[12] F. Lagattu, J. Brillaud, M. Lafarie-Frenot. High strain gradient measurements by using digital image correlation technique. *Materials Characterization* **53**(1):17–28, 2004. DOI:10.1016/j.matchar.2004.07.009.

[13] T. Proulx (ed.). *Application of Imaging Techniques to Mechanics of Materials and Structures, Volume 4*. Springer New York, 2013. DOI:10.1007/978-1-4419-9796-8.

[14] J. Fish, T. Belytschko. *A First Course in Finite Elements*. Wiley-Blackwell, 2007. DOI:10.1002/9780470510858.

[15] D. L. Logan. *A First Course in the Finite Element Method*. Chris Carson, 2007.

[16] P. Cheng, M. Sutton, H. Schreier, S. McNeill. Full-field speckle pattern image correlation with b-spline deformation function. *Experimental Mechanics* **42**(3):344–352, 2002. DOI:10.1177/001448502321548445.

[17] G. Besnard, F. Hild, S. Roux. "finite-element" displacement fields analysis from digital images: Application to portevin–le châtelier bands. *Experimental Mechanics* **46**(6):789–803, 2006. DOI:10.1007/s11340-006-9824-8.

[18] L. Wittevrongel, P. Lava, S. V. Lomov, D. Debruyne. A self adaptive global digital image correlation algorithm. *Experimental Mechanics* **55**(2):361–378, 2014. DOI:10.1007/s11340-014-9946-3.

[19] P. J. Withers. Strain measurement by digital image correlation. *Strain* **44**(6):421–422, 2008. DOI:10.1111/j.1475-1305.2008.00556.x.

[20] B. Pan, H. Xie, Z. Wang, et al. Study on subset size selection in digital image correlation for speckle patterns. *Optics Express* **16**(10):7037, 2008. DOI:10.1364/oe.16.007037.

[21] P. Bing, X. Hui-min, X. Bo-qin, D. Fu-long. Performance of sub-pixel registration algorithms in digital image correlation. *Measurement Science and Technology* **17**(6):1615–1621, 2006. DOI:10.1088/0957-0233/17/6/045.

[22] S. Yaofeng, J. H. Pang. Study of optimal subset size in digital image correlation of speckle pattern images. *Optics and Lasers in Engineering* **45**(9):967–974, 2007. DOI:10.1016/j.optlaseng.2007.01.012.

[23] H. W. Schreier, M. A. Sutton. Systematic errors in digital image correlation due to undermatched subset shape functions. *Experimental Mechanics* **42**(3):303–310, 2002. DOI:10.1007/bf02410987.

[24] H. W. Schreier. Systematic errors in digital image correlation caused by intensity interpolation. *Optical Engineering* **39**(11):2915, 2000. DOI:10.1117/1.1314593.

[25] P. Hung, A. S. Voloshin. In-plane strain measurement by digital image correlation. *Journal of the Brazilian Society of Mechanical Sciences and Engineering* **25**(3), 2003. DOI:10.1590/s1678-58782003000300001.

[26] Y. Q. Wang, M. A. Sutton, H. A. Bruck, H. W. Schreier. Quantitative error assessment in pattern matching: Effects of intensity pattern noise, interpolation, strain and image contrast on motion measurements. *Strain* **45**(2):160–178, 2009. DOI:10.1111/j.1475-1305.2008.00592.x.

[27] M. e. a. Bornert. Assessment of digital image correlation measurement errors: Methodology and results. *Experimental Mechanics* **49**(3):353–370, 2008. DOI:10.1007/s11340-008-9204-7.

[28] J. Dupré, M. Bornert, L. Robert, B. Wattrisse. Digital image correlation: displacement accuracy estimation. *EPJ Web of Conferences* **6**:31006, 2010. DOI:10.1051/epjconf/20100631006.

[29] B. Pan, K. Qian, H. Xie, A. Asundi. On errors of digital image correlation due to speckle patterns. In X. He, H. Xie, Y. Kang (eds.), *ICEM 2008: International Conference on Experimental Mechanics 2008*. SPIE-Intl Soc Optical Eng, 2008. DOI:10.1117/12.839326.

[30] T. Hua, H. Xie, S. Wang, et al. Evaluation of the quality of a speckle pattern in the digital image correlation method by mean subset fluctuation. *Optics & Laser Technology* **43**(1):9–13, 2011. DOI:10.1016/j.optlastec.2010.04.010.

[31] C. Lane, R. L. Burguete, A. Shterenlikht. An objective criterion for the selection of an optimum dic pattern and subset size. In *Proceedings of the SEM XI international congress and exposition on experimental and applied mechanics*. 2008.

[32] B. Pan, Z. Lu, H. Xie. Mean intensity gradient: An Effective global parameter for quality assessment of the speckle patterns used in digital image correlation. *Optics and Lasers in Engineering* **48**:469–477, 2010.

[33] G. Crammond, S. W. Boyd, J. M. Dulieu-Barton. Speckle pattern quality assessment for digital image correlation. *Optics and Lasers in Engineering* **51**(12):1368–1378, 2013. DOI:10.1016/j.optlaseng.2013.03.014.

[34] C. E. Shannon. A mathematical theory of communication. *Bell System Technical Journal* **27**(3):379–423, 1948. DOI:10.1002/j.1538-7305.1948.tb01338.x.

[35] R. Cintrón, V. Saouma. Strain measurements with the digital image correlation system vic-2d, report cunees-08-06. Tech. rep., NEES at CU Boulder, 2008.

[36] O. Duda, E. H. Peter. Pattern classification and scene analysis. *Artificial Intelligence* **4**(2):139–143, 1973. DOI:10.1016/0004-3702(73)90004-0.

[37] R. C. Gonzalez, R. E. Woods, B. R. Masters. Digital image processing, third edition. *Journal of Biomedical Optics* **14**(2):029901, 2009. DOI:10.1117/1.3115362.

[38] R. Brunelli, T. Poggio. Face recognition: features versus templates. *IEEE Transactions on Pattern Analysis and Machine Intelligence* **15**(10):1042–1052, 1993. DOI:10.1109/34.254061.

[39] D. I. Barnea, H. F. Silverman. A class of algorithms for fast digital image registration. *IEEE Transactions on Computers* **C-21**(2):179–186, 1972. DOI:10.1109/tc.1972.5008923.

[40] D. Lecompte, S. Bossuyt, S. Cooreman, et al. Study and generation of optimal speckle patterns for dic. In *Proceedings of the SEM annual conference and exposition on experimental and applied mechanics*. 2007.

[41] G. Stoilov, V. Kavardzhikov, D. Pashkouleva. A comparative study of random patterns for digital image correlation. *Journal of Theoretical and Applied Mechanics* **42**:55–66, 2012.

Appendix E

J. Antoš, **V. Nežerka**, and M. Somr, Real-time optical measurement of displacements using subpixel image registration, *Experimental Techniques* 43 (2019) 315–323, doi: 10.1007/s40799-019-00315-1

Author's contribution: main idea, supervision, data analysis, programming.

Experimental Techniques (2019) 43:315–323
https://doi.org/10.1007/s40799-019-00315-1

Real-Time Optical Measurement of Displacements Using Subpixel Image Registration

J. Antoš[1] · V. Nežerka[1] · M. Somr[1]

Received: 7 August 2018 / Accepted: 14 February 2019 / Published online: 22 March 2019

Abstract
An open-source tool for real-time measurement of relative displacements based on image registration is presented. The use of upsampled matrix-multiplication discrete Fourier transform and measurement limited to predefined points of interest by virtual extensometers allows high sampling frequencies with a subpixel accuracy. This solution was designed primarily for laboratory testing in order to eliminate the problem with inaccurate measurement of cross-head displacement due to compliance of testing frames and difficulties connected to the attachment of strain-gauges or extensometers. However, the portable hardware allows for outdoor applications in which remote monitoring of displacements and deformations is required. The accuracy of the system was assessed, and the software was successfully verified through experimental testing.

Keywords Image registration · Virtual extensometers · Real-time · Optical measurement · Displacements

Introduction

Digital image correlation (DIC) algorithms became indispensable when monitoring and analyzing the development of displacement or strain fields in time by matching a stochastic pattern of deformed images with respect to a reference one. Unlike conventional measurement techniques, the DIC is capable of capturing strain localization on a surface of a loaded structure or specimen at any location within the observed region of interest (ROI) and in any direction [1, 2]. More over, the DIC-based measurement can be more accurate than monitoring using extensometers or strain-gauges that can suffer from fatigue [3], imperfect attachment to the measured surface [4, 5], or influence the behavior of tested specimens [6]. Employing this advanced tool can significantly reduce the cost of experiments for its easy preparation and smaller consumption of auxiliary material or components. The boom of the DIC has been reflected by the emergence of new commercial and open-source software packages to perform calculations with differently optimized correlation functions and calculation methods, most recently summarized by Pan et al. [7].

To ensure an accurate correlation, a random homogeneous pattern must be applied, if not present naturally, to the observed surface to provide grey-level variations so that shifts of any subset of points can be evaluated. The evaluation is accomplished by minimizing the correlation function using a chosen optimization algorithm [8–11]. The position differences between reference and target subsets yield the in-plane displacement vector [12]. As the size of subsets decreases, the uncertainty in the measurement increases due to a reduction in the number of features to track [13]. Therefore, the resolution of the calculated displacement/deformation fields and the DIC precision are limited by the image resolution. Besides the factors influencing the accuracy of image correlation, the DIC measurements can be influenced by the entire surrounding environment. As suggested by Reu [14], lens distortions, changes in camera temperature, and camera or sample motion can introduce the most significant inaccuracies during image acquisition if not prevented.

Despite the rapid emergence of advanced turnkey commercial DIC systems during the last two decades [15], a simple open-source DIC tool for real-time monitoring displacements has not been available. The proposed solution offers real-time measurement of displacements in 2D at predefined locations by using virtual extensometers, being a couple of pixel subsets.

✉ V. Nežerka
vaclav.nezerka@fsv.cvut.cz

[1] Faculty of Civil Engineering, Czech Technical University in Prague, Thákurova 7, 166 29 Praha 6, Czech Republic

The developed open-source software utilizes algorithms based on discrete Fourier transform (DFT) optimized for fast evaluation of subset translations with subpixel accuracy. It is worth mentioning that real time 3D positioning and tracking systems have been developed [16], but these require much more sophisticated equipment, skilled operators, and to the best of our knowledge their use is limited to laboratory conditions.

Hardware

The real-time measurement system consists of three fundamental elements: a camera, a communication channel (cable or wireless), and a computer. There are several requirements on the camera, including high resolution, low digital noise, and a long lifetime period. The last requirement rules out reflex cameras that have a limited lifespan regarding the number of acquired images. On the other hand, cameras equipped with monochrome CMOS (complementary metal-oxide semiconductor) chips allow for obtaining the same or higher spatial resolution with the satisfying sensitivity at a lower price. The communication channel should not be the weakest link in the system; commonly used USB 3.x or Ethernet cables are sufficient and reliable.

Besides these basic components, a strong illumination is recommended to reduce digital noise by allowing a high signal to noise ratio. High levels of illumination also enable a reduction in a lens diaphragm opening by setting lower f-number (aperture), resulting in a higher depth of field for the acquired images. This is particularly advantageous if the observed surface is uneven. Moreover, a sufficient exposure can be reached at higher shutter speed, providing blur-free images at higher displacement/deformation rates.

The design and quality of optical lenses also play a crucial role in providing high-quality undistorted images. Optical aberration results in non-uniform geometric distortions of images and introduces additional errors in the measurement [17]. Short objective lenses are not suitable for DIC because of large distortions at the edges of acquired images [18–20]. A perfectly orthographic view can be achieved using telecentric lenses [21], but even in the orthographic view out-of-plane deformations caused by rotations of an observed object cause errors in 2D-DIC and should be avoided [22, 23].

Algorithms and Program Work Flow

The software tool RTCorr (Real-Time Correlation) for real-time optical measurement of displacements was developed in Python 3.6. It offers a user-friendly graphical user interface (GUI), see Fig. 1 enabling placement and management of virtual extensometers, setting DIC parameters, and export of data. In addition, it provides information about the camera chip temperature and allows for precise focusing by calculation of a mean intensity gradient [24, 25], defined as

$$\Psi_f = \sum_{i=1}^{W} \sum_{j=1}^{H} |\nabla f(x,y)| \frac{1}{WH}, \tag{1}$$

where $|\nabla f(x,y)| = \sqrt{f_x(x,y)^2 + f_y(x,y)^2}$, in which $f_x(x,y)$ and $f_y(x,y)$ are the x- and y-directional intensity derivatives at pixel located at (x,y) within the image f, respectively. W and H are the image width and height, respectively. After zooming to a region of interest, maximizing Ψ leads to a perfect camera focus, see the demonstration in Fig. 2.

Sub-Pixel Registration

RTCorr employs the upsampled matrix-multiplication discrete Fourier transform (DFT), proposed by Guizar-Sicairos et al. [26], to reach subpixel accuracy of aligning subsets. Using this approach, cross-correlation for each square subset of pixels of a side length N is accomplished in a frequency domain [27, 28]. The utilization of Fourier transform renders the registration computationally efficient [29] and insensitive to optical noise or changes in illumination [30, 31]. Unlike the majority of DIC software, based on determining locations of reference subsets within current images, the subsets in RTCorr are fixed and represent an imaginary window through which a motion of the underlying pattern is observed. Since the pixel subsets are registered by phase retrieval, only their translation is evaluated, and the displacement field is averaged over the subset area.

The employed registration algorithm is capable of computing subset shifts within a fraction of a pixel, $1/\kappa$. The difference between the pixel and subpixel accuracy of results is clearly illustrated in Fig. 3 on an example of a 2D displacement field, calculated considering $\kappa = 1$ px $^{-1}$ (pixel accuracy) and $\kappa = 50$ px $^{-1}$ (subpixel accuracy).

The program is capable of accomplishing simultaneous measurements of relative displacements in 2D using an arbitrary number of virtual extensometers, equivalent to physical ones. A full-field 2D DIC analysis can be carried out once the measurement is finished from the acquired images that are saved (if required) to a project folder. The measurement is carried out in pixels, but it can be scaled to physical units. Otherwise, it is carried out in pixels. The collected data are saved on a hard drive during the measurement so that they cannot be lost in the case of a software crash. The saved data include time steps, displacements of extensometer ends and relative displacements, calculated as the ratio of an extensometer extension to its length.

The source files and manual with a thorough description of the program structure and GUI controls are provided at GitHub.[1]

[1] https://github.com/jacobantos/RTCorr

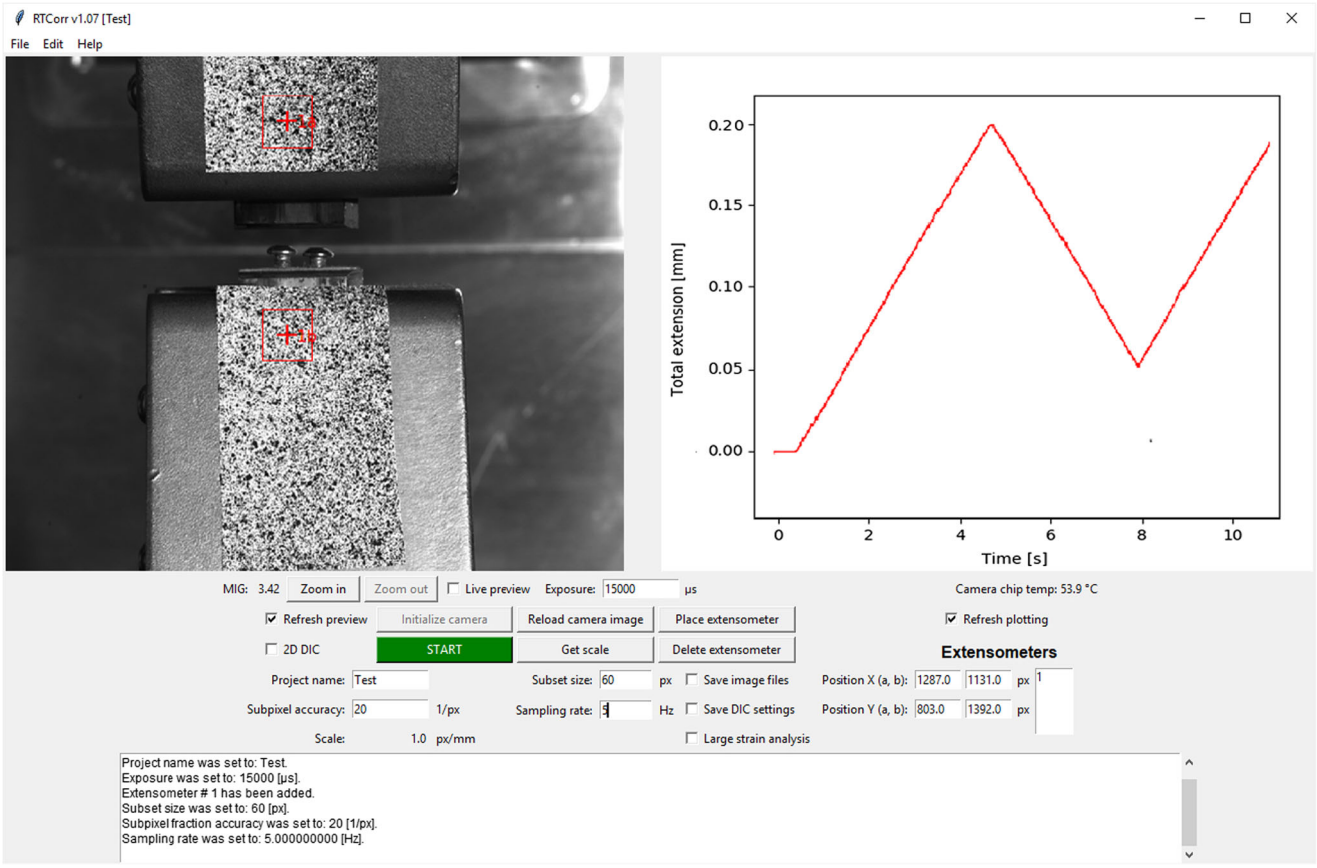

Fig. 1 Graphical user interface of RTCorr v1.07

Registration of Large Displacements

In the small-displacement mode, reaching up to about 1/4 N, the shift of subsets Δu at a time T is calculated by comparing their configuration with the one in a reference image acquired at $T = 0$, so that

$$\mathbf{u}(T) = \Delta u(0, T). \tag{2}$$

RTCorr also offers a large-displacement mode, in which the shift is calculated as

$$u(T) = \Delta u(T{-}1, T) + u(T{-}1). \tag{3}$$

By relating the subsets at time T to their configuration at $T - 1$, an arbitrary displacement can be tracked, limited only by the ROI size. However, the displacement of a subset between T and $T - 1$ still should not exceed the value of 1/4 N. The large-displacement mode should be used only if needed because summing the measured shifts may result in accumulating measurement errors.

The small-displacement mode is analogic to the Eulerian approach to observing motion of a body [32]. In this mode the deformed and shifted image flows through the fixed extensometers. In the large-displacement mode the extensometers deform with the underlaying image and their position is updated for each frame, analogically to the Lagrangian approach

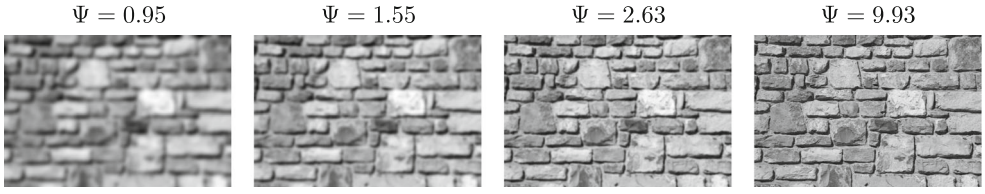

Fig. 2 Dependence of the mean intensity gradient on a camera focus

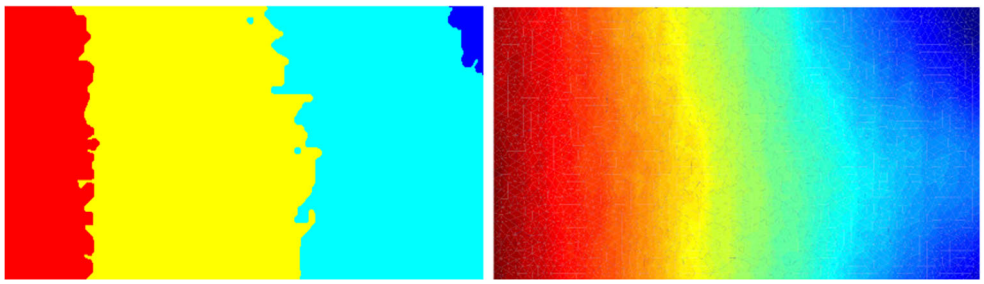

Fig. 3 Illustration of pixel (left) and subpixel (right) accuracy of displacements ranging between 0.2 and 3.7 pixels on results of a direct tensile test

Table 1 Computers used for the performance tests; the abbreviations in parentheses are used in the following figures

Computer	CPU (CPU cores)	π_{10^6} test	Operating system
Laptop Lenovo T440 (L1)	Intel i5-4200 U, 1.6 GHz (4)	72.91 s	Ubuntu 18.04.1
Laptop Lenovo T480 (L2)	Intel i5-8250 U, 1.6 GHz (8)	52.31 s	Ubuntu 18.04.1
Custom-built desktop (D1)	Intel i3-8350 K, 4.4 GHz (4)	44.34 s	Ubuntu 18.04.1
Desktop Dell T1600 (D2)	Intel Xeon E31280, 3.5 GHz (8)	51.69 s	Ubuntu 18.04.1

[33]. This allows for evaluating displacements exceeding the subset size and severe deformations of subsets.

Testing and Validation

The testing and validation were primarily accomplished on a laptop computer equipped with the Intel i5-4200 U CPU, 4 GB RAM, and 500 GB SSD hard drive. Besides, performance tests were carried out on three different computers, listed in Table 1; CPU $\pi_{10^6}\kappa$ test score refers to a time needed to computing 10^6 digits of π using SymPy package in Python. All the computers were equipped with a USB 3.1 hub. The performance test was focused on the impact of CPU, but the influence of drive type (HDD vs. SSD) and RAM size was also tested. The analysis ruled out th to see that they have no impact on the performance of RTCorr.

The images were taken using a Ximea MC050MG-SY monochromatic camera, equipped with a 3.45 × 3.45 × m pixel-size CMOS sensor capable of delivering 76 frames per second at a 5 Mpx resolution. Low distortion was ensured by using a Kowa LM50HC C-mount objective lens with a fixed focal length of 50 mm. Using long objective lenses is favorable to reduce the distortions if telecentric lenses are not available. The data transfer was accomplished using a USB 3.1 cable.

With the specified hardware available and setting of DIC parameters as $N = 132$ and $\kappa = 128$, the maximum sampling frequency ν reached for a single extensometer with RTCorr during a 10-min monitoring was equal to 7.65 ± 0.03 Hz, see Fig. 4. Only the desktop computer D2, equipped with a USB 3.1 PCI-e card instead of a native USB 3.1 port, reached the maximum sampling frequency of 6.35 ± 0.02 Hz. This indicates that the data transfer limits the software performance if the image registration is not demanding (low number of virtual extensometers or small values of N or κ as demonstrated next). After reaching the threshold at which the CPU became limiting, ν decreased at a rate depending on the CPU speed.

Measurement Bias

A static test with a perfectly fixed specimen was performed in order to assess the systematic error of the measurement system. The monitored random pattern, consisting of black speckles ranging approximately between 0.05 and 2 mm in diameter, was applied to an illuminated white wall. LED lights with a constant current driver were used provide flicker-free illumination. The distance between the camera and the observed surface was 50 cm, yielding a scaling factor of 22.89 px/mm.

The study was focused on the impact of a subset size N and the required subpixel accuracy κ on measurement errors and a maximum sampling frequency. The observed random pattern contained speckles small enough so that even the smallest

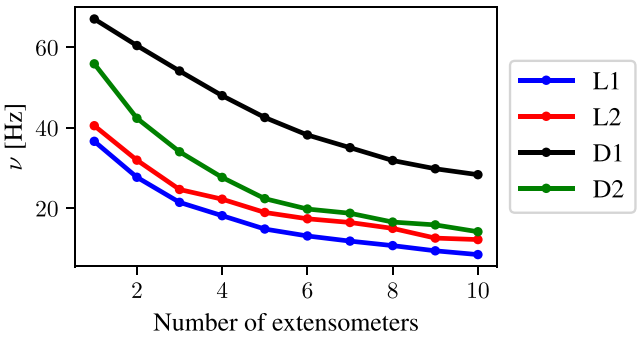

Fig. 4 Relationship between the maximum sampling frequency ν and a number of extensometers with the specified hardware available and setting of DIC parameters as $N = 132$ and $\kappa = 128$

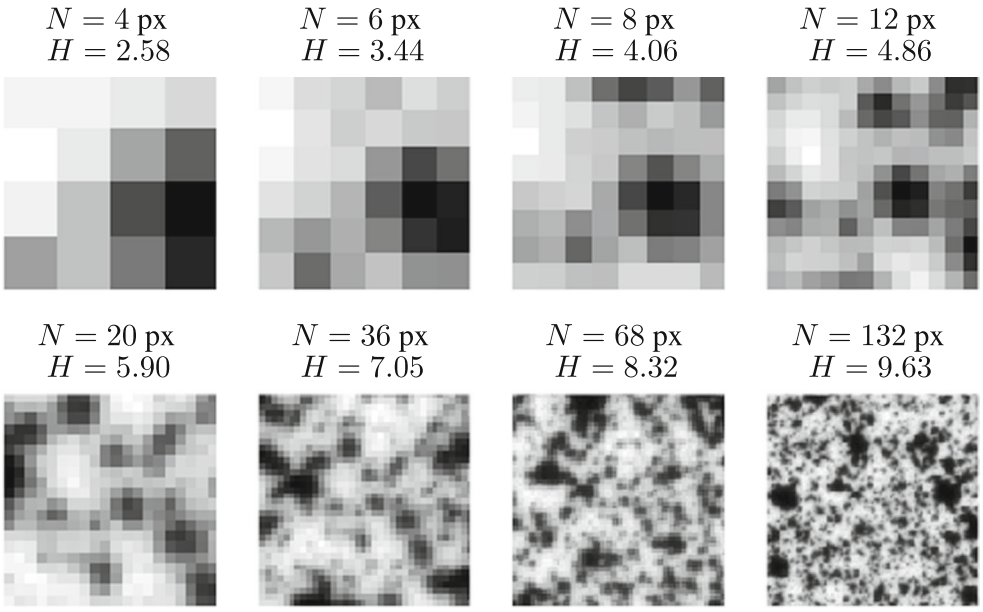

Fig. 5 Studied subsets of various size, $N \times N$, and their entropy, H, being a measure of gray intensity randomness

studied subset of $N = 4$ px was unique in its neighborhood and contained sufficient amount of features to track. With larger N the pattern randomness within subsets increased, as demonstrated by their entropy [34], see Fig. 5. The entropies of the model subsets were calculated as

$$H = -\sum p_k \log_2(p_k), \tag{4}$$

where k is the number of intensity levels within subsets, and p_k is the probability associated with the particular intensity level [35]. The length of a virtual extensometer, i.e., the distance between the centroids of two coupled subsets, was 100 mm. The oscillations of the extensometer extensions were monitored for 10 min at a maximum possible sampling frequency. Themeasurement variation σ was calculated as a standard deviation of relative extensions:

$$\sigma = \sqrt{\frac{\sum_{i=1}^{n} \in_k^2}{n}}, \tag{5}$$

where n is a number of images (measurements) and $\in_k$ is a relative extension of the k^{th} measurement, calculated as the ratio of the extensometer extension to its length, i.e., strain.

The relationships between the both user-defined DIC parameters, N and κ, and the system performance in terms of σ and ν are presented in Figs. 6 and 7. First, $\kappa = 32$ px^{-1} was fixed and the influence of N was tested. Next, $N = 36$ px was fixed and the same procedure was repeated for κ.

Larger subsets contribute to a lower oscillation around the true (zero) extension, and the measurement variation, σ, was very small, around $0{:}8 \times 10^{-5}$, and almost constant for $N > 70$ px. However, increasing the subset size, N, came at a cost of higher demands on CPU resulting in a lower sampling frequency, ν, and

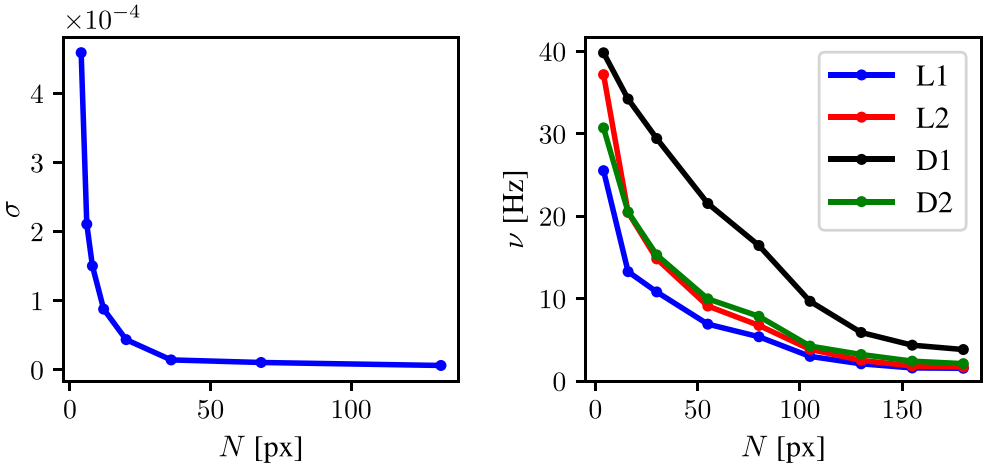

Fig. 6 Relationship between the subset size and the measurement variation of results (left) and the maximum sampling frequency (right); the required subpixel accuracy was fixed at $\kappa = 32$ px^{-1}

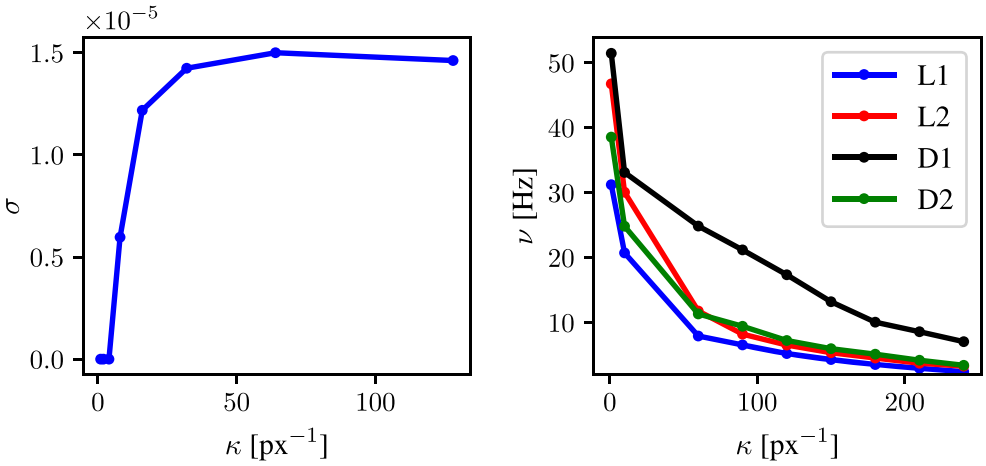

Fig. 7 Relationship between the required subpixel accuracy and the measurement variation of results (left) and the maximum sampling frequency (right); the subset size was fixed at $N = 36$

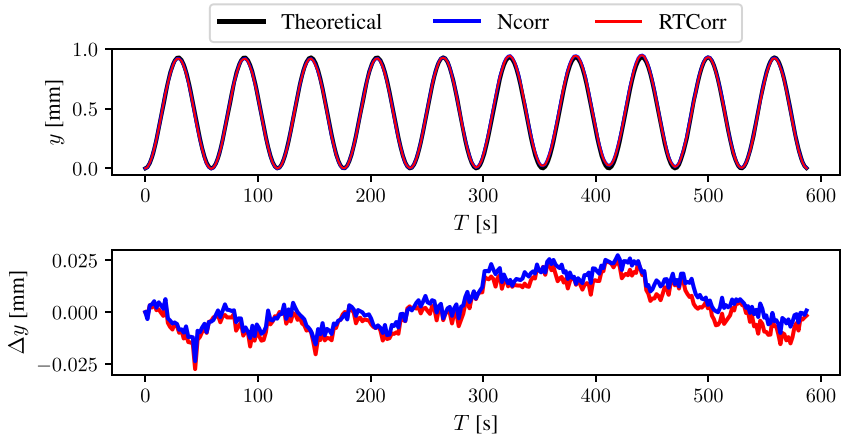

Fig. 8 Comparison of theoretical displacement and results from RTCorr and Ncorr (top) and deviations from a theoretical curve (bottom) in the small-displacement mode

the measured shift was averaged over a larger area. The value of ν for $N > 36$ px was dependent on the CPU speed.

An opposite trend was observed regarding κ. For values of $\kappa < 4$ px^{-1} there was no oscillation in extensions and $\sigma = 0$. The measurement variation stabilized for $\kappa > 40$ px^{-1} at $\sigma \approx 1{:}5 \times 10^{-5}$. The reduction in ν with increasing κ was also dependent on the CPU speed and once the CPU became limiting, ν decreased proportionally to κ.

It may be concluded that for the hardware used and the experimental setup considered here, the optimum setting of the image registration parameters is $N \approx 40$ px and $\kappa \leq 4$ px^{-1} if large displacements are anticipated or $\kappa \geq 60$ px^{-1} for measurement of small displacements where setting of high κ makes sense. The measurement error, σ, appears to be constant beyond these thresholds.

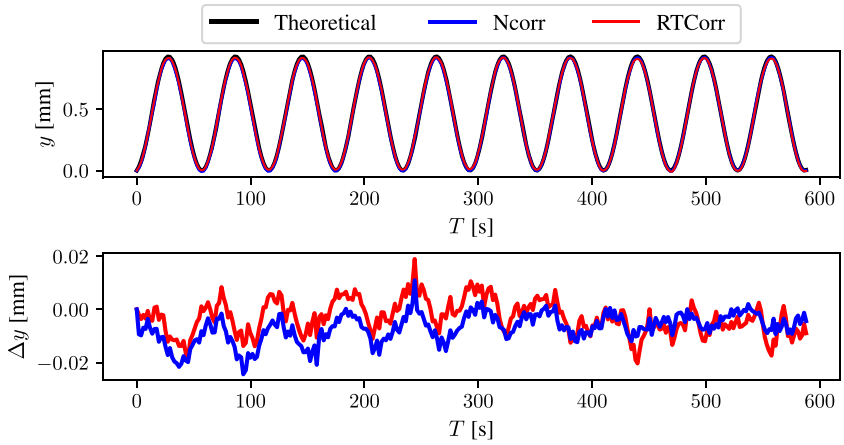

Fig. 9 Comparison of results from RTCorr and Ncorr (top) and deviations from a theoretical curve (bottom) in the large-displacement mode

Experimental Verification

A periodically displaced steel plate with a sprayed random pattern was observed and the vertical motion evaluated in order to verify the measurement procedure thoroughly. The periodic harmonic motion was accomplished using a hydraulic dynamic actuator. The camera was positioned perpendicularly to the observed plane at a distance of 60 cm. The camera was turned on 5 min before the experimental testing in order to reach a saturation temperature and eliminate the error due to the camera self-heating [36]. The correlation parameters were set as $N = 80$ px and $\kappa = 60$ px^{-1}. The displacements were recorded during 10 sine waves having an amplitude of 0.93 mm and frequency 0.017 Hz. The images were saved during the analysis, thus significantly reducing the sampling frequency to approximately 0.5 Hz.

The saved images were collected and used after the test for a calculation of displacements using a DIC software Ncorr. This software was thoroughly tested and validated using distorted synthetic images and analysis of experimental datasets from the SEM 2D-DIC challenge [37, 38]. Ncorr was selected for benchmarking because it is robust, open-source, and accepted by a scientific community [39]. However, the algorithms implemented in Ncorr, based on subset matching in the spatial domain, do not allow for the real-time analysis.

The measurement was carried out twice, separately for the modes for small and large displacements, recall Section 3.2. The comparison of vertical displacement, $y(T)$, evaluated using RTCorr and Ncorr and deviations from the theoretical curves, Δy, are provided in Figs. 8 and 9. The theoretical curves follow the prescribed harmonic displacement function defined as

$$y(T) = 0.93\sin(2\pi 0.017T). \tag{6}$$

There was an almost perfect overlap of curves (theoretical according to equation (6)) and outcomes of Ncorr and real-time measurement using RTCorr), manifesting a high accuracy of the real-time correlation procedure. The Δy plots provide more detailed information about the measurement errors. The encountered discrepancy, in order of 10^{-5} m, between the measured vertical displacements, both by RTCorr and Ncorr, is attributed to asynchronous motion of the observed specimen with respect to the prescribed displacement according to equation (6). More importantly, there is an agreement between RTCorr and Ncorr. The possible error cumulation was not observed in the case of RTCorr measurement in large-displacement mode. However, compared to the small-displacement mode, the disagreement between Ncorr and RTCorr was slightly increased.

Even though RTCorr was primarily developed for and tested during laboratory measurements, it can be exploited for structural health monitoring [40, 41]. To demonstrate that capability, an experimental measurement of bridge deflections under passing trains was carried out. Such a measurement enabled continuous monitoring without affecting both the railway and road traffic. The displacements were recorded from a 11 m distance, yielding a scaling factor of 1.16 px/mm. The sampling frequency was set to 5 Hz for 1 h and the DIC parameters as $N = 70$ px and $\kappa = 20$ px^{-1}. The measurement setup is presented Fig. 10 and the results in Fig. 11. Even though there are no reference data, the maximum deflections correspond to predictions based on previous measure ments. Moreover, there is a proportionality between the train weight and measured deflections. The high sampling frequency allowed to capture also the bridge vibrations after its unloading.

Fig. 10 Real-time measurement of a steel bridge deflection under a 40 t train engine using RTCorr

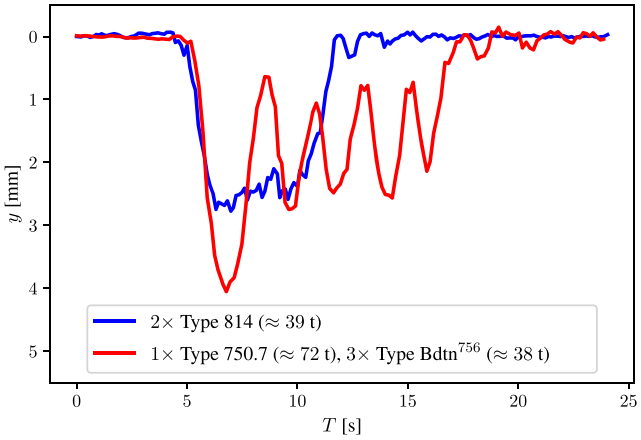

Fig. 11 Bridge deflection due to loading by a passing train measured near the midspan

Conclusion

An optical system for real-time non-contact measurement of displacements offering an arbitrary number of virtual extensometers was presented. In order to reach high sampling rates, an efficient image registration algorithm based on upsampled matrix-multiplication DFT was employed. Using this strategy, sampling frequencies exceeding 3 Hz can be reached with a subpixel accuracy, as demonstrated through an experimental study. After finding an agreement with the outcomes of the established and well-tested DIC software Ncorr, it can be concluded that the proposed measurements system is comparably accurate and reliable.

RTCorr was developed primarily for laboratory measurements to overcome inconveniences connected to the use of strain-gauges or extensometers and to substitute inaccurate cross-head displacement readings. However, such a solution is not limited purely to monitoring or control of laboratory experiments, and it can also be utilized, e.g., for long-term monitoring of structures as demonstrated by a trial monitoring of a railway bridge. The use of RTCorr in biomechanical analyses or automatic quality-control on production lines during non-destructive testing is also envisaged.

Acknowledgments The support by the Technology Agency of the Czech Republic [grant number TACR TJ01000263] and the Faculty of Civil Engineering at CTU in Prague [grant number SGS18/037/OHK1/1 T/11] is gratefully acknowledged.

References

1. Schreier H, Orteu J-J, Sutton MA (2009) Image correlation for shape, motion and deformation measurements. Springer US. https://doi.org/10.1007/978-0-387-78747-3.
2. Nežerka V, Antoš J, Sajdlová T, Tesárek P (2016) Open source DIC tools for analysis of multiple cracking in fiber-reinforced concrete. Appl Mech Mater 827:336–339. https://doi.org/10.4028/www.scientific.net/AMM.827.336.
3. Koval YI, Boiko VI (1980) Reliability of foil strain gauges in multiple cyclic deformations. Strength Mater 12:1047–1050. https://doi.org/10.1007/bf00770540
4. Cho S-D, Lee K-W, Li Z, Kim U-G (2015) Evaluation of reliability of strain gauge measurements for geosynthetics. J Korean Geosynth Soc 14:87–96. https://doi.org/10.12814/jkgss.2015.14.4.087
5. Talebi M, Meehan CL, Poggiogalle TM (2018) Strain in a GRS bridge abutment: strain gauge attachment techniques, performance and survivability during construction and operation, in: IFCEE 2018. Am Soc Civil Eng. https://doi.org/10.1061/9780784481608.025
6. Zike S, Mikkelsen LP (2013) Correction of gauge factor for strain gauges used in polymer composite testing. Exp Mech 54:393–403. https://doi.org/10.1007/s11340-013-9813-7
7. Pan B, Qian K, Xie H, Asundi A (2009) Two-dimensional digital image correlation for in-plane displacement and strain measurement: a review. Meas Sci Technol 47:062001. https://doi.org/10.1088/0957-0233/20/6/062001
8. Gruen AW (1985) Adaptive least squares correlation: a powerful image matching technique. South African journal of photography. Remote Sens Cartogr 14:175–187
9. Altunbasak Y, Mersereau RM, Patti AJ (2003) A fast parametric motion estimation algorithm with illumination and lens distortion correction. IEEE Trans Image Process 12:395–408. https://doi.org/10.1109/tip.2003.809012
10. Pan B, Asundi A, Xie H, Gao J (2009) Digital image correlation using iterative least squares and pointwise least squares for displacement field and strain field measurements. Opt Lasers Eng 47:865–874. https://doi.org/10.1016/j.optlaseng.2008.10.014
11. Pan B, Wang Z, Xie H (2009) Generalized spatial-gradient-based digital image correlation for displacement and shape measurement with subpixel accuracy. J Strain Anal Eng Des 44:659–669. https://doi.org/10.1243/03093247jsa546
12. Pan B, Xie H, Wang Z (2010) Equivalence of digital image correlation criteria for pattern matching. Appl Opt 49:5501–5509. https://doi.org/10.1364/ao.49.005501
13. Triconnet K, Derrien K, Hild F, Baptiste D (2009) Parameter choice for optimized digital image correlation. Opt Lasers Eng 47:728–737. https://doi.org/10.1016/j.optlaseng.2008.10.015
14. Reu PL (2016) A realistic error budget for two dimension digital image correlation. Adv Opt Methods Exp Mech 3:189–193. https://doi.org/10.1007/978-3-319-22446-6_24
15. Pan B (2018) Digital image correlation for surface deformation measurement: historical developments, recent advances and future goals. Meas Sci Technol 29:082001. https://doi.org/10.1088/1361-6501/aac55b
16. Xue Y, Cheng T, Xu X, Gao Z, Li Q, Liu X, Wang X, Song R, Ju X, Zhang Q (2017) High accuracy and real-time 3d positioning, tracking system for medical imaging applications based on 3d digital image correlation. Opt Lasers Eng 88:82–90. https://doi.org/10.1016/j.optlaseng.2016.07.002.
17. Bezdidko SN (2016) Orthogonal aberrations: theory, methods, and practical applications in computational optics. J Opt Technol 83:351. https://doi.org/10.1364/jot.83.000351
18. Jiang J (2003) Distortion correction for a wide-angle lens based on real-time digital image processing. Opt Eng 42:2029. https://doi.org/10.1117/1.1580155
19. Yoneyama S (2006) Lens distortion correction for digital image correlation by measuring rigid body displacement. Opt Eng 45:023602. https://doi.org/10.1117/1.2168411
20. Sun Q, Hou Y, Chen J (2015) Lens distortion correction for improving measurement accuracy of digital image correlation. Optik 126:3153–3157. https://doi.org/10.1016/j.ijleo.2015.07.068
21. Bigger R, Blaysat B, Boo C, Grewer M, Hu J, Jones A, Klein M, Raghavan K, Reu P, Schmidt T, Siebert T, Simenson M, Turner D, Vieira A, Weikert T (2018) A good practices guide for digital image correlation. Tech Rep. https://doi.org/10.32720/idics/gpg.ed1
22. Sutton M, Yan J, Tiwari V, Schreier H, Orteu J (2008) The effect of out-of-plane motion on 2D and 3D digital image correlation measurements. Opt Lasers Eng 46:746–757. https://doi.org/10.1016/j.optlaseng.2008.05.005
23. Wittevrongel L, Badaloni M, Balcaen R, Lava P, Debruyne D (2015) Evaluation of methodologies for compensation of out of plane motions in a 2D digital image correlation setup. Strain 51:357–369. https://doi.org/10.1111/str.12146
24. Pan B, Lu Z, Xie H (2010) Mean intensity gradient: an effective global parameter for quality assessment of the speckle patterns used in digital image correlation. Opt Lasers Eng 48:469–477. https://doi.org/10.1016/j.optlaseng.2009.08.010
25. Antoš J, Nežerka V, Somr M (2017) Assessment of 2D-DIC stochastic patterns. Acta Polytech CTU Proceed 13:1–10. https://doi.org/10.14311/app.2017.13.0001

26. Guizar-Sicairos M, Thurman ST, Fienup JR (2008) Efficient subpixel image registration algorithms. Opt Lett 33:156–158. https://doi.org/10.1364/ol.33.000156
27. Fienup JR (1978) Reconstruction of an object from the modulus of its Fourier transform. Opt Lett 3:27–29. https://doi.org/10.1364/ol.3.000027
28. Fienup JR (1982) Phase retrieval algorithms: a comparison. Appl Opt 21:2758–2769. https://doi.org/10.1364/ao.21.002758
29. Castro ED, Morandi C (1987) Registration of translated and rotated images using finite fourier transforms. IEEE Trans Pattern Anal Mach Intell 9:700–703. https://doi.org/10.1109/tpami.1987.4767966
30. Ren J, Jiang J, Vlachos T (2010) High-accuracy sub-pixel motion estimation from noisy images in Fourier domain. IEEE Trans Image Process 19:1379–1384. https://doi.org/10.1109/tip.2009.2039056
31. Scharpf WJ (2010) Global registration and moving objects detection in noisy airborne image sequences. Opt Eng 49:127005. https://doi.org/10.1117/1.3520057
32. Kennedy J, Belytschko T (1982) Theory and application of a finite element method for arbitrary lagrangian-eulerian fluids and structures. Nucl Eng Des 68:129–146. https://doi.org/10.1016/0029-5493(82)90026-7
33. Xiao H, Bruhns O, Meyers A (1998) Direct relationship between the lagrangean logarithmic strain and the lagrangean stretching and the lagrangean kirchhoff stress. Mech Res Commun 25:59–67. https://doi.org/10.1016/s0093-6413(98)00007-x
34. Shannon CE (1948) A mathematical theory of communication. Bell Syst Tech J 27:623–656. https://doi.org/10.1002/j.1538-7305.1948.tb00917.x
35. Wu Y, Zhou Y, Saveriades G, Agaian S, Noonan JP, Natarajan P (2013) Local shannon entropy measure with statistical tests for image randomness. Inf Sci 222:323–342. https://doi.org/10.1016/j.ins.2012.07.049
36. Ma Q, Ma S (2013) Experimental investigation of the systematic error on photomechanic methods induced by camera self-heating. Opt Express 21:7686. https://doi.org/10.1364/oe.21.007686
37. Blaber J, Adair B, Antouniou A (2015) Ncorr: open-source 2D digital image correlation Matlab software. Exp Mech 55:1105–1122. https://doi.org/10.1007/s11340-015-0009-1
38. Reu PL, Toussaint E, Jones E, Bruck HA, Iadicola M, Balcaen R, Turner DZ, Siebert T, Lava P, Simonsen M (2017) DIC challenge: developing images and guidelines for evaluating accuracy and resolution of 2D analyses. Exp Mech 58:1067–1099. https://doi.org/10.1007/s11340-017-0349-0
39. Harilal R, Ramji M (2014) Adaptation of open source 2D DIC software Ncorr for solid mechanics applications, 9th International Symposium on Advanced Science and Technology in Experimental Mechanics. https://doi.org/10.13140/2.1.4994.1442.
40. Winkler J, Hendy C (2017) Improved structural health monitoring of London's docklands light railway bridges using digital image correlation. Struct Eng Int 27:435–440. https://doi.org/10.2749/101686617x14881937384648
41. Acikgoz S, DeJong MJ, Soga K (2018) Sensing dynamic displacements in masonry rail bridges using 2D digital image correlation. Struct Control Health Monit 25:e2187. https://doi.org/10.1002/stc.2187

Appendix F

V. Nežerka and P. Havlásek, A lightweight DFT-based approach to the optical measurement of displacements using an open-source python code, *Experimental Techniques* (2021), doi: 10.1007/s40799-021-00488-8

Author's contribution: data analysis, programming.

Experimental Techniques
https://doi.org/10.1007/s40799-021-00488-8

RESEARCH PAPER

A Lightweight DFT-Based Approach to the Optical Measurement of Displacements Using an Open-Source Python Code

V. Nežerka[1] · **P. Havlásek**[1]

Received: 22 January 2021 / Accepted: 4 June 2021

Abstract
Commonly available digital image correlation (DIC) tools are designed to evaluate displacement/deformation fields using well-optimized correlation functions and computational procedures. However, real-time monitoring at high sampling rates or tracking motion at predefined locations from large sequence images can be hardly accomplished due to extreme computational costs. As shown in this paper, a lightweight approach based on the registration of subpixel subset shifts using discrete Fourier transform (DFT) can easily tackle large sets of images if the measurement is limited to discrete locations. A simple open-source python software designed for evaluation of displacements using virtual extensometers is described in this paper, along with the analysis of its performance. It is shown that the DFT-based algorithms outperform a commonly used DIC package in terms of computational efficiency and required user interactions, without sacrificing precision and accuracy.

Keywords Digital image correlation · Displacements · Motion tracking · Image analysis · Python programming

Introduction

In the early 1980s, Yamaguchi [1] and Peters and Ranson [2] first proposed the use of digital image correlation (DIC) to evaluate shifts and deformations of surfaces speckled with random patterns. The evaluation of a subset displacements and deformations is usually accomplished in the intensity domain (gray-scale/rgb fields) by minimizing a correlation function [3] using various optimization algorithms [4–7]. The optimization becomes computationaly costly with an increasing size of subsets, yet correlation of subsets that do not contain a sufficient number of features to track results in poor results [8]. Even if the subsets are large enough, traditional DIC algorithms fail if subsets exhibit large rotations; this issue was tacked by Zhong and Quan [9] who proposed a method based on the polar coordinate system. DIC analysis can be further extended when employing stereo (3D) DIC to obtain 3D displacement vectors calculated from a series of image pairs acquired by synchronized cameras [10–14]. The capability of stereo DIC come at a cost—the system must be calibrated before each measurement and it is computationally much more demanding than DIC in 2D using a single camera.

DIC has been extensively used in a wide range of applications, spanning from biomechanics [15, 16] to structural mechanics [17, 18] or dynamics [19], from microscopic [20, 21] to large-scale monitoring of displacements on dams [22] or bridges [23]. The discussions about the use of DIC for real-time health monitoring of bridges was promoted by their recent failures [24–26]; the information about displacements at critical points under a certain loading can indicate deterioration or overloading of a structure [27–29] and alert people in case of suspicious behavior [30, 31].

Despite recent developments in the field of digital image correlation (DIC) for the measurement of structural deformations, devices capable of accomplishing continuous real-time DIC-based monitoring are rarely employed outdoors. This goal was accomplished by utilizing efficient image registration algorithms based on discrete Fourier transform (DFT) [32]. The present work extends the use of the DFT-based measurement of displacements to the off-line mode for cases when (i) there are multiple regions of interests within images to be analyzed and seeding for DIC analysis becomes laborious, or (ii) the sequence of images is too large to be processed using conventional DIC algorithms [15, 33]. The motivation to develop a DFT-based code for calculation of displacements came

✉ V. Nežerka
vaclav.nezerka@fsv.cvut.cz

[1] Faculty of Civil Engineering, Czech Technical University in Prague, Thákurova 7, 166 29 Praha 6, Czech Republic

Published online: 15 July 2021

from our recent projects focused, e.g., on monitoring of shrinkage cracking [34], measurements of volume changes for cementitious materials [35], or analysis of drop impact tests using high-speed cameras.

All DFT-based measurements presented in this paper were accomplished using an open-source Python software, *PyVEx* (Python Virtual Extensometers).[1] The code was optimized to provide all the needed functionalities for a convenient evaluation of displacements at distinct locations from a sequence of images without a need for preprocessing of excessive user interactions. Even though DFT-based algorithms have been extensively used for image registration, the presented approach, case studies, and the developed Python code can benefit researchers preferring open-source software to black-box mainstream DIC tools.

DFT-Based Image Registration

Using conventional DIC algorithms operating in the intensity domain (usually grayscale), the evaluation of subset displacements and deformations is accomplished by minimizing the correlation function [3–7]. The optimization becomes more demanding with the increasing size of subsets, but subsets that are too small do not contain a sufficient number of features to track, resulting in poor correlation results [8]. Therefore, a resolution of calculated displacement/deformation fields and DIC precision are limited by image resolution and density and sharpness of the observed random pattern. According to an extensive study on the biases and accuracy of DIC measurements by Reu [36], besides the wrong setting of DIC parameters, lens distortions and changes in camera temperature can introduce significant inaccuracies in the measurements. The requirements on equipment and image acquisition for precise DIC measurements are valid also for the DFT-based approach to register image shifts.

DFT

The Fourier transform $F(\alpha)$ decomposes a signal, being a function of time $f(t)$, into the frequencies α the signal consists of, being the frequency domain representation of a signal in the time domain. $F(\alpha)$ of $f(t)$ is a complex-valued function of frequency, whose absolute value represents the amount of that frequency present in the original function and the complex argument represents the phase offset in that frequency [37]. Mathematically, the Fourier transform can be written as

$$\mathcal{F}\{f(t)\} = F(\alpha) = \int_{-\infty}^{\infty} f(t)\, \mathrm{e}^{-2\pi \mathrm{i}\alpha t} dt, \tag{1}$$

[1] Available at https://omlab.fsv.cvut.cz/software/

where α is a frequency, $-2\pi\alpha$ is the angular frequency, t represents time, and $\mathrm{i} = \sqrt{-1}$. In practice the continuous signal $f(t)$ is measured as a sequence $f(x)$ containing N consecutive samples, and the function of frequency attains the form of an array called discrete Fourier transform (DFT) defined as [38]:

$$\mathcal{D}\{f(x)\} = F(\xi) = \sum_{x=1}^{N-1} f(x)\, \mathrm{e}^{-2\pi \mathrm{i}\frac{x\xi}{N}}. \tag{2}$$

To compute a transformation of the original (time or spatial) domain into a frequency domain, fast Fourier transform algorithms (FFT) based on factorizing the DFT matrix into a product of sparse matrices are used [39, 40]. Such an approach allows reducing the complexity of computing the DFT from $O(N^2)$ to $O(N \log(N))$. The number of frequencies in $F(\xi)$ always equals the number of samples in the time/spatial domain. Here, the DFT extension into two dimensions is illustrated considering a square matrix $N \times N$ representing an image. The expression equation (1) becomes [41]

$$\mathcal{D}\{f(x,y)\} = F(\xi,\eta) = \sum_{x=1}^{N-1}\sum_{y=1}^{N-1} f(x,y)\, \mathrm{e}^{-2\pi \mathrm{i}\left(\frac{x\xi}{N}+\frac{y\eta}{N}\right)}, \tag{3}$$

where $f(x,y)$ is the image represented by the matrix of pixel intensities, while $F(\xi,\eta)$ having the same size as $f(x,y)$ represents the image in the frequency domain. The inverse transform is calculated as

$$\mathcal{D}^{-1}\{F(\xi,\eta)\} = f(x,y) = \frac{1}{N^2}\sum_{\xi=1}^{N-1}\sum_{\eta=1}^{N-1} F(\xi,\eta)\, \mathrm{e}^{2\pi \mathrm{i}\left(\frac{x\xi}{N}+\frac{y\eta}{N}\right)}, \tag{4}$$

where $\frac{1}{N^2}$ is the normalization term in the inverse transformation.

Analogically to one-dimensional arrays, DFT decomposes an image into its sine and cosine components [42, 43]. Then, each component (pixel) in $F(\xi,\eta)$ (Fig. 1) represents a particular frequency contained in the spatial domain image; the complex valued output which can be displayed with two images, either with the real and imaginary part or with magnitude and phase. To obtain the results from equation (4) in two dimensions, a double sum has to be calculated for each image pixel. Because the Fourier transform is separable, the expression can be written as

$$F(\xi,\eta) = \frac{1}{N}\sum_{y=1}^{N-1} P(\xi,y)\, \mathrm{e}^{-2\pi \mathrm{i}\frac{y\eta}{N}}, \tag{5}$$

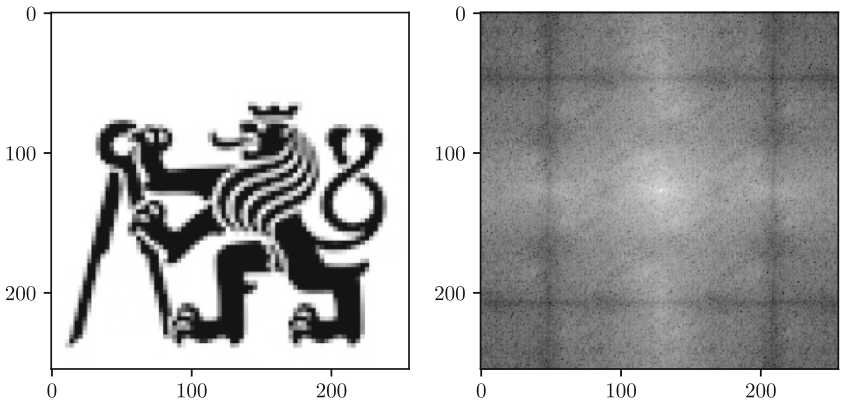

Fig. 1 Gray scale image (left) transformed to a frequency domain displayed in a logarithmic scale (right)

where

$$P(\xi, y) = \frac{1}{N} \sum_{x=1}^{N-1} f(x, y)\, \mathrm{e}^{-2\pi \mathrm{i} \frac{\xi x}{N}}, \tag{6}$$

Expressing the two-dimensional Fourier transform in the form of $2N$ one-dimensional transforms decreases the number of required computations and allows to use DFT matrix multiplication for each dimension separately.

DFT is an essential operation in the field of image processing, especially in filtering, image reconstruction, or image compression [44]. Moreover, the Fourier transform can be exploited for image registration—translation, rotation, reflection, and scaling.

DFT-Based Registration

The mathematical principles of the phase correlation alignment method for measuring translation, rotation, and scaling are thoroughly described in numerous handbooks and papers, e.g., [45–48]. The approach proposed by Kuglin and Hines [49] can be exploited for registering images that have been shifted relative to each other as described next.

The Fourier transform $F(\xi, \eta)$ can be decomposed into its real $R(\xi, \eta)$ and imaginary part $I(\xi, \eta)$:

$$F(\xi, \eta) = R(\xi, \eta) + i\, I(\xi, \eta), \tag{7}$$

which can be also expressed using the exponential form as

$$F(\xi, \eta) = |F(\xi, \eta)|\, \mathrm{e}^{\mathrm{i}\phi(\xi, \eta)}, \tag{8}$$

where $|F(\xi, \eta)|$ is the magnitude of the Fourier transform and $\phi\,(\xi, \eta)$ is the phase angle [45].

Let $f_1(x, y)$ and $f_2(x, y)$ be two images which are related through $f_2(x, y) = f_1(x - x_0, y - y_0)$, as indicated in Fig. 2, and there are no periodic structures in these images. Their corresponding Fourier transforms $F_1(\xi, \eta)$ and $F_2(\xi, \eta)$ will be related by

$$F_2(\xi, \eta) = F_1(\xi, \eta) \mathrm{e}^{-2\pi \mathrm{i}(\xi x_0 + \eta y_0)}. \tag{9}$$

The normalized cross-power spectrum of the two images $f_1(x, y)$ and $f_2(x, y)$ with their Fourier transforms $F_1(\xi, \eta)$ and $F_2(\xi, \eta)$ is defined as

$$Z_{f_1, f_2}(\xi, \eta) = \frac{F_1(\xi, \eta)\, F_2^*(\xi, \eta)}{|F_1(\xi, \eta)\, F_2(\xi, \eta)|} = \mathrm{e}^{2\pi \mathrm{i}(\xi x_0 + \eta y_0)} \tag{10}$$

where $F^*(\xi, \eta)$ is the complex conjugate of $F(\xi, \eta)$.

As the correlation theorem [45] states, the Fourier transform of the correlation of two images is the product of the Fourier transform of one image and the complex conjugate of the Fourier transform of the other. Therefore, as the shift theorem [49] guarantees, the cross-power spectrum is equivalent to the phase difference between the images. However, the cross-correlation must be normalized

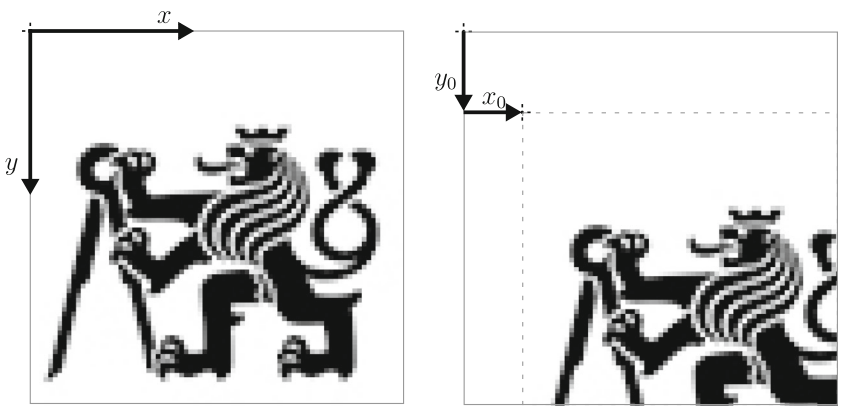

Fig. 2 Example of two images shifted by $x_0 = 15.5\%$ and $y_0 = 21.5\%$, corresponding to 39.7 and 54.9 px, respectively

since illumination intensity fluctuations would influence the measurement. The inverse Fourier transform of the cross-power spectrum yields a discrete impulse function

$$\delta_{f_1,f_2}(x,y) = \mathcal{D}^{-1}\{Z_{f_1,f_2}(\xi,\eta)\}, \tag{11}$$

which is approximately zero everywhere except at the coordinates corresponding to the shift $(-x_0, -y_0)$:

$$\delta(x,y) = \begin{cases} 1 & \text{if } (x,y) = (-x_0,-y_0) \\ 0 & \text{otherwise} \end{cases}. \tag{12}$$

In practice, there is never a sharp peak in $\delta(x, y)$ because of optical noise, mutual rotation of images, and displacements different from whole pixels.

Subpixel Registration

There are several alternatives how to reach a subpixel accuracy for image registration: (i) fitting a parabolic function around the correlation peak [50, 51], (ii) computing the ratio between pixel values near the correlation peak [52], or (iii) upsampling the correlation peak in the Fourier space [53, 54]. The first approach (i) appears to be a bad solution since it was demonstrated that the peak fitting methods yield systematic errors [55, 56], while the second approach (ii) lacks robustness [54]. The algorithms based on (iii) that involve upsampling the Fourier transform around the correlation peak appear to be the most robust and resistant to noise, yet accurate and computationally efficient [53, 56].

The upsampling in the Fourier transform is a commonly used technique when enhancing the resolution of an image. This is accomplished by embedding the image in the Fourier domain in a larger matrix of zeros (zero padding) and its size is dictated by the required size of input/output images. In the case of image registration, the size of correlated images (pixel subsets) N and required subpixel accuracy κ. The size of zero-padding band α can be calculated as

$$\alpha = \frac{N(\kappa - 1)}{2}. \tag{13}$$

Such addition of zero frequencies does not have any impact on the distribution of features within the image in the spatial domain since the non-zero frequencies and amplitudes are preserved and only the number of samples increases. By applying the same technique on the cross-power spectrum, a refinement around of correlation peak can be achieved. A comprehensive study on the impact of parameters N and κ on the performance of DFT-based calculation of displacements is provided in our previous [32].

The upsampling of $Z_{f_1,f_2}(\xi,\eta)$ by zero-padding of the product $F_1(\xi,\eta)\,F_2^*(\xi,\eta)$ and using the inverse DFT would be a straightforward approach to compute x_0 and y_0 with a subpixel accuracy. However, this procedure is computationally very inefficient since registering an image with the size of $N \times N$ and the required accuracy κ requires the computation of $\kappa N \times \kappa N$ Fourier transforms. The developed software employs the algorithm proposed by Guizar-Sicairos et al. [53]. Using their approach, the upsampling is carried efficiently. It obtains an initial estimate of the cross-correlation peak by the FFT-based procedure with the setting of $\kappa = 2$. Once the location of the cross-correlation peak is computed to within half a pixel, a matrix multiplication implementation of the DFT is used to refine the estimate of x_0 and y_0 by calculating the fully (to the factor of κ) upsampled product $F_1(\xi,\eta)\,F_2^*(\xi,\eta)$ in a $1.5\kappa \times 1.5\kappa$ region around the initial estimate [57]. This approach was classified as one of the most reliable algorithms to register images using a phase correlation method [58, 59].

Image Acquisition

Even though modern cell phones offer seemingly high-quality photos, the limited size of CCD/CMOS sensors results in a low signal-to-noise ratio. The noise is often eliminated using sophisticated correction firmware and these corrections negatively impact delicate subpixel measurements. On the other hand, large digital single-lens reflect (DSLR) cameras with sensors reaching full-frame size offer images with a high dynamic range, less noise, and improved quality when acquired in low-light conditions without artificial enhancements. To fully benefit from large sensors of DSLRs and avoid high noise-to-signal ratios, it is necessary to keep the light sensitivity (ISO number) as low as possible. First of all, strong and constant illumination should be provided during the experiment. It is also possible to limit the depth of field by opening the light entrance pupil, controlled with the aperture (f-number) setting since only the in-plane deformation can be detected. On the other hand, high shutter speeds result in dark images but might be needed for capturing a rapidly changing scene.

Despite the availability of correction algorithms [60–63], it is of major importance to use high-quality lenses. The rule of thumb is to use long lenses and zoom the photographed scene as much as possible. The use of telecentric lenses eliminates the effects of perspective and fish eye completely [64], but even in the perfectly orthographic view, out-of-plane deformations caused by rotations of an observed object cause errors in 2D-DIC and should be avoided [15, 65]. Moreover, to reach a very precise measurement, one has to keep in mind that even in the case of extremely expensive high-quality telecentric lenses image distortions may exist due to aberrations and misalignment of optical elements [63].

The artificial pattern or natural texture needs to be adjusted according to the expected displacement field to maximize measurement accuracy, as speckles can be both too large and too small for a particular measurement [66]. The random patterns should be isotropic, having high contrasts, and contain speckles of an appropriate size (as a rule of thumb, ranging between 2 and 20 px) [67–69]. Processing the 12 bits of memory per pixel in RAW image files [70] to yield compressed images [71] must be also accomplished carefully to avoid excessive compression and elimination of fine pattern features [8]. Lossy compression can therefore lower correlation peaks and hence the precision of a calculation. To test the texture quality, several measures have been proposed, such as the mean intensity gradient [72] or Shannon entropy [73–75].

Case Studies

It is indisputable that the efficiency of DFT-based registration makes the method suitable for real-time measurements, especially when using computers with limited computational power. However, the same algorithms are suitable also for batch processing of a large amount of data, e.g., generated by long-term measurements or, typically, by high-speed cameras. The presented studies were selected as representative cases demonstrating the capabilities of the developed PyVEx software. The efficient algorithms enabled fast evaluation of displacements as opposed to tedious and time-consuming use of a conventional DIC software requiring user interactions and more computational power in terms of CPU and RAM. In the following examples, Ncorr [76, 77] was selected as a representative mainstream DIC software to compare the performance and evaluate the benefits of lightweight algorithms implemented in PyVEx.

Validation of the Algorithm

Unlike the following studies demonstration of the practicality of the lightweight approach, this study presents a simple laboratory experiment whose purpose was to present the accuracy of the DFT-based registration approach and complement the verifications presented in our previous work [32], including large-displacement mode when the subset changes its location as the underlying scene deforms.

A prescribed sinusoidal motion of a sample attached to a hydraulic actuator was captured in a laboratory using the Canon EOS 70D DLSR camera with a 4684×2185 px resolution. The distance between the camera and the moving steel plate was approximately 1.5 m, and the focal length (zoom) was set to 55 mm, yielding the metric-to-pixel-scale equal to 0.302 mm/px.

The measurement accuracy is demonstrated in Fig. 3. Theoretically, the precision could reach up to 1/256 px ($\kappa_{\max} = 256$) for 8 bit monochrome/24-bit color images. Despite optimal measurement conditions, there was a measurement error approximately 3×10^{-2} px/10^{-2} mm,

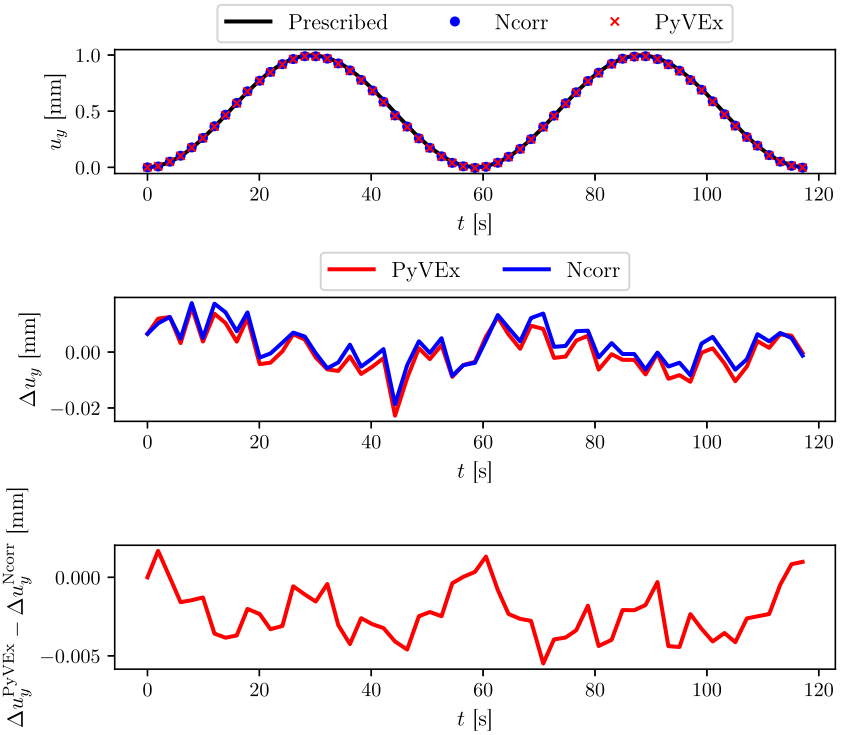

Fig. 3 Comparison of the prescribed vertical displacements u_y evaluated with PyVEx and Ncorr (top) and deviations from the prescribed curve $\bar{u}_y(t) = \sin(2\pi\ 0.017\,t)$ (middle), and differences between the deviations of measurement by PyVEx and Ncorr (bottom)

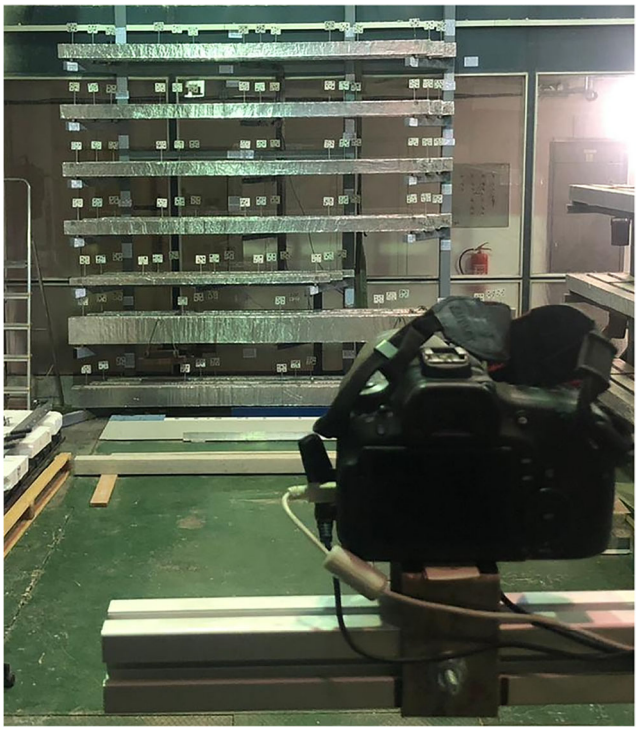

Fig. 4 Monitoring of displacements in the laboratory, the specimens and the DLSR camera connected to an external power source and a triger

however, this deviation from the prescribed vertical displacements are almost identical for measurements by Ncorr and PyVEx, indicating rather imperfect actuation. The difference between PyVEx and Ncorr did not exceed 0.006 mm, being about 2% of the measured displacement; for comparison, state-of-the-art laser-based axial extensometers have accuracy of about 0.001 mm but very limited measurement range.

Long-Term Concrete Creep Measurement

The first study was focused on the evaluation of deflections due to rheology on 7×3 simply supported concrete beams (Fig. 4) subjected to various drying conditions, each with 5 distinct targets (yielding 102 regions of interest in total). The evolution was captured at irregular intervals reflecting the expected rate of deformation, yielding 1491 images over one year of monitoring; again Canon EOS 70D DLSR camera was used for the image acquisition. For reference, the displacements were also measured manually using digital indicators [78] (Fig. 5). The initial elastic deflection due to self-weight is not included in the measurement.

The long-term study of rheology in concrete is fundamental for the research and calibration of advanced material models for creep and shrinkage and interpretation of data is not within the scope of this paper. Here, only the midspan deflection of two selected beams was analyzed to evaluate the performance of different DIC approaches.

One beam (specimen 4a) was subjected to symmetric drying (from the upper and lower surfaces) causing severe microcracking due to nonuniform and internally restrained drying shrinkage. The other beam (specimen 6a) was continuously loaded by external weights located $L/5$ from the supports and subjected to non-symmetric drying limited to the upper surface. In the compressed areas (top surface except above supports), the tensile stresses were eliminated due to compression caused be bending. For this reason, the influence of microcracking on deflection could be neglected. The delayed deflection can be primarily attributed to non-symmetric drying shrinkage and only partially to creep. The joint action results into a deflection line very close to 2^{nd}-order parabola; therefore, the beam 6a was selected for the analysis of curvature development presented next. The cross-sectional height and span of the 4a beam were equal to 100 mm and 2.5 m, respectively; the 6a beam was 200 mm high and spanning 3 m.

The measurement conditions were far from optimal—illumination changed rather significantly (Fig. 6), lab personnel sabotaged the measurement by ignoring the ongoing measurement and frequently blocked the view onto a portion of targets attached to the specimens, the random pattern placed on the targets lacked small-scale speckles, temperature changes influenced the focus and hence sharpness of the images, and the resolution of 0.65 mm/px was not satisfactory considering rather small deflections. Despite these obstacles, the agreement between manual measurements and PyVEx results was good and consistent (Fig. 7). The deviations from the manually measured data on the 4a specimen correspond to periods of overexposure causing losses in the resolution of the observed random pattern. It turned out that the DFT-based approach outperforms the traditional intensity-based correlation algorithms implemented in the Ncorr software if a poor pattern is present and light conditions are not optimal.

Fig. 5 Manual measurement of displacements at selected cross-sections using gauges

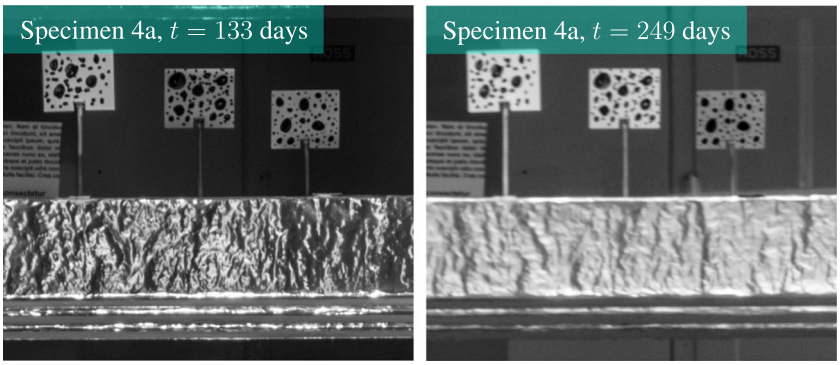

Fig. 6 Fixed window extracted from images taken at different light conditions and temperature, which influenced the focus and hence image sharpness

The calculation of curvature $\rho(t)$ from measured displacements at quarters of the beam 6a and at its midspan (Fig. 8) demonstrates precision and accuracy of the DIC measurements. The evolution of curvature (assumed as constant along the beam axis) can be calculated from the vertical deflection $w(t, \zeta)$ as

$$\rho(t) = \frac{2w(t, \zeta)}{\zeta L - \zeta^2}, \tag{14}$$

where L is the span of the beam between supports (3 m) and the local coordinate ζ has its origin at the left support. Curvatures were evaluated for all monitored cross-sections ($\zeta = 0.25\,L, 0.5\,L, 0.75\,L$) separately, from which mean values and standard deviations were calculated for each time image.

Despite the utilization of a powerful custom-built desktop computer equipped with an Intel 12 core i7-5820K 3.3 GHz CPU and 64 GB RAM, it was possible to evaluate only two beams at a time not to run out of memory. Moreover, the sequence of images had to be significantly reduced by retaining only each fifth image. Using Ncorr, processing of each seed took 11.8 s per image, and correlation of two targets took on average 5.6 s (for subset radius 70 px and spacing 4 px, small-strain mode). In total, without the time needed for numerous user interactions, the calculation for all regions of interest and 1491 images using Ncorr would have taken about 608 h, not considering user interactions such as seeding and data evaluation. On the other hand, PyVEx allowed to painlessly evaluate the displacements within 6 hours, requiring only to define the position of extensometers within the reference image and a metric scale.

Audio Recovery from Sound-Induced Vibrations

High-speed imaging enables the investigation of the dynamic behavior of structures and materials. Even though the DIC algorithms are rate-independent, many software tools are unable to process hundreds of thousands of images documenting a dynamic event. Here, the advantage of using computationally efficient algorithms implemented in the PyVEx software is demonstrated by processing over 80,000 images at which minute vibrations of a plant's leaf due to sound excitation could be detected. The reproduction of the experiment presented by Davis et al. [79] demonstrates offline capabilities of the DFT-based image registration for measurement of displacements and recovery of an audio

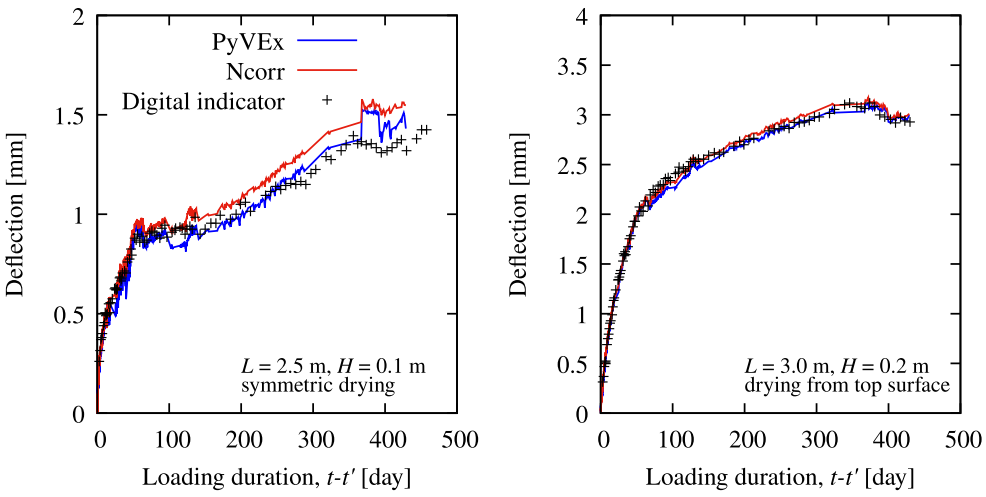

Fig. 7 Evolution of midspan deflection for beams 4a (left) and 6a (right); comparison between manually measured data using gauges and DIC results provided by Ncorr and PyVEx. Time $t - t'$ (horizontal axis) represents the duration of measurement starting from the start of loading, t'

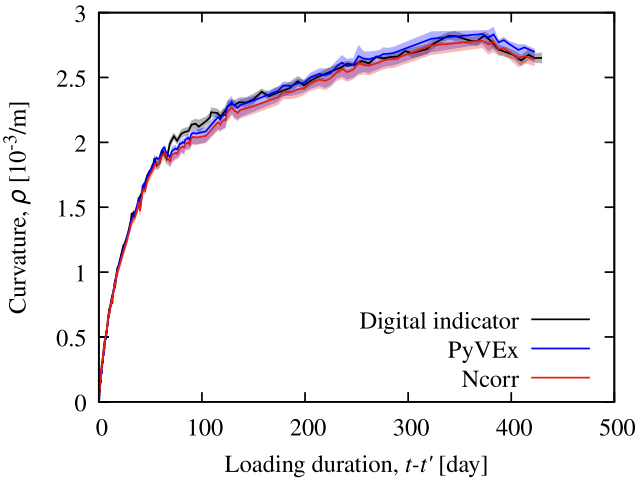

Fig. 8 Evolution of beam 6a curvature calculated from displacements at the quarters and the midspan; the thick solid lines represent mean values for each measurement and the shades represent the corresponding standard deviations

signal from the sequence of images recorded using a high-speed camera. Such an approach mimics traditional microphones that convert the motion of a diaphragm into an electrical signal. Here, a microphone diaphragm was replaced with a withered part of a potted plant's leaf partially covered with an artificial random pattern (Fig. 9). The images were taken using an iX i-SPEED 726 high-speed camera equipped with a CMOS sensor with a 13.5 µm pixel size at a frame rate of 20,000 fps and 1344×978 px resolution.

The experiment fully tested the efficiency of the proposed methodology for calculation of local displacement fields; the 4 second-recording at 20,000 fps yielded an enormous amount of images to be processed and commonly used DIC software could not handle such an amount of data. Using PyVEx, the calculation of 50×50 subset's displacements with 1/200 px accuracy took only about 7 minutes using an average laptop (Lenovo T480, equipped with Intel i5-8250U CPU 1.6 GHz, 8 cores).

First, synthetic tones of 200, 400, 600, 800, and 1000 Hz were played by a loudspeaker to validate the procedure. It can be seen from the spectral analysis presented in Fig. 10 that the frequency peaks of the reproduced sound to match those played by the loudspeaker. The observed potted plant's leaf resonated with a different normalized amplitude for each frequency.

After the successful validation, a piano solo of Beethoven's famous composition Für Elise was played by the loudspeaker and the leaf vibrations were monitored. The sound reproduced from the leaf displacements could be easily recognized by a human and the similarity is demonstrated by a sound spectra plot shown in Fig. 11. The presented audio recovery procedure is sensitive to noise at low frequencies (lower than 300 Hz) and the noise presented in the recovered signal can be attributed to the movement of the camera induced by a cooling fan. Vibrations of the leaf due to the draft were eliminated by a high-pass filter eliminating all displacements with a frequency lower than 200 Hz.

Conclusion

The present work extends the use of the DFT-based measurement of displacements with subpixel accuracy to off-line mode. This lightweight approach enabled the evaluation of displacements from a large sequence of images without the need for tedious user interactions. The algorithms and procedures were implemented in a simple freely available open-source python software PyVEx, whose performance was compared with a commonly

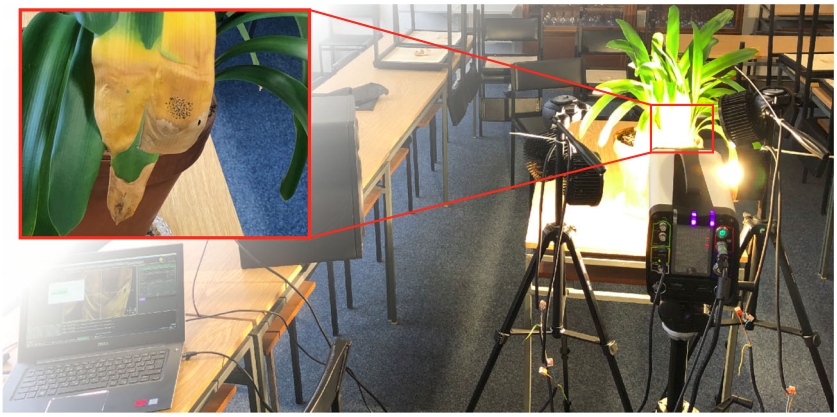

Fig. 9 Experimental setup: leafs of potted plant excited by a sound from a loudspeaker (observed part of the leaf surface zoomed-in); a powerful LED illumination was required for high frame rate recording

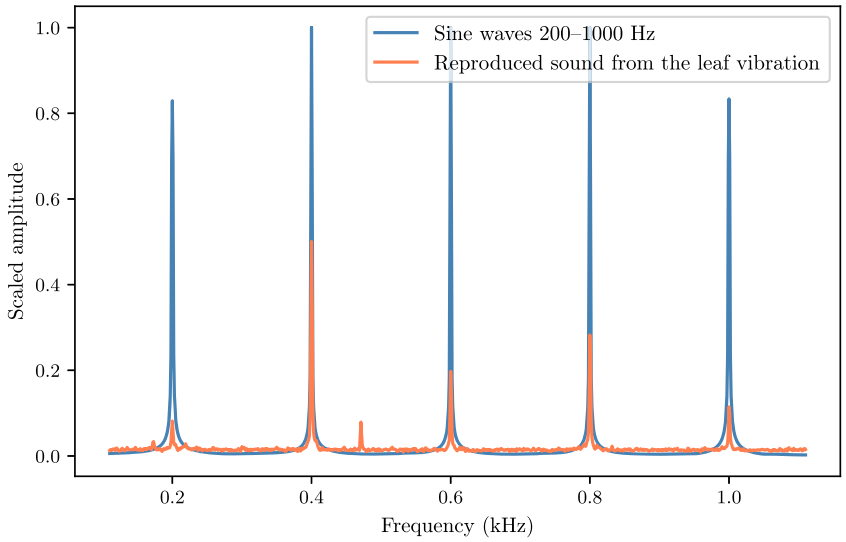

Fig. 10 Comparison original and recovered synthetic tones of 200, 400, 600, 800, and 1,000 Hz using spectral analysis

used DIC software Ncorr, along with the assessment of precision and accuracy. It was demonstrated that the lightweight DFT-based image registration approach significantly outperformed conventional algorithms if the measurements were limited to distinct locations. Not only PyVEx performed about 100× faster, but it also provided more accurate results in the case of long-term experiment hindered by poor illumination of the scene and changing sharpness of the images.

The lightweightness of the proposed approach comes at a cost. By evaluating displacements solely at the points of interest prevents from relocating virtual extensometers in the post-processing. Moreover, having the information about displacements only for discrete points requires anterior knowledge about anticipated deformation fields and unexpected behavior of structures can be easily misinterpreted.

Regarding the measurement accuracy, DIC has no inherent lenght-scale and it depends mostly on the pixel-to-length ratio. Precision can be stronly affected by lens distortions, changes in camera temperature, or unwanted camera or sample motion. Therefore, both accuracy and precision cannot be quantified in general terms and careful design and execution of the experiment is always required. In this study, it was demonstrated that both accuracy and precision are within 2% of the measured displacements in optimal laboratory conditions and within 4% (after elimination of corrupted data) in non-optimal setting of the experiment in terms of pixel-to-length ratio, lighting, camera focus, and temperature changes.

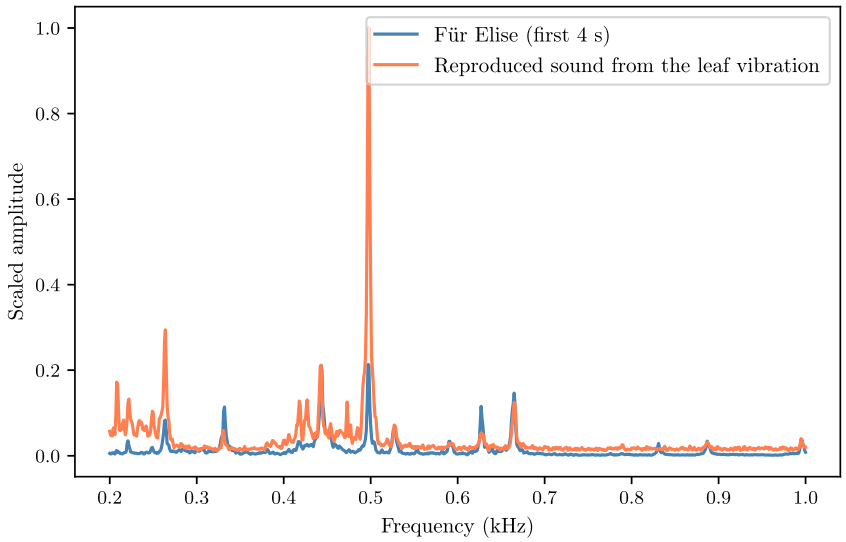

Fig. 11 Comparison original and recovered beginning of the Mozart's Für Elise spectral analysis

Acknowledgments The authors wish to thank Jakub Antoš at the FCE CTU in Prague for assistance with the preparation of experiments.

Funding This work was supported by the Czech Science Foundation [grant GA ČR 19-20666S] (Havlásek) and the FCE CTU in Prague [grant number SGS21/036/OHK1/1T/11] (Nežerka).

References

1. Yamaguchi I (1981) A laser speckle strain gauge. J Phys E Sci Instrum 14:1270. https://doi.org/10.1088/0022-3735/14/11/012
2. Peters WH, Ranson WF (1982) Digital imaging techniques in experimental stress analysis. Opt Eng 21:427–431. https://doi.org/10.1117/12.7972925
3. Pan B, Xie H, Wang Z (2010) Equivalence of digital image correlation criteria for pattern matching. Appl Opt 49:5501–5509
4. Gruen AW (1985) Adaptive least squares correlation: a powerful image matching technique. South African J Photogr Remote Sens Cartogr 14:175–187
5. Altunbasak Y, Mersereau RM, Patti AJ (2003) A fast parametric motion estimation algorithm with illumination and lens distortion correction. IEEE Trans Image Process 12:395–408. https://doi.org/10.1109/tip.2003.809012
6. Pan B, Asundi A, Xie H, Gao J (2009) Digital image correlation using iterative least squares and pointwise least squares for displacement field and strain field measurements. Opt Lasers Eng 47:865–874. https://doi.org/10.1016/j.optlaseng.2008.10.014
7. Pan B, Wang Z, Xie H (2009) Generalized spatial-gradient-based digital image correlation for displacement and shape measurement with subpixel accuracy. J Strain Anal Eng Des 44:659–669. https://doi.org/10.1243/03093247jsa546
8. Triconnet K, Derrien K, Hild F, Baptiste D (2009) Parameter choice for optimized digital image correlation. Opt Lasers Eng 47:728–737. https://doi.org/10.1016/j.optlaseng.2008.10.015
9. Zhong F, Quan C (2017) Digital image correlation in polar coordinate robust to a large rotation. Opt Lasers Eng 98:153–158. https://doi.org/10.1016/j.optlaseng.2017.06.019
10. Siebert T, Becker T, Spiltthof K, Neumann I, Krupka R (2007) Error estimations in digital image correlation technique. Appl Mech Mater 7–8:265–270. https://doi.org/10.4028/www.scientific.net/amm.7-8.265
11. Hu Z, Xie H, Lu J, Hua T, Zhu J (2010) Study of the performance of different subpixel image correlation methods in 3d digital image correlation. Appl Opt 49:4044–4052. https://doi.org/10.1364/ao.49.004044
12. Hu Z, Xie H, Lu J, Wang H, Zhu J (2011) Error evaluation technique for three-dimensional digital image correlation. Appl Opt 50:6239–6248. https://doi.org/10.1364/ao.50.006239
13. Zhong FQ, Shao XX, Quan C (2018) 3d digital image correlation using a single 3ccd colour camera and dichroic filter. Meas Sci Technol 29:045401. https://doi.org/10.1088/1361-6501/aaab02
14. Zhong FQ, Indurkar PP, Quan CG (2018) Three-dimensional digital image correlation with improved efficiency and accuracy. Measurement 128:23–33. https://doi.org/10.1016/j.measurement.2018.06.022
15. Sutton M, Yan J, Tiwari V, Schreier H, Orteu J (2008) The effect of out-of-plane motion on 2D and 3D digital image correlation measurements. Opt Lasers Eng 46:746–757. https://doi.org/10.1016/j.optlaseng.2008.05.005
16. Palanca M, Tozzi G, Cristofolini L (2015) The use of digital image correlation in the biomechanical area: a review. Int Biomech 3:1–21. https://doi.org/10.1080/23335432.2015.1117395
17. H Salmanpour A, Mojsilović N (2021) Application of digital image correlation for strain measurements of large masonry walls, APCOM & ISCM
18. Tung SH, Shih MH, Sung WP (2008) Development of digital image correlation method to analyse crack variations of masonry walls. Sadhana 33:767–779
19. Niezrecki C, Avitabile P, Warren C, Pingle P, Helfrick M, Tomasini EP (2010) A review of digital image correlation applied to structura dynamics. AIP. https://doi.org/10.1063/1.3455461
20. Russev S, Tsutsumanova G, Angelov S, Bachev K (2007) An electron beam lithography and digital image acquisition system for scanning electron microscopes. J Microsc 226(1):64–70. https://doi.org/10.1111/j.1365-2818.2007.01753.x
21. Slone C, Mills M (2016) Analysis of strain localization at high angle grain boundaries during creep of a polycrystalline superalloy using SEM-based digital image correlation. Microsc Microanal 22:2018–2019. https://doi.org/10.1017/s143192761601093x
22. Popescu C, Sas G, Arntsen B (2019) Structural health monitoring of a buttress dam using digital image correlation. In: Sustainable and safe dams around the world. CRC Press, pp 1671–1680. https://doi.org/10.1201/9780429319778-151
23. Hoag A, Hoult N, Take A, Le H (2015) Monitoring of rail bridge displacements using digital image correlation. In: Structural health monitoring 2015. Destech Publications. https://doi.org/10.12783/shm2015/52
24. Şener S, Çağlar Y, Benzer MA, Şener KC (2015) Vertical displacement of collapsed bridge in palau. Challenge J Struct Mech 1:84–89. https://doi.org/10.20528/cjsmec.2015.06.016
25. Wong S (2019) Genoa bridge demolished. New Scientist 243:10. https://doi.org/10.1016/s0262-4079(19)31206-0
26. Moravcik M, Bujnakova P, Bahleda F (2020) Failure and damage of a first-generation precast prestressed bridge in Slovakia. Struct Concr 114:1–10. https://doi.org/10.1002/suco.201900526
27. Jenkins CH, Kjerengtroen L, Oestensen H (1997) Sensitivity of parameter changes in structural damage detection. Shock Vib 4:27–37. https://doi.org/10.1155/1997/807239
28. Chang PC, Flatau A, Liu SC (2003) Review paper: Health monitoring of civil infrastructure. Struct Health Monitor Int J 2:257–267. https://doi.org/10.1177/1475921703036169
29. Bob C (2014) About the causes of the koror bridge collapse. Open J Safety Sci Technol 04:119–126. https://doi.org/10.4236/ojsst.2014.42013
30. Handayani HH, Yuwono M (2015) Taufik Preliminary study of bridge deformation monitoring using GPS and CRP (case study: Suramadu bridge). Procedia Environ Sci 24:266–276. https://doi.org/10.1016/j.proenv.2015.03.035
31. Moschas F, Stiros S (2011) Measurement of the dynamic displacements and of the modal frequencies of a short-span pedestrian bridge using GPS and an accelerometer. Eng Struct 33:10–17. https://doi.org/10.1016/j.engstruct.2010.09.013
32. Antoš J, Nežerka V, Somr M (2019) Real-time optical measurement of displacements using subpixel image registration. Exp Tech 43:315–323. https://doi.org/10.1007/s40799-019-00315-1
33. Pan B, Li K (2011) A fast digital image correlation method for deformation measurement. Opt Lasers Eng 49:841–847
34. Nežerka V, Havlásek P, Trejbal J (2020) Mitigating inclusion-induced shrinkage cracking in cementitious composites by incorporating recycled concrete fines. Construction Build Mater 248:118673. https://doi.org/10.1016/j.conbuildmat.2020.118673

35. Prošek Z, Nežerka V, Hlůžek R, Trejbal J, Tesárek P, Karra'a G (2019) Role of lime, fly ash, and slag in cement pastes containing recycled concrete fines. Construct Build Mater 201:702–714. https://doi.org/10.1016/j.conbuildmat.2018.12.227
36. Reu PL (2016) A realistic error budget for two dimension digital image correlation. In: Advancement of optical methods in experimental mechanics, vol 3, pp 189–193. https://doi.org/10.1007/978-3-319-22446-6_24
37. Čížek V (1981) Diskrétní Fourierova transformace a její použití, Matematický seminář SNTL SNTL
38. Nussbaumer HJ (1982) Fast fourier transform and convolution algorithms. Springer, Berlin. https://doi.org/10.1007/978-3-642-81897-4
39. Loan CV (1992) Computational frameworks for the fast fourier transform. Society for industrial and applied mathematics. https://doi.org/10.1137/1.9781611970999
40. Heideman M, Johnson D, Burrus C (1984) Gauss and the history of the fast fourier transform. IEEE ASSP Mag 1:14–21. https://doi.org/10.1109/massp.1984.1162257
41. Bezvoda V (1988) Dvojrozměrná diskrétní Fourierova transformace a její použití: pro posl. fak. přírodověd. Teorie a obecné užití, no. díl 1 SPN
42. Stade E (2005) Fourier analysis. Hoboken, Wiley. https://doi.org/10.1002/9781118165508
43. Khare K (2015) Fourier optics and computational imaging. Hoboken, Wiley. https://doi.org/10.1002/9781118900352
44. Rao K, Kim D, Hwang J-J (2010) Fast fourier transform - algorithms and applications, Springer Netherlands, Amsterdam. https://doi.org/10.1007/978-1-4020-6629-0
45. Brown LG (1992) A survey of image registration techniques. ACM Comput Surv 24:325–376. https://doi.org/10.1145/146370.146374
46. Reddy B, Chatterji B (1996) An FFT-based technique for translation, rotation, and scale-invariant image registration. IEEE Trans Image Process 5:1266–1271. https://doi.org/10.1109/83.506761
47. Zitová B, Flusser J (2003) Image registration methods: a survey. Image Vis Comput 21:977–1000. https://doi.org/10.1016/s0262-8856(03)00137-9
48. Druckmüller M (2009) Phase correlation method for the alignment of total solar eclipse images. Astrophys J 706:1605–1608. https://doi.org/10.1088/0004-637x/706/2/1605
49. Kuglin CD, Hines DC (1975) The phase correlation image alignment method. In: Proc. Int. Conference Cybernetics Society, pp 163–165
50. Argyriou V, Vlachos T (2006) A study of sub-pixel motion estimation using phase correlation. In: Procedings of the British machine vision conference 2006, British machine vision association. https://doi.org/10.5244/c.20.40
51. Moigne JL, Netanyahu NS, Eastman RD (2009) Image Registration for Remote Sensing, Cambridge University Press, Cambridge. https://doi.org/10.1017/cbo9780511777684
52. Foroosh H, Zerubia J, Berthod M (2002) Extension of phase correlation to subpixel registration. IEEE Trans Image Process 11:188–200. https://doi.org/10.1109/83.988953
53. Guizar-Sicairos M, Thurman ST, Fienup JR (2008) Efficient subpixel image registration algorithms. Opt Lett 33:156. https://doi.org/10.1364/ol.33.000156
54. Wang CL, Zhao CX, Yang JY (2011) Local upsampling fourier transform for high accuracy image rotation estimation. Adv Mater Res 268-270:1488–1493. https://doi.org/10.4028/www.scientific.net/amr.268-270.1488
55. Dvornychenko VN (1983) Bounds on (deterministic) correlation functions with application to registration. IEEE Trans Pattern Anal Mach Intell 5:206–213. https://doi.org/10.1109/tpami.1983.4767373
56. Almonacid-Caballer J, Pardo-Pascual J, Ruiz L (2017) Evaluating fourier cross-correlation sub-pixel registration in landsat images. Remote Sens 9:1051. https://doi.org/10.3390/rs9101051
57. Guizar-Sicairos M, Thurman ST, Fienup JR (2007) Efficient image registration algorithms for computation of invariant error metrics. In: Adaptive optics: analysis and methods/computational optical sensing and imaging/information photonics/signal recovery and synthesis topical meetings on CD-ROM, OSA. https://doi.org/10.1364/srs.2007.smc3
58. Reed RA (2010) Comparison of subpixel phase correlation methods for image registration. Tech rep. https://doi.org/10.21236/ada519383
59. Yousef A, Li J, Karim M (2015) High-speed image registration algorithm with subpixel accuracy. IEEE Signal Process Lett 22:1796–1800. https://doi.org/10.1109/lsp.2015.2437881
60. Tsai R (1987) A versatile camera calibration technique for high-accuracy 3d machine vision metrology using off-the-shelf TV cameras and lenses. IEEE J Robot Autom 3:323–344. https://doi.org/10.1109/jra.1987.1087109
61. Weng J, Cohen P, Herniou M (1992) Camera calibration with distortion models and accuracy evaluation. IEEE Trans Pattern Anal Mach Intell 14:965–980. https://doi.org/10.1109/34.159901
62. Zhang Z (2000) A flexible new technique for camera calibration. IEEE Trans Pattern Anal Mach Intell 22:1330–1334. https://doi.org/10.1109/34.888718
63. Pan B, Yu L, Wu D, Tang L (2013) Systematic errors in two-dimensional digital image correlation due to lens distortion. Opt Lasers Eng 51:140–147. https://doi.org/10.1016/j.optlaseng.2012.08.012
64. Bigger R, Blaysat B, Boo C, Grewer M, Hu J, Jones A, Klein M, Raghavan K, Reu P, Schmidt T, Siebert T, Simenson M, Turner D, Vieira A, Weikert T (2018) A good practices guide for digital image correlation. Tech rep. https://doi.org/10.32720/idics/gpg.ed1
65. Wittevrongel L, Badaloni M, Balcaen R, Lava P, Debruyne D (2015) Evaluation of methodologies for compensation of out of plane motions in a 2D digital image correlation setup. Strain 51:357–369. https://doi.org/10.1111/str.12146
66. Hung P, Voloshin AS In-plane strain measurement by digital image correlation. J Br Soc Mech Sci Eng 25. https://doi.org/10.1590/s1678-58782003000300001
67. Pan B, Qian K, Xie H, Asundi A (2008) On errors of digital image correlation due to speckle patterns. In: He X, Xie H, Kang Y (eds) ICEM 2008: International conference on experimental mechanics 2008. https://doi.org/10.1117/12.839326
68. Pan B, Lu Z, Xie H (2010) Mean intensity gradient: An effective global parameter for quality assessment of the speckle patterns used in digital image correlation. Opt Lasers Eng 48:469–477
69. Antoš J, Nežerka V, Somr M (2017) Assessment of 2D-DIC stochastic patterns. Acta Polytech CTU Proc 13:1–10. https://doi.org/10.14311/app.2017.13.0001
70. Salvaggio N (2013) Basic photographic materials and processes, Routledge, London. https://doi.org/10.4324/9780080927664
71. Kou W (1995) Principles of digital image compression. In: Digital image compression. Springer US, pp 1–8. https://doi.org/10.1007/978-1-4757-2361-8_1
72. Pan B, Xie H, Wang Z, Qian K, Wang Z (2008) Study on subset size selection in digital image correlation for speckle patterns. Opt Express 16:7037. https://doi.org/10.1364/oe.16.007037
73. Shannon CE (1948) A mathematical theory of communication. Bell Syst Technic J 27:379–423. https://doi.org/10.1002/j.1538-7305.1948.tb01338.x
74. Lecompte D, Bossuyt S, Cooreman S, Sol H, Vantomme J (2007) Study and generation of optimal speckle patterns for dic. In:

Proceedings of the SEM annual conference and exposition on experimental and applied mechanics
75. Crammond G, Boyd SW, Dulieu-Barton JM (2013) Speckle pattern quality assessment for digital image correlation. Opt Lasers Eng 51:1368–1378. https://doi.org/10.1016/j.optlaseng.2013.03.014
76. Blaber J (2017) Ncorr digital image correlation software, http://www.ncorr.com/, Georgia Institute of Technology
77. Blaber J, Adair B, Antouniou A (2015) Ncorr: Open-source 2d digital image correlation matlab software. Exp Mech 55:1105–1122. https://doi.org/10.1007/s11340-015-0009-1
78. Havlásek P., Šmilauer V., Dohnalová L., Sovják R. (2021) Shrinkage-induced deformations and creep of structural concrete: 1-year measurements and numerical prediction, vol 144, p 106402. https://doi.org/10.1016/j.cemconres.2021.106402
79. Davis A, Rubinstein M, Wadhwa N, Mysore GJ, Durand F, Freeman WT (2014) The visual microphone. ACM Trans Graph 33:1–10. https://doi.org/10.1145/2601097.2601119

Appendix G

R. Hlůžek, J. Trejbal, **V. Nežerka** et al., Improvement of bonding between synthetic fibers and a cementitious matrix using recycled concrete powder and plasma treatment: from a single fiber to FRC, *European Journal of Environmental and Civil Engineering* (2020) 1–18, doi: 10.1080/19648189.2020.1824821

Author's contribution: DIC, design and preparation of experiments, programming.

EUROPEAN JOURNAL OF ENVIRONMENTAL AND CIVIL ENGINEERING
https://doi.org/10.1080/19648189.2020.1824821

Improvement of bonding between synthetic fibers and a cementitious matrix using recycled concrete powder and plasma treatment: from a single fiber to FRC

R. Hlůžek[a], J. Trejbal[a], V. Nežerka[a], P. Demo[a,b], Z. Prošek[a] and P. Tesárek[a]

[a]Faculty of Civil Engineering, Czech Technical University in Prague, Praha 6, Czech Republic; [b]Institute of Physics, Czech Academy of Sciences, Praha 6, Czech Republic

ABSTRACT

Poor adhesion of synthetic macro fibers to a cementitious matrix limits their reinforcing capacity when used in fiber-reinforced cementitious composites (FRCCs). As a remedy to this problem, high concentrations of fibers must be incorporated into such mixtures, which makes their dispersion in fresh mixtures difficult to achieve. Several strategies have been adopted to improve bonding between synthetic fibers and a cementitious matrix, but most of them cause deterioration of fiber properties. In previous studies, plasma treatment of polymer fibers and strengthening of the fiber-matrix interface using recycled concrete powder (RCP) increased pull-out resistance at a scale of a single fiber. Here, it was found that these results cannot be easily scaled, and the tension-softening behavior of FRCCs can be influenced negatively, despite positive pull-out test results, due to random orientation of fibers. Treating fibers with plasma appears reasonable at any scale, but RCP matrix modification must be carefully performed. Nevertheless, RCP may contribute to more sustainable concrete mixtures and considering its use when designing FRCC elements is recommended.

ARTICLE HISTORY
Received 8 April 2020
Accepted 11 September 2020

KEYWORDS
Synthetic macro fibers; polymer fibers; recycled concrete; plasma treatment; bonding; FRC

1. Introduction

In the set of cementitious materials, the use of plain concrete is limited to a very narrow range of engineering applications due to its low tensile strength and brittle nature. This limitation can be overcome by reinforcement, rendering concrete stronger and more ductile (di Prisco et al., 2009; Li, 2003; Maalej et al., 1995; Meddah & Bencheikh, 2009; Zhang & Li, 2002). Steel bars or meshes have been traditionally used for this purpose, but in some applications, it is advantageous to complement or even replace such discrete reinforcement by using fibers (di Prisco et al., 2009; Mazaheripour et al., 2011; Mohammadi et al., 2008; Oh et al., 2007). FRCCs can be produced using steel (Cagatay & Dincer, 2011; Kim & Yoo, 2019; Lee & Kim, 2010; Tiberti et al., 2015), glass (Ali & Qureshi, 2019; Kasagani & Rao, 2018; Schwartzentruber et al., 2004), carbon (Hambach et al., 2016; Lavagna et al., 2018; Xu & Chung, 1999), natural (Krishna et al., 2018; Razak & Ferdiansyah, 2005; Zakaria et al., 2020), and synthetic fibers (Kotecha & Abolmaali, 2019; Li et al., 2018; Ochi et al., 2007; Trejbal et al., 2016).

Synthetic fibers have become a popular alternative to steel fibers because of their high tensile strength, low density, ease of dispersion, relatively low cost, and resistance to chemicals within

CONTACT J. Trejbal jan.trejbal@fsv.cvut.cz Faculty of Civil Engineering, Czech Technical University in Prague, Thákurova 7, Praha 6, 166 29, Czech Republic
Preprint submitted to European Journal of Environmental and Civil Engineering July 24, 2020

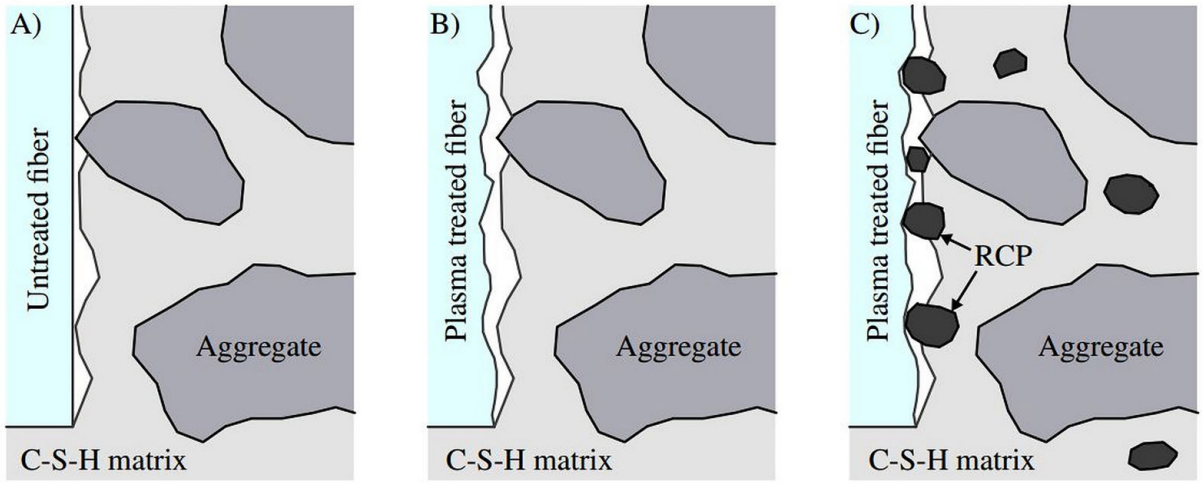

Figure 1. Hypothetical reinforcement of fiber-matrix interfaces with the combination of plasma treatment and the addition of RCP; (A) no reinforcement, (B) roughening of a fiber using plasma treatment, (C) a plasma treated fiber and interlocks provided by RCP.

cementitious materials (Bordelon & Roesler, 2014; Foti, 2016; Kim et al., 2010; Sadrinejad et al., 2018; Silva et al., 2005; Zheng, 1995). Furthermore, the ends of soft synthetic fibers protruding from FRCC elements do not pose a risk of injury and are also less harmful to concreting machines (Luňáček et al., 2012). Even though strong synthetic macro fibers have become broadly accepted by engineers as reliable concrete reinforcements, their limited ability to adhere to a cementitious matrix limits their capacity (Bartos, 1981; Foti, 2019; Lee et al., 1997; Li et al., 1987; Singh et al., 2004). In turn, fibers must be added to a mixture in concentrations high enough to sustain stresses and can become tangled and difficult to homogeneously disperse within mixtures. Various strategies have been developed to make synthetic fibers more hydrophilic and to increase their bonding with a matrix in order to enable use of lower fiber concentrations in mixtures. Wet chemical treatment and flame treatment cause fibers to be weaker and more brittle (Felekoglu et al., 2009), while micro-indentation reduces fiber cross-section and cannot be implemented in the case of fibers with small diameters (Singh et al., 2004). Cold plasma treatment appears to be a suitable, non-damaging alternative with controllable outcomes (Felekoglu et al., 2009; Grundke et al., 2015; Li et al., 1997; Tosun et al., 2012; Wang & He, 2006). Even though plasma can activate polar groups on a surface of polymers and promote chemical bonding (Li et al., 1997; Mittal, 2004; Öktem et al., 2000; Tosun et al., 2012), such activation can be very unstable and temporary (Trejbal et al., 2018); increased bonding can be attributed to fiber surface roughening due to ion beam bombardment.

The properties of the interfacial transition zone (ITZ) in the vicinity of fibers can be also modified to promote fiber bonding and to increase pull-out fiber resistance (Leung et al., 2005; Li & Stang, 1997; Maida et al., 2018; Trejbal, 2018; Trejbal et al., 2015). Adding nano-fillers into a concrete mixture modifies the ITZ by reducing porosity (Bentz et al., 2000; Bentz & Stutzman, 1994; Han et al., 2015; Park & Lee, 2013). In previous studies (Hlůžek & Trejbal, 2019; Trejbal et al., 2018), pull-out resistance at the scale of a single fiber was shown to increase with the addition of finely ground recycled concrete containing sharp fragments into mixtures (Prošek et al., 2020), especially when combined with plasma treatment. A hypothetical mechanism for this process is presented in Figure 1. Meaningful utilization of recycled concrete powder (RCP) would likely be beneficial for environmental reasons, because such subsieve fractions constitute up to 50% of crushed concrete weight (Ma & Wang, 2013; Shui et al., 2008) and there is, to the best of our knowledge, no clear way to reuse this kind of waste (Anastasiou et al., 2014; Cartuxo et al., 2015; Evangelista & de Brito, 2014, 2019). In this study, the focus was on upscaling the results from a single fiber to fiber-reinforced pastes and fiber-reinforced concrete (FRC) to see if plasma treatment and the addition of RCP to mixtures were efficient and led to improved tension-softening behavior in such cementitious composites.

2. Materials and methods

The composition of tested mixtures, design of specimens, and the experimental agenda were proposed in such a way to reveal the role of RCP and plasma treatment on the strength of specimens at multiple

Table 1. Size characteristics, PC and RCP.

	Sauter mean diameter, d32 [μm]	De Brouckere mean diameter, d43 [μm]	Specific surface [m2/kg]
PC	2.65	18.5	380
RCP	3.71	9.98	460

Table 2. Aggregate grading.

					Sand					Gravel
Sieve size [mm]	0	0.0625	0.125	0.25	0.5	1.0	2.0	4.0	8.0	16.0
Sand passing [%]	0	2.08	3.51	5.40	9.13	16.45	29.74	52.50	78.88	100.00

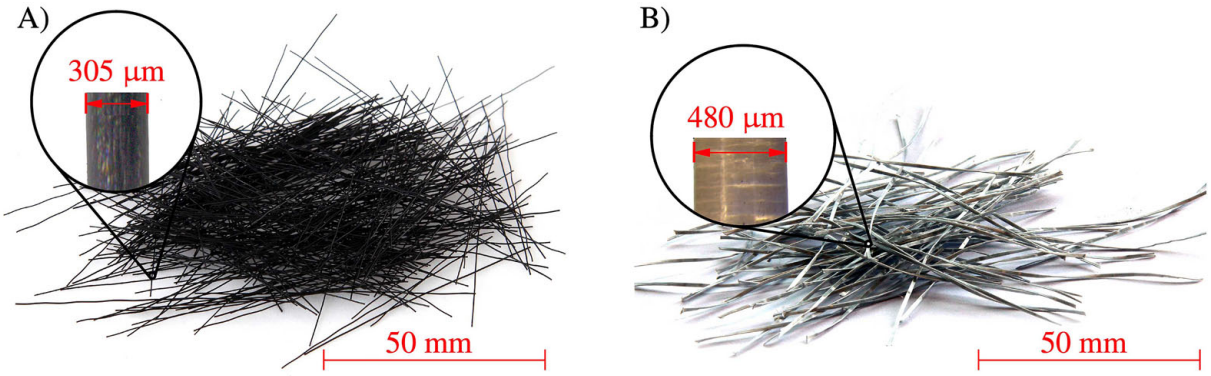

Figure 2. Fibers used in this study: (A) straight PP fibers (round cross-sections), (B) twisted PP + PE fibers (flat cross-sections).

Table 3. Characteristics of fibers.

Cross-section	Material	Shape	Diameter [mm]	Length [mm]	Tensile strength [MPa]	Young's modulus [MPa]
Round	PP	Straight	305	55	440	6100
Flat	PP + PE	Twisted	408	55	610	5170

scales. The study involved two fiber types, but a comparison between the performance of these fibers was out of scope of this study; the emphasis on revealing the role of RCP and plasma treatment is reflected by ordering of specimens in tables and figures throughout this paper.

2.1. Used materials

The input materials for the production of cementitious pastes and concrete were selected based on findings from previous studies (Nežerka et al., 2019; Prošek et al., 2019, 2020). An ordinary PC CEM I/42.5R (EN 197-1:2001, 2001) was selected for production of pastes and concrete. A recycled drainage channel was the source of RCP. The channel, which had been stored in a warehouse for approximately four years, was made of class C 20/25 (EN 1992-1-1:2004, 2004) unreinforced prefabricated concrete. The channel was crushed, and coarse fragments were further processed, yielding a 0-1 mm fraction, using a high-speed Lavaris SKD 600 electric mill (2 × 30 kW). Table 1 provides a comparison of PC and RCP size characteristics analyzed using laser granulometry (a Fritsch Analyssete 22 Micro Tec Plus device). The Blaine method (Matest E009 device) was used to determine the specific surface.

Sieving was used to determine the grading of the pit sand and basalt aggregate used for production of concrete (Table 2).

Two types of polymer macrofibers commonly used in the construction industry were used to study the impact of plasma treatment and the addition of RCP on the cementitious matrix of mixtures studied. These polypropylene (PP)/polypropylene-polyethylene (PE) fibers differed mainly in shape and mechanical properties, see Figure 2 and Table 3. The PP fibers, having a round cross section, were primarily intended for the production of brushes, while the PP + PE fibers having a flat cross-section were originally designed to perform well as concrete reinforcement by their manufacturers.

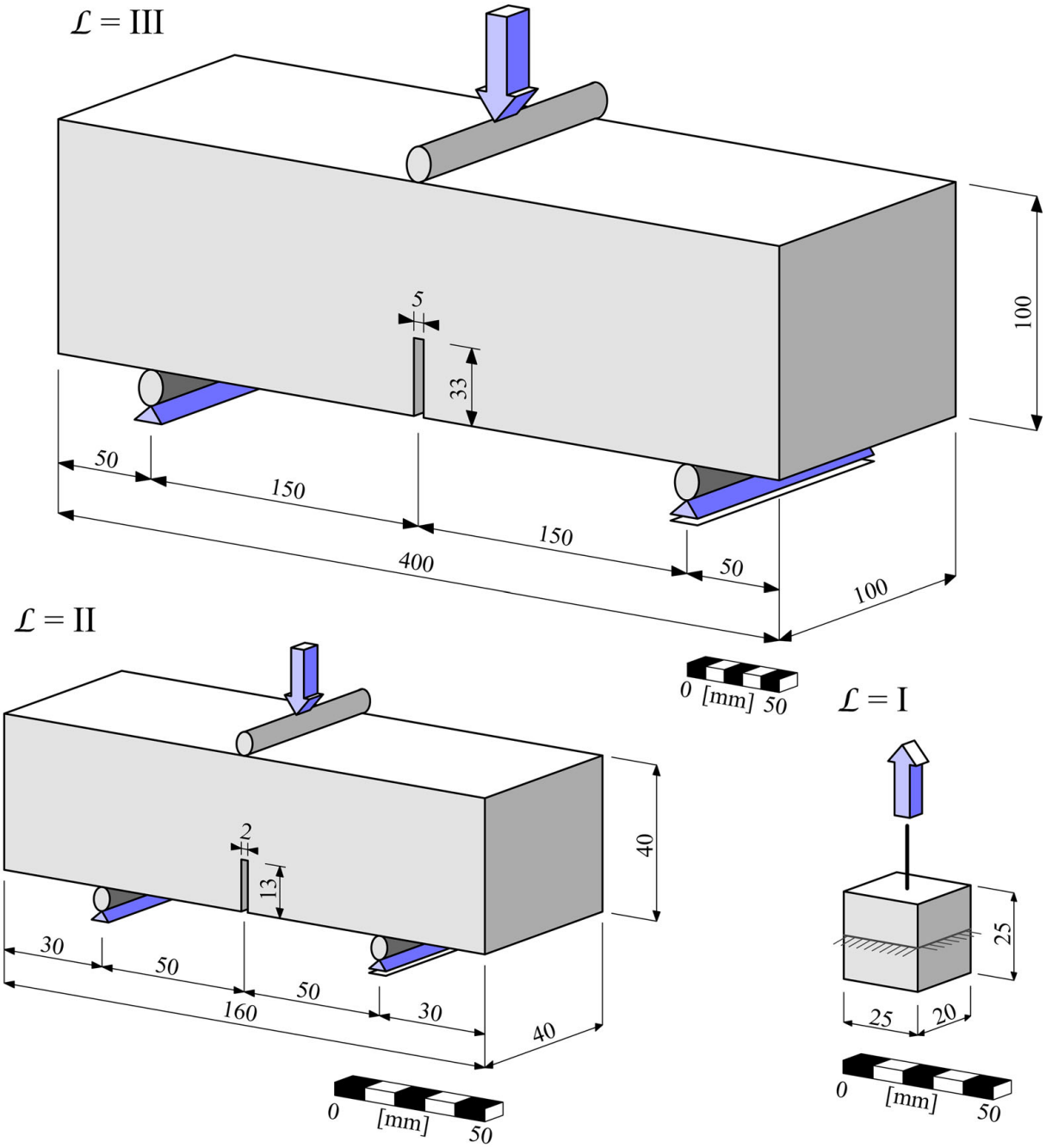

Figure 3. Geometry of specimens tested at the scale of a single fiber (L = I), fiber-reinforced paste (L = II), and FRC (L = III); the arrows indicate the direction of prescribed displacement during testing.

2.2. Mixes and specimens

Three experimental set-ups operating at different length scales were created to reveal the role of fiber-interface modifications at various scales and the scalability of results obtained by wettability and pull-out tests (Figure 3).

First, the ability of fibers to bond to cementious pastes was assessed using pull-out tests (scale L = I). A single fiber per specimen was embedded in $25 \times 20 \times 25$ mm molds filled with fresh pastes. The anchoring length was equal to the height of the specimens, i.e. 25 mm. Eight sets of specimens, each containing different combinations of a paste (pure PC paste and pastes containing different amounts of PC and RCP), fiber type (round and flat), and treatment (untreated or plasma-treated) – see Figure 4 – were prepared and tested. Each set (mixture) at L = I was represented by six specimens. The composition of individual mixtures is provided in Table 4.

The same mixtures were tested at scale L = II using $40 \times 40 \times 100$ mm specimens; only the fibers were incorporated into the mix in a concentration equal to 1.35% of the weight of binder materials (PC/PC

X_1-$X_2(X_3X_4)$

X_1 . . . binder specification; C = containing PC only, R = containing PC and RCF

X_2 . . . type of fiber(s); R = having a round cross-section, F = having a flat cross-section

X_3 . . . optional, P = plasma treated fibers

X_4 . . . optional, specimen number

Figure 4. Key for naming mixtures and specimens.

Table 4. Composition of paste mixtures at L = I and II.

	Input materials [wt.%]					
Mixture	PC	RCP	Fibers (only at L = I)	Water	w/b	Fiber type
C-R	70.75	–	0.95	28.3	0.40	round, untreated
C-RP		round, treated				
R-R	42.15	28.10		28.8	0.41	round, untreated
R-RP						round, treated
C-F	70.75	–		28.3	0.40	flat, untreated
C-FP		flat, treated				
R-F	42.15	28.10		28.8	0.41	flat, untreated
R-FP						flat, treated

Table 5. Composition of FRC mixtures at L = III.

			Input materials [kg/m3]						w/c	Fiber type
Mixture	RC	RCP	Sand	Gravel	Gravel	Fibers	Water	Plasticizer		
0–4 mm	4–8 mm	8–16 mm								
C-R	350	–	870	100	860	6.825	192.5	3.0	0.55	round, untreated
C-RP		round, treated								
R-R		174	696							round, untreated
R-RP										round, treated
C-F		–	870							flat, untreated
C-FP		flat, treated								
R-F		174	696							flat, untreated
R-FP										flat, treated

and RCP combined). This concentration was selected based on findings by other authors (Khaloo et al., 2014; Machovič et al., 2013; Ochi et al., 2007) and findings from previous studies (Trejbal et al., 2016; 2018). The high water-to-binder ratio ($w/b \approx 0.4$) facilitated dispersion of fibers. Each mixture at L = II was represented by six specimens.

100 × 100 × 400 mm FRC specimens at scale L = III were prepared according to EN 14845-1 (BS EN 14845-1:2007, 2007) and EN 14651 (BS EN 14651:2005, 2005) standards, requiring: maximum aggregate size equal to 16 mm, maximum PC amount 350 kg/m3, and water-to-cement ratio $w/c = 0.55$. The concentration of fibers, 0.75% of mixture volume, was selected to facilitate dispersion and sufficient workability. This concentration also ensured a plateau in the load-deflection diagrams and hardening following a drop after the matrix failure during three-point bending tests. FRC mixture workability was enhanced by using a Stachement 2180 FM plasticizer, produced by Stachema CZ. Here, RCP replaced sand and the amount of PC was kept constant to rule out the impact of a poor cementitious matrix on the tensile parameters due to an insufficient amount of PC in the mix. Table 5 provides a summary of the concrete mixtures. Each mixture at L = III was represented by six specimens. Similar FRC mixtures have also been tested by other authors (Buratti et al., 2011; Maida et al., 2018; Nobili et al., 2013; Paegle et al., 2016).

All specimens were compacted and kept completely sealed at 22 ± 1 °C for 24 h prior to unmolding. They were then submerged in tap water for 27 days. After this period, the specimens at L = II and III were

partially cut at midspan with a water-cooled diamond circular saw to produce 2 and 5 mm thick notches, respectively, reaching 1/3 of the height of specimens.

2.3. Plasma treatment

Low pressure, inductively coupled oxygen plasma was used to treat the smooth and chemically inert fibers. This treatment makes surfaces more hydrophilic by reducing surface energy (Mittal, 2004; Mutlu et al., 2008; Öktem et al., 2000) and creating microscopic dents (Trejbal et al., 2016). A Tesla VT 214 device (50 sccm oxygen flow, 56 Pa gas 100 pressure) was used to induce cold plasma. Based on previous research (Trejbal et al., 2018), an optimal treatment for macroscopic polymer fibers was employed: a power supply of 100 W for 30 s.

2.4. Microscopy

A FEG SEM Merlin ZEISS scanning electron microscope (SEM) equipped with Schottky emission cathodes and a detector for secondary electrons was used to investigate the surface topology of fibers before and after plasma treatment. Fiber surfaces were coated with platinum dust (3 nm thick) in an argon atmosphere in order to provide the required electric conductivity. The accelerating voltage was set to 5 kV and the current to 120 pA.

2.5. Contact angle measurement

Static contact angles were evaluated using images of fibers submerged in demineralized water. An in-house software, CAMTIA (Nežerka et al., 2018), was used to quantify changes in wettability due to plasma treatment. A single-lens reflex Canon EOS 600 D digital camera was used for taking images of fibers half-submerged in distilled water. The camera was equipped with a Tamron 70–300 mm objective lens and a grey neutral-density filter. Backlight illumination was provided by an LED lamp together with a dispersing screen. The images were taken one day after plasma treatment. Ten fibers represented each set.

2.6. Destructive testing

The pull-out tests at L = I were displacement controlled at a rate of 2 mm/min, using Veb Tiw Rauenstein FP 100 loading frame. The specimens were fixed with self-tightening clamps, while fiber free-ends were anchored using special clamping jaws to prevent notch formation. The response of fibers during pull-out testing was evaluated in the form of force versus free-end displacement diagrams; displacements were recorded using an in-built linear position sensor.

The same frame was used for testing of notched specimens in three-point bending at L = II and L = III, but the displacements were evaluated using RTCorr in-house digital image correlation (DIC) software (Antoš et al., 2019). These results were verified using the Ncorr DIC package (Blaber et al., 2015; Nežerka, n.d.) on selected specimens. The three-point bending tests were displacement-controlled at a rate of 1 mm/min to provide sharp images for DIC analysis.

3. Results and discussions

3.1. Treatment impacts on morphology and wettability of fibers

Changes in the surface morphologies of the investigated fibers were observed using SEM under a 12k× magnification. The microscopy images presented in Figure 5 show that the longitudinal grooves formed during the extrusion of round PP fibers were more pronounced after plasma treatment. Moreover, surface roughening due to plasma treatment was more significant for flat PP + PE fibers, making their effective area larger. The longitudinal grooves and loose polymer droplets on their surfaces were eliminated, but newly formed transversal fissures emerged.

To measure fiber surface wettability, the mean of contact angles measured between the menisci of the water level in the vicinity of a fiber and the fiber itself was used. The measurements revealed that

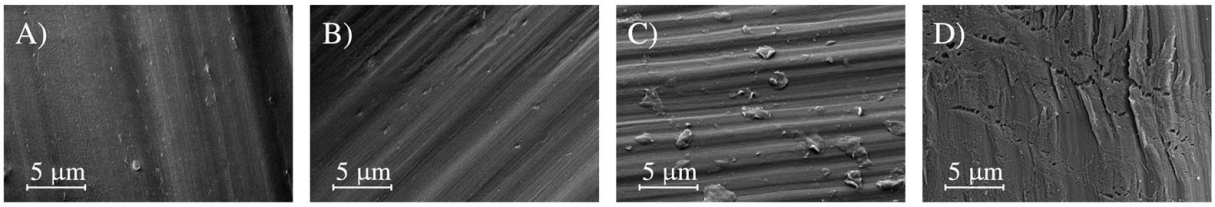

Figure 5. Surface of fibers under 12k× magnification: (A) an untreated round fiber, (B) a treated round fiber, (C) an untreated flat fiber, and (D) a treated flat fiber.

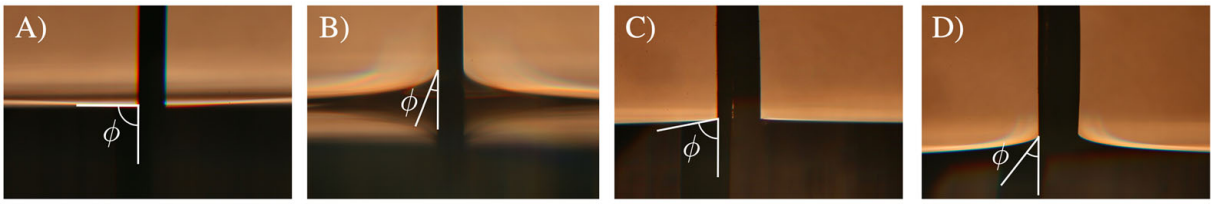

Figure 6. Silhouettes of water level and partially submerged fibers showing the impact of plasma treatment contact angles φ: (A) an untreated round fiber, (B) a treated round fiber, (C) an untreated flat fiber, and (D) a treated flat fiber.

Table 6. Contact angles for untreated fibers and fibers subjected to 30 s plasma treatment.

Fiber	Round	Round treated	Flat	Flat treated
Contact angle [°]	88.3 ± 0.6	29.1 ± 5.2	82.6 ± 4.6	36.9 ± 3.0

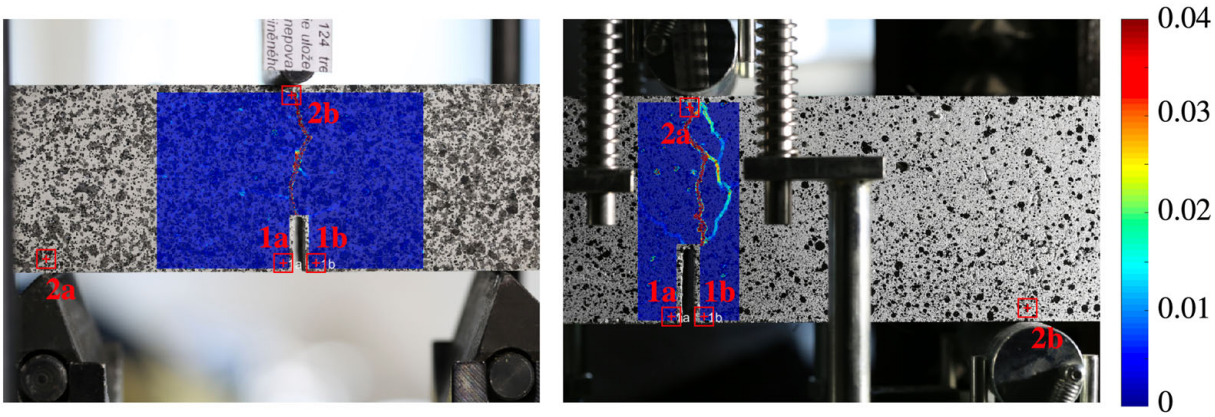

Figure 7. Maps of principal strain on C-RP specimens at L = II (left) and III (right) evaluated using Ncorr software (Blaber et al., 2015; Nežerka et al., 2016) and position of virtual extensometers 1a–1b and 2a–2b for evaluation of CMODs and deflections using RTCorr software (Antoš et al., 2019).

plasma treatment rendered fibers more hydrophilic and resulted in a decrease of contact angles, as shown in Figure 6. The results summarized in Table 6 indicate that hydrophilization resulting from plasma treatment was more efficient for round fibers.

3.2. Performance of fiber reinforcement at different scales

To compare the performance of individual fiber/matrix configurations, pull-out/bending forces $F_{0.5}$, $F_{1.5}$, $F_{2.5}$, and $F_{3.5}$, respectively, were evaluated at CMOD levels 0.5, 1.5, 2.5, and 3.5, following the methodology proposed in the EN 14651 (BS EN 14651:2005, 2005) standard. Locations of virtual extensometers for evaluation of deflections and CMOD using DIC are plotted in Figure 7. According to Li et al. (1991) and Li and Leung (1992), the maximum interfacial shear stress, $\tau_{max} = F_{max}/C_f\, l_e$, is related mainly to chemical bonding, while after reaching a maximum force during fiber pull-out, the magnitude of interfacial shear stress is exclusively related to mechanical bonding. C_f and l_e refer to a fiber circumference and effective fiber length, respectively. By capturing post-peak behavior during mechanical loading, the impact of plasma treatment and the presence of RCP could be assessed from the displacement-controlled

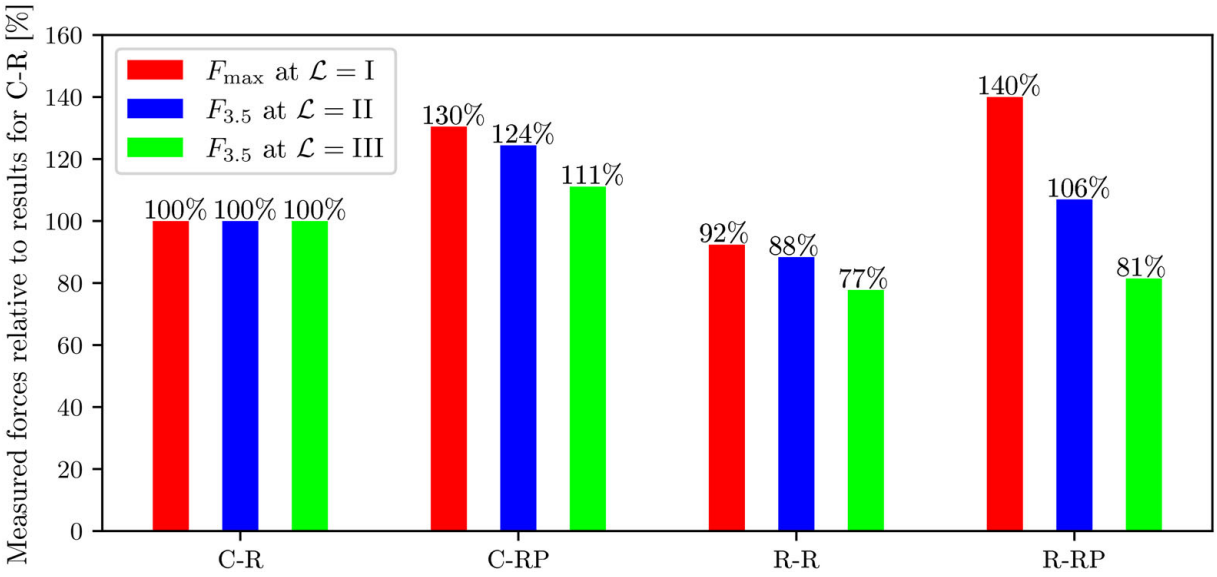

Figure 8. Effect of RCP in a cementitious matrix and plasma treatment of round fibers on performance of specimens at L = I, II, and III; the results for modified specimens are related to the results for reference configuration C-R.

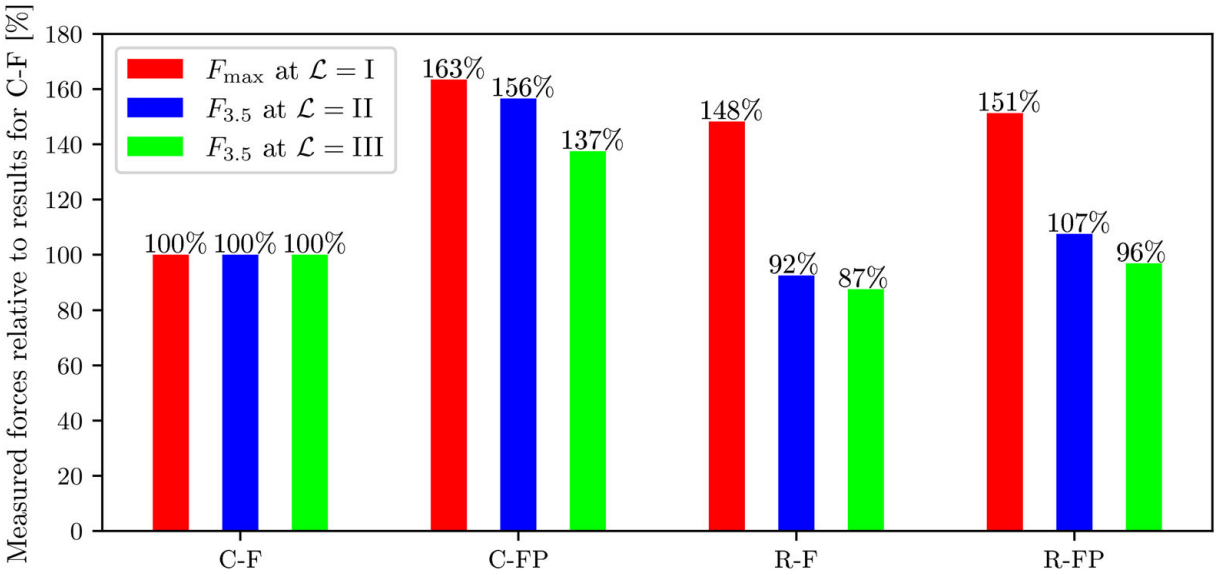

Figure 9. Effect of RCP in a cementitious matrix and plasma treatment of flat fibers on performance of specimens at L = I, II, and III; the results for modified specimens are related to the results for reference configuration C-F.

loading of notched specimens. All measured force-displacement curves are provided in Appendix A, Figures A1–A10, along with the summary of these results in Tables A1–A3.

Force-displacement diagrams at the scale of a single fiber pull-out, L = I, exhibited an almost bilinear relationship without significant drops after fiber debonding for both types of fibers. The stiffer response and higher pull-out strength for flat fibers, compared to round ones, can be attributed to their larger effective surface areas. To assess the impact of plasma treatment and the presence of different amounts of RCP in specimens, a summary of average values F_{max} for individual mixtures normalized by F_{max} for a reference configuration (cement paste and untreated fibers) is provided for round and flat fibers in Figures 8 and 9, respectively. In these plots, plasma treatment increased F_{max} at L = I, regardless of fiber type and matrix composition. The addition of RCP led to greater pull-out resistance except for untreated round fibers, which had the smoothest surface. In other cases, the impact of plasma treatment and RCP additions was significant, increasing F_{max} by 30–63%.

For three-point bending test results at levels L = II and III, $F_{3.5}$ averages were compared. $F_{3.5}$ was selected as the most appropriate indicator of residual post-peak strength because the course of force-displacement curves stabilized before reaching a CMOD level of 3.5 mm, the point at which their tangents were nearly parallel.

The positive impacts of plasma treatment for L = I were also reflected in the performance of fiber-reinforced pastes at L = II. Pastes containing plasma-treated fibers were 15–56% stronger than their counterparts containing untreated fibers. On the other hand, the addition of RCP to pastes at L = II reduced their residual strength. Only in combination with plasma-treated fibers did the addition of RCP to reference mixtures not cause residual strength to deteriorate.

At L = III, the matrices containing RCP performed even worse. The bond strengthening resulting from plasma treatment increased residual strength less than for L = I and L = II, but the increase by 11–37% in mixtures without RCP cannot be considered negligible. Adding RCP to mixtures at L = III resulted in reducing residual strength by up to 23% for untreated round fibers.

The 'unscability' of pull-out test results can most likely be attributed to substantial differences in the micromechanical behavior of matrices at the distinct scales. Matrices containing RCP are weaker (Prošek et al., 2020), which can amplify the impact of snubbing if fibers are not perpendicular to a fracture plane (Li, 1992; Morton & Groves, 1976). Pull-out of these inclined fibers may result in a failure of the matrix weakened by the presence of RCP as in the research by Hong et al. (Hong et al., 2020). The effect of bond strength might be counteracted by the impact of fibers on porosity, homogeneity (Khaloo et al., 2014), and microstructure development during hardening (Leung et al., 2005; Shen et al., 2008) at the scale of FRC, but an examination of these impacts was beyond the scope of this study.

4. Conclusion

This study assessed the impacts of plasma treatment and RCP added to specimens on their tension-softening behavior. Pull-out forces at scales of a single fiber, reinforced cementitious paste, and FRC were examined. Among the most important findings:

1. Plasma treatment affected the morphology of fibers, making them rougher and less hydrophobic,
2. Plasma treatment and additions of RCP to paste/concrete mixes led to most significant effects at the scale of a single fiber pull-out and least significant at the FRC scale,
3. Plasma treatment led to enhanced bonding of fibers to a cementitious matrix and increased pull-out/residual strength for all specimens examined in this study,
4. The addition of RCP to specimens was advantageous only for the single fiber pull-out and for flat PP + PE fibers, but it appears that plasma treatment may diminish or reverse any negative effects of adding RCP to a mixture.

Based on these findings, plasma treating of synthetic macro fibers before producing any fiber-reinforced cementitious composite appears to be beneficial. Despite relatively low cost of low-pressure plasma treatment (about €0,5/h), the procedure is slow and therefore not feasible for real-world applications. This limitation can be overcome by employing plasma treatment induced at atmospheric pressure.

For increasing the residual strength of such composites, RCP additions appear to weaken a cementious matrix and thus cannot be recommended because a weakened matrix is susceptible to failure when fiber pull-out is not perpendicular to a crack plane. However, replacing large amounts of PC/sand with RCP in cement mixtures and further improving the performance of such mixtures using plasma treatment may still hold promise. This concept is worth investigating in future studies due to the potential environmental benefits of using RCP in a sustainable manner.

Acknowledgment

The authors wish to thank Dr. Šeps (Faculty of Civil Engineering, CTU in Prague) for his assistance during experimental testing. The help of Dr. Stephanie Krueger, who as an English native speaker provided editorial assistance, is gratefully acknowledged. Thanks also go to the Joint Laboratory of Polymer Nanofiber Technologies of Institute of Physics AS CR and Faculty of Civil Engineering, CTU in Prague.

Disclosure statement

No potential conflict of interest was reported by the authors.

Funding

This work was supported by the Czech Science Foundation [grant number GA ČR 17-06771S] and the Faculty of Civil Engineering at CTU in Prague [grant number SGS20/037/OHK1/1T/11].

References

Ali, B., & Qureshi, L. A. (2019). Influence of glass fibers on mechanical and durability performance of concrete with recycled aggregates. *Construction and Building Materials*, *228*, 116783. https://doi.org/10.1016/j.conbuildmat.2019.116783

Anastasiou, E., Filikas, K. G., & Stefanidou, M. (2014). Utilization of fine recycled aggregates in concrete with fly ash and steel slag. *Construction and Building Materials*, *50*, 154–161. https://doi.org/10.1016/j.conbuildmat.2013.09.037

Antoš, J., Nežerka, V., & Somr, M. (2019). Real-time optical measurement of displacements using sub-pixel image registration. *Experimental Techniques*, *43*(3), 315–323. https://doi.org/10.1007/s40799-019-00315-1

Bartos, P. (1981). Review paper: Bond in fibre reinforced cements and concretes. *International Journal of Cement Composites and Lightweight Concrete*, *3*(3), 159–177. https://doi.org/10.1016/0262-5075(81)90049-X

Bentz, D., Jensen, O., Coats, A., & Glasser, F. (2000). Influence of silica fume on diffusivity in cement-based materials. *Cement and Concrete Research*, *30*(6), 953–962. https://doi.org/10.1016/S0008-8846(00)00264-7

Bentz, D. P., & Stutzman, P. E. (1994). Evolution of porosity and calcium hydroxide in laboratory concretes containing silica fume. *Cement and Concrete Research*, *24*(6), 1044–1050. https://doi.org/10.1016/0008-8846(94)90027-2

Blaber, J., Adair, B., & Antoniou, A. (2015). Ncorr: Open-source 2d digital image correlation matlab software. *Experimental Mechanics*, *55*(6), 1105–1122. https://doi.org/10.1007/s11340-015-0009-1

Bordelon, A. C., & Roesler, J. R. (2014). Spatial distribution of synthetic fibers in concrete with x-ray computed tomography. *Cement and Concrete Composites*, *53*, 35–43. https://doi.org/10.1016/j.cemconcomp.2014.04.007

BS EN 14651:2005. (2005). *Test method for metallic fibre concrete. Measuring the flexural tensile strength (limit of proportionality (*LOP), *R*esidual). BSI British Standards. https://doi.org/10.3403/30092475

BS EN 14845-1:2007. (2007). *Test methods for fibres in concrete. Reference concretes.* BSI British Standards. https://doi.org/10.3403/30095427u.

Buratti, N., Mazzotti, C., & Savoia, M. (2011). Post-cracking behaviour of steel and macro-synthetic fibre-reinforced concretes. *Construction and Building Materials*, *25*(5), 2713–2722. https://doi.org/10.1016/j.conbuildmat.2010.12.022

Cagatay, L. H., & Dincer, R. (2011). Modeling of concrete containing steel fibers: Toughness and mechanical properties. *Computers & Concrete*, *8*(3), 357–369. https://doi.org/10.12989/cac.2011.8.3.357

Cartuxo, F., de Brito, J., Evangelista, L., Jimenez, J., & Ledesma, E. (2015). Rheological behaviour of concrete made with fine recycled concrete aggregates – Influence of the superplasticizer. *Construction and Building Materials*, *89*, 36–47. https://doi.org/10.1016/j.conbuildmat.2015.03.119

di Prisco, M., Plizzari, G., & Vandewalle, L. (2009). Fibre reinforced concrete: New design perspectives. *Materials and Structures*, *42*(9), 1261–1281. https://doi.org/10.1617/s11527-009-9529-4

EN 197-1:2011. (2011). *Cement. Composition, specifications and conformity criteria for very low heat special cements*. BSI British Standards. https://doi.org/10.3403/03054726.

EN 1992-1-1:2004. (2004). *Design of concrete structures, Part 1-1: General rules and rules for buildings*. BSI British Standards. https://doi.org/10.12691/ajcea-4-1-6.

Evangelista, L., & de Brito, J. (2014). Concrete with fine recycled aggregates: A review. *European Journal of Environmental and Civil Engineering*, *18*(2), 129–172. https://doi.org/10.1080/19648189.2013.851038

Evangelista, L., & de Brito, J. (2019). Durability of crushed fine recycled aggregate concrete assessed by permeability-related properties. *Magazine of Concrete Research*, *71*(21), 1142–1149. https://doi.org/10.1680/jmacr.18.00093

Felekoglu, B., Tosun, K., & Baradan, B. (2009). A comparative study on the flexural performance of plasma treated polypropylene fiber reinforced cementitious composites. *Journal of Materials Processing Technology*, *209*(11), 5133–5144. https://doi.org/10.1016/j.jmatprotec.2009.02.015

Foti, D. (2016). Innovative techniques for concrete reinforcement with polymers. *Construction and Building Materials*, *112*, 202–209. https://doi.org/10.1016/j.conbuildmat.2016.02.111

Foti, D. (2019). *Recycled waste PET for sustainable fiber reinforced concrete*. Woodhead Publishing.

Grundke, K., Pöschel, K., Synytska, A., Frenzel, R., Drechsler, A., Nitschke, M., Cordeiro, A., Uhlmann, L. P., & Welzel, P. B. (2015). Experimental studies of contact angle hysteresis phenomena on polymer surfaces – Toward the understanding and control of wettability for different applications. *Advances in Colloid and Interface Science*, *222*, 350–376. https://doi.org/10.1016/j.cis.2014.10.012.

Hambach, M., Möller, H., Neumann, T., & Volkmer, D. (2016). Portland cement paste with aligned carbon fibers exhibiting exceptionally high flexural strength (>100 MPa). *Cement and Concrete Research*, *89*, 80–86. https://doi.org/10.1016/j.cemconres.2016.08.011

Han, J.-W., Jeon, J.-H., & Park, C.-G. (2015). Bond characteristics of macro polypropylene fiber in cementitious composites containing nanosilica and styrene butadiene latex polymer. *International Journal of Polymer Science*, *2015*, 1–9. https://doi.org/10.1155/2015/207456

Hlůžek, R., & Trejbal, J. (2019). Use of finely ground recycled concrete for improvement of interfacial adhesion in fiber-reinforced cementitious composites. *Acta Polytechnica CTU Proceedings*, *21*, 5–9. https://doi.org/10.14311/app.2019.21.0005.

Hong, L., Chen, Y., Li, T., Gao, P., & Sun, L. (2020). Microstructure and bonding behavior of fiber-mortar interface in fiber-reinforced concrete. *Construction and Building Materials*, *232*, 117235. https://doi.org/10.1016/j.conbuildmat.2019.117235

Kasagani, H., & Rao, C. (2018). Effect of graded fibers on stress strain behaviour of glass fiber reinforced concrete in tension. *Construction and Building Materials*, *183*, 592–604. https://doi.org/10.1016/j.conbuildmat.2018.06.193

Khaloo, A., Raisi, E. M., Hosseini, P., & Tahsiri, H. (2014). Mechanical performance of self-compacting concrete reinforced with steel fibers. *Construction and Building Materials*, *51*, 179–186. https://doi.org/10.1016/j.conbuildmat.2013.10.054

Kim, J.-J., & Yoo, D.-Y. (2019). Effects of fiber shape and distance on the pullout behavior of steel fibers embedded in ultra-high-performance concrete. *Cement and Concrete Composites*, *103*, 213–223. https://doi.org/10.1016/j.cemconcomp.2019.05.006

Kim, S. B., Yi, N. H., Kim, H. Y., Kim, J.-H J., & Song, Y.-C. (2010). Material and structural performance evaluation of recycled PET fiber reinforced concrete. *Cement and Concrete Composites*, *32*(3), 232–240. https://doi.org/10.1016/j.cemconcomp.2009.11.002

Kotecha, P., & Abolmaali, A. (2019). Macro synthetic fibers as reinforcement for deep beams with discontinuity regions: Experimental investigation. *Engineering Structures*, *200*, 109672. https://doi.org/10.1016/j.engstruct.2019.109672

Krishna, N. K., Prasanth, M., Gowtham, R., Karthic, S., & Mini, K. (2018). Enhancement of properties of concrete using natural fibers. *Materials Today: Proceedings*, *5*(11), 23816–23823. https://doi.org/10.1016/j.matpr.2018.10.173

Lavagna, L., Musso, S., Ferro, G., & Pavese, M. (2018). Cement-based composites containing functionalized carbon fibers. *Cement and Concrete Composites*, *88*, 165–171. https://doi.org/10.1016/j.cemconcomp.2018.02.007

Lee, C., & Kim, H. (2010). Orientation factor and number of fibers at failure plane in ring-type steel fiber reinforced concrete. *Cement and Concrete Research*, *40*(5), 810–819. https://doi.org/10.1016/j.cemconres.2009.11.009

Lee, S. D., Sarmadi, M., Denes, E., & Shohet, J. L. (1997). Surface modification of polypropylene under argon and oxygen-RF-plasma conditions. *Plasmas and Polymers*, *2*(3), 177–197. https://doi.org/10.1007/BF02766153

Leung, C. K., Lai, R., & Lee, A. Y. (2005). Properties of wet-mixed fiber reinforced shotcrete and fiber reinforced concrete with similar composition. *Cement and Concrete Research*, *35*(4), 788–795. https://doi.org/10.1016/j.cemconres.2004.05.033

Li, R., Ye, L., & Mai, Y.-W. (1997). Application of plasma technologies in fibre-reinforced polymer composites: A review of recent developments. *Composites Part A: Applied Science and Manufacturing*, *28*(1), 73–86. https://doi.org/10.1016/S1359-835X(96)00097-8

Li, V. C. (1992). Postcrack scaling relations for fiber reinforced cementitious composites. *Journal of Materials in Civil Engineering*, *4*(1), 41–57. https://doi.org/10.1061/(asce)

Li, V. C. (2003). On engineered cementitious composites (ECC). *Journal of Advanced Concrete Technology*, *1*(3), 215–230. https://doi.org/10.3151/jact.1.215

Li, V. C., & Leung, C. K. Y. (1992). Steady-state and multiple cracking of short random fiber composites. *Journal of Engineering Mechanics*, *118*(11), 2246–2264. https://doi.org/10.1061/(ASCE)0733-9399(1992)118:11(2246)

Li, V. C., & Stang, H. (1997). Interface property characterization and strengthening mechanisms in fiber reinforced cement based composites. *Advanced Cement Based Materials*, *6*(1), 1–20. https://doi.org/10.1016/S1065-7355(97)90001-8

Li, V. C., Wang, Y., & Backer, S. (1987). Effect of fiber-matrix bond strength on the crack resistance of synthetic fiber reinforced cementitious composites. *MRS Proceedings*, *114*, 167–173. https://doi.org/10.1557/PROC-114-167

Li, V. C., Wang, Y., & Backer, S. (1991). A micromechanical model of tension-softening and bridging toughening of short random fiber reinforced brittle matrix composites. *Journal of the Mechanics and Physics of Solids*, *39*(5), 607–625. https://doi.org/10.1016/0022-5096(91)90043-N

Li, Y., Li, W., Deng, D., Wang, K., & Duan, W. H. (2018). Reinforcement effects of polyvinyl alcohol and polypropylene fibers on flexural behaviors of sulfoaluminate cement matrices. *Cement and Concrete Composites*, *88*, 139–149. https://doi.org/10.1016/j.cemconcomp.2018.02.004

Luňáček, M., Suchánek, P., & Bader, R. (2012). Application of bicomponent synthetic macro fibres Concrix in tunneling. *Tunnel*, *8*, 54–56.

Ma, X., & Wang, Z. (2013). Effect of ground waste concrete powder on cement properties. *Advances in Materials Science and Engineering*, *2013*, 1–5. https://doi.org/10.1155/2013/918294

Maalej, M., Li, V. C., & Hashida, T. (1995). Effect of fiber rupture on tensile properties of short fiber composites. *Journal of Engineering Mechanics*, *121*(8), 903–913. https://doi.org/10.1061/(ASCE)0733-9399(1995)121:8(903)

Machovič, V., Lapčák, L., Borecká, L., Lhotka, M., Andertová, J., Kopecký, L., & Mišková, L. (2013). Microstructure of interfacial transition zone between PET fibers and cement paste. *Acta Geodynamica et Geomaterialia*, *10*, 121–127. https://doi.org/10.13168/agg.2013.0012.

Maida, P. D., Sciancalepore, C., Radi, E., & Bondioli, F. (2018). Effects of nano-silica treatment on the flexural post cracking behaviour of polypropylene macro-synthetic fibre reinforced concrete. *Mechanics Research Communications*, *88*, 12–18. https://doi.org/10.1016/j.mechrescom.2018.01.004

Mazaheripour, H., Ghanbarpour, S., Mirmoradi, S. H., & Hosseinpour, I. (2011). The effect of polypropy-lene fibers on the properties of fresh and hardened lightweight self-compacting concrete. *Construction and Building Materials*, *25*(1), 351–358. https://doi.org/10.1016/j.conbuildmat.2010.06.018

Meddah, M. S., & Bencheikh, M. (2009). Properties of concrete reinforced with different kinds of industrial waste fibre materials. *Construction and Building Materials*, *23*(10), 3196–3205. https://doi.org/10.1016/j.conbuildmat.2009.06.017

Mittal, K. L. (2004). *Polymer surface modification: Relevance to adhesion*. Taylor & Francis Group.

Mohammadi, Y., Singh, S. P., & Kaushik, S. K. (2008). Properties of steel fibrous concrete containing mixed fibres in fresh and hardened state. *Construction and Building Materials*, *22*(5), 956–965. https://doi.org/10.1016/j.conbuildmat.2006.12.004

Morton, J., & Groves, G. W. (1976). The effect of metal wires on the fracture of a brittle-matrix composite. *Journal of Materials Science*, *11*(4), 617–622. https://doi.org/10.1007/BF01209446

Mutlu, S., Çökeliler, D., ¸ Shard, A., Goktas, H., Ozansoy, B., & Mutlu, M. (2008). Preparation and characterization of ethylenediamine and cysteamine plasma polymerized films on piezo-electric quartz crystal surfaces for a biosensor. *Thin Solid Films*, *516*(6), 1249–1255. https://doi.org/10.1016/j.tsf.2007.06.074

Nežerka, V. (2014). *Ncorr post: DIC post-processing tool*. http://mech.fsv.cvut.cz/nezerka/dic/index.htm

Nežerka, V., Antoš, J., Litoš, J., Tesárek, P., & Zeman, J. (2016). An integrated experimental-numerical study of the performance of lime-based mortars in masonry piers under eccentric loading. *Construction and Building Materials*, *114*, 913–926. https://doi.org/10.1016/j

Nežerka, V., Bílý, P., Hrbek, V., & Fládr, J. (2019). Impact of silica fume, fly ash, and metakaolin on the thickness and strength of the ITZ in concrete. *Cement and Concrete Composites*, *103*, 252–262. https://doi.org/10.1016/j.cemconcomp.2019.05.012

Nežerka, V., Somr, M., & Trejbal, J. (2018). Contact angle measurement tool based on image analysis. *Experimental Techniques*, *42*(3), 271–278. https://doi.org/10.1007/s40799-017-0231-0

Nobili, A., Lanzoni, L., & Tarantino, A. (2013). Experimental investigation and monitoring of a polypropylene-based fiber reinforced concrete road pavement. *Construction and Building Materials*, *47*, 888–895. https://doi.org/10.1016/j.conbuildmat.2013.05.077

Ochi, T., Okubo, S., & Fukui, K. (2007). Development of recycled PET fiber and its application as concrete-reinforcing fiber. *Cement and Concrete Composites*, *29*(6), 448–455. https://doi.org/10.1016/j.cemconcomp.2007.02.002

Oh, B. H., Kim, J. C., & Choi, Y. C. (2007). Fracture behavior of concrete members reinforced with structural synthetic fibers. *Engineering Fracture Mechanics*, *74*(1-2), 243–257. https://doi.org/10.1016/j.engfracmech.2006.01.032

Öktem, T., Seventekin, N., Ayhan, H., & PİŞKİN, E. (2000). Modification of polyester and polyamide fabrics by different in situ plasma polymerization methods. *Turkish Journal of Chemistry*, *24*, 269–274.

Paegle, I., Minelli, F., & Fischer, G. (2016). Cracking and load-deformation behavior of fiber reinforced concrete: Influence of testing method. *Cement and Concrete Composites*, *73*, 147–163. https://doi.org/10.1016/j.cemconcomp.2016.06.012

Park, C.-G., & Lee, J.-W. (2013). Effect of nanosilica and silica fume content on the bond properties of macro-synthetic fibre in cement-based composites. *Magazine of Concrete Research*, *65*(3), 148–157. https://doi.org/10.1680/macr.12.00036

Prošek, Z., Nežerka, V., Hlůžek, R., Trejbal, J., Tesárek, P., & Karra'a, G. (2019). Role of lime, fly ash, and slag in cement pastes containing recycled concrete fines. *Construction and Building Materials*, *201*, 702–714. https://doi.org/10.1016/j.conbuildmat.2018.12.227

Prošek, Z., Trejbal, J., Nežerka, V., Goliáš, V., Faltus, M., & Tesárek, P. (2020). Recovery of residual anhydrous clinker in finely ground recycled concrete. *Resources, Conservation and Recycling*, *155*, 104640–104648. 104640. https://doi.org/10.1016/j.resconrec.2019

Razak, H. A., & Ferdiansyah, T. (2005). Toughness characteristics of arenga pinnata fibre concrete. *Journal of Natural Fibers*, *2*(2), 89–103. https://doi.org/10.1300/J395v02n02_06

Sadrinejad, I., Madandoust, R., & Ranjbar, M. M. (2018). The mechanical and durability properties of concrete containing hybrid synthetic fibers. *Construction and Building Materials*, *178*, 72–82. https://doi.org/10.1016/j.conbuildmat.2018.05.145

Schwartzentruber, A., Philippe, M., & Marchese, G. (2004). Effect of PVA, glass and metallic fibers, and of an expansive admixture on the cracking tendency of ultrahigh strength mortar. *Cement and Concrete Composites*, *26*(5), 573–580. https://doi.org/10.1016/S0958-9465(03)00076-3

Shen, B., Hubler, M., Paulino, G. H., & Struble, L. J. (2008). Functionally-graded fiber-reinforced cement composite: Processing, microstructure, and properties. *Cement and Concrete Composites*, *30*(8), 663–673. https://doi.org/10.1016/j.cemconcomp.2008.02.002

Shui, Z., Xuan, D., Wan, H., & Cao, B. (2008). Rehydration reactivity of recycled mortar from concrete waste experienced to thermal treatment. *Construction and Building Materials*, *22*(8), 1723–1729. https://doi.org/10.1016/j.conbuildmat.2007.05.012

Silva, D. A., Betioli, A. M., Gleize, P. J. P., Roman, H. R., Gómez, L. A., & Ribeiro, J. L. D. (2005). Degradation of recycled PET fibers in portland cement-based materials. *Cement and Concrete Research*, *35*(9), 1741–1746. https://doi.org/10.1016/j.cemconres.2004.10.040

Singh, S., Shukla, A., & Brown, R. (2004). Pullout behavior of polypropylene fibers from cementitious matrix. *Cement and Concrete Research*, *34*(10), 1919–1925. https://doi.org/10.1016/j.cemconres.2004.02.014

Tiberti, G., Minelli, F., & Plizzari, G. (2015). Cracking behavior in reinforced concrete members with steel fibers: A comprehensive experimental study. *Cement and Concrete Research*, *68*, 24–34. https://doi.org/10.1016/j.cemconres.2014.10.011

Tosun, K., Felekoğlu, B., & Baradan, B. (2012). Multiple cracking response of plasma treated polyethy-lene fiber reinforced cementitious composites under flexural loading. *Cement and Concrete Composites*, *34*(4), 508–520. https://doi.org/10.1016/j.cemconcomp.2011.12.001

Trejbal, J. (2018). Mechanical properties of lime-based mortars reinforced with plasma treated glass fibers. *Construction and Building Materials*, *190*, 929–938. https://doi.org/10.1016/j.conbuildmat.2018.09.175

Trejbal, J., Ďureje, J., Hlůžek, R., & Prošek, Z. (2018). Interaction assessment between fiber reinforcement and cement matrix containing finely ground recycled concrete. *IOP Conference Series: Materials Science and Engineering*, *379*, 012016. https://doi.org/10.1088/1757-899X/379/1/012016

Trejbal, J., Kopecký, L., Tesárek, P., Fládr, J., Antoš, J., Somr, M., & Nežerka, V. (2016). Impact of surface plasma treatment on the performance of PET fiber reinforcement in cementitious composites. *Cement and Concrete Research*, *89*, 276–287. https://doi.org/10.1016/j.cemconres.2016.08.018

Trejbal, J., Nežerka, V., Somr, M., Fládr, J., Potocký, Š., Artemenko, A., & Tesárek, P. (2018). Deterioration of bonding capacity of plasma-treated polymer fiber reinforcement. *Cement and Concrete Composites*, *89*, 205–215. https://doi.org/10.1016/j.cemconcomp.2018.03.010

Trejbal, J., Šmilauer, V., Kromka, A., Potocký, S., Kopecky, L. (2015). *Wettability enhancement of polymeric and glass micro fiber reinforcement by plasma treatment*. Proceedings of the 7-th International Conference on Research & Application, Brno, pp. 315––320.

Wang, C., & He, X. (2006). Polypropylene surface modification model in atmospheric pressure dielectric barrier discharge. *Surface and Coatings Technology*, *201*(6), 3377–3384. https://doi.org/10.1016/j.surfcoat.2006.07.205

Xu, Y., & Chung, D. (1999). Carbon fiber reinforced cement improved by using silane-treated carbon fibers. *Cement and Concrete Research*, *29*(5), 773–776. https://doi.org/10.1016/S0008-8846(99)00015-0

Zakaria, M., Ahmed, M., Hoque, M., & Shaid, A. (2020). A comparative study of the mechanical properties of jute fiber and yarn reinforced concrete composites. *Journal of Natural Fibers*, *17*(5), 676–612. https://doi.org/10.1080/15440478.2018.1525465

Zhang, J., & Li, V. C. (2002). Monotonic and fatigue performance in bending of fiber-reinforced engineered cementitious composite in overlay system. *Cement and Concrete Research*, *32*(3), 415–423. https://doi.org/10.1016/S0008-8846(01)00695-0

Zheng, Z. (1995). Synthetic fibre-reinforced concrete. *Progress in Polymer Science*, *20*(2), 185–210. https://doi.org/10.1016/0079-6700(94)00030-6

Appendix A. Load-displacement diagrams

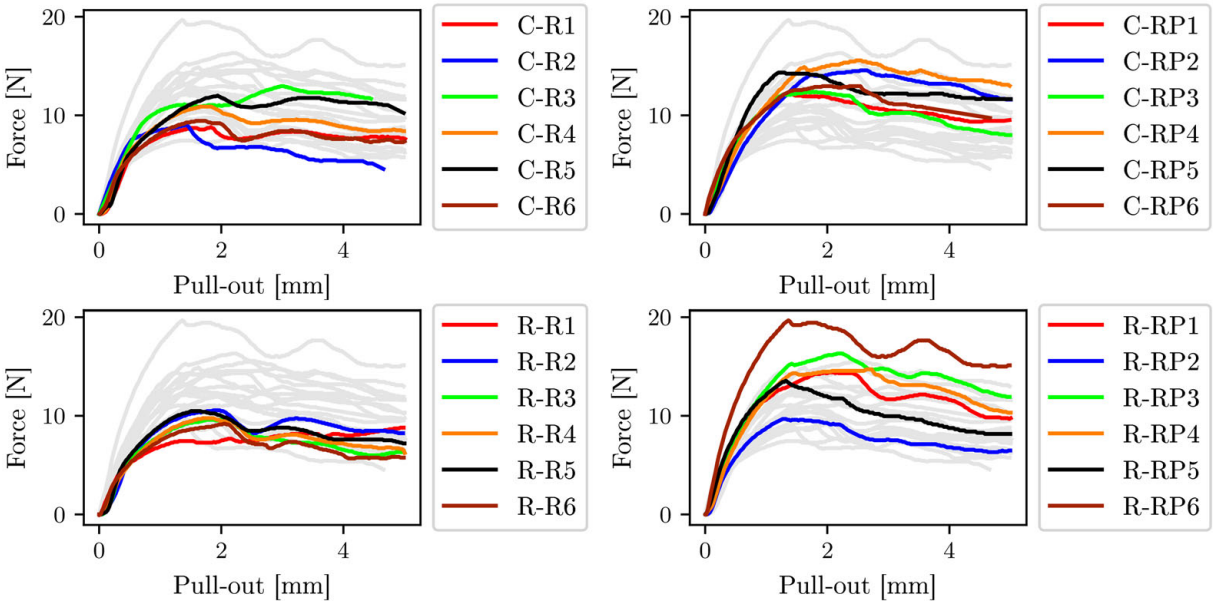

Figure A1. Load-displacement diagrams recorded during pull-out tests on round fiber specimens at L = l.

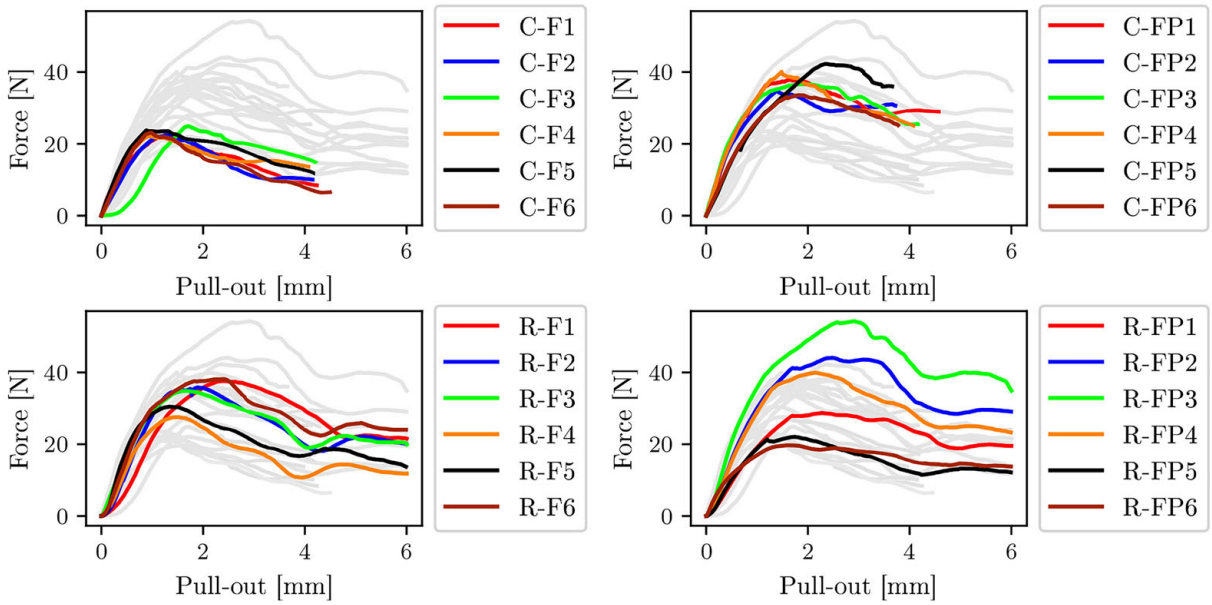

Figure A2. Load-displacement diagrams recorded during pull-out tests on flat fiber specimens at L = I.

Table A1. Averages and standard deviations for maximum force F_{max} and forces at displacements 0.5, 1.5, 2.5, and 3.5 ($F_{0,5}$, $F_{1,5}$, $F_{2,5}$, and $F_{3,5}$, respectively), measured during pull-out tests at L = I for individual fiber/matrix configurations.

Set of specimens	Fmax [N]	F0.5 [N]	F1.5 [N]	F2.5 [N]	F3.5 [N]
C-R	10.5 ± 1.56	6.3 ± 0.54	9.9 ± 1.07	9.0 ± 1.85	9.2 ± 2.32
C-RP	13.7 ± 1.22	7.0 ± 0.78	13.1 ± 0.92	13.0 ± 1.61	11.9 ± 1.66
R-R	9.7 ± 0.63	5.4 ± 0.26	9.3 ± 1.01	7.9 ± 0.44	8.0 ± 0.84
R-RP	14.7 ± 3.00	8.1 ± 1.74	14.1 ± 2.86	13.3 ± 3.10	12.3 ± 3.34
C-F	23.0 ± 1.07	13.1 ± 4.80	21.4 ± 0.90	18.0 ± 2.35	17.7 ± 2.50
C-FP	37.6 ± 2.93	19.1 ± 2.56	35.3 ± 2.49	34.6 ± 3.99	32.8 ± 3.24
R-F	34.1 ± 3.83	14.0 ± 3.76	32.2 ± 2.84	30.4 ± 6.50	24.3 ± 6.47
R-FP	34.8 ± 12.36	13.8 ± 3.87	31.1 ± 9.17	33.8 ± 12.81	30.4 ± 12.36

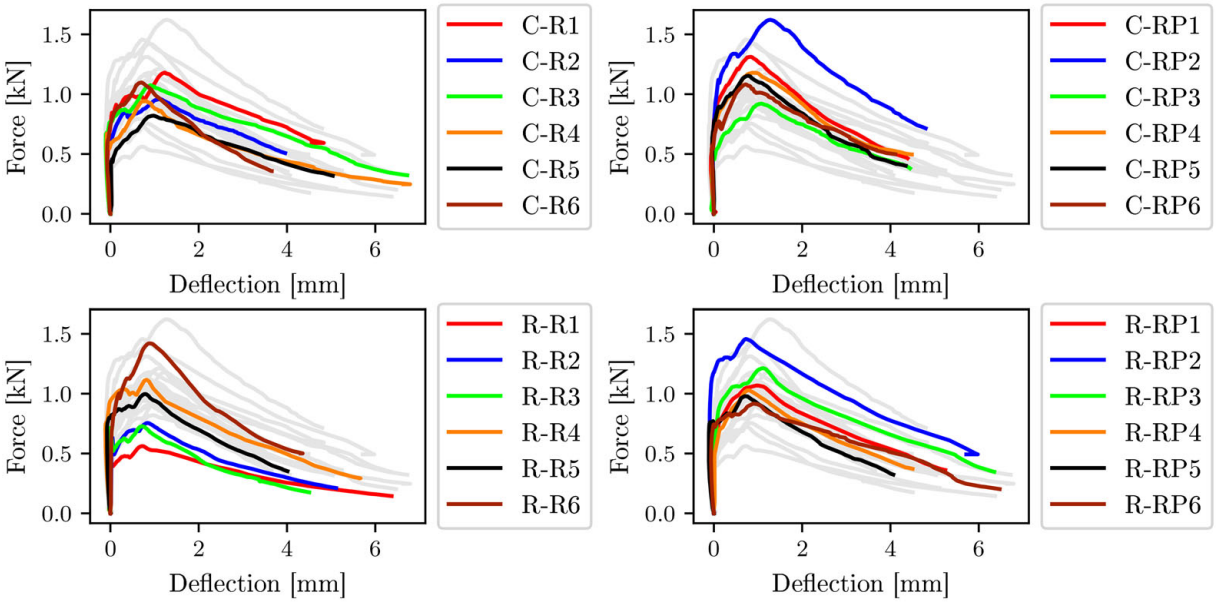

Figure A3. Deflection of specimens reinforced with round fibers tested at L = II.

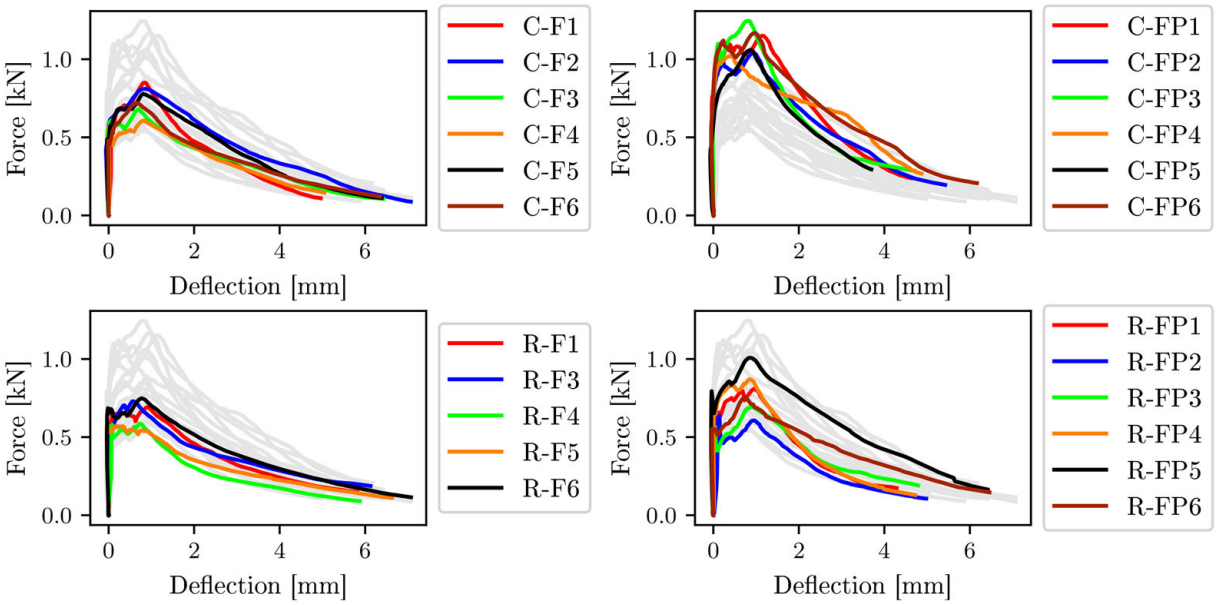

Figure A4. Deflection of specimens reinforced with flat fibers tested at L = II.

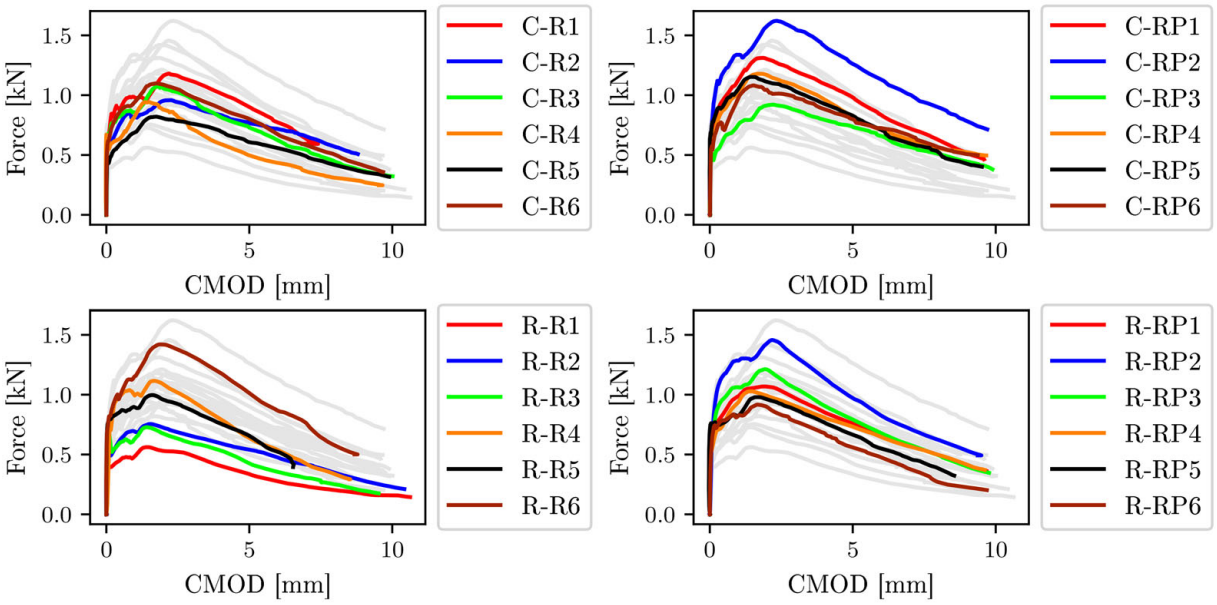

Figure A5. CMOD measured on specimens reinforced with round fibers tested at L = II.

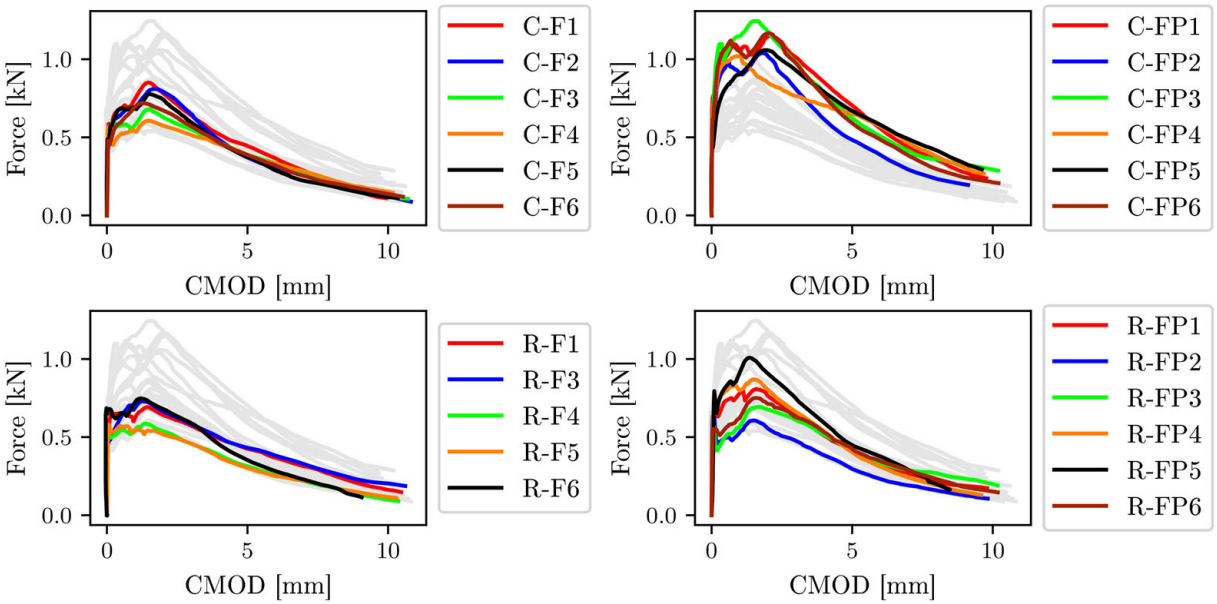

Figure A6. CMOD measured on specimens reinforced with flat fibers tested at L = II.

Table A2. Averages and standard deviations for maximum force F_{max} and forces at CMODs equal to 0.5, 1.5, 2.5, and 3.5 mm ($F_{0,5}$, $F_{1,5}$, $F_{2,5}$, and $F_{3,5}$, respectively), measured during three-point bending tests at L = II for individual fiber/matrix configurations.

Set of specimens	F_{max} [N]	$F_{0.5}$ [N]	$F_{1.5}$ [N]	$F_{2.5}$ [N]	$F_{3.5}$ [N]
C-R	1.01 ± 0.118	0.77 ± 0.111	0.95 ± 0.090	0.96 ± 0.133	0.86 ± 0.135
C-RP	1.21 ± 0.218	0.89 ± 0.182	1.15 ± 0.185	1.17 ± 0.226	1.07 ± 0.215
R-R	0.93 ± 0.285	0.76 ± 0.207	0.91 ± 0.265	0.86 ± 0.287	0.76 ± 0.260
R-RP	1.11 ± 0.180	0.88 ± 0.147	1.06 ± 0.126	1.05 ± 0.189	0.92 ± 0.158
C-F	0.74 ± 0.082	0.62 ± 0.060	0.74 ± 0.081	0.65 ± 0.065	0.53 ± 0.028
C-FP	1.11 ± 0.079	0.97 ± 0.079	1.04 ± 0.099	0.99 ± 0.109	0.83 ± 0.081
R-F	0.67 ± 0.071	0.61 ± 0.047	0.65 ± 0.076	0.57 ± 0.062	0.49 ± 0.055
R-FP	0.79 ± 0.122	0.65 ± 0.136	0.79 ± 0.126	0.68 ± 0.097	0.57 ± 0.070

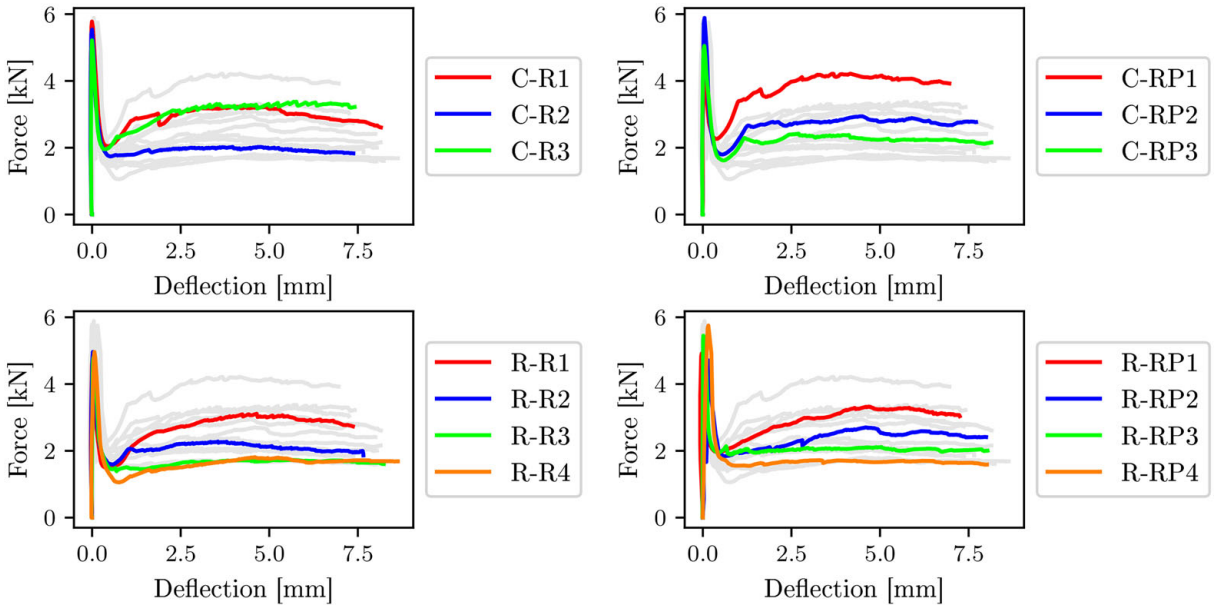

Figure A7. Deflection of specimens reinforced with round fibers tested at L = III.

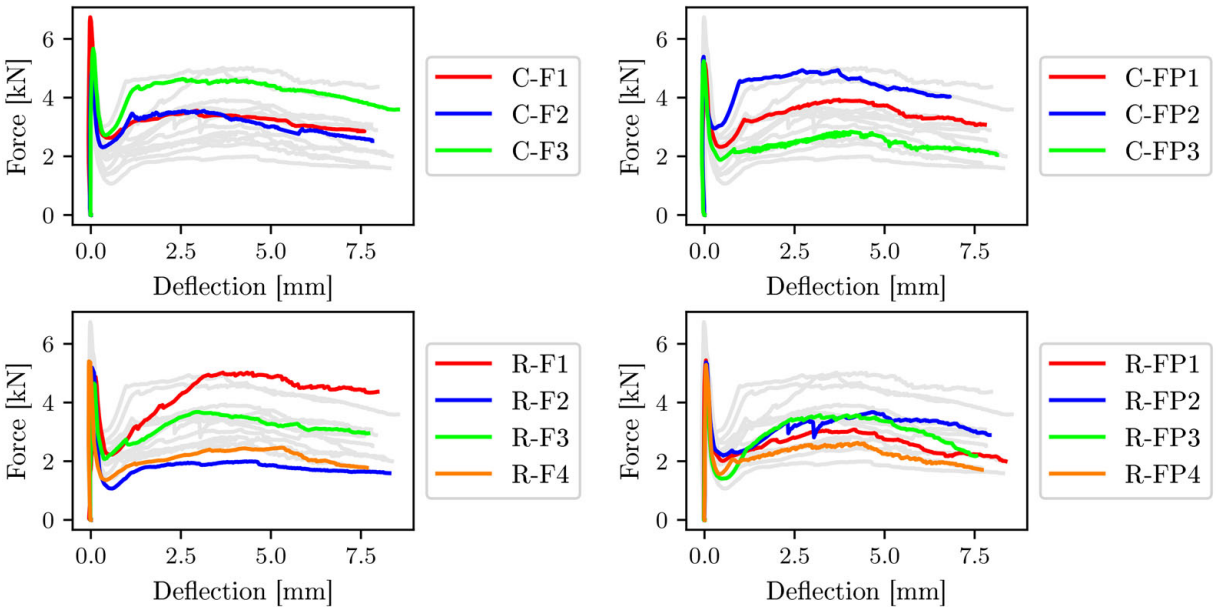

Figure A8. Deflection of specimens reinforced with flat fibers tested at L = III.

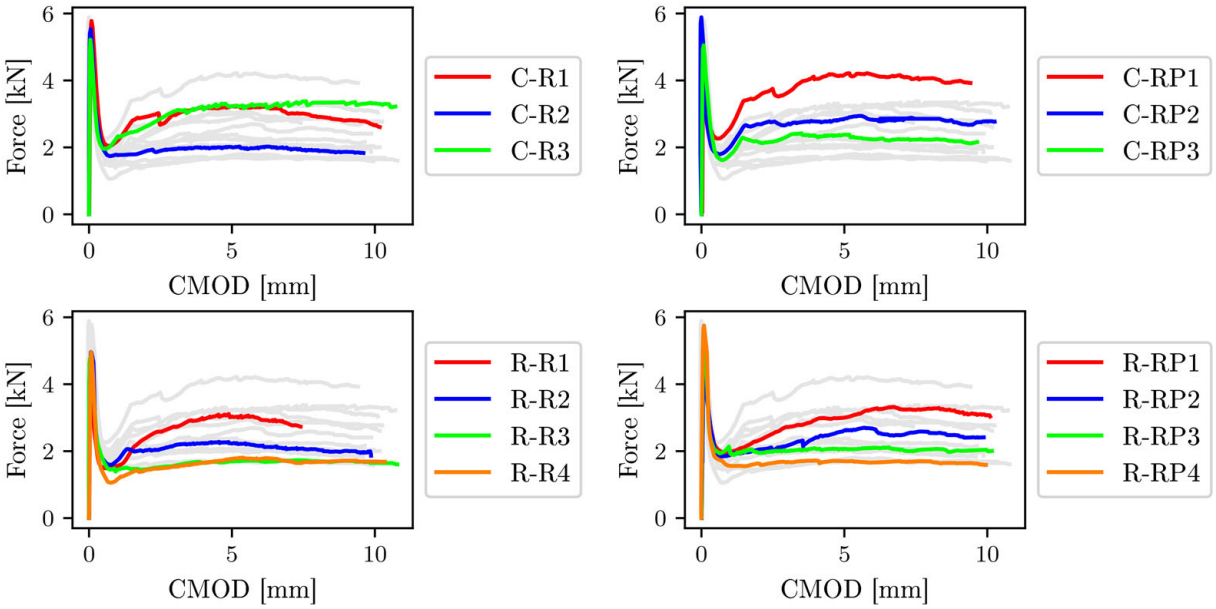

Figure A9. CMOD measured on specimens reinforced with round fibers tested at L = III.

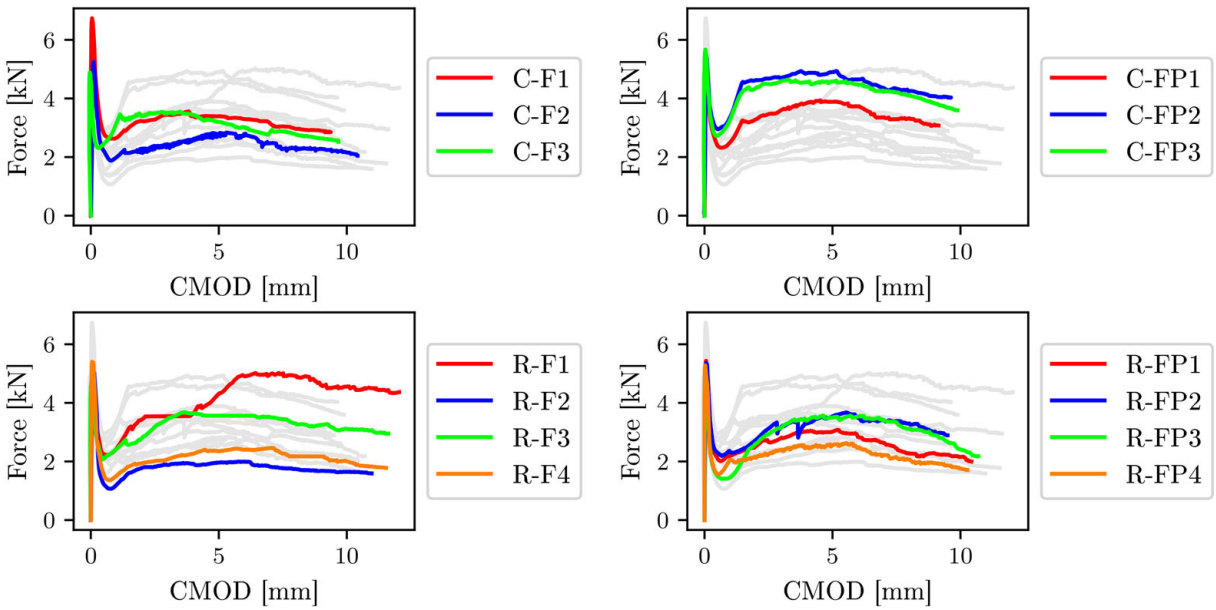

Figure A10. CMOD measured on specimens reinforced with flat fibers tested at L = III.

Table A3. Averages and standard deviations for maximum force F_{max} and forces at CMODs equal to 0.5, 1.5, 2.5, and 3.5 mm ($F_{0,5}$, $F_{1,5}$, $F_{2,5}$, and $F_{3,5}$, respectively), measured during three-point bending tests at L = III for individual fiber/matrix configurations.

Set of specimens	F_{max} [N]	$F_{0.5}$ [N]	$F_{1.5}$ [N]	$F_{2.5}$ [N]	$F_{3.5}$ [N]
C-R	5.5 ± 0.23	2.0 ± 0.12	2.3 ± 0.41	2.5 ± 0.42	2.7 ± 0.52
C-RP	5.1 ± 0.68	2.0 ± 0.22	2.8 ± 0.47	2.9 ± 0.63	3.0 ± 0.66
R-R	4.9 ± 0.12	1.6 ± 0.16	1.7 ± 0.31	1.9 ± 0.45	2.1 ± 0.53
R-RP	5.2 ± 0.41	2.0 ± 0.11	1.9 ± 0.22	2.0 ± 0.32	2.2 ± 0.40
C-F	5.6 ± 0.80	2.5 ± 0.25	2.8 ± 0.51	3.0 ± 0.51	3.2 ± 0.47
C-FP	5.4 ± 0.21	2.7 ± 0.23	4.0 ± 0.56	4.2 ± 0.53	4.4 ± 0.47
R-F	5.1 ± 0.28	1.8 ± 0.41	2.3 ± 0.61	2.6 ± 0.73	2.8 ± 0.77
R-FP	5.3 ± 0.17	1.9 ± 0.34	2.2 ± 0.18	2.7 ± 0.33	3.1 ± 0.37